Universidad Autónoma de San Luis Potosí
Doctorado Institucional en Ingeniería y Ciencia de Materiales

DESIGNED NANOMATERIALS FOR SENSING

Presenta
M.C. Selene Concepción Acosta Morales

Tesis para obtener el Grado de
Doctor en Ingeniería y Ciencia de Materiales

Dirigida por
Dra. Mildred Quintana Ruiz
Dra. Carla Bittencourt

Septiembre 2021

Acknowledgments

Agradezco a la Universidad Autónoma de San Luis Potosí por el financiamiento de este proyecto de Tesis. A la institución CONACyT por el financiamiento con el numero de beca 486938.

Agradezco profundamente a los miembros del jurado por tomarse el tiempo para evaluar este trabajo.

Expreso mi total agradecimiento a mi asesora en la Universidad de San Luis Potosí, la Dra. Mildred Quintana quien me inspiró y me guío durante todo el proceso de doctorado y me brindó su apoyo para estudiar parte de este trabajo en el extranjero.

I am very grateful with my adviser in the University of Mons Dr. Carla Bittencourt for having welcome me as her student and giving me the opportunity to learn so many new things and live new experiences. I am also grateful for giving me confidence in my person and my abilities. Dr. Carla Bittencourt is not only an excellent advisor but also an exceptional person.

I thank to Prof. Rony Snyders for having welcomed me in the ChIPS laboratory in the University of Mons in Belgium.

Among the people in the ChIPS laboratory and Materia Nova, I specially thank to Xavier Noirfalise and Alice Belfiore for the training in XPS and for giving me their knowledge and help during these time always with a lot of patience and kindness. To Dany, thanks for all the hard work, and your always timely help. I want to thank also to Sabine, Philippe, Damien, and Lisa for your help in my training and work.

I also thank to all the collaborators of this work: Prof. Chris Ewels, Prof. Colomer, Ayrton Sierra, Dr. Polona Umek, Dr. Maja Garvas, Prof. Eduard Llobet, and Dr. Juan Casanova. We definitely had a very productive collaboration, it was an honor to work with all of you. Specially, I want to thank to Polona and Maja that welcome me in Slovenia and share its knowledge and company with me during my short but very rewarding stay in Slovenia.

A mi amiga Gabriela Garzón, conocerte fue uno de los mejores sucesos de esta experiencia, me divertí muchísimo a tu lado, hiciste que estos dos años fuera de mi casa y de mi país parecieran poco, me has enseñado lo que es tener una amistad verdadera. Eres una persona única, de verdad muchas gracias por todo tu apoyo.

A mis amigos Gabriela, Joel, William y Fedoua, mi pequeña familia de Mons, los llevo en mi corazón, gracias por todo.

Quiero agradecer especialmente a mis padres por haberme dado educación, un hogar donde crecer, equivocarme, aprender y por enseñarme con el ejemplo los valores que hoy definen mi vida. A mis hermanos Luis y Ronaldo por cuidar de mis papás mientras yo no estuve en casa y por hacerme sentir siempre acompañada aunque estuviéramos lejos físicamente.

Y finalmente, agradezco a mi compañero de vida Jonathan Said, gracias por emprender la aventura de vivir lejos de tu país para estar conmigo. Gracias por tu apoyo incondicional, este logro también es tuyo.

Abstract

A sensor is a device developed for detecting or measuring a physical or bio-chemical quantity such as light, sound, pressure, temperature as well as magnetic field strength. Sensors have an important impact in our daily life, they are used to obtain information of our surroundings and body in real time. Nowadays, we use sensors to detect toxic analytes in the air, to examine the quality of food, and also to monitor our health. However, the majority of the sensors currently used have high power consumptions. Therefore, there is still the need to develop small, portable, reliable, autonomous and low power consumption sensors. Nanomaterials are perfect candidates to be used as active materials in novel sensors. For example, for the case of chemical sensors, the interaction between the sensor and the molecules of interest takes place at the surface of the sensor, nanomaterials have the most of its atoms at their surfaces, that is, a high surface-to-volume ratio that increases the number of available sites for interaction with the molecules to be detected. Besides this, the unique chemical, mechanical, optical and magnetic properties of nanomaterials open up numerous possibilities to develop new active materials with tailored properties for sensors. The aim of this thesis was the design and investigation of new active nanomaterials based on lanthanide and carbon nanotubes for the development of two different types of sensors. Lanthanide based nanomaterials (Eu^{3+}-TiO_2) were evaluated in the biological photoluminescence window as temperature sensors and carbon based nanomaterials were investigated as gas sensors.

In the first part of the thesis carbon nanotubes based nanomaterials are investigated for gas detection of the following toxic gases: toluene, ethanol, NO_2 and H_2. The intrinsically inert surface of CNTs is the main limitation for the achievement of high sensitivity carbon nanotubes based gas sensors. For this reason, the carbon nanotubes surface is firstly functionalized with oxygen groups. The functionalization is carried out with low kinetic energy ion irradiation. Low kinetic energy ion irradiation is a very trending technique for functionalization of carbon nanomaterials because is fast, clean and defect controllable. Four different types of oxygen groups were attached to the surface of carbon nanotubes: hydroxyl

(C-OH), epoxy (C-O), carbonyl (C=O) and carboxyl (COOH). Then, the thermal stability of the oxygen groups is evaluated trough a resistive heating treatment in ultra high vacuum. Carbonyl and hydroxyl are the most stable groups at the CNTs surface. Afterwards, the Ox-CNTs are decorated with metal nanoparticles in order to improve their reactivity to the gas molecules, Pd and Ni-Pd nanoparticles were deposited at the surface of the CNTs trough plasma sputtering deposition. Finally, Pd-Ox-CNTs and Ni-Pd-Ox-CNTs are tested as active materials for the sensing of harmful gases. The Ox-CNTs decorated with bimetallic Ni-Pd nanoparticles have improved sensing response compared to Ox-CNTs for detection of toluene, ethanol, NO_2, and H_2. The sensors show high sensitivity for detection of gases at near room temperature measurements, these characteristics allow the development of sensors with low power consumption, one of the main objectives in the gas sensing research field.

In the second part of this Ph.D. thesis work TiO_2 nanomaterials doped with trivalent europium ion (Eu^{3+}) are investigated as temperature sensors in the first biological photoluminescence window. The luminescence intensity of Eu^{3+} critically depends on temperature, this property is used to develop a luminescent nanothermometer. First, Eu^{3+}-TiO_2 nanoparticles with three concentrations of europium (1, 3 and 5 wt. %) are synthetized by the sol-gel technique. After the synthesis, the nanoparticles are characterized through several techniques: XRD, TEM, SEM and XPS. Then, the dependence of luminescence intensity with temperature of Eu^{3+}-TiO_2 is investigated, two different electronic transitions were used to develop a radiometric nanothermometer with relative sensitivity values between 1.78 and 1.41% K^{-1}. In the final part of this work, Eu^{3+}-TiO_2 nanoparticles are internalized in mouse fibroblast cells (L929), the successful internalization is observed through fluorescence microscopy and fluorescence microspectroscopy. The luminescence of nanoparticles internalized in L929 fibroblast cells is measured when the system is heated at five different temperatures. An appropriate calibration curve using the luminescence intensity of the nanoparticles is obtained. Finally, the temperature variation inside the cells is determined using the Eu^{3+}-TiO_2 nanothermometer with sensitivity of 0.5 K per 1% of luminosity change when heated.

Table of Contents

List of acronyms

AOTFs	Acousto-optical Tunable Filters
ATM	Atomic Force Microscopy
CBM	Conduction Band Minimum
CCD	Charge Coupled Device
CNTs	Carbon Nanotubes
Covid-19	Coronavirus Disease 19
CVD	Chemical Vapor Deposition
DC	Direct Current
DFT	Density-functional theory
DOS	Density of States
ED	Electric Dipole
EMCCD	Electron Multiplying Charge-Coupled Device
EQ	Electric Quadrupole
FMS	Fluorescence Microspectroscopy System
IC	Internal Conversion
ICCD	International Centre for Diffraction Data
LCFTs	Liquid Crystal Tunable Filters
LED	Light-Emitting Diode
MD	Magnetic Dipole

MWCNTs	Multi Walled Carbon Nanotubes
NIR	Near Infrared
Ox-CNTs	Oxygen functionalized Carbon Nanotubes
PBS	Phosphate Buffered Saline
pH	Potential of Hydrogen
QDs	Quantum Dots
RF	Radio Frequency
RT	Room Temperature
SARS-Cov-2	Severe Acute Respiratory Syndrome Coronavirus 2
SEM	Scanning Electron Microscopy
STEM	Scanning Thermal Microscopy
SWCNTs	Single Wall Carbon Nanotubes
TEM	Transmission Electron Microscopy
TPIS	Tectra Plasma Ion Source
UHV	Ultra High Vacuum
UV	Ultra Violet
VBM	Valence Band Maximum
v-CNTs	Vertically aligned Carbon Nanotubes
VOCs	Volatile Organic Compounds
WHO	World Health Organization
XPS	X-Ray Photoelectron Spectroscopy
XRD	X-Ray Diffraction

Chapter 1

Context

Here, the main scientific questions raised in this work are presented. The fundamental scientific motivations and the potentialities for the development of novel sensors based on nanostructured materials are given, showing the consequent breakthroughs in science and technology. Additionally, the research objectives of this Ph.D. thesis are explained and the experimental methodology employed to accomplish these objectives is described.

1.1 Motivation: sensors as guardian angels

Sensors are devices developed to detect or measure a physical or bio-chemical quantity such as chemicals, light, sound, pressure, temperature or magnetic field strength. Nowadays, sensors are used in a huge variety of technological subjects and in all areas of our daily life. For example, in the industry, the location of persons working in risk environments can be followed by body monitored sensors. In traffic control, sensors are now used to obtain locations, warn about traffic jams, and alert to the driver about the vehicle status, and information on the vehicle surroundings can be obtained using sensors in order to prevent accidents. In health, sensors are used to monitor real time data of our bodies such as blood pressure and glucose concentration, providing a comfortable life for those patients who suffer from chronic diseases or helping people suffering from allergies with preventing warnings, for example, the concentration of pollen in a determinate place. In the current Covid-19 health crisis caused by the virus SARS-CoV-2 blood oxygen sensors are saving the lives of millions of people. In environment control, sensors are used to measure the quality of the ambient air, and some advices are given to the population of high contaminate cities to prevent outdoors activities when toxic substances exceed their permitted concentration. Taking in consideration all these examples, sensors can be considered nowadays as an extension of our senses (smell, sight, hear, touch and taste), they give us relevant information at real time from our complex surroundings. With the use of sensors, we can get advises when we are in confuse or dangerous situations, making our life easier in terms of security and health. Because of all of these implementations, sensors have been entitled as “guardian angels”.

The majority of the sensors currently used as guardian angels are based on bulk materials and have high power consumption, for example smartphones and smart watches need to be

charged approximately every 24 hours, besides, a number of these sensors cannot be miniaturized. There is still the need to develop sensors that are small, portable, autonomous and easy to manage, that can be used personally, be secure and reliable and very important, that have low power consumption. The use of nanostructured materials to develop these optimal portable sensors is of scientific and technological interest due to their promising and unique properties.

Besides improving the characteristics of currently sensors used, nanomaterials can be employed to create novel nanosensors, that is, nanometric scale sensors that open completely new avenues for novel applications. Here, we studied in detail nanostructures and their modification aiming at understanding their characteristics and properties as sensing materials.

1.2 Research objectives

Novel sensors to monitor the quality of our surroundings, such as quality of the drinking water, food and air and sensors to monitor our body, are being developed to increase the quality of our daily life. The majority of the research for the development of novel, small, portable, low consumption power and high sensitive sensors relies on the use of nanomaterials (materials with one or more of their dimensions measuring between 1-100 nm). Nanomaterials can be classified in nanocarbons, nanometals, nanoceramics and nanocomposites, they have interesting and different mechanical, optical, and physicochemical properties from their bulk counterparts. Taking advantage of these properties to develop novel sensors is the main objective of this thesis.

During this work two types of sensors were investigated: a chemical sensor used to detect hazardous gases in air and a temperature sensor used to measure temperature of a single cell with submicrometric spatial resolution.

In this perspective the objectives of this thesis are:

(1) Design a novel chemical sensor based on carbon nanotubes decorated with bi-metallic nanoparticles to detect hazardous gases in air.

Carbon nanotubes are used to develop chemical sensors to detect hazardous gases in air. The chemical reactivity of carbon nanotubes with gas molecules is tailored by functionalizing carbon nanotubes with oxygen groups and decorating their surface with bimetallic nanoparticles. The technique for oxygen functionalization employed is low kinetic ion irradiation, this technique is fully discussed and compared with other carbon nanotubes functionalization techniques. Afterwards, carbon nanotubes are decorated with bimetallic nanoparticles aiming at increasing their responses to hazardous gases. The conjugation with metal nanoparticles is carried out by plasma sputtering deposition and the chemical and physical properties of the obtained hybrid nanomaterial are investigated and discussed. The designed sensor active layer is used to detect: toluene, ethanol, NO_2 and H_2 in part per million in air.

(2) Design of a temperature sensor based on trivalent europium-doped titanium oxide nanoparticles.

The luminescence dependency with temperature of the trivalent europium ion (Eu^{3+}) is used to design a novel temperature nanosensor that measures temperature with submicrometric spatial resolution. Europium ions are hosted in a titanium oxide matrix nanoparticles (TiO_2) synthetized by the Sol-gel method. The physicochemical properties of Eu^{3+}-doped TiO_2 nanoparticles are investigated in detail, and the temperature effect on their luminescence properties is evaluated. Appropriated temperature calibration curves are generated aiming at the use of the Eu^{3+}-doped TiO_2 nanoparticles as temperature nanosensors for biological systems. Finally, the Eu^{3+}-doped TiO_2 nanoparticles are applied as nanothermometers to detect changes in the temperature of single cells.

1.3 Experimental methodology

Based on the research objectives the manuscript is organized as follows:

Chapter 2 provides a detailed introduction of the topic covered by this thesis, the relevance of nanomaterials for optimal sensor design and the state of the art of the two types of sensors here designed is reviewed.

Chapter 3 is centered in the experimental work performed for the development of a chemical gas sensor based on carbon nanotubes to detect toxic gases, the results obtained from each step of this investigation are discussed. Figure 1.1 describes the research strategy employed for this part of the thesis.

The results presented in this chapter are published in:

Acosta, S., Casanova Chafer, J., Sierra Castillo, A., Llobet, E., Snyders, R., Colomer, J. F., Ewels, C., Bittencourt, C. (2019). Low Kinetic Energy Oxygen Ion Irradiation of Vertically Aligned Carbon Nanotubes. *Applied Sciences*, *9*(24), 5342.

Acosta, S., Sierra-Castillo, A., Colomer, J. F., Ewels, C., Snyders, R., Bittencourt, C. Thermal stability of oxygen functionalizations in v-CNTs introduced by low kinetic energy ion irradiation. (Under consideration in *Vacuum* journal).

In Chapter 4 is reported the experimental work performed to design a temperature nanosensor based on the luminescence properties of Eu^{3+}-doped titanium oxide. This nanosensor was used to measure temperature of single cells, the results obtained from each step of this investigation are discussed here. Figure 1.2 explains the research strategy employed for this part of the thesis.

The results presented in this chapter are published in:

Borrero-González, L. J., **Acosta, S**., Bittencourt, C., Garvas, M., Umek, P., Nunes, L. A. O. (2020). Eu^{3+}− doped titanium oxide nanoparticles for optical thermometry in the first biological window. *Optical Materials*, *101*, 109770.

Garvas, M., **Acosta, S.**, Urbančič, I., Koklič, T., Štrancar, J., Nunes, L. A. O., Guttmann, P., Umek, P., Bittencourt, C. Single cell temperature probed by Eu^{3+} doped TiO_2 nanoparticles luminescence. (2020). Nano Select.

Chapter 5 contains the conclusions and perspectives of the thesis work. Finally, in the appendix section the characterization techniques used in the design and application of the two novel sensors here developed are described.

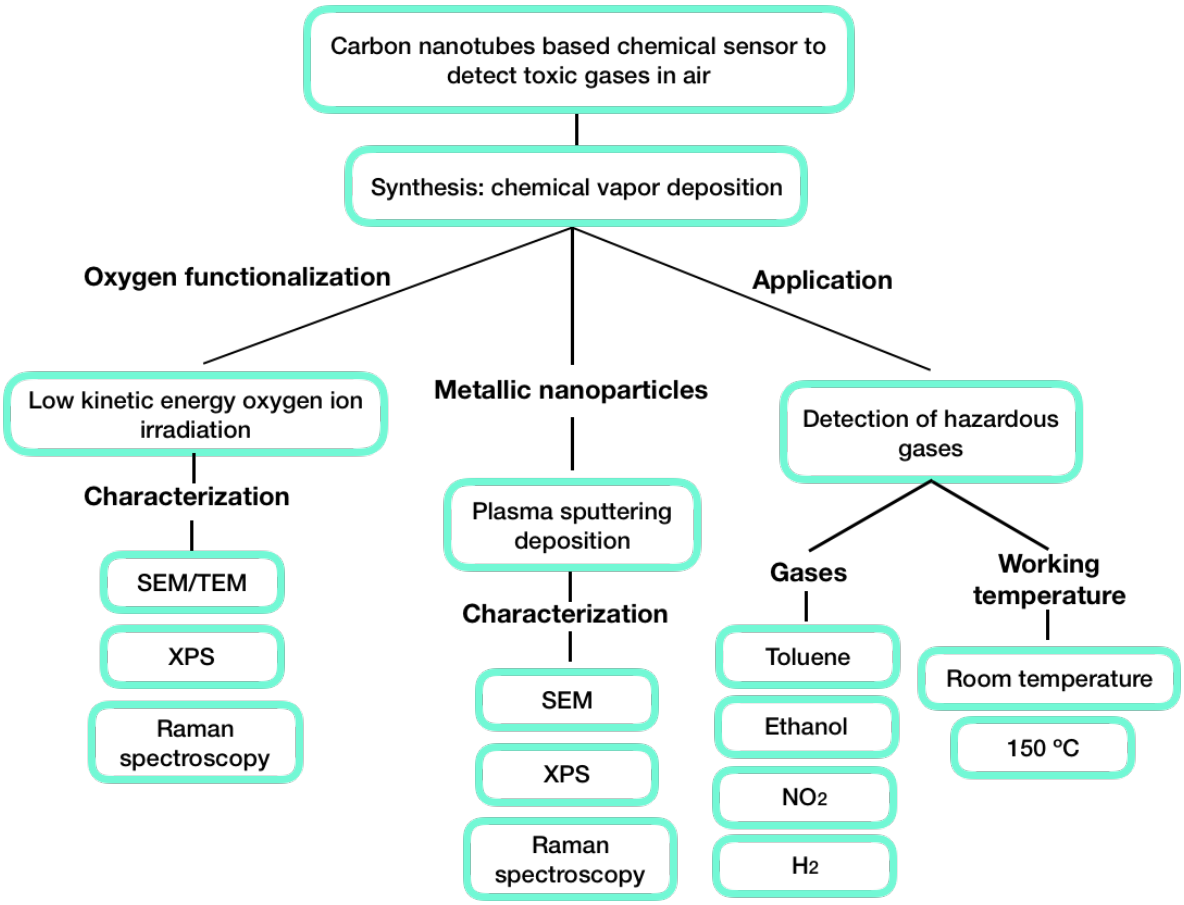

Figure 1.1. Diagram of the research strategy employed in the first part of this work.

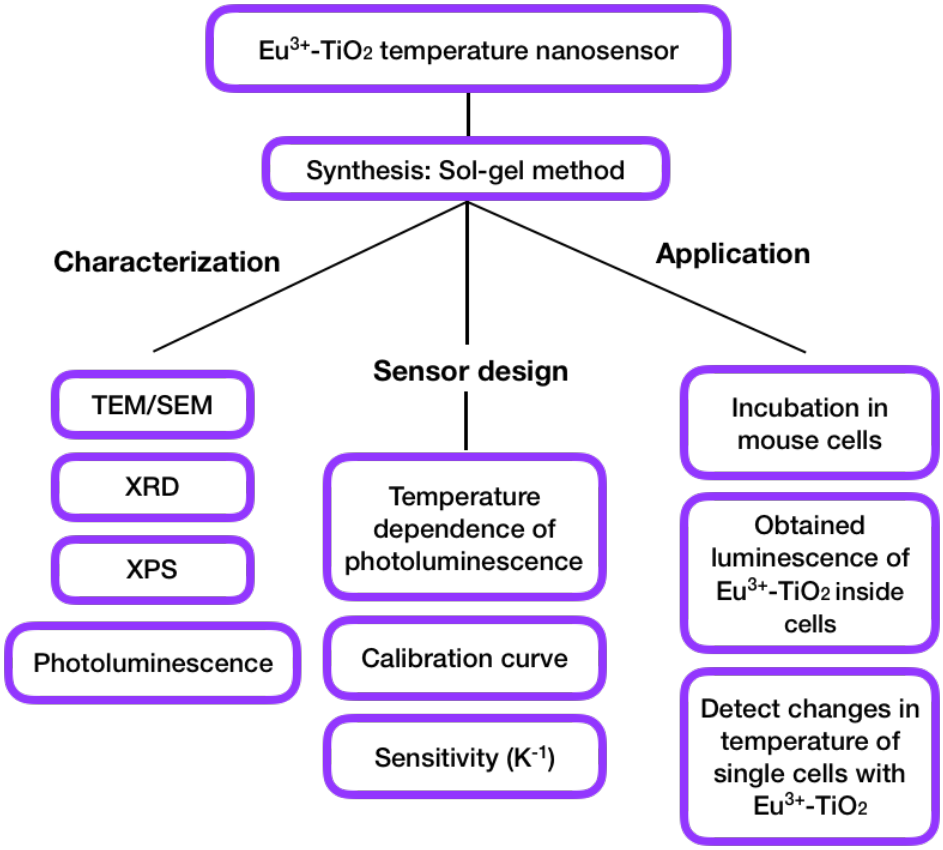

Figure 1.2. Diagram of the research strategy employed in the second part of this work.

Chapter 2

Introduction

2.1 Nanomaterials

Neal Lane defined nanotechnology as the knowledge and engineering (design and control) of physical, chemical, and biological systems at the nanometer scale (10^{-9} m) [1]. From the importance of nanotechnology, new more specialized fields have surged, among them it is nanomaterials, which study the production, properties, and applications of materials at the nanometer scale. Materials with one or more of their dimensions measuring between 1-100 nm having different physical and chemical properties to their bulk-form counterparts are considered nanomaterials. There are plenty families of nanomaterials, such as nanocarbons, nanometals, nanoceramics and nanocomposites (Figure 2.1) [1].

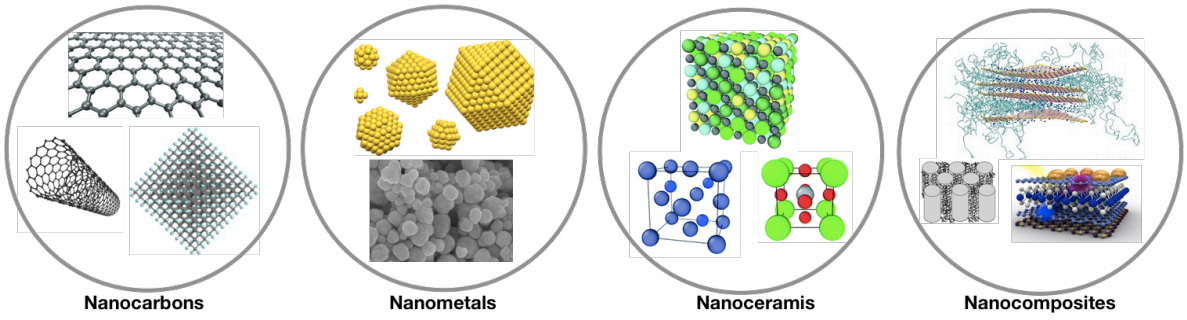

Figure 2.1. Examples of different types of nanomaterials classified as nanocarbons, nanometals, nanoceramics and nanocomposites.

The methods of synthesis of nanomaterials can be classified in two types: top-down methods or bottom-up methods (Figure 2.2). The top-down methods refers to techniques were bulk materials are used as raw materials to generate nanomaterials, these techniques includes, sonothermal synthesis, exfoliation of bulk materials, photolithography, among others [2]. In the other hand, the bottom-up techniques use atoms or molecules to synthetize nanomaterials.

For example, nucleation to from nanoparticles, and the most used technique chemical vapor deposition [3,4].

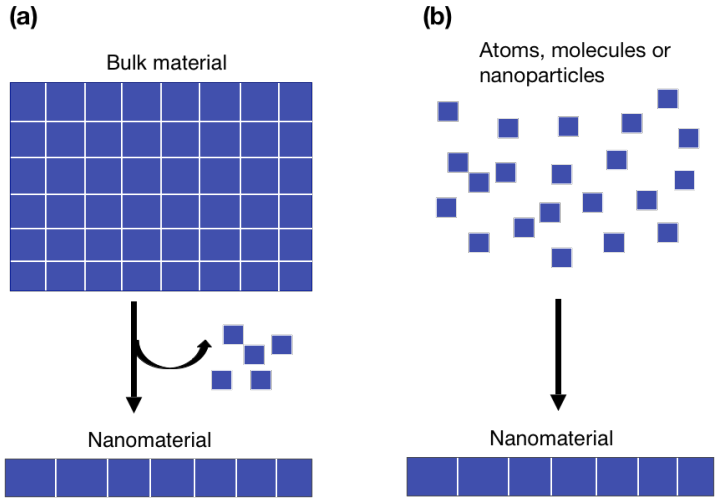

Figure 2.2. Schematic representation of synthesis methods of nanomaterials. (a) top-down method (b) bottom-up methods.

Nanomaterials differ from bulk materials in several ways, these differences explain why nanomaterials are being intensively studied and being proposed to improve and substitute bulk materials in numerous applications. Quantum confinement is the spatial confinement of electron–hole pairs in one or more dimensions within a material to specific discrete energy levels and occurs as particle size becomes the same or smaller than the Bohr radius. The effect of quantum confinement at the nanoscale becomes very significant in nanomaterials affecting their properties, for example, the energy of the band gap of semiconductors and the photoluminescence of some materials like quantum dots. Another important characteristic of nanomaterials is that the great majority of their atoms are at their surfaces, these atoms have different properties than the bulk atoms [1]. These features change the mechanical, electrical, optical, and thermal properties of the nanomaterials.

The properties of nanomaterials depend on their size and morphology (porosity, surface roughness, dimensionality). Referring to mechanical properties, there is a contraction on the bond length (metallic, covalent, and ionic) of nanomaterials compared to bulk materials (effect of nanomaterials having the major of their atoms at their surface) the shorter the bond length results in stronger and stiffer materials. For example, in the case of metals there is an increase in the hardness to 3-100 times when the nanoparticle size is smaller than 100 nm [1]. The electrical properties of nanomaterials also differ from bulk material properties. Nanomaterials conduct electrical current in different way than bulk conductor materials. For example, in the case of carbon nanotubes, the conductance mechanism is reported to be

diffusive at room temperature [5]. Carbon nanotubes present a high current-carrying-capacity without failure caused by electromigration due to the covalent bonding between carbon atoms that impede that charge carriers and high temperature move the atoms from its original position. This explains why the specific conductivity of carbon nanotubes is higher than all conventional metallic conductors [6]. Regarding to optical properties, differences between bulk materials and nanomaterials can be also observed due to the quantum confinement, the lower dimensionality and the smaller size having as consequence larger energy difference between energy levels in the density of states giving as a result higher excitation energies. Besides, the absorption wavelength in the spectrum becomes shorter for smaller particles. Thermal properties like thermal conductivity, melting point and specific heat depend also on the size and shape of the nanoparticles.

Due to their unique and interesting properties, nanomaterials have been proposed to be used in a vast number of fields and applications such biomedicine, energy conversion and storage, sensors, among many others [7–11]. Nowadays, nanomaterials are used to improve the efficiency and quality of several products such as: computers, stain-resistant clothes, suntan creams, and food-packages [12–15]. In this work, nanomaterials were designed and characterized with the aim to be applied as active materials into the development of novel gas and temperature sensors.

2.2 Sensors

A sensor is a device developed for detecting or measuring a physical or bio-chemical quantity. Sensors have an output which vary according to variations in the quantity that is being detected. They are composed of an active material, that as the name said, is the part of the sensor that exhibits a change on its properties after its exposure to a given stimulus. Other components may be necessary to obtain a functional sensor such as a support or packing material, electrical connections and signal processing hardware.

Sensors have an important impact in our daily life. Nowadays, we can use sensors to detect toxic analytes in the air, to examine the quality of food, and to monitor our health [16–18]. Figure 2.3 shows sensors that can be used to monitor a great variety of chemical processes involving living systems and processes that surround them.

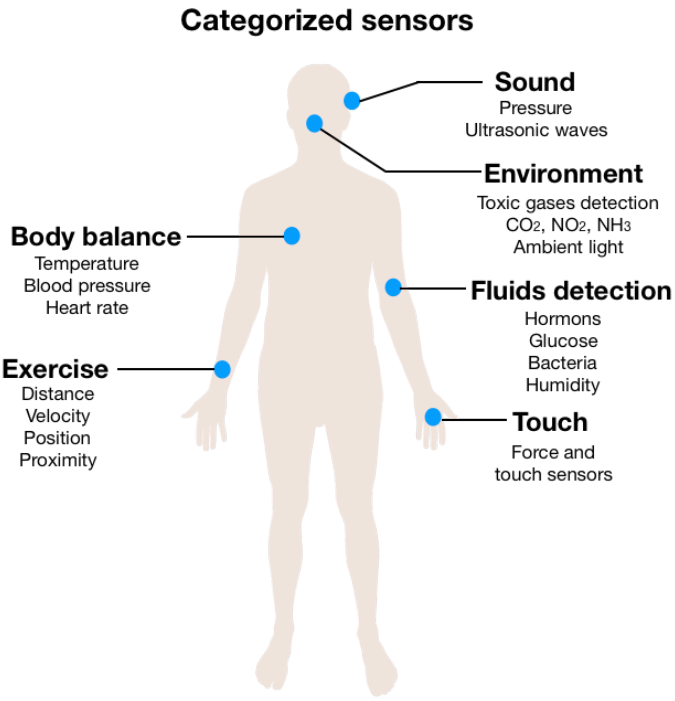

Figure 2.3. Categorized sensors. There are hundreds of different types of sensors available today to measure almost anything, light, sound, temperature, pressure, position, change of altitude and distance, types of gases, movement, liquids, among others.

Scientists have been attracted to the investigation and development of sensors due to the large number of potential applications. However, most of the sensors used in the present time have high power consumptions, that is, they use a high quantity of energy to work. Sensors that are portable and have low power consumption still needed to be developed. The use of nanostructured materials to develop these optimal portable sensors is of huge scientific and technological interest due to unique nanomaterial's properties described in the previous section. The development of novel sensors and optimization of the existing ones may have an important positive impact in the quality of life, for example, preventing or detecting diseases in early stages, monitoring chronic diseases, and alerting about the presence of toxic compounds in outdoor and indoor air.

The designed sensors must accomplish several characteristics to be successfully used in real applications. These features depend on the type of application aimed, nevertheless, there are general requirements to be accomplish: the sensors must be portable, they should be stable in performance, have a low detection limit, high selectivity, and sensitivity, they must show a fast response and recovery, besides, they must be low power consumption. All these requisites depend on the characteristics of the active material in the sensor; therefore, the design of the active material is a key issue for the development of novel sensor technologies. Additional important characteristics of sensors are low cost of fabrication, simple preparation

and operation, and the possibility of miniaturization [19].

In this work, two novel sensors were investigated: a chemical sensor and a temperature sensor. The chemical sensor is based on carbon nanotubes and is probed in the detection of harmful gases in air. The temperature sensor is based in the ceramic nanomaterial TiO_2 doped with the lanthanide ion, Eu^{3+}, and is evaluated as submicrometric thermometer for biological systems.

2.3 Chemical sensor: gas detection

Gas sensors can detect harmful and toxic gases in air at real time. The first commercial gas sensor was developed by Taguchi in 1970 and consisted of a semiconductor element SnO_2 whith changing conductivity in the presence of reducing gases, the semiconductor was connected to a very simple circuit as showed in Figure 2.4 [20]. Sensing gas molecules is crucial in various fields such as in environmental monitoring, biomedicine, pharmaceutics, agriculture, and space exploration [21–24]. The detection of $NO_2(g)$, for instance, is important to monitoring environmental pollution resulting from combustion or automotive emissions. Whereas, detection of $NH_3(g)$, is needed in industrial, medical, and living environments [25,26].

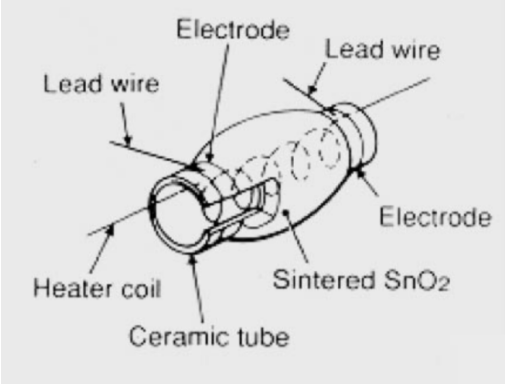

Figure 2.4. Schematic representation of the first commercial gas sensor (Taguchi Gas Sensor from Figaro Engineering Inc., Osaka, Japan). The sensor consists of sintered SnO_2 mounted on a ceramic tube with two gold electrodes that allow the measurement of gas through changes in the electrical conductivity of SnO_2. A heater is inserted inside the tube to achieve the working temperature of SnO_2.

The World Health Organization (WHO) defines the atmospheric pollution as the main environmental risk to human health and a crucial challenge towards climate change, unfortunately, the majority of the available gas sensors employs the use of bulky, high-cost,

and complex instrumentation. As consequence, there is an increasing need to develop low cost, miniaturized, low power consumption and stable gas sensing devices.

2.3.1 Working principles of gas sensing

In chemical gas sensors, the transduction mechanism is the route to transforming a chemical property variable into an electrical or optical signal. The mechanism consists of two parts, first, the recognition of the target molecule by a solid-gas interaction that induces a change in the electronic properties of the active sensor material named as the receptor function, and second, the transduction of the surface phenomena into an electrical resistance change of the sensor, named as the transducer function [27]. The receptor function is provided by the surface chemical properties of the active material in the sensor. Particularly, during the adsorption the active material react with the gas molecules, accepting or donating an electron (reduction/oxidation process) according to the nature of the gas, this interaction leads to a change in the conductivity of the sensing material. Therefore, it is through this change in conductivity that gas sensing is done (Figure 2.5). The sign of the resistance variation depends on the type of semiconducting layer n- or p- type depending on the electron or hole doping and on the donor/acceptor behavior of the detected molecule.

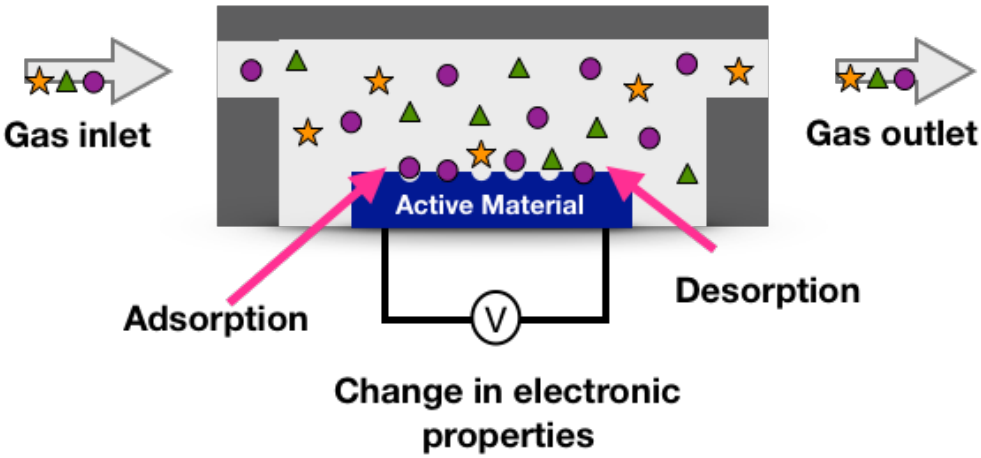

Figure 2.5. Working principles of gas sensing. The gas target gets inside the sensor testing chamber via a gas inlet, the gas molecules are selectively adsorbed in the active material of the sensor, during the adsorption a change in the electronic properties of the active material occurs, this change is collected by the electrical connections in the sensor, then the gas molecules are desorbed and leave the sensor via a gas outlet.

2.3.2 Gas sensors characteristics

The following parameters are used to analyze and compare the quality and efficiency of gas sensors:

Sensitivity: ability to detect and quantify small differences in the gas concentration.

Selectivity: ability to distinguish a target gas from another interfering compounds present in the same atmosphere.

Optimum working temperature: temperature at which is obtained the higher sensitivity.

Response and recovery times: these parameters reveal the time needed for the adsorption and desorption of gases, respectively. The faster the absorption and desorption are achieved; the sensing performance is better.

Reproducibility: level of consistency between different batches of sensors for the same experimental conditions.

Stability: ability to maintain the same response over a specified period, in which the several experimental conditions can change.

Limit of detection: lowest concentration of gas that can be qualitative detected.

Limit of quantification: lowest concentration of gas that can be quantitatively measured.

A suitable gas sensor must accomplish the following characteristics: be portable, have stability in performance and low detection limit, have high selectivity and require low power consumption. It should have high sensitivity to ensure the detection capability, presents fast response, and recovery to guarantee the device efficiency and shows optimal operation at low temperature.

2.3.3 Types of gas sensors

Since the invention of the first gas detector by Taguchi in 1970, different types of gas sensors have been developed, gas sensors can be classified depending on its transduction mechanism as: electrochemical, optical, resistive, gravimetric and field-effect transistor sensors.

Electrochemical sensors are composed of two electrodes, one function as working electrode and the other as counter electrode, the two electrodes are immersed in an electrolyte solution. The sensing of gases is made through the measurement of the potential difference between the electrodes, this difference is generated by a reduction or oxidation on the working

electrode by the gas molecules (Figure 2.6). Electrochemical sensors are sensitive to low concentration gases, they are low-cost sensors and they are not easily affected by humidity [28]. For the case of optical sensors, the absorption of light by the gas molecules at a specific wavelength is used for the gas detection, all gas molecules have unique absorption characteristics. These types of sensors are composed of a light source, a gas chamber, and a light detector. The gas molecules will absorb light of a certain wavelength among the light of various wavelengths coming from the light source, in this way, the presence of a certain gas can be detected by the light detector [29]. Optical sensors have high stability, long lifetime, high selectivity, and fast response speed [30]. Resistive sensors, known as chemoresistors, are low-cost sensors with an easy fabrication, this sensors interact with the absorbed gas molecules trough the transfer of charge, as a result, there is a change in their electrical resistance that match up with the presence of certain gases and allow also obtain information about its concentration (Figure 2.7).

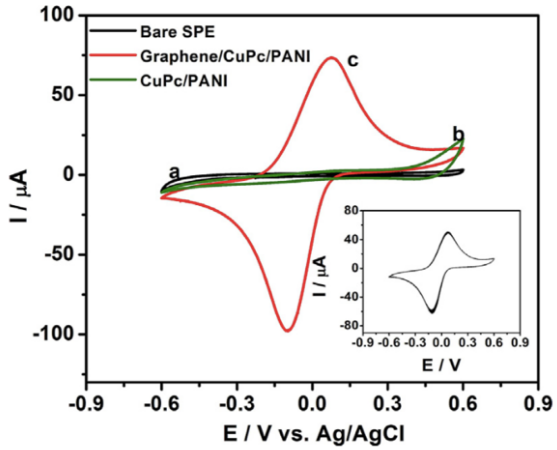

Figure 2.6. Electrochemical response of a sensor based on hybrid graphene-copper phthalocyanine-polyaniline nanocomposite for the detection of ascorbic acid. Adapted from reference [31].

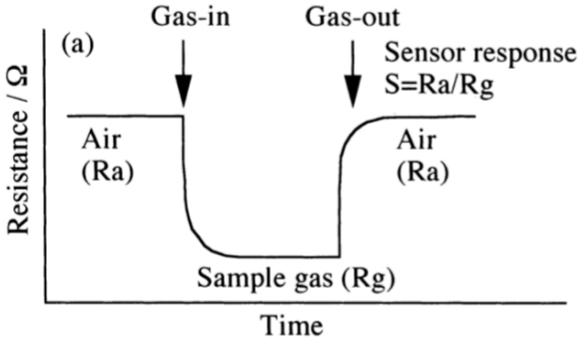

Figure 2.7. Typical response of a resistive gas sensor. The change in the electrical resistance is from a level in air (Ra) to a level (Rg) on exposure to the target gas. The sensor respond (S) is reported as the quotient between Ra and Rg. Adapted from reference [27].

In this work, resistive gas sensors were investigated due to their low cost and easy fabrication. A great variety of materials can be used as active layer in this type of sensors, for example, semiconducting metal oxide, carbon materials and transition metal dichalcogenides [32–34]. However, during the last decades, resistive sensors have been focused on metal oxide (MOx) sensitive layers such as ZnO, SnO_2 or WO_3 [35–37]. MOx-based gas sensors offer extremely high responses, short-time analysis, and good repeatability [38]. Unfortunately, these nanomaterials show significant drawbacks such as their requirement to work at high temperature to activate the oxidation/reduction processes involved in the gas sensing mechanisms [39]. As a consequence, high power consumption is needed to operate MOx sensors, reducing their applicability for the establishment of a large sensor network. In addition, these high temperatures usually induce irreversible changes in the crystalline structure and tend to induce agglomeration of the MOx nanostructures into larger entities. In consequence, the surface area to volume ratio is decreased, as well as the sensor stability at long-term due to the lowering of the sensing properties [40]. Furthermore, MOx shows poor selectivity and specificity, being unsolved problems until now [41]. In addition, the high operating temperatures limits the use of more specific and selective compounds to functionalize the MOx such as organics molecules. More recently, carbon-based nanomaterials have been proposed for gas sensing applications to replace MOx nanostructures and tackle their drawbacks. In fact, carbon nanotubes-based sensors can be operated at lower temperatures that MOx-based sensors lowering the power consumption of gas sensors [42,43].

2.3.4 Gas sensors based on carbon materials

To achieve high sensitivities in gas sensor devices, a high number of interactions between gas molecules and sensing materials must occur. In this context, nanomaterials are perfect candidates to be used as the active material in chemical sensors, the interaction between the active layer and the molecules takes place at the surface layer, as nanomaterials have the most of its atoms at the surface, that is, a high surface-to-volume ratio, phenomena occurring at the surface are increased. Therefore, gas sensors based on nanomaterials, especially in carbon-based materials have attracted huge interest. Ideal gas molecules adsorption and storage can be done by a material with a pitted structure and high surface-to-volume ratio a characteristic of carbon nanostructured materials, besides this, the unique chemical, mechanical, optical, and magnetic properties of carbon nanomaterials open numerous possibilities to develop efficient active materials for sensors.

The implementation of carbon allotropes such as CNTs in gas sensor technology has been suggested to meet the demand of improved criteria as sensitivity, selectivity, long term stability and low cost. A new family of gas sensors based on carbon materials, such as carbon

nanotubes (CNTs), graphene or graphene oxide has emerged [44,45]. Particularly, carbon nanotubes-based gas sensors have attracted a great research interest during the last years [46–48]. The first works reporting the use of carbon nanofibers were published Matthews et al. in 2002 [49].

2.3.5 Carbon nanotubes for gas sensing

Carbon nanotubes (CNTs) were reported by Iijima in 1991 [50]. Their applications' potential in many fields of science was anticipated from the very beginning and the number of researchers that are studying and implementing them in several applications increases every day. They have been employed in components of nanoelectronic technology, as probes in scanning probe microscopy, in high-sensitivity microbalances, in hydrogen storage devices, in field emission type displays, as electrodes in organic light-emitting diodes, as tiny tweezers for nanoscale manipulation, and as gas detectors [51–54].

Carbon nanotubes consist of rolled-up sheets of single-layer carbon atoms (graphene). CNTs are classified as single wall carbon nanotubes (SWCNTs) and multiwall carbon nanotubes (MWCNTs). Due to their structure, CNTs have unique and very interesting properties. They are the strongest and stiffest fibers known, they also have high thermal stability. Referring to its electronic properties CNTs can be metallic or semiconducting depending on their diameter and chirality, CNTs are capable of carry high currents with no significantly heating effect [55].

CNTs are suitable material for gas sensing applications because of its large surface-to-area ratio, an important requirement of gas sensing applications. Carbon nanotubes function as excellent sensing platforms as their whole surface is involved in the process leading to a maximization of the sensing performance upon exposure to the gas molecules. Also, their property of carry high current with negligible heating effect is an advantage for gas sensing. In 2000, Kong et al. [56] showed that a single semiconducting carbon nanotube changes its resistance when is exposed to the NO_2 and NH_3 gases (Figure 2.8). Recent studies have proved that CNT-based gas sensors can detect hazardous gases at low temperature (e.g., below 200 ºC), and even at room temperature (Figure 2.8) [57,58]. This reduces the power consumption of the sensors and enables the safe detection of flammable gases in potentially explosive atmospheres.

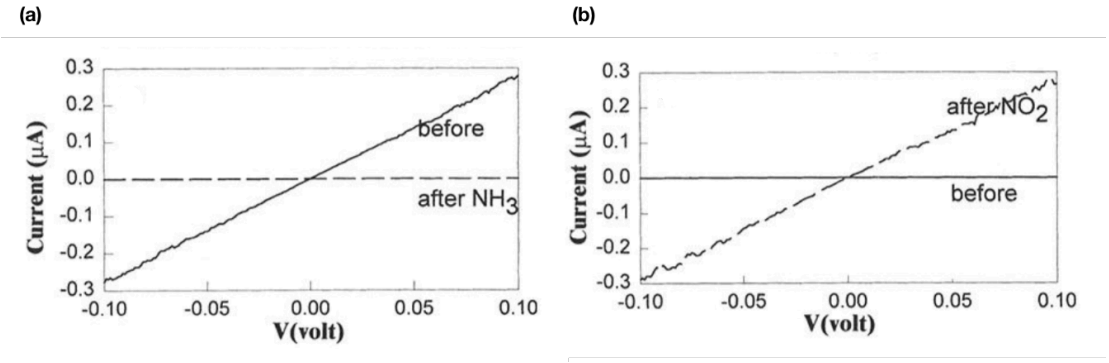

Figure 2.8. Current versus voltage curves of single wall carbon nanotubes collected before and after exposure to NH_3 (a) and NO_2 (b). Exposure to NO_2, molecules increased the conductance of the nanotube sample by about three orders of magnitude, conversely, exposure to NH_3 showed a 100-fold conductance depletion. Adapted from reference [56].

2.3.6 Boosting the CNTs properties for gas sensing

Functionalization of carbon nanotubes creates the opportunity of application of CNTs in a large quantity of fields [43,59]. Carbon nanotubes are doped, functionalized, or conjugated with atoms, molecules, and compounds in order to improve their properties (Figure 2.9) [53,60,61]. The intrinsically inert surface of CNTs is the main limitation on the achievement of high sensitivity carbon nanotubes-based gas sensors. However, it has been proved that the doping and functionalization of carbon nanotubes with different atoms, functional groups or metal nanoparticles, lead to the introduction of active sites in CNTs structure that boost their reactivity to gas molecules facilitating the development of highly sensitive and selective sensors for a great variety of gases [48,62,63]. Penza et. al in 2010 demonstrate that vertically aligned carbon nanotubes sensors have a better response to sense NO_2(g) when they are functionalized with Ag and Ru nanoparticles [64] (Figure 2.10). Besides, functionalizing nanotubes allows their chemical compatibility with other materials. For example, they can be incorporated within polymers, attached to metals, or other materials, transferring their properties to the new composite material.

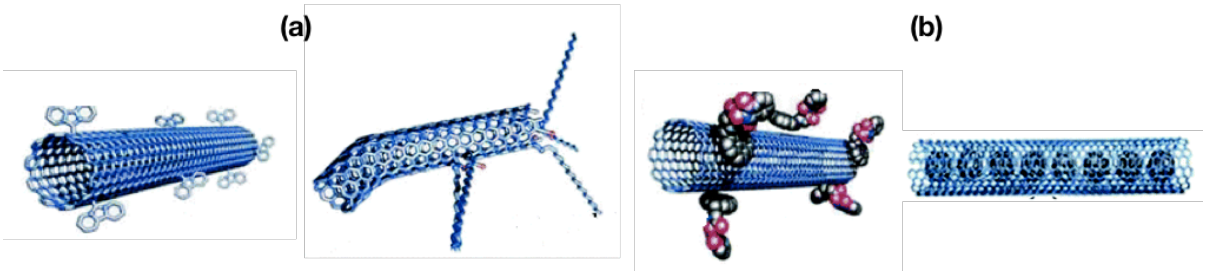

Figure 2.9. Examples of functionalization of carbon nanotubes. (a) Covalent bonding of molecules in the sidewall or defects sides, (b) non-covalent functionalization: adsorbed molecules and encapsulated nanoparticles.

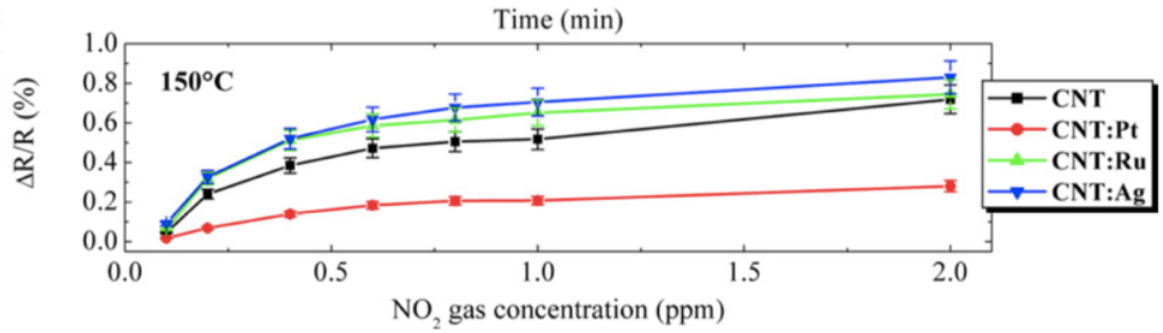

Figure 2.10. Calibration curves of the vertically aligned carbon nanotubes-based sensor functionalized with different metal nanoparticles for the detection of NO_2 gas at 150 ºC. Adapted from reference [64].

Nowadays innovation in chemical sensors implies the design of sensors with new transduction mechanisms, improvement on the sensitivity and selectivity of well-known active materials, decreasing the detection limit, increase the possibility of large-scale production and portable sensors and lower their power consumption.

In this work, a high sensitivity CNTs-based chemical gas sensor was developed to detect harzardous gases. CNTs were investigated as active material due to their unique properties for gas sensing such as high surface-to-volume ratio and the possibility of detecting gases at low temperatures. CNTs were functionalized with oxygen-containing functional groups to tackle their intrinsic inert surface, the oxygen functionalization was performed using low kinetic energy oxygen ion irradiation, this technique allows to graft functional groups into the CNTs surface with short treatment time and under conditions that can be tuned to control the type and quantity of functional groups without generate liquid waste. After this, the thermal stability of the oxygen functional groups in CNTs was investigated through a thermal

annealing treatment to predict their possible behavior when gas sensors are heated to improve their sensitivity or implemented in the final device. Moreover, oxygen functionalized CNTs were conjugated with bimetallic nanoparticles with the aim of developing gas sensors with improved sensitivity. The active materials developed are evaluated to detect the following gases: ethanol, toluene, NO_2 and H_2. The experimental work performed, and the results obtained for the development of this chemical gas sensor based on carbon nanotubes are presented and discussed in the Chapter 3 of this thesis.

2.4 Temperature sensors

The measurement of temperature, a fundamental thermodynamic parameter, is essential in a vast number of scientific investigations and technological developments. According to the zeroth law of thermodynamics, if we have three systems, A, B and C, such that A and B are in thermal equilibrium with C, then A and B must be in thermal equilibrium with each other and thus they all have the same temperature (Figure 2.10). From this we can resolve that a temperature sensor must be in thermal equilibrium with the system to be characterized [65].

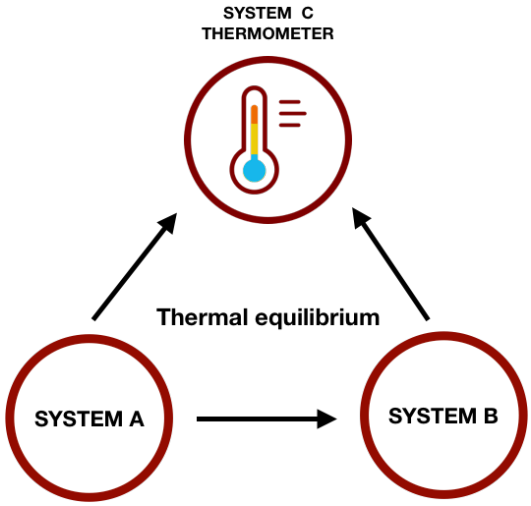

Figure 2.10. Schematic representation of the zeroth law of thermodynamics and its application into temperature sensors.

Conventional temperature sensors are based on electrical or optical properties of materials. Some of these sensors are thermocouples and infrared thermometers, which are capable of measuring temperature with a spatial resolution up to a few microns. The efficiency of a thermometer is determined by their accuracy to measure temperature and by the thermal range within which they can work. In fact, the universal thermometer that can be used in all systems and situations does not exist, but rather different thermometers that adapt better to each different situation most be developed.

In the last decades, there has been a huge increase in the investigation and development of materials and applications in the nanometric scale. As mentioned previously, nanotechnology is one of the most promising fields of science for the improvement of new applications that may increase our life quality. In several of these applications it is important to evaluate the temperature with submicrometric spatial resolution, for example to determine the optimum power consumption of nanochips or measure the temperature of early stages tumors. Unfortunately, the conventional methods to measure temperature are too bulky to be used in these systems and they do not reach the resolutions required. To address this necessity, new methods for measuring temperature have been proposed and are enclosed in a new field of investigation named nanothermometry.

2.4.1 Nanothermometry

The purpose of nanothermometry is to obtain information about temperature of objects with a high spatial (submicron) and thermal resolution (below 0.5 °C). The main techniques developed to measure temperature at the nanoscale can be classified in three categories: electrical, mechanical, and optical thermometers [66].

Electrical thermometers are based on the junction of two different metals, differences on their voltage, conductivity or resistance that are induced by changes in temperature are used to build nanothermometers. An example of this is scanning thermal microscopy (STM) [67,68]. On the other hand, mechanical thermometers are based on the difference between the thermal expansion coefficients of two materials, the temperature is calculated by the material bending. Atomic Force Microscopy (AFM) has employed this to measure temperature in submicrometric scale [69], likewise, micro-thermocouples have also been used [70]. Other alternative that exploits mechanical properties of materials is the nanothermometer based on a liquid that changes its volume with temperature confined in a nanoprobe. The first of these nanothermometers was based on carbon nanotubes filled with gallium [71]. The techniques exemplified above may be able to measure temperature at submicrometric scales, however, they require sophisticated and expensive experimental set ups and most of them can only read temperature of surfaces which limits the type of objects that can be studied [65].

Optical thermometers can extract temperature information from inside the target object. Besides, they can be operated in a remote mode. Among the relatively new optical nanothermometry techniques there are interferometry and Raman spectroscopy. Interferometry is based on the comparison of two light beams, one that passes through the sample and other that bypasses it. The difference between one beam and the other have information about the sample temperature, interferometry is usually used for samples immersed in fluids. For example, this technique was used to measure the heat dissipated by

a gold microwire in 2014 by Baffou et al [72].

For the case of Raman spectroscopy, when light of a certain wavelength illuminates a molecule, a small fraction of the light energy is either absorbed or emitted by the molecule and then, the wavelength of the resulting scattered light is slightly shifted, this is named Raman scattering. The amount of energy absorbed or emitted by the molecule is related to its molecular vibrational modes (phonons). The vibrational modes are linked to the position and energy of atoms in a molecule and they may reflect temperature variations, thus the temperature of the samples can be determined by Raman spectroscopy analyzing the vibrational modes in terms of peak wavelength, width, or intensity [73]. The advantages of measuring temperature with Raman spectroscopy includes a simple preparation, small volumes of sample required and that can be used in a vast range of environments. However, it is limited to high temperatures. Raman spectroscopy has been used to study the thermal properties of nanomaterials like graphene and to investigate micro-heating devices [74,75].

Interferometric techniques and Raman spectroscopy can be successful strategies to measure local temperature in microstructured samples. However, due to their limitations, they cannot be employed in biological applications which are of interest for this thesis work. In terms of measuring temperature, biological systems present two main complications: first, samples are highly heterogeneous regarding composition and refractive index; second, even in the simplest case of cells cultured, samples are embedded in a complex medium. Recent advances toward resolving this need are based on luminescent nanoparticles that show temperature dependent luminescence. This technique is named luminescence nanothermometry and is based on the nanosensors temperature dependent emission spectrum to measure temperature with submicrometric spatial resolution by analyzing the emitted light traveling through the sample obtained by remote excitation of a luminescent object. This technique combines high relative thermal sensitivity (>1% K^{-1}) and spatial resolution (<10 μm) in short acquisition times (<1 ms).

2.4.2 Luminescence nanothermometry

Luminescence is the emission of light from an object after being excited by an external source (Figure 2.11). The photon emitted comes from energy levels that were populated after the excitation. The properties of the emitted photon depend on the energy levels involved in the absorption and emission of light and in certain cases this also depend on the temperature. Luminescence nanothermometry uses the correlation between temperature and luminescence to develop thermal sensors. The measurement of temperature is done through the analysis of the luminescence spectrum of the object of interest. However, when the system of interest lacks of natural luminescence, the conjugation with probes which luminescence is temperature dependent is required [76,77]. Different properties of the photoluminescence

spectrum are affected by changes in temperature and therefore can be used to develop thermometers: intensity, band-shape, spectral position, polarization, lifetime, and bandwidth (Figure 2.12) [66].

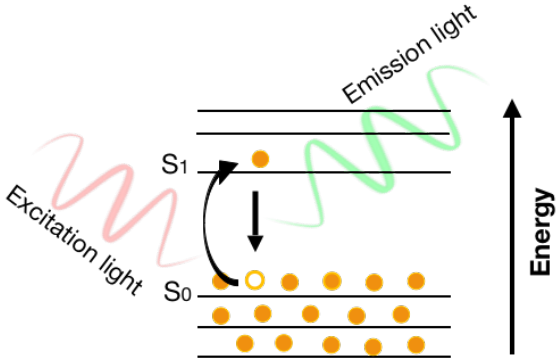

Figure 2.11. Jablonski diagram of luminescence. Electronic transition from the ground state S_0 due to the absorption of light to an exited state S_1 followed by the relaxation to the ground state by the emission of light.

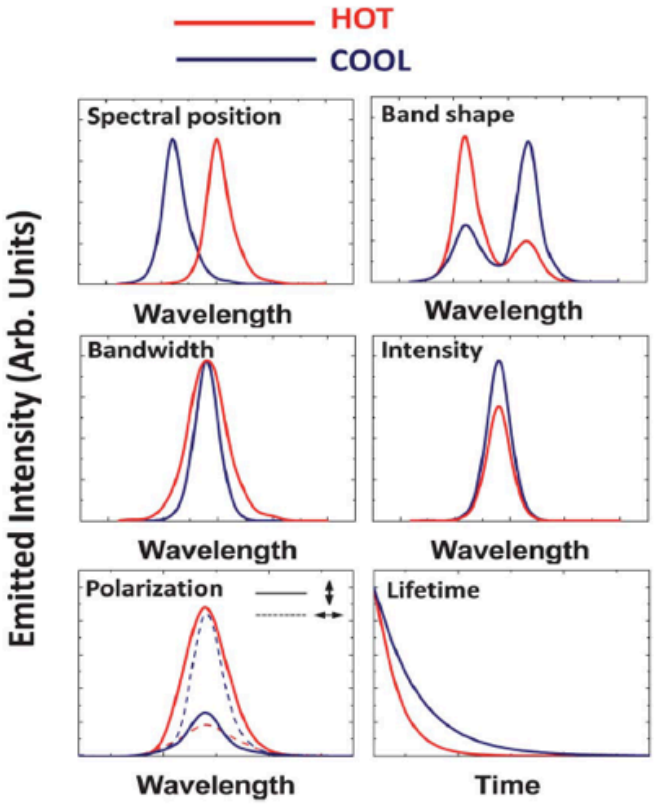

Figure 2.12. Schematic representation of the different properties of luminescence that may be affected by a change in temperature. Adapted from reference [66].

Luminescence intensity is the most studied property of luminescence for the development of nanothermometers [78,79]. In this case, the change of temperature affects the number of photons emitted per second, thus the intensity in the emission spectrum becomes higher or lower with temperature. This phenomenon is produced by the thermal activation of certain transitions or due to the increment of non-radiative decay probabilities [66]. Otherwise, band-shape based thermometers uses the relative intensity between two different spectral lines that are thermally coupled. The spectral position of spectral lines depends on the energy of separation between the levels involved and this is also affected by temperature, therefore can be used in nanothermometry. In terms of polarization luminescence, in anisotropic media the shape and intensity of the luminescence spectrum depends on its polarization. On the other hand, the bandwidth of certain lines of emission depends likewise on temperature, as the temperature increases, there is an increase in the density of photons resulting in the broadening of the lines in the spectrum that change linearly with temperature. And last, but not least important, the lifetime luminescence, defined as the average time a luminescent object stays in its excited state and is given by $\tau = \frac{1}{K_f + K_{nr}}$ where K_f is the radiative decay and K_{nr} is the non-radiative decay rate [66]. Luminescence lifetime depends on several factors such as, energy transfer processes and multiphonon decays, that are at the same time dependent of temperature making possible in this way to obtain information about temperature employing lifetime luminescence.

As showed above, luminescence nanothermometry can be performed by several methods always analyzing the emission spectrum of the material used. In this thesis work, the variation of luminescence intensity with temperature of Eu^{3+}-doped TiO_2 nanoparticles will be used to engineer a temperature sensor for biological systems.

2.4.2.1 Luminescent materials used for nanothermometry

Different kinds of luminescent nanomaterials have been proposed and tested as nanothermometers. The most studied materials include semiconductor nanocrystals named as quantum dots (QDs), luminescent organic dyes, proteins conjugated systems, luminescent polymers and lanthanide ions-based materials [65,66,79]. QDs nanocrystals are nanoprobes with high photostability and large luminescence yield, they can be tuned to absorb and emit light at different wavelengths by changing their size [80,81]. However, QDs are not recommended for biological applications due to its intrinsic toxicity [82]. Organic compounds with high luminescence yields are named organic dyes. Generally, their luminescence intensity decreases as the temperature increases. Even tough organic dyes are low cost materials they present the important disadvantage that besides temperature their luminescence properties also depend on other factors such as the type of solvent, concentration, and pH [66]. Polymers based nanothermometers show relatively low

luminescence efficiencies and their luminescent properties depend critically on their structure, small changes in the structure properties would change the luminescence of the polymer making it difficult to develop reliable nanothermometers [83]. Nevertheless, they have been extensively used to monitor temperature of fluids and biological systems due to their solubility in water [84,85]. For the case of proteins conjugated systems, even though they are the best option for biological applications, clearly they do not have biocompatibility problems, they present the disadvantage of having low photostability [86].

Nanothermometers based in trivalent lanthanide ions (Ln^{3+}) are a promising type of temperature sensors. Lanthanides comprise fifteen metallic chemical elements with atomic numbers from 57-71, located in the sixth row of the periodic table. Lanthanides have unique luminescent properties due to electronic transitions in their partially filled *4f* orbital, the emission lines generated from these transitions are very narrow and with relatively long lifetimes (from a few μs to a few ms), these characteristics are owing to the partial screening of the *4f* levels by the *5s* and *5p* energy levels that protect *f-f* transitions from perturbations from their environment. Besides their narrow emission lines and long lifetimes luminescence, other characteristics make Ln^{3+} important candidates as nanothermometers, they have high emission quantum yields [79], the emission lines of different lanthanides appear in all the region of the spectrum, from UV (Gd^{3+}), visible range (Eu^{3+}, Sm^{3+}) to near infrared (NIR) range (Nd^{3+}, Er^{3+}, Yb^{3+}) [87], also different lanthanides can be used to develop different temperature ranges nanothermometers (Figure 2.13) [88], this lanthanides properties allow to adjust the emission of the nanothermometer and the temperature range for a desired application. Furthermore, it has been reported that temperature is the most critical parameter affecting the luminescence intensity of lanthanide ions [66]. As a result of this, the implementation of Ln^{3+}-based thermometers in diverse applications was extensively studied in the past decade. They have been incorporated in a great variety of matrices including molecular complexes and organic–inorganic hybrids using just one lanthanide ion or a combination of different ions as active material [89–91].

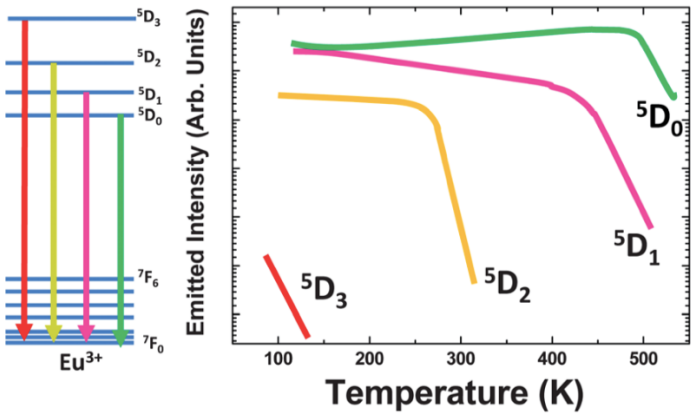

Figure 2.13. Temperature dependence of luminescence intensity associated with different transitions of Eu^{3+} indicated in the diagram on the left (excitation 355 nm). It can be observed that different transitions can be used to develop thermometers working at different temperature ranges. Adapted from reference [66].

2.4.2.2 Luminescence nanothermometry for biology

Luminescence nanothermometry has been proposed to be applied in a great variety of fields, including nanofluids, catalytic reactions and microelectronics [92–94], however the most studied are related to biology such as cell basic biology, preclinical research, and diagnostics of diseases [95–98]. Investigations that go from intracellular temperature measurements to early detection tumors have been performed (Figure 2.14) [99–101]. Different techniques have been used, ranging from insertion of a micro-thermocouple in the cell, a glass micropipette full of luminescent thermometric material, or by delivering different luminescent molecules or nanoparticles in the cytoplasm or the nucleus [67,102]. The functionality of nanothermometers in biological systems is proved through *in vitro* assays changing the temperature of the system by local heating with a laser or using specific drugs that stimulate changes in temperature of cells [103]. However, heating with a laser permits to control the change in temperature in a more efficient and well-regulated mode.

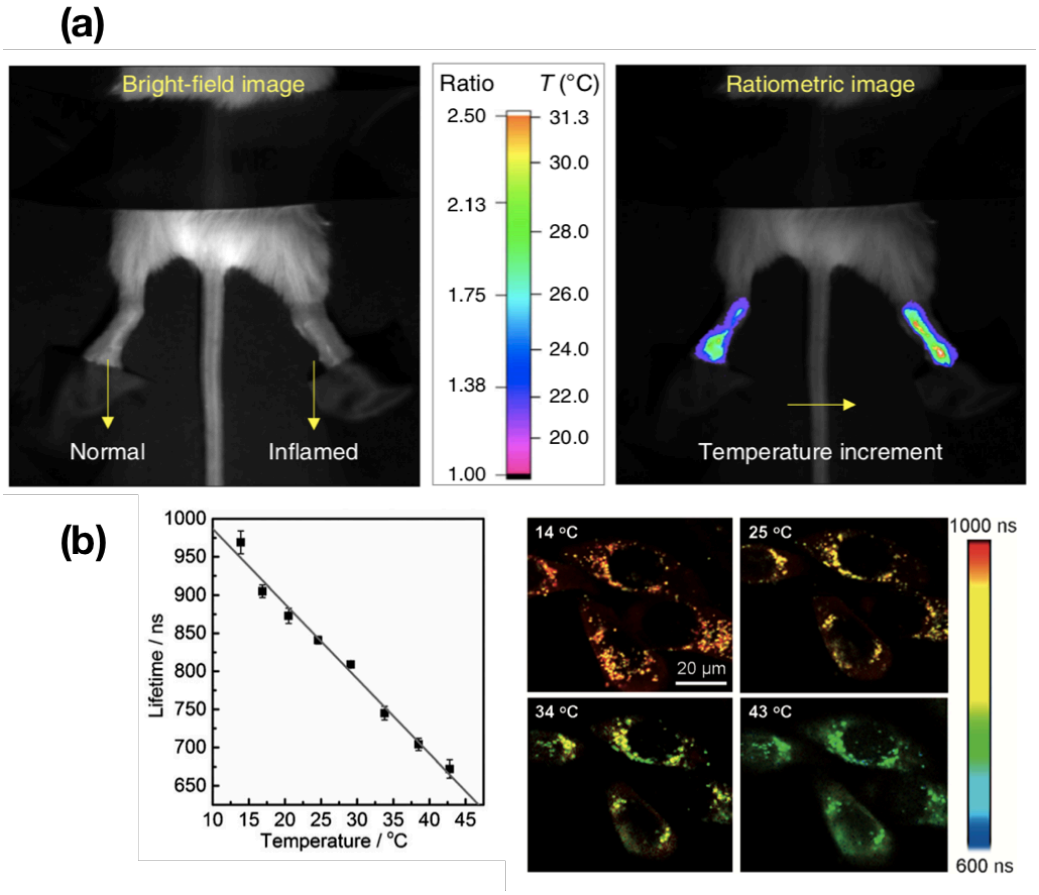

Figure 2.14. Examples of intracellular and in vivo temperature sensing using luminescence nanothermometers. (a) Nanothermometer based in $NaYF_4$: Nd^{3+} nanophosphors with NIR emission used to measure the change in body temperature caused by the inflammatory process due to arthritis in a Kunming mouse. Left leg was used as control leg [96]. (b) Intracellular thermometry in HeLa cells using fluorescent gold nanoclusters, the lifetime dependence with temperature was used to develop the nanothermometer, the calibration curve is showed in the left figure [100].

Nanothermometers can be distributed inside cells by endocytosis, chemical diffusion, or microinjection [103], this is an important issue if intracellular temperature measurements are aimed. Most complex nanothermometers can be designed by modifying their surface and size to improve their biocompatibility. Furthermore, the possibility to adjust nanothermometers to reach specific organelles inside the cell has been also proposed, this may allow the measurement of local temperature changes inside the cells related to organelle functions. Nevertheless, there is still the need to fully investigate luminescence nanothermometers in biological systems, such as the reliability of the sensors incubated in cells or tissues as well as the toxicity induced into the biological system after their conjugation with the luminescent material, to accomplish a complete understanding of

nanothermometers in the biological window and achieve real biological applications.

In this thesis work, the luminescence dependency with temperature of the europium ion in oxidation state 3+ is used to design a novel temperature nanosensor that measures temperature changes with submicrometric spatial resolution. Eu^{3+} ions are hosted in a titanium oxide matrix (TiO_2). The physicochemical properties of Eu^{3+}-doped TiO_2 nanoparticles are investigated in detail, and the temperature effect on their luminescence properties is evaluated. Appropriated temperature calibration curves are generated. Finally, the Eu^{3+}-doped TiO_2 nanoparticles are applied as temperature sensors to detect changes in the temperature of single cells. The experimental work performed, and the results obtained for the development of this temperature sensor are presented and discussed in the Chapter 4 of this thesis.

2.5 Summary

Nowadays sensors are used in a huge variety of technological subjects and in all areas of our daily life. However, there is still the need to develop small, portable, reliable, and low power consumption sensors. Nanostructured materials to develop these optimal novel sensors is of huge scientific and technological interest due to the promising and unique nanomaterial's properties. In this thesis work, nanomaterials are studied in detail aiming at understanding their characteristics and properties as sensing materials. Two types of sensors are investigated: a chemical gas sensor used to detect hazardous gases in air based on carbon nanotubes decorated with metal nanoparticles, and a temperature sensor used to measure temperature of biological systems based on Eu^{3+}-doped TiO_2 nanoparticles.

The intrinsically inert surface of CNTs is the main limitation for the achievement of high sensitivity on carbon nanotubes-based gas sensors. However, it has been proved that doping and functionalize carbon nanotubes with different atoms, functional groups or metal nanoparticles, lead to the introduction of active sites in CNTs structure that boost their reactivity to gas molecules facilitating the development of highly sensitive and selective sensors for a great variety of gases. Here, carbon nanotubes are functionalized with oxygen groups and decorated with bimetallic nanoparticles to increase their reactivity to the hazardous gases: toluene, ethanol, NO_2 and H_2.

Nanothermometers based on lanthanide ions (Ln^{3+}) are a promising type of temperature sensors. Lanthanides owe their luminescent properties to electronic transitions in their *4f* orbitals, the emission lines generated from these transitions depend critically on the temperature. Here, Eu^{3+}-doped TiO_2 nanoparticles are used to develop luminescence

nanothermometers with submicrometric spatial resolution and high sensitivities to measure changes in temperature of single cells.

2.6 References

[1] R. Vajtai, ed., Springer Handbook of Nanomaterials, Springer Berlin Heidelberg, Berlin, Heidelberg, 2013. https://doi.org/10.1007/978-3-642-20595-8.

[2] F.A. Khan, Synthesis of Nanomaterials: Methods & Technology, in: Appl. Nanomater. Hum. Heal., Springer Singapore, Singapore, 2020. https://doi.org/10.1007/978-981-15-4802-4_2.

[3] J.-O. Carlsson, P.M. Martin, Chemical Vapor Deposition, in: Handb. Depos. Technol. Film. Coatings, Elsevier, 2010. https://doi.org/10.1016/B978-0-8155-2031-3.00007-7.

[4] N.T.K. Thanh, N. Maclean, S. Mahiddine, Mechanisms of Nucleation and Growth of Nanoparticles in Solution, Chem. Rev. 114 (2014). https://doi.org/10.1021/cr400544s.

[5] R. Martel, T. Schmidt, H.R. Shea, T. Hertel, P. Avouris, Single- and multi-wall carbon nanotube field-effect transistors, Appl. Phys. Lett. 73 (1998). https://doi.org/10.1063/1.122477.

[6] Y. Zhao, J. Wei, R. Vajtai, P.M. Ajayan, E. V. Barrera, Iodine doped carbon nanotube cables exceeding specific electrical conductivity of metals, Sci. Rep. 1 (2011). https://doi.org/10.1038/srep00083.

[7] S. Das, B. Sen, N. Debnath, Recent trends in nanomaterials applications in environmental monitoring and remediation, Environ. Sci. Pollut. Res. 22 (2015). https://doi.org/10.1007/s11356-015-5491-6.

[8] J.A. Barreto, W. O'Malley, M. Kubeil, B. Graham, H. Stephan, L. Spiccia, Nanomaterials: Applications in Cancer Imaging and Therapy, Adv. Mater. 23 (2011). https://doi.org/10.1002/adma.201100140.

[9] H. Feng, L. Tang, G. Zeng, Y. Zhou, Y. Deng, X. Ren, B. Song, C. Liang, M. Wei, J. Yu, Core-shell nanomaterials: Applications in energy storage and conversion, Adv. Colloid Interface Sci. 267 (2019). https://doi.org/10.1016/j.cis.2019.03.001.

[10] L.R. Khot, S. Sankaran, J.M. Maja, R. Ehsani, E.W. Schuster, Applications of nanomaterials in agricultural production and crop protection: A review, Crop Prot. 35 (2012). https://doi.org/10.1016/j.cropro.2012.01.007.

[11] G. Fytianos, A. Rahdar, G.Z. Kyzas, Nanomaterials in Cosmetics: Recent Updates, Nanomaterials. 10 (2020). https://doi.org/10.3390/nano10050979.

[12] C. Silvestre, D. Duraccio, S. Cimmino, Food packaging based on polymer nanomaterials, Prog. Polym. Sci. 36 (2011). https://doi.org/10.1016/j.progpolymsci.2011.02.003.

[13] E. Inshakova, O. Inshakov, World market for nanomaterials: structure and trends, MATEC Web Conf. 129 (2017). https://doi.org/10.1051/matecconf/201712902013.

[14] W.J. Stark, P.R. Stoessel, W. Wohlleben, A. Hafner, Industrial applications of nanoparticles, Chem. Soc. Rev. 44 (2015). https://doi.org/10.1039/C4CS00362D.

[15] C.A. Charitidis, P. Georgiou, M.A. Koklioti, A.-F. Trompeta, V. Markakis, Manufacturing nanomaterials: from research to industry, Manuf. Rev. 1 (2014). https://doi.org/10.1051/mfreview/2014009.

[16] S. Li, A. Simonian, B.A. Chin, Sensors for Agriculture and the Food Industry, Electrochem. Soc. Interface. 19 (2010). https://doi.org/10.1149/2.F05104if.

[17] D.R. Seshadri, R.T. Li, J.E. Voos, J.R. Rowbottom, C.M. Alfes, C.A. Zorman, C.K. Drummond, Wearable sensors for monitoring the physiological and biochemical profile of the athlete, Npj Digit. Med. 2 (2019). https://doi.org/10.1038/s41746-019-0150-9.

[18] S. Gupta Chatterjee, S. Chatterjee, A.K. Ray, A.K. Chakraborty, Graphene–metal oxide nanohybrids for toxic gas sensor: A review, Sensors Actuators B Chem. 221 (2015). https://doi.org/10.1016/j.snb.2015.07.070.

[19] E. Comini, Metal oxide nanowire chemical sensors: innovation and quality of life, Mater. Today. 19 (2016). https://doi.org/10.1016/j.mattod.2016.05.016.

[20] Naoyoshi Taguchi, Gas-detecting device, US3631436A, 1970.

[21] W. Tsujita, A. Yoshino, H. Ishida, T. Moriizumi, Gas sensor network for air-pollution monitoring, Sensors Actuators B Chem. 110 (2005). https://doi.org/10.1016/j.snb.2005.02.008.

[22] P. Mirtaheri, T. Omtveit, T. Klotzbuecher, S. Grimnes, Ø.G. Martinsen, T.I. Tønnessen, Miniaturization of a biomedical gas sensor, Physiol. Meas. 25 (2004). https://doi.org/10.1088/0967-3334/25/6/015.

[23] T. Pobkrut, T. Eamsa-ard, T. Kerdcharoen, Sensor drone for aerial odor mapping for agriculture and security services, in: 2016 13th Int. Conf. Electr. Eng. Comput. Telecommun. Inf. Technol., IEEE, 2016. https://doi.org/10.1109/ECTICon.2016.7561340.

[24] M. Rossi, D. Brunelli, Autonomous Gas Detection and Mapping With Unmanned Aerial Vehicles, IEEE Trans. Instrum. Meas. 65 (2016). https://doi.org/10.1109/TIM.2015.2506319.

[25] S.T. Shishiyanu, T.S. Shishiyanu, O.I. Lupan, Novel NO2 gas sensor based on cuprous oxide thin films, Sensors Actuators B Chem. 113 (2006). https://doi.org/10.1016/j.snb.2005.03.061.

[26] K. Sel, S. Demirci, O.F. Ozturk, N. Aktas, N. Sahiner, NH 3 gas sensing applications of metal organic frameworks, Microelectron. Eng. 136 (2015). https://doi.org/10.1016/j.mee.2015.04.035.

[27] N. Yamazoe, Oxide Semiconductor Gas Sensors, Catal. Surv. from Asia. 7 (2003) 63–75. https://doi.org/10.1023/A:1023436725457.

[28] M. Khan, M. Rao, Q. Li, Recent Advances in Electrochemical Sensors for Detecting Toxic Gases: NO2, SO2 and H2S, Sensors. 19 (2019) 905. https://doi.org/10.3390/s19040905.

[29] J. Hodgkinson, R.P. Tatam, Optical gas sensing: a review, Meas. Sci. Technol. 24 (2013) 012004. https://doi.org/10.1088/0957-0233/24/1/012004.

[30] A. Paliwal, A. Sharma, M. Tomar, V. Gupta, Room temperature detection of NO2 gas using optical sensor based on surface plasmon resonance technique, Sensors Actuators B Chem. 216 (2015). https://doi.org/10.1016/j.snb.2015.03.095.

[31] S. Pakapongpan, J.P. Mensing, D. Phokharatkul, T. Lomas, A. Tuantranont, Highly selective electrochemical sensor for ascorbic acid based on a novel hybrid graphene-copper phthalocyanine-polyaniline nanocomposites, Electrochim. Acta. 133 (2014). https://doi.org/10.1016/j.electacta.2014.03.167.

[32] M. Tonezzer, D.T.T. Le, S. Iannotta, N. Van Hieu, Selective discrimination of hazardous gases using one single metal oxide resistive sensor, Sensors Actuators B Chem. 277 (2018). https://doi.org/10.1016/j.snb.2018.08.103.

[33] X. Zhang, V.S. Turkani, S. Hajian, A.K. Bose, D. Maddipatla, A.J. Hanson, B.B. Narakathu, M.Z. Atashbar, Novel Printed Carbon Nanotubes Based Resistive Humidity Sensors, in: 2019 IEEE Int. Conf. Flex. Printable Sensors Syst., IEEE, 2019. https://doi.org/10.1109/FLEPS.2019.8792298.

[34] N. Joshi, T. Hayasaka, Y. Liu, H. Liu, O.N. Oliveira, L. Lin, A review on chemiresistive room temperature gas sensors based on metal oxide nanostructures, graphene and 2D transition metal dichalcogenides, Microchim. Acta. 185 (2018). https://doi.org/10.1007/s00604-018-2750-5.

[35] V.B. Platonov, M.N. Rumyantseva, A.S. Frolov, A.D. Yapryntsev, A.M. Gaskov, High-temperature resistive gas sensors based on ZnO/SiC nanocomposites, Beilstein J. Nanotechnol. 10 (2019) 1537–1547. https://doi.org/10.3762/bjnano.10.151.

[36] M. Tonezzer, S.C. Izidoro, J.P.A. Moraes, L.T.T. Dang, Improved Gas Selectivity Based on Carbon Modified SnO2 Nanowires, Front. Mater. 6 (2019). https://doi.org/10.3389/fmats.2019.00277.

[37] M. Penza, M.. Tagliente, L. Mirenghi, C. Gerardi, C. Martucci, G. Cassano, Tungsten trioxide (WO3) sputtered thin films for a NOx gas sensor, Sensors Actuators B Chem. 50 (1998) 9–18. https://doi.org/10.1016/S0925-4005(98)00149-X.

[38] A. Dey, Semiconductor metal oxide gas sensors: A review, Mater. Sci. Eng. B. 229 (2018) 206–217. https://doi.org/10.1016/j.mseb.2017.12.036.

[39] A. Lahlalia, O. Le Neel, R. Shankar, S. Selberherr, L. Filipovic, Improved Sensing Capability of Integrated Semiconducting Metal Oxide Gas Sensor Devices, Sensors. 19 (2019) 374. https://doi.org/10.3390/s19020374.

[40] C. Wang, L. Yin, L. Zhang, D. Xiang, R. Gao, Metal Oxide Gas Sensors: Sensitivity and Influencing Factors, Sensors. 10 (2010) 2088–2106. https://doi.org/10.3390/s100302088.

[41] N.D. Hoa, N. Van Duy, S.A. El-Safty, N. Van Hieu, Meso-/Nanoporous Semiconducting Metal Oxides for Gas Sensor Applications, J. Nanomater. 2015 (2015) 1–14. https://doi.org/10.1155/2015/972025.

[42] S. Ju, J.M. Lee, Y. Jung, E. Lee, W. Lee, S.-J. Kim, Highly sensitive hydrogen gas sensors using single-walled carbon nanotubes grafted with Pd nanoparticles, Sensors Actuators B Chem. 146 (2010). https://doi.org/10.1016/j.snb.2010.01.055.

[43] Y.-P. Sun, K. Fu, Y. Lin, W. Huang, Functionalized Carbon Nanotubes: Properties and Applications, Acc. Chem. Res. 35 (2002). https://doi.org/10.1021/ar010160v.

[44] J.-M. Tulliani, B. Inserra, D. Ziegler, Carbon-Based Materials for Humidity Sensing: A Short Review, Micromachines. 10 (2019). https://doi.org/10.3390/mi10040232.

[45] W. Tian, X. Liu, W. Yu, Research Progress of Gas Sensor Based on Graphene and Its Derivatives: A Review, Appl. Sci. 8 (2018). https://doi.org/10.3390/app8071118.

[46] Y. Wang, J.T.W. Yeow, A Review of Carbon Nanotubes-Based Gas Sensors, J. Sensors. 2009 (2009). https://doi.org/10.1155/2009/493904.

[47] I. V. Zaporotskova, N.P. Boroznina, Y.N. Parkhomenko, L. V. Kozhitov, Carbon nanotubes: Sensor properties. A review, Mod. Electron. Mater. 2 (2016). https://doi.org/10.1016/j.moem.2017.02.002.

[48] P. Bondavalli, P. Legagneux, D. Pribat, Carbon nanotubes based transistors as gas sensors: State of the art and critical review, Sensors Actuators B Chem. 140 (2009). https://doi.org/10.1016/j.snb.2009.04.025.

[49] K. Matthews, B.A. Cruden, B. Chen, M. Meyyappan, L. Delzeit, Plasma-Enhanced Chemical Vapor Deposition of Multiwalled Carbon Nanofibers, J. Nanosci. Nanotechnol. 2 (2002) 475–480. https://doi.org/10.1166/jnn.2002.133.

[50] S. Iijima, Helical microtubules of graphitic carbon, Nature. 354 (1991).

https://doi.org/10.1038/354056a0.

[51] S. Kumar, R. Rani, N. Dilbaghi, K. Tankeshwar, K.-H. Kim, Carbon nanotubes: a novel material for multifaceted applications in human healthcare, Chem. Soc. Rev. 46 (2017). https://doi.org/10.1039/C6CS00517A.

[52] R. Rao, C.L. Pint, A.E. Islam, R.S. Weatherup, S. Hofmann, E.R. Meshot, F. Wu, C. Zhou, N. Dee, P.B. Amama, J. Carpena-Nuñez, W. Shi, D.L. Plata, E.S. Penev, B.I. Yakobson, P.B. Balbuena, C. Bichara, D.N. Futaba, S. Noda, H. Shin, K.S. Kim, B. Simard, F. Mirri, M. Pasquali, F. Fornasiero, E.I. Kauppinen, M. Arnold, B.A. Cola, P. Nikolaev, S. Arepalli, H.-M. Cheng, D.N. Zakharov, E.A. Stach, J. Zhang, F. Wei, M. Terrones, D.B. Geohegan, B. Maruyama, S. Maruyama, Y. Li, W.W. Adams, A.J. Hart, Carbon Nanotubes and Related Nanomaterials: Critical Advances and Challenges for Synthesis toward Mainstream Commercial Applications, ACS Nano. 12 (2018). https://doi.org/10.1021/acsnano.8b06511.

[53] A. Muhulet, F. Miculescu, S.I. Voicu, F. Schütt, V.K. Thakur, Y.K. Mishra, Fundamentals and scopes of doped carbon nanotubes towards energy and biosensing applications, Mater. Today Energy. 9 (2018). https://doi.org/10.1016/j.mtener.2018.05.002.

[54] J. Simon, E. Flahaut, M. Golzio, Overview of Carbon Nanotubes for Biomedical Applications, Materials (Basel). 12 (2019). https://doi.org/10.3390/ma12040624.

[55] R. Saito, M. Fujita, G. Dresselhaus, M.S. Dresselhaus, Electronic structure of chiral graphene tubules, Appl. Phys. Lett. 60 (1992). https://doi.org/10.1063/1.107080.

[56] J. Kong, Nanotube Molecular Wires as Chemical Sensors, Science (80-.). 287 (2000). https://doi.org/10.1126/science.287.5453.622.

[57] L.A. Panes-Ruiz, M. Shaygan, Y. Fu, Y. Liu, V. Khavrus, S. Oswald, T. Gemming, L. Baraban, V. Bezugly, G. Cuniberti, Toward Highly Sensitive and Energy Efficient Ammonia Gas Detection with Modified Single-Walled Carbon Nanotubes at Room Temperature, ACS Sensors. 3 (2018). https://doi.org/10.1021/acssensors.7b00358.

[58] H.Y. Jeong, D.-S. Lee, H.K. Choi, D.H. Lee, J.-E. Kim, J.Y. Lee, W.J. Lee, S.O. Kim, S.-Y. Choi, Flexible room-temperature NO2 gas sensors based on carbon nanotubes/reduced graphene hybrid films, Appl. Phys. Lett. 96 (2010). https://doi.org/10.1063/1.3432446.

[59] E. Katz, I. Willner, Biomolecule-Functionalized Carbon Nanotubes: Applications in Nanobioelectronics, ChemPhysChem. 5 (2004). https://doi.org/10.1002/cphc.200400193.

[60] S.T.R. Naqvi, T. Rasheed, D. Hussain, M. Najam ul Haq, S. Majeed, S. shafi, N. Ahmed, R. Nawaz, Modification strategies for improving the solubility/dispersion of carbon nanotubes, J. Mol. Liq. 297 (2020). https://doi.org/10.1016/j.molliq.2019.111919.

[61] S. Merum, J.B. Veluru, R. Seeram, Functionalized carbon nanotubes in bio-world: Applications, limitations and future directions, Mater. Sci. Eng. B. 223 (2017). https://doi.org/10.1016/j.mseb.2017.06.002.

[62] M. Asad, M.H. Sheikhi, M. Pourfath, M. Moradi, High sensitive and selective flexible H2S gas sensors based on Cu nanoparticle decorated SWCNTs, Sensors Actuators B Chem. 210 (2015). https://doi.org/10.1016/j.snb.2014.12.086.

[63] S.-W. Choi, J. Kim, Y.T. Byun, Highly sensitive and selective NO2 detection by Pt nanoparticles-decorated single-walled carbon nanotubes and the underlying sensing mechanism, Sensors Actuators B Chem. 238 (2017). https://doi.org/10.1016/j.snb.2016.07.153.

[64] M. Penza, R. Rossi, M. Alvisi, E. Serra, Metal-modified and vertically aligned carbon nanotube sensors array for landfill gas monitoring applications, Nanotechnology. 21 (2010). https://doi.org/10.1088/0957-4484/21/10/105501.

[65] M. Quintanilla, L.M. Liz-Marzán, Guiding Rules for Selecting a Nanothermometer, Nano Today. 19 (2018). https://doi.org/10.1016/j.nantod.2018.02.012.

[66] D. Jaque, F. Vetrone, Luminescence nanothermometry, Nanoscale. 4 (2012). https://doi.org/10.1039/c2nr30764b.

[67] C. Wang, R. Xu, W. Tian, X. Jiang, Z. Cui, M. Wang, H. Sun, K. Fang, N. Gu, Determining intracellular temperature at single-cell level by a novel thermocouple method, Cell Res. 21 (2011). https://doi.org/10.1038/cr.2011.117.

[68] K. Kim, J. Chung, G. Hwang, O. Kwon, J.S. Lee, Quantitative Measurement with Scanning Thermal Microscope by Preventing the Distortion Due to the Heat Transfer through the Air, ACS Nano. 5 (2011). https://doi.org/10.1021/nn2026325.

[69] O. Nakabeppu, M. Chandrachood, Y. Wu, J. Lai, A. Majumdar, Scanning thermal imaging microscopy using composite cantilever probes, Appl. Phys. Lett. 66 (1995). https://doi.org/10.1063/1.114102.

[70] A. Balčytis, M. Ryu, S. Juodkazis, J. Morikawa, Micro-thermocouple on nano-membrane: thermometer for nanoscale measurements, Sci. Rep. 8 (2018). https://doi.org/10.1038/s41598-018-24583-w.

[71] Y. Gao, Y. Bando, Carbon nanothermometer containing gallium, Nature. 415 (2002). https://doi.org/10.1038/415599a.

[72] G. Baffou, J. Polleux, H. Rigneault, S. Monneret, Super-Heating and Micro-Bubble Generation around Plasmonic Nanoparticles under cw Illumination, J. Phys. Chem. C. 118 (2014). https://doi.org/10.1021/jp411519k.

[73] S. Choi, E.R. Heller, D. Dorsey, R. Vetury, S. Graham, Thermometry of AlGaN/GaN HEMTs Using Multispectral Raman Features, IEEE Trans. Electron Devices. 60

(2013). https://doi.org/10.1109/TED.2013.2255102.

[74] M. Freitag, M. Steiner, Y. Martin, V. Perebeinos, Z. Chen, J.C. Tsang, P. Avouris, Energy Dissipation in Graphene Field-Effect Transistors, Nano Lett. 9 (2009). https://doi.org/10.1021/nl803883h.

[75] X. Xie, D.G. Cahill, Thermometry of plasmonic nanostructures by anti-Stokes electronic Raman scattering, Appl. Phys. Lett. 109 (2016). https://doi.org/10.1063/1.4966289.

[76] A. Benayas, B. del Rosal, A. Pérez-Delgado, K. Santacruz-Gómez, D. Jaque, G.A. Hirata, F. Vetrone, Nd:YAG Near-Infrared Luminescent Nanothermometers, Adv. Opt. Mater. 3 (2015). https://doi.org/10.1002/adom.201400484.

[77] G. Xiang, Q. Xia, S. Xu, X. Liu, S. Jiang, Y. Wang, X. Zhou, L. Li, L. Ma, X. Wang, J. Zhang, Multipath optical thermometry realized in $CaSc_2O_4:Yb^{3+}/Er^{3+}$ with high sensitivity and superior resolution, J. Am. Ceram. Soc. (2021). https://doi.org/10.1111/jace.17686.

[78] Q. Wang, M. Liao, Q. Lin, M. Xiong, Z. Mu, F. Wu, A review on fluorescence intensity ratio thermometer based on rare-earth and transition metal ions doped inorganic luminescent materials, J. Alloys Compd. 850 (2021). https://doi.org/10.1016/j.jallcom.2020.156744.

[79] C.D.S. Brites, S. Balabhadra, L.D. Carlos, Lanthanide- Based Thermometers: At the Cutting- Edge of Luminescence Thermometry, Adv. Opt. Mater. 7 (2019). https://doi.org/10.1002/adom.201801239.

[80] X. Michalet, Quantum Dots for Live Cells, in Vivo Imaging, and Diagnostics, Science (80-.). 307 (2005). https://doi.org/10.1126/science.1104274.

[81] O.I. Mićić, H.M. Cheong, H. Fu, A. Zunger, J.R. Sprague, A. Mascarenhas, A.J. Nozik, Size-Dependent Spectroscopy of InP Quantum Dots, J. Phys. Chem. B. 101 (1997). https://doi.org/10.1021/jp9704731.

[82] A. Shiohara, A. Hoshino, K. Hanaki, K. Suzuki, K. Yamamoto, On the Cyto-Toxicity Caused by Quantum Dots, Microbiol. Immunol. 48 (2004). https://doi.org/10.1111/j.1348-0421.2004.tb03478.x.

[83] A. Rassamesard, Y.-F. Huang, H.-Y. Lee, T.-S. Lim, M.C. Li, J.D. White, J.H. Hodak, T. Osotchan, K.Y. Peng, S.A. Chen, J.-H. Hsu, M. Hayashi, W. Fann, Environmental Effect on the Fluorescence Lifetime and Quantum Yield of Single Extended Luminescent Conjugated Polymers, J. Phys. Chem. C. 113 (2009). https://doi.org/10.1021/jp905996p.

[84] Y. Wu, J. Liu, J. Ma, Y. Liu, Y. Wang, D. Wu, Ratiometric Nanothermometer Based on Rhodamine Dye-Incorporated F127-Melamine-Formaldehyde Polymer Nanoparticle: Preparation, Characterization, Wide-Range Temperature Sensing, and

Precise Intracellular Thermometry, ACS Appl. Mater. Interfaces. 8 (2016). https://doi.org/10.1021/acsami.6b03366.

[85] J.R. Shakirova, N.N. Shevchenko, V.A. Baigildin, P.S. Chelushkin, A.F. Khlebnikov, O.A. Tomashenko, A.I. Solomatina, G.L. Starova, S.P. Tunik, Eu-Based Phosphorescence Lifetime Polymer Nanothermometer: A Nanoemulsion Polymerization Approach to Eliminate Quenching of Eu Emission in Aqueous Media, ACS Appl. Polym. Mater. 2 (2020). https://doi.org/10.1021/acsapm.9b00952.

[86] O.A. Savchuk, O.F. Silvestre, R.M.R. Adão, J.B. Nieder, GFP fluorescence peak fraction analysis based nanothermometer for the assessment of exothermal mitochondria activity in live cells, Sci. Rep. 9 (2019). https://doi.org/10.1038/s41598-019-44023-7.

[87] J.-C.G. Bünzli, S. V. Eliseeva, Basics of Lanthanide Photophysics, in: 2010. https://doi.org/10.1007/4243_2010_3.

[88] W.H. Fonger, C.W. Struck, Eu+35D Resonance Quenching to the Charge- Transfer States in Y_2O_2S, La_2O_2S, and LaOCl, J. Chem. Phys. 52 (1970). https://doi.org/10.1063/1.1672952.

[89] O.S. Wolfbeis, Sensor Paints, Adv. Mater. 20 (2008). https://doi.org/10.1002/adma.200702276.

[90] D. Jaque, L. Martínez Maestro, B. del Rosal, P. Haro-Gonzalez, A. Benayas, J.L. Plaza, E. Martín Rodríguez, J. García Solé, Nanoparticles for photothermal therapies, Nanoscale. 6 (2014). https://doi.org/10.1039/C4NR00708E.

[91] C.D.S. Brites, A. Millán, L.D. Carlos, Lanthanides in Luminescent Thermometry, in: 2016. https://doi.org/10.1016/bs.hpcre.2016.03.005.

[92] C.D.S. Brites, X. Xie, M.L. Debasu, X. Qin, R. Chen, W. Huang, J. Rocha, X. Liu, L.D. Carlos, Instantaneous ballistic velocity of suspended Brownian nanocrystals measured by upconversion nanothermometry, Nat. Nanotechnol. 11 (2016). https://doi.org/10.1038/nnano.2016.111.

[93] R.G. Geitenbeek, A.-E. Nieuwelink, T.S. Jacobs, B.B. V. Salzmann, J. Goetze, A. Meijerink, B.M. Weckhuysen, In Situ Luminescence Thermometry To Locally Measure Temperature Gradients during Catalytic Reactions, ACS Catal. 8 (2018). https://doi.org/10.1021/acscatal.7b04154.

[94] C. Mi, J. Zhou, F. Wang, G. Lin, D. Jin, Ultrasensitive Ratiometric Nanothermometer with Large Dynamic Range and Photostability, Chem. Mater. 31 (2019). https://doi.org/10.1021/acs.chemmater.9b03466.

[95] S. Kiyonaka, T. Kajimoto, R. Sakaguchi, D. Shinmi, M. Omatsu-Kanbe, H. Matsuura, H. Imamura, T. Yoshizaki, I. Hamachi, T. Morii, Y. Mori, Genetically encoded fluorescent thermosensors visualize subcellular thermoregulation in living cells, Nat.

Methods. 10 (2013). https://doi.org/10.1038/nmeth.2690.

[96] M. Xu, X. Zou, Q. Su, W. Yuan, C. Cao, Q. Wang, X. Zhu, W. Feng, F. Li, Ratiometric nanothermometer in vivo based on triplet sensitized upconversion, Nat. Commun. 9 (2018). https://doi.org/10.1038/s41467-018-05160-1.

[97] K. Okabe, N. Inada, C. Gota, Y. Harada, T. Funatsu, S. Uchiyama, Intracellular temperature mapping with a fluorescent polymeric thermometer and fluorescence lifetime imaging microscopy, Nat. Commun. 3 (2012). https://doi.org/10.1038/ncomms1714.

[98] X. Zhu, J. Li, X. Qiu, Y. Liu, W. Feng, F. Li, Upconversion nanocomposite for programming combination cancer therapy by precise control of microscopic temperature, Nat. Commun. 9 (2018). https://doi.org/10.1038/s41467-018-04571-4.

[99] H. Zhou, M. Sharma, O. Berezin, D. Zuckerman, M.Y. Berezin, Nanothermometry: From Microscopy to Thermal Treatments, ChemPhysChem. 17 (2016). https://doi.org/10.1002/cphc.201500753.

[100] L. Shang, F. Stockmar, N. Azadfar, G.U. Nienhaus, Intracellular Thermometry by Using Fluorescent Gold Nanoclusters, Angew. Chemie Int. Ed. 52 (2013). https://doi.org/10.1002/anie.201306366.

[101] M. Suzuki, T. Plakhotnik, The challenge of intracellular temperature, Biophys. Rev. 12 (2020). https://doi.org/10.1007/s12551-020-00683-8.

[102] M. Suzuki, V. Tseeb, K. Oyama, S. Ishiwata, Microscopic Detection of Thermogenesis in a Single HeLa Cell, Biophys. J. 92 (2007). https://doi.org/10.1529/biophysj.106.098673.

[103] J. Zhou, B. del Rosal, D. Jaque, S. Uchiyama, D. Jin, Advances and challenges for fluorescence nanothermometry, Nat. Methods. 17 (2020). https://doi.org/10.1038/s41592-020-0957-y.

Chapter 3

Chemical sensor based on carbon nanotubes decorated with metal nanoparticles

Due to their unique mechanical, electronic, and thermal properties, CNTs have been employed in a vast number of applications that range from energy storage, building reinforcement, devices with nanochips, biological applications and as active layers in chemical sensors. This last application triggered our interest on the modification of carbon nanotubes for improving gas sensing properties discussed in this PhD thesis. CNTs are considered promising candidates for active layers in chemical sensors due to their large surface-to-volume ratio, an important characteristic for active materials in sensors. Nevertheless, the intrinsically inert surface of CNTs makes it difficult to react with target molecules, this is the main drawback to develop high sensitivity chemical sensor based on carbon nanotubes. A possible solution to tackle this disadvantage is the functionalization or conjugation of carbon nanotubes with chemical groups or materials that increase their chemical reactivity towards selected molecules.

In this part of this research project multiwall CNTs were synthetized by chemical vapor deposition and functionalized with oxygen groups through low kinetic energy oxygen ion irradiation, a clean, fast, and efficient functionalization technique, to increase their chemical reactivity. Different parameters (ion energy and irradiation time) were used for oxygen ion irradiation, aiming at controlling the type and concentration of the oxygen functional groups grafted to the CNTs surface. Subsequently, the thermal stability of the grafted oxygen groups was investigated combining a thermal annealing treatment with XPS analysis to evaluate the chemical changes at the CNT surface as a function of annealing temperature. This step is important because often chemical sensors are heated to reach an optimal detection efficiency.

The oxygen groups grafted to CNT surface were further used as active sites for the decoration of CNTs with metal nanoparticles. It has been shown that decoration of CNTs with metal nanoparticles can improve their sensing properties. Palladium and nickel bimetallic nanoparticles were deposited on the surface of CNTs using plasma sputtering deposition.

Finally, the CNTs decorated with Ni-Pd nanoparticles were used as active layers on resistive chemical sensors for the detection of hazardous gases such as: NO_2, H_2, toluene and ethanol. The resistance variation of Ni-Pd-Ox-CNTs network when is exposed to different concentrations of the gases was used to evaluate the interaction gas-active layer occurring in the chemical sensor. A schematic representation of the sensor is showed in the Figure 3.1.

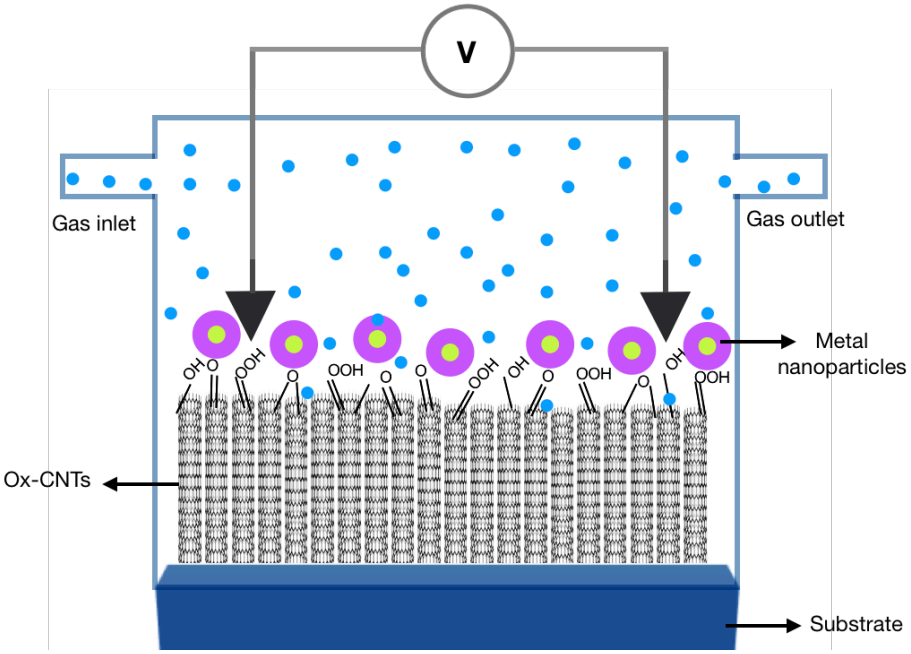

Figure 3.1. Schematic representation of the Ni-Pd-Ox-CNTs chemical sensor.

3.1 Oxygen functionalization of carbon nanotubes

Carbon nanotubes (CNTs) are good candidates to be used as chemical sensors due to their high thermal conductivity that prevents the formation of hotspots next to the catalytic site and, high surface-to-volume ratio that increases the surface interaction with the target molecules, increasing the sensitivity of the sensor. However, CNTs possess an inert surface responsible by their poor chemical reactivity. To increase the chemical reactivity of CNTs, functionalization, *i. e.*, doping with heteroatoms, decoration with nanoparticles and/or grafting of functional groups to their surface have been suggested.

Oxygen functionalization of CNTs has a significant positive effect in the reactivity of the nanotubes surface [1,2], besides of decreasing their hydrophobicity improving their dispersion in aqueous media. In addition, oxygen functional groups can be used as active sites for further functionalization which enlarges the implementation of CNTs to improve and develop other applications such as water purification and drug delivery [3]. The

electronic properties of CNTs can be also modified by oxygen functionalization, Barinov et al, reported that grafting oxygen groups in the surface of metallic carbon nanotubes leads to their conversion into semiconducting CNTs [4].

3.1.1 Low kinetic energy ion irradiation

Different techniques are reported in literature to accomplish the oxygen functionalization of CNTs, among the most common we can found wet chemistry, simultaneous functionalization during the synthesis and plasma functionalization [5–8]. These techniques have been successfully used during the last years. However, a precise functionalization method must be used to obtain the fine tuning of the CNTs properties by grafting oxygen groups to their surface. It is in this framework, that oxygen functionalization through low kinetic energy ion irradiation has been developed.

Ion irradiation as functionalization technique basically consist of irradiating a target (in this work, CNTs) with ions of a certain kinetic energy. Ion irradiation is classified in two regimes: low kinetic energy ion irradiation (less than a few keV) and the high kinetic energy ion irradiation (from several keV to MeV) [9,10]. During ion irradiation four different physical phenomena can be observed: ion transmission, reflection, adsorption, and damage of the target. The damage induced by ion irradiation in nanomaterials is classified as: substitution, single or multiple vacancies and in-plane disorder: substitution is referred to the replacement of one atom from the target by the irradiated ion, creation of vacancies is the ejection of one or more atoms in the target that are not filled by other atoms and, in-plane disorder indicates the disorder of atoms in the target generated by the incident ions where these disordered atoms are not removed from the sample [11]. For the case of low kinetic energy ion irradiation, most of the ions interact with the target and remain grafted to its surface, predominantly at the defect sites generating surface functional groups. The first ions arriving create defects, these recently created defects will react with following irradiated ions to create further functionalizations (Figure 3.2). The type of the defects created by ion irradiation depends on the ion mass and kinetic energy [12]. The defect creation by interaction of the irradiated ions with the atoms in the target also depends on the minimum energy required to eject an atom from its original position by the impact of an energetic particle, this is known as displacement threshold energy (T_d) and it is different for every material [13]. Just when the energy of the irradiated ions is higher than the T_d of the atoms in the target the atoms will be displaced. The value of T_d for carbon materials varies between carbon allotropes because depends on the bond energy and the local chemical bonding. For carbon sp^2 the T_d energy is between 15 and 20 eV, and for carbon sp^3 ranges from 30 to 48 eV [13]. It is important to mention that the threshold energy (T_d) of carbon atoms in carbon nanotubes will depend also on the geometry of the tube like the diameter and size.

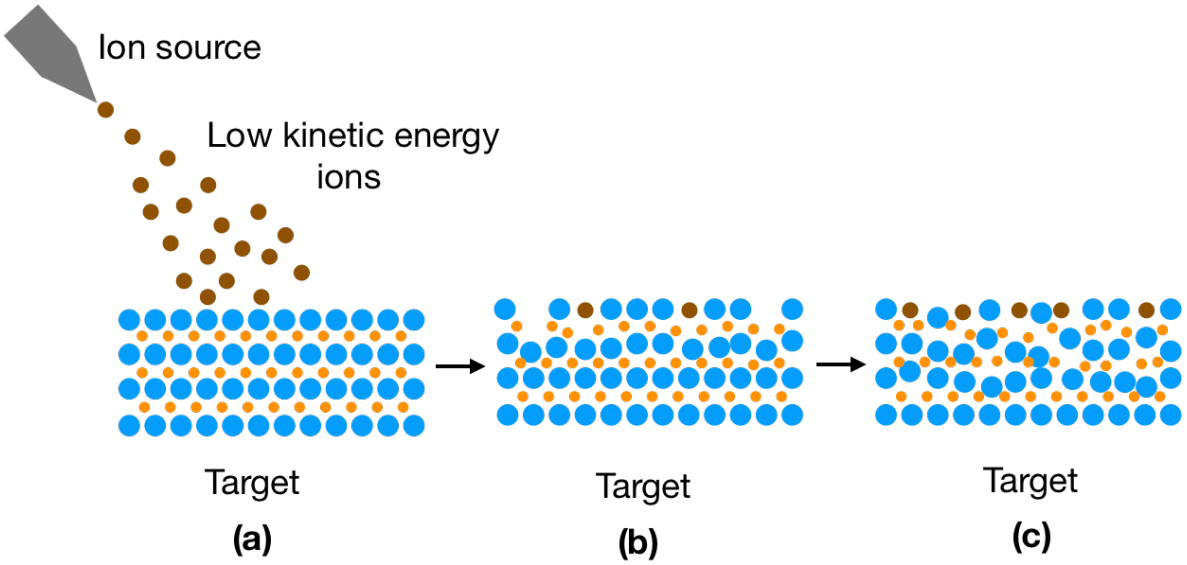

Figure 3.2. Schematic representation of low kinetic energy ion irradiation. (a) The ions are brought to the target by an ion source. (b) Some ions are grafted to the target surface resulting in functionalization, here also some defects are created. (c) Final result after ion irradiation, defects and functionalization are created.

Compared with other functionalization techniques, low kinetic energy ion irradiation has the advantages of being environmental friendly because does not generate liquid waste like the wet chemistry functionalization, with the use of a proper mask, ion irradiation can be site-selective, the functionalization is carried out with precise ion dose control allowing fine tuning of the type and amount of grafted species. Low kinetic energy ion irradiation is also very efficient, a reasonable concentration of functional groups are created in short treatment times, besides, this technique offers the possibility of scaling up to produce large quantities of functionalized CNTs for commercial use.

3.1.2 Synthesis of vertically aligned carbon nanotubes by chemical vapor deposition

The vertically aligned multiwall carbon nanotubes (v-CNTs) used in this work were synthetized via chemical vapor deposition (CVD) by our collaborators in the University of Namur (Figure 3.3) [14]. During the synthesis, C_2H_4(g) is used as a carbon source and a multilayer system composed of Si/Al/Fe works as the catalyst. Si wafers are used as substrates. An Al thin film (30 nm) is deposited on Si wafers and then, after its oxidation, a 1.5 nm thick Fe layer is deposited and heated to 300 ºC for three hours to form nanoparticles, which are used for the CNTs as growth active sites (catalyst). The Al and Fe layers are prepared by magnetron sputtering using a Quorum device. For the v-CNTs growth, a CVD

reactor is heated to 750 ºC in atmospheric pressure under He flow (500 sccm). The catalyst is placed inside the reactor and H_2 flow (200 sccm) is introduced into the reactor for 20 min. After that, C_2H_4 flow (60 sccm) is introduced into the reactor for 24 min. After the growth, H_2 and C_2H_4 flows are switched off and a flow of He is used to clean the reactor (500 sccm). The outer diameter distribution of the v-CNTs obtained was 10–40 nm.

Vertically aligned carbon nanotubes (v-CNTs) are used due to their unidirectional electron transport that facilitates the transducer operation in sensors [14]. Besides, their vertical geometry avoids the use of wet chemistry preventing contamination of the CNTs walls during integration of the active layer in sensor devices.

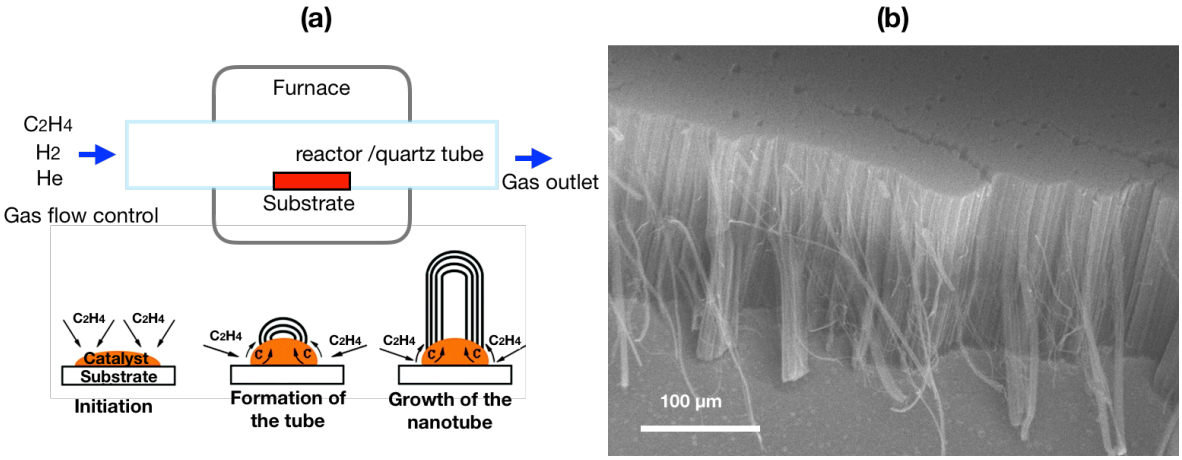

Figure 3.3. (a) Diagram of CNTs CVD instrumentation and growth mechanism, (b) image captured with scanning electron microscope (SEM) from a cross section of vertically aligned CNTs synthetized by CVD.

3.1.3 Oxygen functionalization of v-CNTs by low kinetic energy ion irradiation

Vertically aligned multiwall carbon nanotubes (v-CNTs) were functionalized with oxygen groups by low kinetic energy ion irradiation. The influence of the ion kinetic energy and the irradiation time in the type and concentration of the grafted functional groups in v-CNTs was investigated.

Vacuum system PREVAC-541. Low kinetic energy oxygen ion irradiation in v-CNTs was carried out in a *Vacuum Chamber System* (PREVAC-541). The system is composed of a ultra high vacuum (UHV) chamber (*Plafon,* a cylindrical chamber made of stainless steel equipped with standard flanges in different sizes for connecting different surface treatment tools) with a sample manipulator, a *linear transfer* for sample transferring between chambers (*Plafon* and XPS analysis) and a *load lock* chamber for fast introduction of the samples into the

system (Figure 3.4). The *plafon* and *load lock* chambers are connected to a set of pumps and pressure sensors with controllers that maintain the chambers in the desired vacuum level (Figure 3.5). The system is provided with strategically placed windows with LED illumination sources that allows easy observation of the interior of the chambers. The system is devoted for sample preparation and surface treatment by using complementary accessories, in this work is an ion source. The samples are introduced in the chamber after being placed in a special sample holder. Figure 3.6 shows a picture of the v-CNTs mounted in the sample holder.

Pumping system for the plafon chamber. This pump permits to achieve and hold the pressure in the range of ~10^{-8} and 10^{-9} mbar. It is composed of a turbomolecular pump (HiPace700), a fore-vacuum pump (NeoDry30E), and two vent valves, one electromagnetic valve on the turbomolecular pump and one safety valve located between the pumps.

Sample manipulator. Mounted on the side flange of the *plafon* chamber, allows the possibility of sample linear motion and rotation. The manipulator has an option of heating and cooling the specimens mounted on the sample holder.

Load lock chamber. Enables entering a sample to UHV conditions without venting the entire system. After placing samples on an appropriate holder (Figure 3.6), the holder is mounted on the hand gripper and placed in the load lock station.

Pumping system for the load lock chamber. Allows to achieve and hold the pressure in the range of 5×10^{-8} mbar. It is composed of a turbomolecular pump (HiPace300), a fore-vacuum pump (NeoDry15E), and two vent valves one electromagnetic valve on the turbomolecular pump and one safety valve located between the pumps.

Vent valves. Installed in pumping circuit installation, valves are used for chambers venting and N_2 gas is used for the ventilation. Vent valves are controlled automatically from electronics.

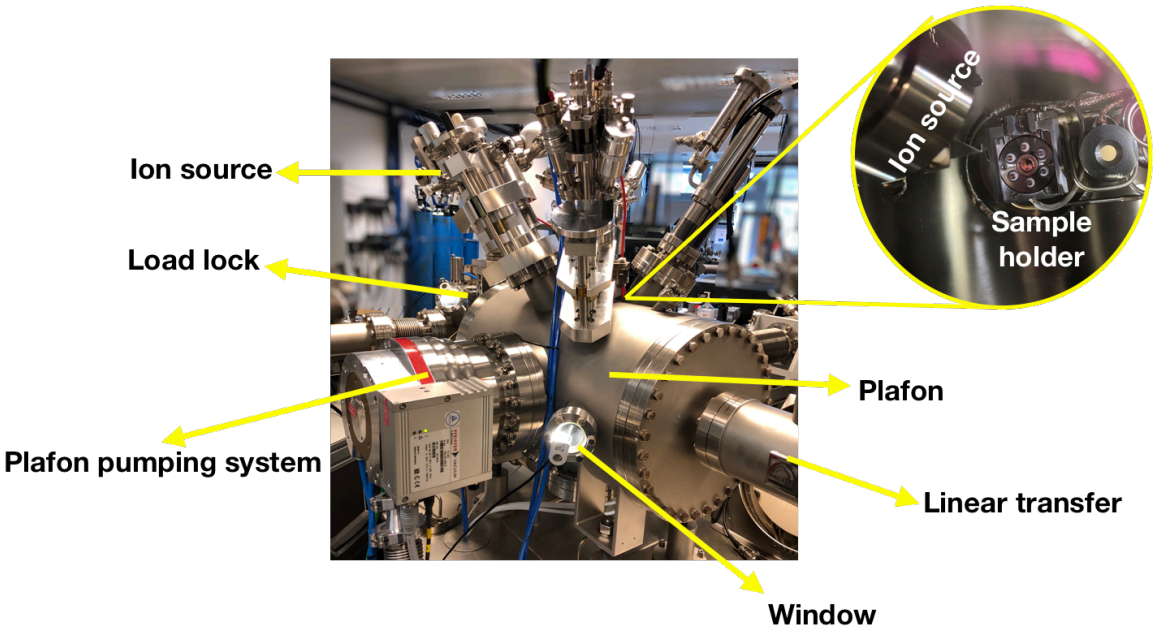

Figure 3.4. Ultra high vacuum (UHV) system PREVAC-541. The main parts of the system are tagged in the figure. The zoomed image shows the tip of the ion source and the sample manipulator inside the *plafon* chamber.

Figure 3.5. Controllers of the vacuum system PREVAC-541 that maintain the chambers in the desired vacuum level. (a) *Plafon* controller, (b) *load lock* controller.

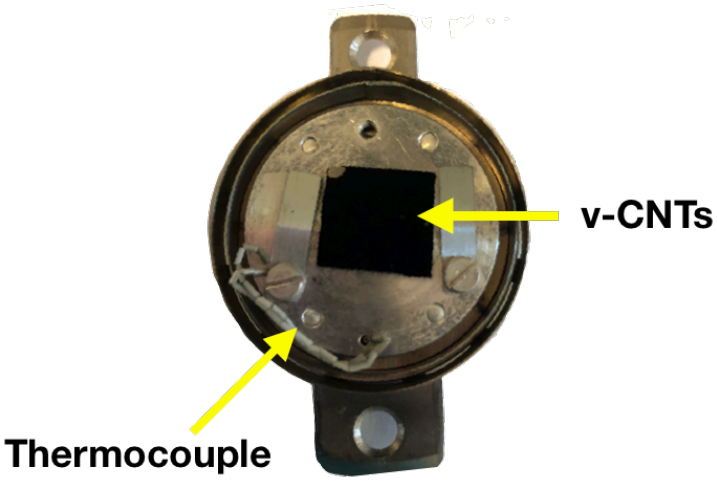

Figure 3.6. Sample holder used for the vacuum system PREVAC-541 showing a sample of vertically aligned carbon nanotubes mounted in the holder. The sample holder is customized with a thermocouple that measures the temperature of the sample.

Ion source. The ion source is a Tectra plasma ion source (TPIS) which schematic representation is showed in Figure 3.7. In the ion source a plasma is created at the plasma cup using microwaves with a frequency of 2.45 GHz energy and low-pressure gas O_2, the pressure used in this work was 2×10^{-5} mbar. The microwaves are generated by a magnetron coupled to a coaxial feedthrough structure, which guided the microwaves into the plasma cup containing low pressure O_2 gas. The electrons generated in the plasma undergo cyclotron resonance motion increasing their perpendicular kinetic energy due to a magnetic quadrupole arranged around the discharge chamber. These energized free electrons collide with the gas in the volume causing ionization of the gas if their kinetic energy is larger than the ionization energy of the atoms or molecules. In the plasma, ions (molecular ions and atomic ions), neutrals species, electrons, and photons are formed, the positive ions are extracted from the plasma using two grids located at the end of the plasma cup. A positive voltage is applied to the first grid to accelerate ions extracting out to the target the other grid had a negative voltage and assisted in the ion extraction and the beam current. The distance between the ion source exit and the surface of the target is 12 cm.

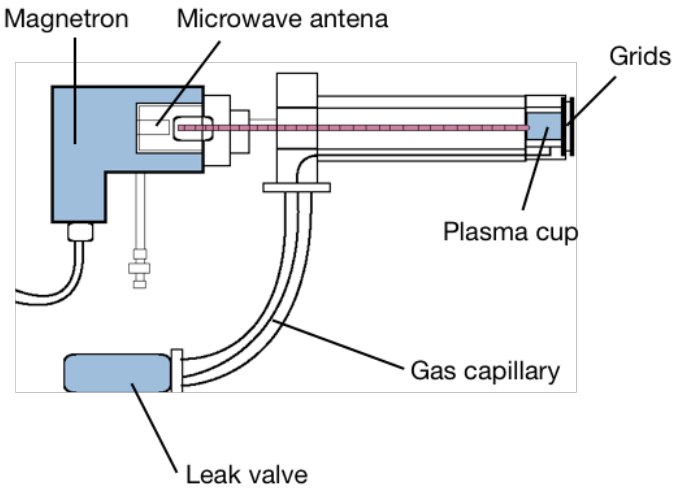

Figure 3.7. Schematic diagram of the ion source TPIS used to functionalize v-CNTs with oxygen groups.

Oxygen ion irradiation parameters. The oxygen functionalization of the v-CNTs was performed varying the irradiation time and the ion kinetic energy separately, when the time was varied (1, 2.5, 5 and 10 minutes) the ion kinetic energy was fixed to 1 keV, while when the kinetic energy was varied (0, 0.1, 0.25, 0.5, 1.0, 1.5 and 2 keV) the time was fixed to 5 minutes. The different parameters are detailed in the Table 3.1. For all the samples the current induced by ion irradiation was 10 μA. The range of kinetic energy was selected from 0 to 2 keV in order to perform all of the irradiations in the low ion kinetic energy regime. The maximum of treatment time was 10 minutes to avoid the production of numerous defects in the nanotubes surface.

Irradiation time (min)	Ion kinetic energy (keV)
0	-
1	1
2.5	1
5	1
10	1
5	0
5	0.1
5	0.25
5	0.5
5	1.5
5	2

Table 3.1 Irradiation parameters used for oxygen functionalization of vertically aligned multiwall carbon nanotubes (v-CNTs).

3.2 Characterization of oxygen functionalized carbon nanotubes

3.2.1 Electron microscopies of oxygen functionalized v-CNTs

To evaluate the damaged that may be induced in the alignment and morphology of v-CNTs after oxygen ion irradiation, v-CNTs were analyzed by scanning electron (SEM) and electron transmission (TEM) microscopies before and after the ion irradiation.

Figure 3.8 shows the SEM images obtained from v-CNTs before (Figure 3.8a) and after (Figure 3.8b) the ion irradiation, no significant changes are observed, this indicate that the macroscopic morphology of v-CNTs as well as its density and alignment are not affected by the oxygen ion irradiation.

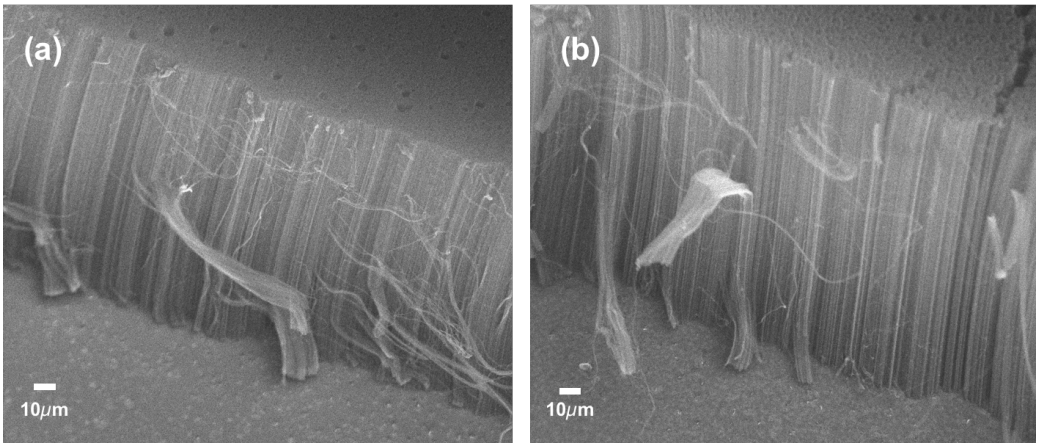

Figure 3.8. Scanning electron microscopy (SEM) of v-CNTs. Cross section image from v-CNTs before (a) and after (b) oxygen ion irradiation (5 minutes 1 keV of ion kinetic energy).

Figure 3.9 shows the comparison of TEM images recorded in the v-CNTs before and after their functionalization with low kinetic energy oxygen ion irradiation. The v-CNTs pristine sample shows the disorder typical of chemical vapor deposition synthesis at low temperature. After the ion irradiation the structure of CNTs is preserved. However, it is possible to distinguish that an important number of the nanotubes exhibit open tips while the tips of the pristine nanotubes are closed. The functionalization of the nanotubes begins at the closed tips of the tubes that are reported to be more reactive than the nanotube wall [15], the oxygen functionalization breaks the bonds that maintain the tips closed and the new functional groups grafted to the tips prevents the tube tip to close again. This observation is an evidence of oxygen functionalization carried out at the tips (defect sites) of the tubes.

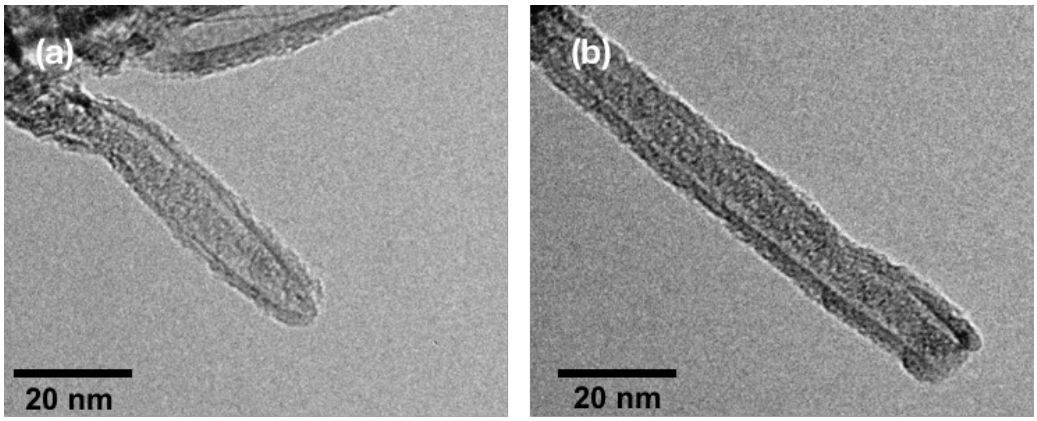

Figure 3.9. Images obtained from transmission electron microscopy (TEM) of a pristine CNT (a) and CNT after 5 minutes of irradiation with ions with 2 keV of kinetic energy.

3.2.2 Chemical composition of oxygen functionalized v-CNTs

X-ray photoelectron spectroscopy (XPS) was used to obtain the relative atomic concentration of the elements present in each sample. A survey spectrum is first recorded for all the samples. Figure 3.10 shows a comparison of the survey spectrum for pristine v-CNTs and v-CNTs after being irradiated for five minutes with ions with 1 keV of kinetic energy. Two peaks are observed in both cases, the first is centered at 284.4 eV associated to photoelectrons ejected from the C1s electronic level, and the second at 532.6 eV assigned to photoelectrons emitted from O1s electronic level.

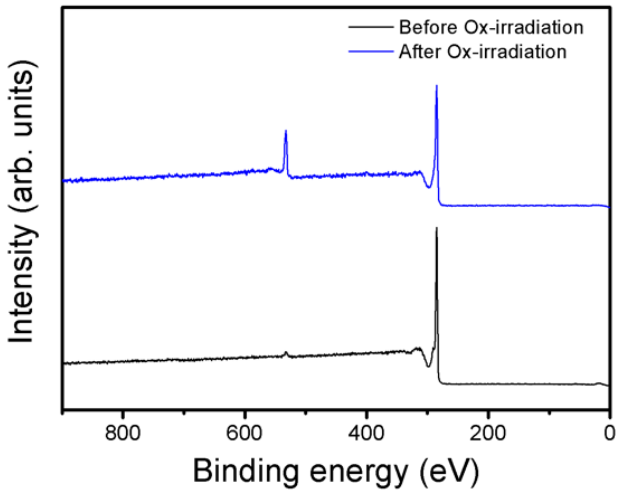

Figure 3.10. XPS survey spectra comparison between v-CNTs before (black line) and after 5 min of irradiation with oxygen ions with 1 keV of kinetic energy (blue line).

The concentration of oxygen and carbon for all samples is shown in the Table 3.2 and graphically represented in the Figure 3.11. The oxygen concentration in v-CNTs pristine (1.7 at. %) is related to oxidation of the sample due to air exposure. For increasing irradiation time with a fixed ion kinetic energy, the relative concentration of oxygen increased from 1.7 to 20.0 at. % (Figure 3.11a). In the other case, for increasing ion kinetic energy, from 0.5 to 2 keV, the relative concentration remains almost constant (15.0 at. %) independent of the ion energy. From these results we can conclude that the ion kinetic energy in the range from 0.5 to 2 keV does not affect the amount of oxo-groups grafted at the CNTs surface (Figure 3.11b).

v-CNTs sample	**Oxygen content (at. %)**	**Carbon content (at. %)**
Pristine	1.7	98.3
1 minute / 1 keV	6.7	93.3
2.5 minutes / 1 keV	10.0	90.0
5 minutes / 1 keV	14.2	85.8
10 minutes / 1 keV	20.0	80.0
5 minutes / 0 keV	8.0	92.0
5 minutes / 0.1 keV	8.4	91.6
5 minutes / 0.25 keV	9.8	90.2
5 minutes / 0.5 keV	15.4	84.6
5 minutes / 1.5 keV	14.5	85.5
5 minutes / 2 keV	16.0	84.0

Table 3.2. Relative atomic concentration (at. %) of oxygen and carbon in v-CNTs samples.

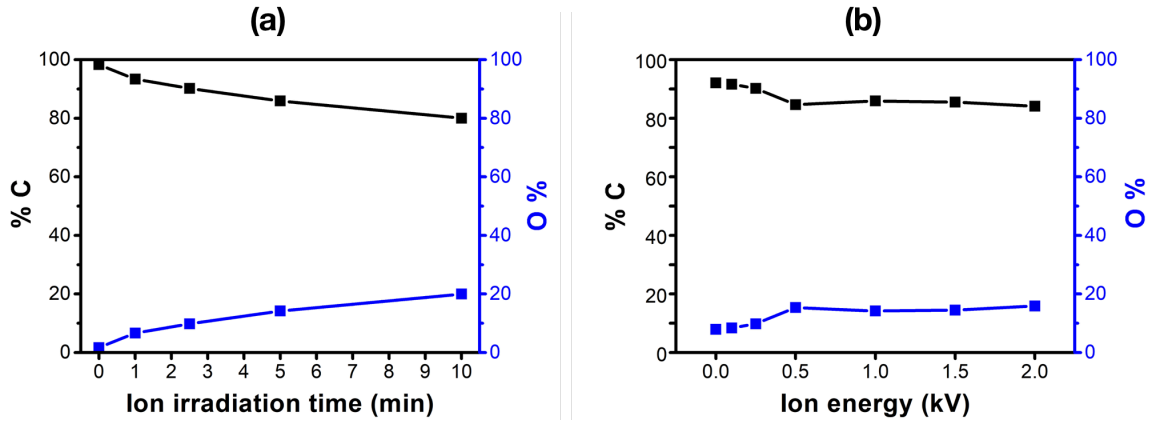

Figure 3.11. Carbon and oxygen content in v-CNTs samples before and after oxygen functionalization. Samples with increasing ion irradiation time are showed in (a) and samples with increasing ion kinetic energy are showed in (b).

3.2.3 Chemical configuration of oxygen functionalized v-CNTs

Besides of giving the relative atomic concentrations of the samples, XPS is also used to characterize changes in the bonding configuration of the atoms via the analysis of the shift in the binding energy of the core electrons of the different atoms composing the sample. A detailed analysis of the C1s XPS spectrum for all the samples was realized to obtain information about the chemical configuration of the oxygen groups grafted at the v-CNTs surface. The components peaks result from a least-squares fitting procedure performed in the software CASA XPS. The Shirley-type background was used for all the fitting procedures and the carbon peak position is calibrated at 284.4 eV. The synthetic line shapes used in the deconvolutions are Doniach-Sunjic functions for asymmetric peaks and Gaussian-Lorentzian functions for symmetric peaks.

Figure 3.12 shows the result of the curve fitting procedure for the C1s spectrum of v-CNTs pristine and after being irradiated for 10 minutes with ions with kinetic energy of 1 keV. C1s spectrum from pristine v-CNTs is an asymmetric peak and is showed in Figure 3.12a. This asymmetry is generated by the interaction of the photoelectron with electrons in the valence band, promoting one electron to upper energy levels (intra band transitions) resulting on energy loss of the photoelectron and C1s peaks distorted with respect to the intrinsic line-shape. Asymmetric peaks are reproduced in the fitting using the Doniach-Sunjic function [16]. This peak is centered at 284.4 eV, assigned to photoelectrons ejected from sp^2 carbon atoms [4,5]. A second peak centered at 290.9 eV is observed, this peak is assigned to photoelectrons that lose kinetic energy due to π-Plasmon excitations, that is collective excitations of electrons in the conduction band. In quantum-mechanics such excitations are described as pseudo particles called Plasmon, this peak is symmetric, a Gaussian-Lorentzian function was used to reproduce it.

C1s spectrum belonging to oxygen functionalized v-CNTs is showed in Figure 3.12b. A widening in the spectrum in the range of 285-290 eV can be observed, this widening is caused by the bonding of oxygen atoms with carbons in v-CNTs. To reproduce the spectrum, the two components of C1s pristine fitting were used in addition to four symmetric peaks. The new components are centered at binding energies of 285.0 eV, 286.6 eV, 287.5 eV and 288.8 eV. The component at 285.0 eV is assigned to photoelectrons emitted from carbon with sp^3 hybridization, this type of carbon bonding occurs at defects sites that are being introduced in the nanotubes by ion irradiation. These defects include inter-tube cross-linking defects and amorphization. The last three components are associated to carbon bonded to oxygen. The increased binding energy of these photoelectrons (286.6, 287.5 and 288.8 eV) is explained by changes in the Coulomb forces interactions that electrons in core levels feel, this change is called the “chemical shift” and permits to differentiate between different chemical environment of the same atom, in this case, the induced positive charge of the electronegative oxygen atoms in the carbon atoms change the electron screening of the carbon nucleus

increasing the binding energy of photoelectrons ejected from C1s core level. The peak assignment was done using the report by Bittencourt et. al who used spin polarized density functional calculations within the local density approximation (LDA) employing the AIMPRO code to analyze in detail XPS spectra of oxygen functionalized CNTs: the component at 286.6 eV is assigned to epoxide groups (C–O), the component 287.5 eV to carbonyl groups (C=O) and 288.8 eV to carboxyl groups (–COOH) [5].

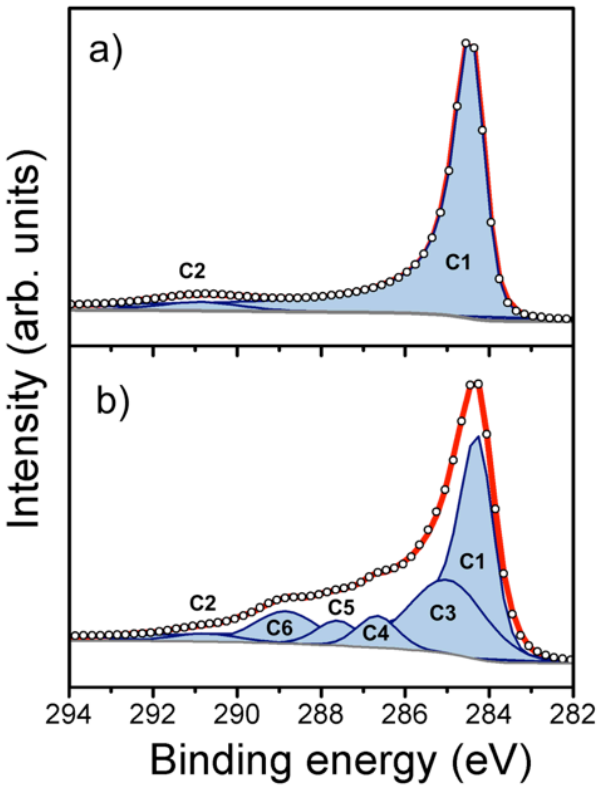

Figure 3.12. XPS analysis of v-CNTs pristine (a) and v-CNTs after 10 min of irradiation with oxygen ions with ion kinetic energy of 1 keV (b). C1 is assigned to sp^2-C (284.4 eV), C2 to π-plasmon excitations (290.9 eV), C3 to sp^3-C (285.0 eV), C4 to epoxide groups C–O (286.6 eV), C5 to carbonyl groups C=O (287.5 eV) and C6 to carboxyl groups –COOH (288.8 eV).

The analysis of the C1s spectrum was performed for all the v-CNTs samples. The relative concentration for each component of the spectra was calculated and it is resumed in the Table 3.3.

Irradiation time (min)	Ion kinetic energy (keV)	sp^2-C (%C) C1 284.4 eV	sp^3-C (%C) C3 285.0 eV	C-O (%C) C4 286.6 eV	C=O (%C) C5 287.5 eV	-COOH (%C) C6 288.8 eV	Plasmon (%C) C2 290.9 eV
0	-	96.3	0	0	0	0	3.7
1	1	80.4	8.4	0.7	1.8	0	2.0
2.5	1	74.8	10.4	1.5	2.2	0	1.3
5	1	61.5	14.4	2.7	4.0	2.5	0.7
10	1	50.2	15.9	3.6	3.0	5.8	1.5
5	0	78.5	8.1	5.0	0	0	0.5
5	0.1	85.1	5.0	1.2	0	0.3	0
5	0.25	75.9	8.8	2.3	0	1.7	1.3
5	0.5	60.2	13.3	2.8	1.7	4.8	1.8
5	1.5	59.6	16.2	3.6	2.0	3.2	0.9
5	2	60.5	13.0	3.3	3.5	2.3	1.4

Table 3.3. Relative concentration (%C) of the components used the reproduce the C1s spectrum for all v-CNTs samples.

Figure 3.13 shows the analysis of the relative concentration of the sp^2-C and sp^3-C components as a function of the treatment time (Figure 3.13a) and the kinetic energy (Figure 3.13b). It can be observed that the intensity of sp^2-C component decreases considerably as the time duration of ion irradiation increases. The concentration is 96.3% in the pristine sample and decreases to 50.2% in the sample irradiated for 10 min (kinetic energy 1 keV). This decrease in concentration indicates that oxygen functionalization is being carried out through the breakdown of π bonding in the sp^2-C bond. As expected, some defects are induced in the carbon nanotube lattice by ion irradiation, this was observed with the increase in the relative concentration of the sp^3-C component from 0 to 15.9% with increase of the treatment time (Figure 3.13a). The sp^3-C component is related to defects in the structure of carbon nanotubes because it is a direct indication of the breaking of sp^2 carbon. As mentioned before, perfect carbon nanotubes are composed of merely carbon with sp^2 hybridization. The presence of sp^3 carbon indicates the honeycomb-like structure breakdown of the carbon nanotube.

When the treatment time was 5 minutes, and the ion kinetic energy was varied from 0 to 2 keV, it can be observed that in the range of 0.5 to 2 keV the relative concentration of the sp^2-C and sp^3-C is not significantly affected by the ion kinetic energy and remain stable in the range of 59.6% to 60.5% and 13.3% to 16.2%, respectively (Figure 3.13b). These results indicated that in the range of 0.5 to 2 keV of ion kinetic energy the same number of ions interact with the carbon nanotubes. The slight decrease in the sp^3-C component observed when the sample was irradiated with 0.1 keV ions can be associated to a preferential removal of physically adsorbed species (amorphous carbon and oxygen species including water)

occurring during the synthesis and due to the exposure to ambient air.

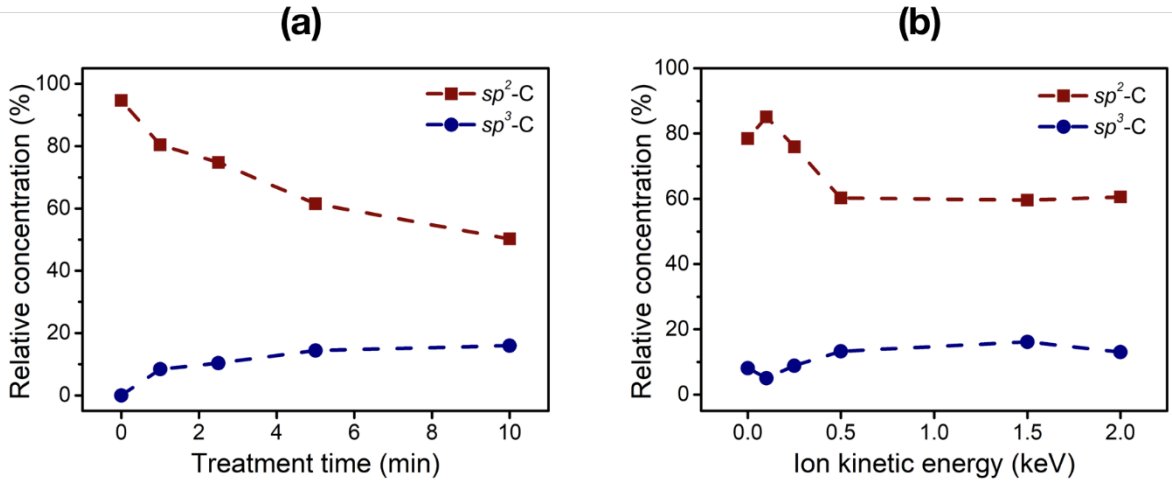

Figure 3.13. Variation in relative concentration of the components of carbon sp^2-C (C1) and carbon sp^3-C (C3) used to reproduce the C1s XPS spectrum of v-CNTs as a function of the treatment time (ion kinetic energy 1 keV; (a)) and the ion kinetic energy (fixed treatment time: 5 min; (b)).

The relative concentration of the different species of carbon bonded to oxygen is showed in Figure 3.14a as a function of irradiation time and in Figure 3.14b as a function of ion kinetic energy. Epoxide groups are the first functional groups formed in the basal plane at the beginning of the irradiation and increases its concentration with the time. Otherwise, carbonyl groups are rapidly formed and their concentration is increasing faster than the one of the epoxide groups. This can be explained with the functionalization of the nanotubes tips which chemical reactivity is higher than the sidewalls of the tube [17]. After 5 minutes of irradiation, enough defects were created in the nanotubes surface, giving rise to an increase in the relative concentration of C=O and COOH groups. Carbonyl groups may be acting as intermediates groups transforming themselves into COOH after oxygen saturation. In this way is explained the large increase in the COOH functional group and the stability in concentration of carbonyl groups with the treatment time (Figure 3.14a). On the other hand, as the ion kinetic energy increased the epoxide relative concentration decreases, this can be caused because at higher ion kinetic energies there is a higher probability of inducing defects in carbon nanotubes and other types of oxygen species are formed (carbonyl and carboxyl forms).

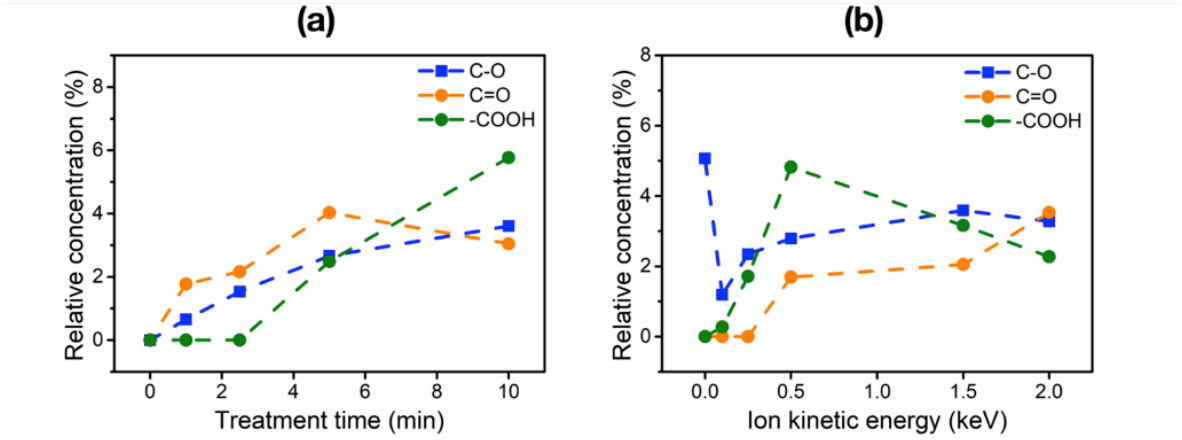

Figure 3.14. Variation in the relative concentration of the components of carbon bonded to oxygen (C4 (C–O), C5 (C=O) and C6 (–COOH)) used to reproduce the C1s XPS spectrum of v-CNTs as a function of the treatment time (ion energy 1 keV; (a)) and the ion kinetic energy (treatment time 5 min; (b)).

Remote plasma functionalization. When the extractor of the ion source is set to 0 keV of kinetic energy all the species generated in the plasma chamber (atoms, electrons, ions, photons) can leave the ion source but none of the species are accelerated to reach the sample surface. This type of functionalization is known as a remote plasma treatment, the term remote is used here because species with short lifetime recombine before reaching the sample surface [18]. Here, remote plasma oxygen functionalization was performed in v-CNTs with a treatment time of 5min (0keV). The oxygen atomic concentration grafted in this sample was 8.0 at. %, about the half of the oxygen grafted by low kinetic ion irradiation with the same treatment time for kinetic energies within the 0.5-2 keV range (Figure 3.11b), this is an evidence of the higher efficiency of low kinetic energy ion irradiation over remote plasma functionalization. The higher efficiency of low kinetic energy ion irradiation can be explained by an increasing probability of defect creation with increasing ion kinetic energy, this was firstly reported by Lehtinen et al. Figure 3.15 summarize their reported results, using atomistic computer simulations based on analytical potential and density-functional theory models, these authors studied effects of ion irradiation on graphene [12]. They identified the type and concentration of defects which appear in graphene under impacts of various ions with energies ranging from tens of electron volts to mega-electron volts. Defects beyond single and double vacancies are formed via in-plane recoils. They demonstrated that the conventional approach based on binary-collision approximation developed for bulk solids cannot be applied to low-dimensional systems as it treats the target as amorphous medium without any account for the actual atomic structure. In Figure 3.15, we can see that during the ion irradiation of carbon nanomaterials the probability to create defects increases considerably up to 0.5 keV of ion kinetic energy [12]. In addition, the shorter lifetime of the

oxygen species generated in remote plasma treatment may result in certain recombination into stable species that are not capable to react with carbon nanotubes. Another advantage of low kinetic energy ion irradiation over remote plasma treatment is the opportunity of control the type of defects created in the sample. In the Figure 3.15 can be observed that the probability of generate different types of defects, like single and double vacancies and more complex defects, by ion irradiation depends on the kinetic energy of the irradiated ions, thus, controlling the ion kinetic energy can be controlled the type of defects created.

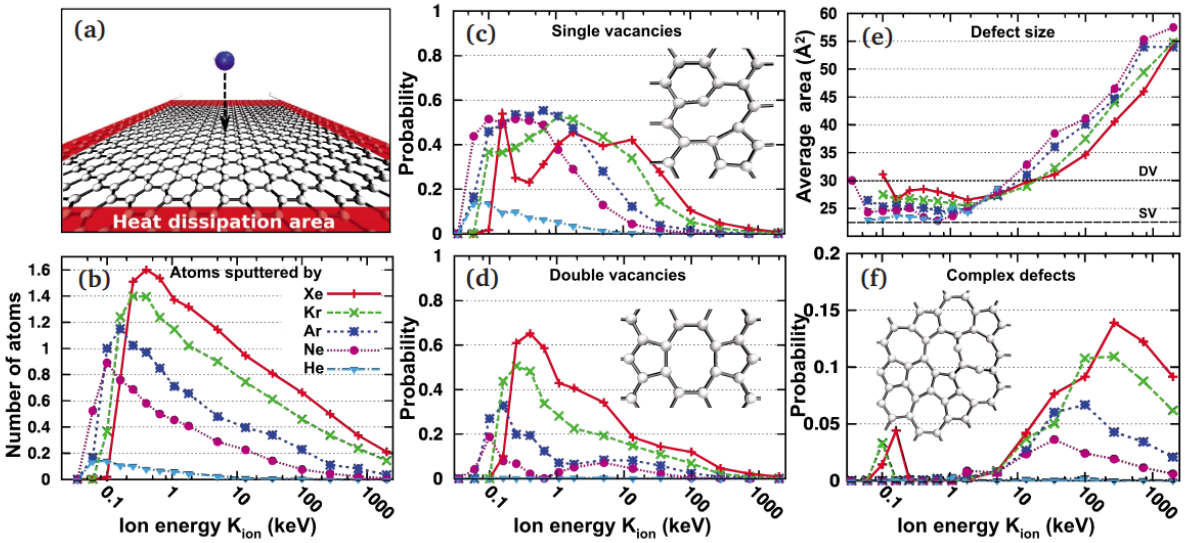

Figure 3.15. Calculated production of defects in graphene under ion irradiation as revealed by the analytical potential molecular dynamics. (a) Geometry of the system used for the theoretical modelling. (b) Number of sputtered atoms per ion impact as a function of ion energy. [(c) and (d)] Probability for single (SV) and double (DV) vacancy formation as a function of ion energy. The insets show the atomic structures of the reconstructed vacancies. (e) Average area covered by a single defect (when formed)—typically still a sp^2-bonded network of carbon atoms. The areas corresponding to a SV and DV are marked. (f) Probability for creating defects other than SV/DV (spatially close Frenkel pairs, adatom-vacancy pairs, and Stone-Wales Defects) Adapted from reference [12] .

A comparison of the analysis of C1s spectrum belonging to remote plasma and low kinetic energy oxygen functionalized v-CNTs with the same treatment time is showed in Figure 3.16. C1s spectrum of plasma functionalization (Figure 3.16a) shows only one component of carbon bonded to oxygen assigned to epoxide groups (C-O), this group is the least disrupting oxygen functional group because dangling bonds, vacancies or reactive edges are not needed to induce its formation in carbon nanomaterials [19]. This confirms that remote plasma

functionalization provides only low kinetic energy ions to the nanotube surface. A disadvantage of the remote plasma functionalization performed in this work is that epoxide groups can be removed from the surface of CNTs very easily through a reducing process. Contrary to remote plasma functionalization, with low kinetic energy oxygen ion irradiation besides epoxy groups, carbonyl and carboxyl groups are formed at the CNT surface (Figure 3.16b). Ion irradiation promotes the disruption of the carbon nanotube lattice inducing the formation of dangling bonds where these groups are grafted. Additionally, an increasing local damage (sp^3 bonds) is observed.

The results detailed above demonstrate that low kinetic energy ion irradiation has important advantages over remote plasma treatment such as higher efficiency and an increased versatility on the type of functional groups grafted to the surface of carbon nanotubes.

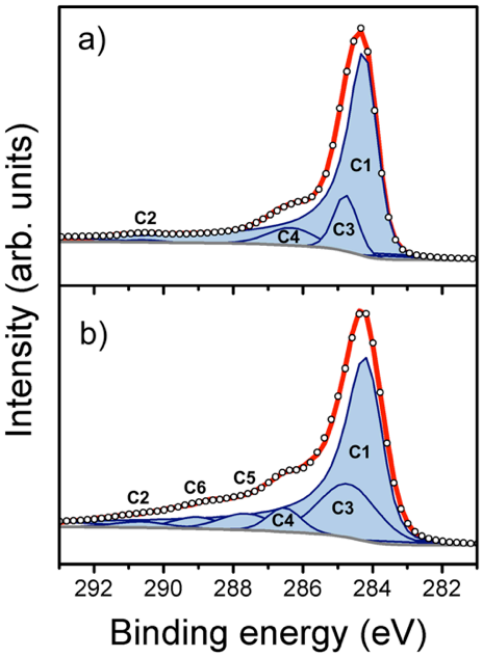

Figure 3.16. XPS analysis of v-CNTs functionalized by plasma treatment (0 keV of ion kinetic energy) (a) and by ion irradiation with 2 keV of ion kinetic energy (b). The treatment time was 5 min for both samples. C1 is assigned to sp^2-C (284.4 eV), C2 to π-plasmon excitations (290.9 eV), C3 to sp^3-C (285.0 eV), C4 to epoxide groups C–O (286.6 eV), C5 to carbonyl groups C=O (287.5 eV) and C6 to carboxyl groups –COOH (288.8 eV).

3.2.4 Raman spectroscopy of carbon nanotubes

Carbon nanotubes are sp^2 hybridized carbon systems, the presence of defects sites on carbon

nanotubes can be better investigated by Raman spectroscopy than by XPS technique because XPS probes the core levels of an atom, while Raman probes directly the chemical bonds in the samples and bonds are directly related to defects.

Raman spectroscopy allows to characterize carbon nanotubes from a "crystalline structure" point of view because the presence of defects in sp^2 systems changes their resonance Raman spectra [20]. Typical Raman spectrum from v-CNTs pristine is showed in the Figure 3.17. The spectrum is distinct by the presence of two strong peaks centered at 1580 and 1350 cm^{-1}. The band at 1580 cm^{-1} is named the G band (graphite band), present in all the graphite-like structure materials (sp^2 carbon systems) and generated by the in-plane optical phonon modes. The band at 1350 cm^{-1} is named as the D band (defect band) and it is assigned to the breathing of the carbon hexagons in the nanotubes that become Raman active at the borders of the crystallite areas due to the loss of symmetry [20]. The intensity of the D band is proportional to the number of defects or disorder in carbon nanotubes. The intensity ratio between the D and G band (I_D/I_G) is generally used as a parameter to quantify disorder not only in carbon nanotubes but in all graphite-like structure (sp^2 carbon) materials like graphene.

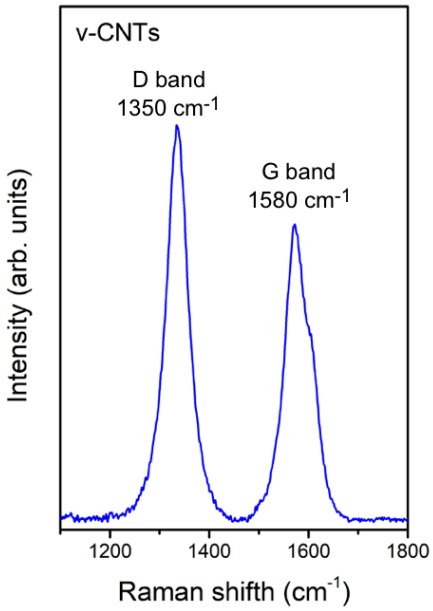

Figure 3.17. Typical Raman spectrum of carbon nanotubes.

3.2.4.1 Raman spectroscopy of oxygen functionalized v-CNTs

The Raman spectra of the v-CNTs before and after oxygen functionalization were recorded as complementary characterization technique to evaluate the introduction of defects in the CNTs lattice by remote plasma and low kinetic energy ion irradiation and compare them with the XPS analysis. The Raman data presented is "as-recorded" with no peak normalization, all spectra were obtained for the same laser intensity with wavelength of 532 nm and 30 seconds of recording time.

Figure 3.18a shows that with increasing oxygen ion irradiation time, there is a notably increment in peak intensity of the D-peak band at ~1350cm^{-1} and a gradual increase of the G-peak at ~1580cm^{-1}. This increase in the relative intensity of the peaks (or peaks area ratio) is a direct indication that the oxygen ion irradiation generates disorder on v-CNTs. The variation of the intensity with varying ion-energy is somewhat subtler: overall the general trend of increasing I_D/I_G ratio, however between the pristine and 0 keV ion irradiation a slight decrease in this ratio is observed (Figure 3.18b). We anticipate that this reduction comes from the oxygen plasma acting to preferentially etch amorphous carbon at the nanotube surface, effectively cleaning the carbon material. CNTs synthesized at low temperatures as the one used in this work are known to have some amorphous carbon at their surface. Therefore, the Raman spectroscopy confirmed the XPS results showing an increment in the defect/oxygen associated components for increasing irradiation ion kinetic energy and removal of amorphous carbon from the surface of the CNTs.

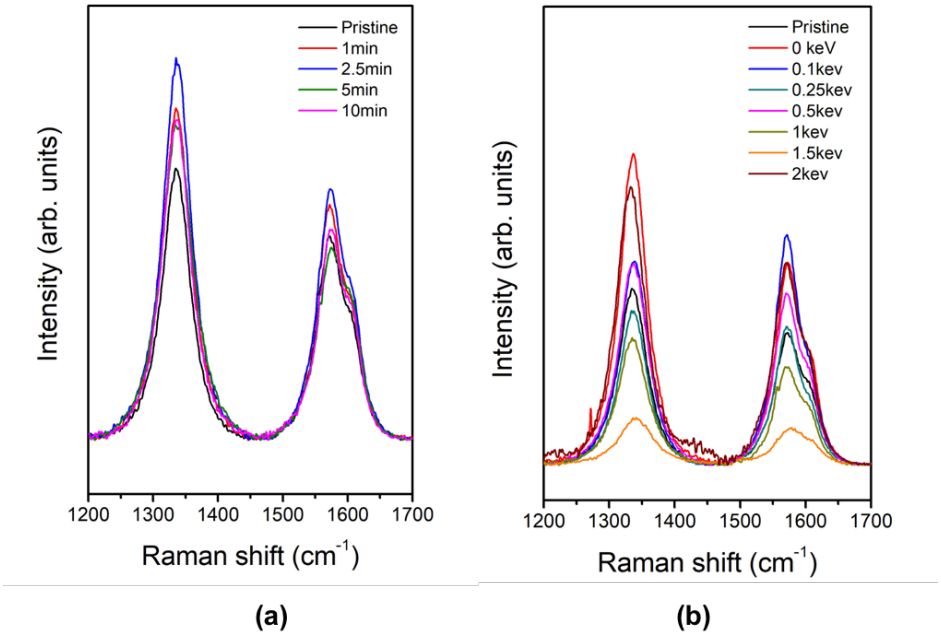

Figure 3.18. Raman spectrum of v-CNTs functionalized with low kinetic energy oxygen ion irradiation with different treatment time (a) and ion kinetic energy (b).

3.3 Thermal stability of oxygen functionalizations in v-CNTs

Heating of chemical sensors is usually used to improve the sensing properties of the active material [21,22]. Furthermore, carbon nanotubes are sometimes heated for its integration in certain electronic devices. Carbon nanotubes have high thermal stability, the overall structure of carbon nanotubes is preserved even at high temperatures, up to 1200 ºC if they are single wall nanotubes and until 2200 ºC if they are multiwall nanotubes (in an inert atmosphere) [23,24]. Mahajan et al. [25] investigate the thermal decomposition of multiwall carbon nanotubes under different atmospheres. The study shows that under air atmosphere there is decomposition after 420°C, which drops to only 200°C under oxygen-rich conditions, while under argon the tubes remain stable up to 1300°C. As mentioned before, high quality tubes can be heated in inert atmospheres even as high as 2200°C. However, during heating, the nature and concentration of the functional chemical groups attached to the surface of carbon nanotubes can be altered. In this framework, thermal treatments of functionalized carbon nanotubes can be used to modify the concentration and type of their functional groups. Therefore, the determination of the thermal stability of the functional groups in the carbon nanotubes surfaces is an important step in the development of chemical sensors.

The thermal stability of the oxygen functional groups grafted at the v-CNTs surface was investigated by heating progressively the sample to five different temperatures (200 °C, 300 °C, 400 °C, and 500 ºC), the investigated sample was first irradiated with oxygen ions with 1 keV of kinetic energy during 10 minutes. The sample was mounted on a sample holder equipped with a resistive heater (Figure 3.6); the heat treatment was performed in the ultra-high vacuum (UHV) *Plafon* chamber. The temperature of the sample was raised to 200 °C, 300 °C, 400 °C and 500 ºC progressively and stabilized at each heating step for 15 minutes (Figure 3.19), after subsequently cooling to room temperature the XPS spectra of the sample annealed at each temperature were recorded, the transportation of the sample from *Plafon* to the XPS chamber was performed under UHV avoiding contamination due to air exposure.

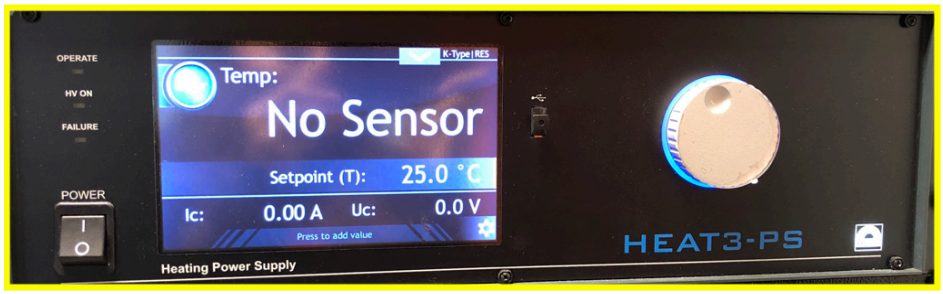

Figure 3.19 Temperature controller used for the thermal treatment of oxygen functionalized v-CNTs.

3.3.1 Chemical configuration of v-Ox-CNTs after thermal treatment

After oxygen ion irradiation (1 keV, 10 min), the relative concentration of oxygen was 17.2 at. % in the v-Ox-CNTs sample. After heating the sample to 200 °C, 300 °C, 400 °C and 500 ºC the amount of oxygen decreases, as was expected, from 14.0 at. % when the sample was heated to 200 ºC, dropping to 5.6 at. % when the v-Ox-CNTs were heated to 500 ºC (Table 3.4). The atomic concentration of oxygen and carbon in the samples was obtained by the analysis of the XPS survey spectra.

v-CNTs sample stage	Carbon (at. %)	Oxygen (at. %)
Pristine	99.0	1.0
After oxygen ion irradiation	82.8	17.2
200 ºC	86.0	14.0
300 ºC	89.5	10.5
400 ºC	92.2	7.8
500 ºC	94.4	5.6

Table 3.4. Relative atomic composition (at. %) of v-CNTs from XPS spectra. Treatment steps: first 10-minutes ion irradiation at 1keV, followed by a progressive 15-minute heating initiating at 200 ºC followed by 300 ºC, 400 ºC and 500 ºC.

The C1s and O1s core levels spectra were recorded at high energy resolution (pass energy, step energy). The effect of the oxygen ion irradiation in the chemical environment of the carbon atoms at the carbon nanotubes surface can be seen in the C1s spectrum (Figure 3.20a), namely a widening in the left part of the spectrum corresponding to photoelectrons ejected from C-OH bonds, with higher binding energies than photoelectrons ejected from C-C bonds. Subsequent heating of the v-Ox-CNTs reduces this widening (Figure 3.20a), consistent with a decrease on the relative concentration of C-OH groups as the annealing temperature is increased. Figure 3.20b shows the high resolution O1s spectra recorded (normalized to the C1s intensity). There is a clear increment in the O1s peak intensity after oxygen ion irradiation, followed by a decrease dependent on the annealing temperature. The peak is centered at 532.6 eV, due to the contribution of C-OH functional groups [26]. The O1s peak changes in shape from a combined single peak to a double peak curve indicating desorption of one or more kinds of functional groups from the v-CNTs surface, this change in peak shape becomes more marked as the annealing temperature increases.

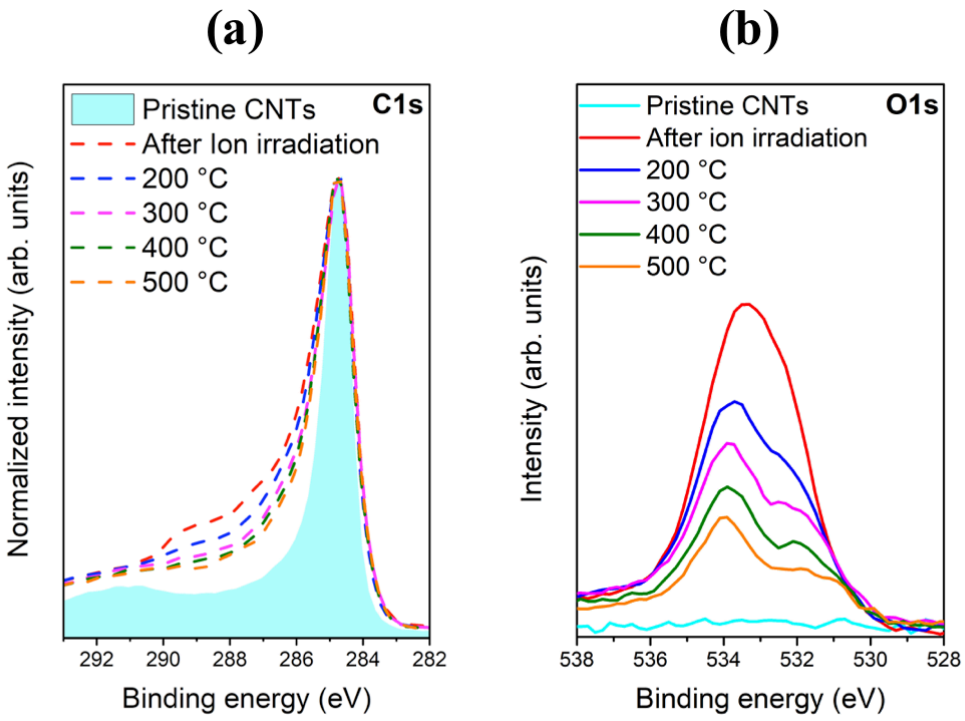

Figure 3.20. v-CNTs high resolution C1s (a) and O1s (b) XPS spectra.

The analysis of C1s peak was carried out using the above mentioned least-squares fitting method using the software CASA XPS. After the oxygen ion irradiation (Figure 3.21) the following components were used to reproduce the spectrum, the one at 284.4 eV belonging to C-sp^2 atoms (C1), and another at 290.9 eV assigned to photoelectrons losing kinetic energy due to π-plasmon excitations (C2), a component at 284.7 eV assigned to photoelectrons ejected from C-sp^3 atoms (C3), and the components assigned to photoelectrons ejected from carbon atoms bonded with oxygen in the following configurations and binding energies: 285.9 eV attributed to C-OH hydroxyl groups (C4), 286.7 eV assigned to C-O epoxy groups (C5), 287.6 eV assigned to C=O carbonyl functional groups (C6) and 289.1 eV assigned to COOH carboxyl functionalization (C7) [5,27].

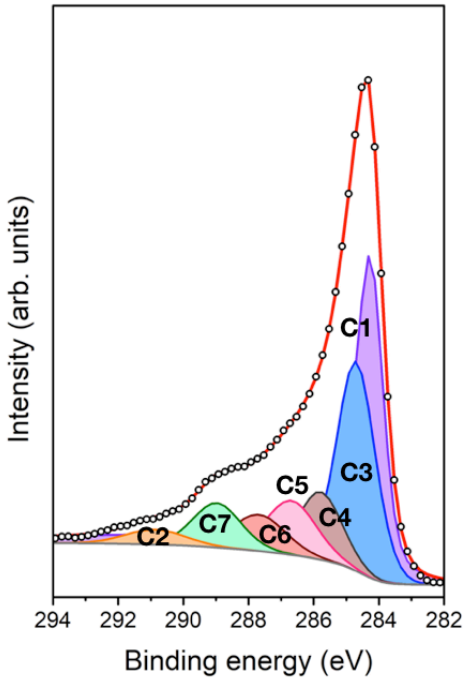

Figure 3.21. C1s XPS spectrum analysis of v-Ox-CNTs after oxygen ion irradiation. Component's assignments: C1 → C-sp^2, C2 → π-plasmon-excitations, C3 → C-sp^3, C4 → C-OH, C5 → C-O, C6 → C=O, C7 → COOH.

Figure 3.22 shows the C1s spectrum analysis recorded after heating at 200 ºC (Figure 3.22a) and 500 ºC (Figure 3.22b), the variation in the relative area of the components assigned to carbon bonded to oxygen can be undoubtedly observed (C4-C7).

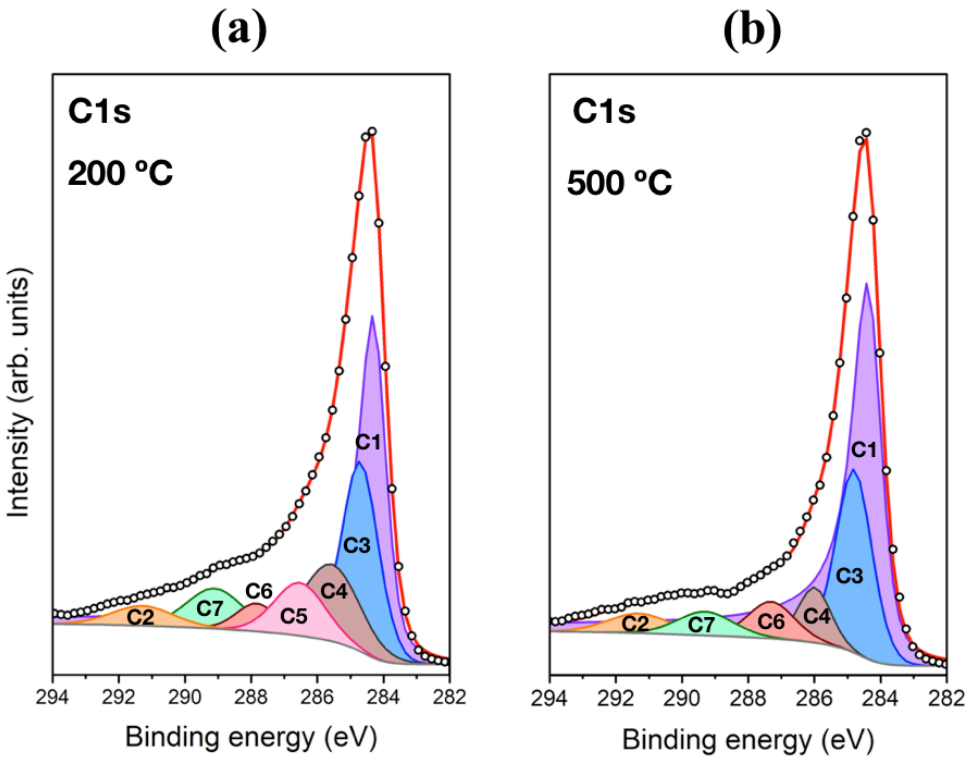

Figure 3.22. C1s XPS spectrum analysis of v-Ox-CNTs heated at 200 ºC (a) and v-Ox-CNTs heated at 500 ºC (b). Component's assignments: C1 → C-sp^2, C2 → π-plasmon-excitations, C3 → C-sp^3, C4 → C-OH, C5 → C-O, C6 → C=O, C7 →COOH.

The C1s spectrum recorded after each heating experiment was analyzed and the variation of the relative concentration of the fitting components was examined (Figure 3.23 and Table 3.5). For the C-sp^2 component (Figure 3.23a), the large decrease from 96.5 % in v-CNTs pristine to 42.7 % in v-Ox-CNTs after oxygen functionalization clearly shows the irradiation disrupting the π-bonding, forming oxygen groups and C-sp^3 defects. Upon heating at different temperatures, a partial 'healing' of the carbon nanotube structure occurs with the formation of new chemical bonds mainly in the C-sp^2 hybridization form, causing the increase in their relative concentration up to 62.1 % at the maximum heating temperature. The healing of C-sp^2 bonding on graphitic-carbon structures with increasing thermal annealing is a known phenomenon usually called graphitization, only those materials with an internal structure amenable to the formation of graphene layers undergo structural reordering by heat treatment, during the healing process, intermolecular cross-linking occurs through oxygen-containing groups or through dehydrogenation in defects sites and the cyclized sections coalesce by cross-linking to form a graphite-like structure [13,28–30]. Oxygen ion irradiation creates C-sp^3 related defects in the graphitic lattice with a relative concentration

of 17.3 %, in agreement with an early work reported by Banhart et al [31] who reported a summary of experimental and molecular dynamics simulations data that demonstrate the introduction of defects in carbon nanomaterials after its irradiation with energetic particles like ions and electrons. Although it was expected the relative concentration of the C-sp^3 component to decrease due to the healing of the defects for increasing heating temperature, such behavior was not observed. The relative concentration of C-sp^3 remains almost constant for all temperatures ~ 17.0 ± 2 %. A certain equilibrium can exist between the number of C-sp^3 defects that are being healed and the formation of new C-sp^3 defects due to the desorption of oxygen atoms when the nanotubes are heated.

The relative concentration of the components assigned to oxygen functional groups in v-Ox-CNTs is detailed in Figure 3.23b. The change in relative concentration of these components gives information about their relative thermal stability. The C-O epoxy group is the most unstable under heating, it is eliminated after heating at 300 ºC. With increasing temperature follows the elimination of carboxyl COOH group whose relative concentration decreases considerably with temperature. These carboxyl groups are expected to fragment to generate C-OH groups, which coupled with potential transformation of epoxy groups together explain the increase in the C-OH relative concentration seen at 200 °C and 300 ºC, which then decreases gradually at 400 °C and 500 ºC. The most thermally stable functional group is the C=O carbonyl, which relative concentration remains almost constant.

Summarizing, we observed a decrease in the amount of oxygen groups grafted at the surface of the carbon nanotubes with increasing temperature, this coincides with the overall decrease of oxygen atomic concentration with increasing temperature. Nevertheless, even when the nanotubes were heated at 500 ºC, a considerable number of oxygen functionalities remain in the surface of the nanotubes, with C=O carbonyl and C-OH hydroxyl the most thermally stable and C-O epoxy group the least stable of all oxygen groups. The drop-off in total oxygen concentration is not abrupt, however it shows a near uniform decrease with temperature, a positive result showing that the application of a short post-functionalization thermal anneal allows good control of both total oxygen concentration and relative functional group concentration. The chemical sensors studied in the next sections are operated and engineered at temperatures far below 500 °C, for this reason, we expect no variation in the final CNT functionalization. However, further investigations of thermal annealing using different atmospheres such as nitrogen, oxygen, and air must be evaluated.

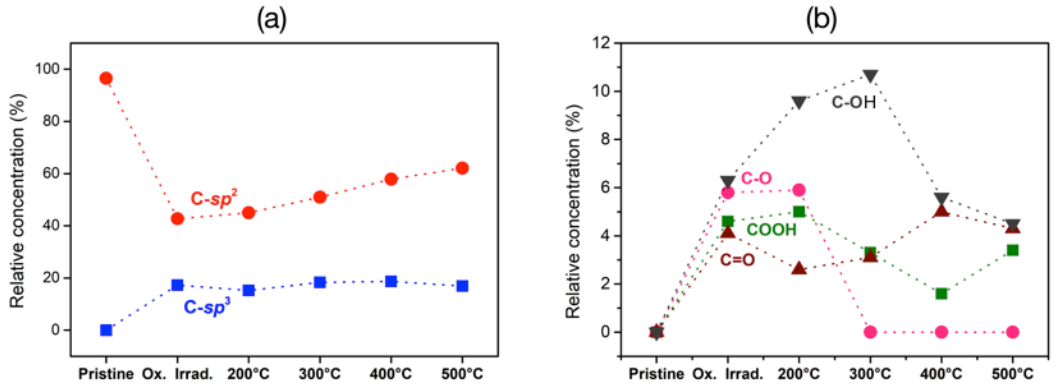

Figure 3.23. Relative concentration of the components in the C1s spectrum at each stage of the v-CNTs thermal annealing and functionalization. C-sp^2 and C-sp^3 (a) C-OH, C-O, COOH and C=O (b).

v-CNTs sample stage	Relative concentration (%)						
	C-sp^2	C-sp^3	C-OH	C-O	C=O	COOH	Plasmon
Pristine	94.2	0	0	0	0	0	3.8
After Oxygen functionalization	42.7	17.3	6.3	5.8	4.1	4.6	1.9
200 ºC	45.0	15.2	9.6	5.9	2.6	5.0	2.7
300 ºC	51.0	18.3	10.7	0	3.1	3.3	3.1
400 ºC	57.9	18.7	5.6	0	5.0	1.6	3.4
500 ºC	62.1	16.9	4.5	0	4.3	3.4	3.1

Table 3.5. Relative concentration of the components in the C1s XPS spectrum recorded on the v-CNTs at each stage of the thermal annealing.

3.3.2 Morphology of v-Ox-CNTs after thermal treatment

The morphology of the aligned carbon nanotubes after the thermal annealing examined by SEM and TEM microscopies is showed in Figure 3.24. Figure 3.24a shows the macroscopic structure and the alignment of the v-Ox-CNTs by SEM microscopy, the density and the alignment of the nanotubes is not affected by the oxygen ion irradiation nor by the heating treatment. Figure 3.24b shows the TEM images of v-Ox-CNTs recorded at the final step of

the heating treatment (500ºC). The overall structure of v-Ox-CNTs was maintained after both, oxygen ion irradiation and the heating treatment with no significant degradation. This agrees with literature, in vacuum, changes in the diameter and the number of walls in CNTs is only observed after heating to typically 1400 ºC [23]. The inset of Figure 3.24b shows carbon nanotubes with both open and closed tips. The open tipped nanotubes result from the oxygen functionalization of the tips, initial oxidation of the tips is via epoxide surface groups bonding to the tip (probably along tip facets), but with time, the tips are chemically opened, and the carbon dangling bond sites terminated with carbonyl and carboxyl groups. The closed tips are thus likely due to the 'healing' effect of annealing resulting in oxygen desorption and structural rearrangement. Scardamaglia et al. used low energy ion irradiation and plasma functionalization methods to graft nitrogen atoms into the lattice of vertically aligned carbon nanotubes (v-CNTs). Then, using ultraviolet and X-ray photoemission spectromicroscopy they showed that the nitrogen functional groups are grafted near the tips, up to 4 μm under the surface of the v-CNTs [29]. The results reported by Scardamaglia supported our observation that functionalization occurs mainly near the CNT tip.

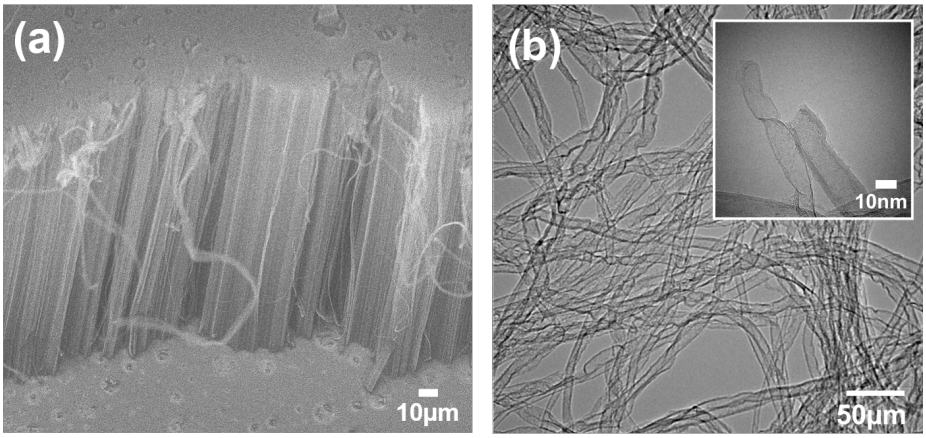

Figure 3.24. Images of v-Ox-CNTs after thermal annealing taken with scanning electron microscope (a) and transmission electron microscope (b).

3.4 Low kinetic energy ion irradiation vs. other functionalization techniques

Our results indicate that low kinetic energy ion irradiation is a faster, efficient, controllable, and clean technique for the functionalization of carbon nanotubes than other common functionalization techniques. In the case of acid functionalization, a long time of treatment is required to graph oxygen groups in carbon nanotubes. Taghvaei et al. reported that at least

2 h were needed to obtain oxygen atomic concentration of 13 at.% [32]. Besides, this type of functionalization is non-environmental friendly because generates a large quantity of liquid waste. For the case of plasma functionalization, even if does not generate liquid waste, the efficiency of functionalization is lower than the ion irradiation technique (in most of the cases). The atomic concentration of oxygen in carbon nanotubes after remote plasma functionalization reported here was almost half of the atomic concentration reached with low kinetic ion irradiation with the same treatment times (8 at. % vs 14.2 at. %). Various examples showing similar results are reported in the literature. Shafarat et al. reported 6.8 at.% of oxygen after 15 minutes of plasma treatment [33], similar to Taghvaei et al. with 7.4 at.% with 45 minutes of functionalization [32]. In addition to this, plasma functionalization does not allow a good control of defect creation at the carbon nanotube surface, it has been reported that the type of defects generated by ion irradiation of carbon nanostructures depends on the kinetic energy of the ions irradiated [11,12], during plasma treatments all kind of species generated in the plasma (ions, photons, electrons, atoms) may arrive in the sample and all kind of defects can be simultaneously generated, contrary to ion irradiation, where the kinetic energy of the ion is easily controlled and in this way the type of defects created can be predicted.

Here, it is shown that the combination of low kinetic energy ion-irradiation followed by short time thermal annealing represents an excellent strategy for oxygen functionalization of carbon nanotubes, allowing simultaneous control over both overall concentration and concentration of individual functional group types. Additionally, this sort of functionalization allows the possibility of treatment after the nanostructure is integrated in the device.

3.5 Ox-CNTs decorated with metal nanoparticles

In search of fabricate highly sensitive chemical sensors, oxygen functionalized carbon nanotubes were decorated with metal nanoparticles. Several reports on carbon nanotubes decorated with Pd nanoparticles have shown that Pd nanoparticles increase the sensitivity of gas sensors [34,35]. In this framework, the development of bimetallic nanoparticles is a relatively new strategy to improve the sensitivity of sensors by the synergy of the metal properties. With the aim of engineering a chemical sensor to detect toluene, ethanol, NO_2 and H_2, Ox-CNTs were decorated with Pd and Ni-Pd nanoparticles. The decoration of Ox-CNTs with metal nanoparticles was carried out by plasma sputtering deposition, for comparison, different deposition times of nickel were used to obtain Ni-Pd nanoparticles with different concentration of nickel. The detailed characterization of the hybrid nanostructures was performed by SEM, XPS and Raman spectroscopy.

3.5.1 Plasma sputtering deposition

Sputtering is the ejection of atoms by the bombardment of a solid or liquid target with energetic particles. The sputtering is the result of collisions between the incident energetic particles with the surface atoms of the target. The sputter yield (Y) of one target is defined as the ratio between the number of sputter-ejected atoms and the number of incident particles. The sputter yield of each target depends on the element bombarded, there is a trend related to the position of the element in the periodic table with the sputter yield (Figure 3.25) [36].

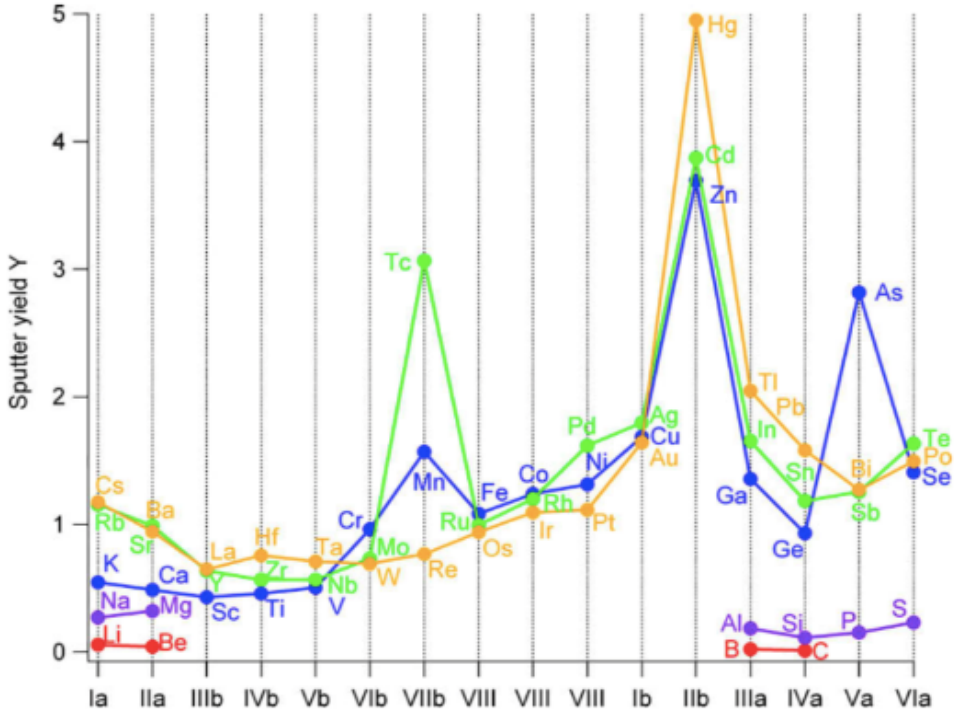

Figure 3.25. Dependence of the sputter yield of several elements ordered according their position in the periodic table, the sputtering was performed using argon with 300 eV of ion energy (Adapted from reference [36]).

P. Sigmund described the sputter yield as a function of energy and projectile-target combination [36], according to his theory, the sputter yield near threshold , i.e., at low ion energy, is given by Equation 3.1.

$$Y = \frac{3}{4\pi^2}\,\alpha\,\frac{4\,M_1M_2}{(M_1+M_2)^2}\,\frac{E}{U_s} \tag{3.1}$$

Where E is the energy of the projectile, and M_1 and M_2 the masses of the projectile and the target atom, U_s is the surface binding energy and α a dimensionless parameter depending on the mass ratio and the ion energy. Equation 3.1 can be understood as the transfer of

momentum from the incoming ion to the target atoms with a maximum when $M_1 = M_2$. To sputter an atom from the target, momentum transfer from the ion-induced collision must overcome the surface barrier given by the surface binding energy U_s. Consequently, there is an inversely proportional relationship between the yield and the surface binding energy [37]. The sputter yield of nickel using argon ions (400 eV) as energetic particles is 1.2 (atoms/ion) and the sputter yield of Pd in the same conditions is 1.7 (atoms/ion) [38].

As mentioned before, sputtering of atoms from a surface begins with the bombardment of energetic particles at one target. These energetic particles are generally ions. The ions used for sputtering are produced mainly by two approaches with ion sources or plasma sources. However, plasma sources are the most used on sputtering deposition due to the complex and expensive nature of ion sources. Plasma is a quasineutral particle system in gas or fluid-like form compound of charge particles (electrons and ions) and neutral particles (atoms and molecules) [39]. By applying a high negative voltage to the target, positively charged ions are attracted from the plasma toward the target with sufficient energy to initiate sputtering.

The experimental system of plasma sputtering deposition used consists of a cathode and an anode that are positioned opposed to each other in a vacuum chamber (Figure 3.26). The vacuum in the chamber is achieved with a pumping system (turbomolecular and rotary pumps are usually used). After pumping and reaching the desired pressure (10^{-4}–10^{-6} Pa) a noble gas (argon in this case) is introduced into the vacuum chamber. Then, a high voltage difference is applied between cathode and anode and a glow discharge plasma is ignited, accelerated electrons ionize the gas molecules. In a diode glow discharge arrangement, electron trajectories are only defined by the electrical field between the cathode and the anode. Hence, the electrons are accelerated over the cathode sheath, and move with high velocity toward the anode. The classical approach to avoid the rapid loss of electrons from the discharge is to apply a magnetic field. By applying a magnetic field during glow discharge sputter deposition, one can trap the electrons in the discharge longer and, hence, produce more ions for the same electron density, magnetrons are used to generates this magnetic field. In this way, the ions can reach the cathode with almost the full discharge voltage and the sputtered atoms can reach the substrate with only a few collisions. Magnetrons can be powered by a variety of methods between radio frequency (RF), direct current (DC) and pulsed DC. In this work, a RPG-50 pulsed DC plasma generator from ONI was used.

Sputtered particles leaving the target can collide with the gas atoms present in the vacuum chamber during transit to the substrate. Collisions will alter particle energy, direction, and momentum, and therefore also the morphology and microstructure of the growing film. The number of collisions will depend on the pressure value.

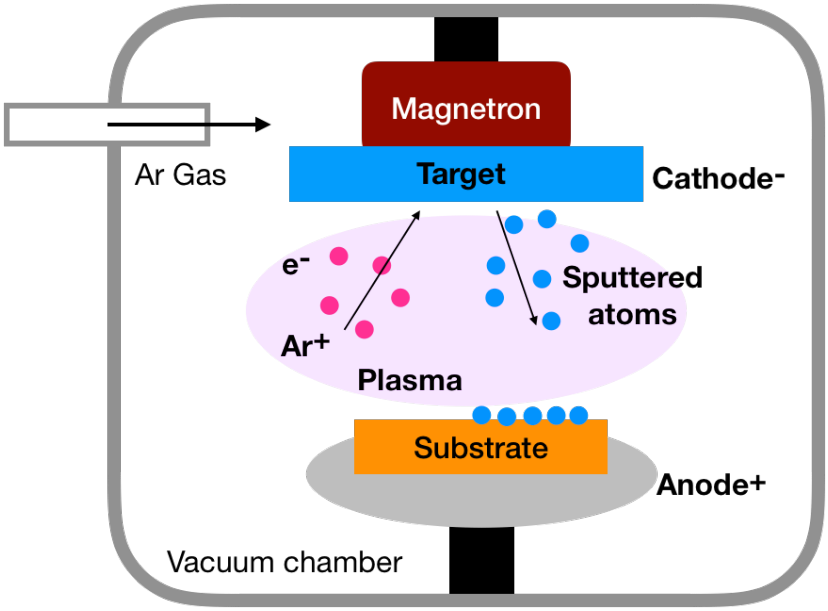

Figure 3.26. Scheme of the sputtering deposition process.

3.5.2 Palladium sputtering deposition into Ox-CNTs

Oxygen functionalized carbon nanotubes were decorated with palladium atoms using the plasma sputtering deposition as described. The sample containing oxygen functionalized carbon nanotubes was placed inside the sputtering chamber, and the chamber was pumped down to10^{-5} torr. Afterwards, a flux of argon gas was set into the chamber with a pressure of 25 mTorr and a flux of 20 sccm. Then a plasma is created by turning on the magnetron power at 50W (Figure 3.27). The sputtering was carried out for 5 seconds. This sputtering time allows to obtain a thin film of palladium with a nominal thickness of 10 Å. After the sputtering, the inlet gas was closed, the pumping was turned off and the vacuum chamber was vented to take out the samples from the chamber.

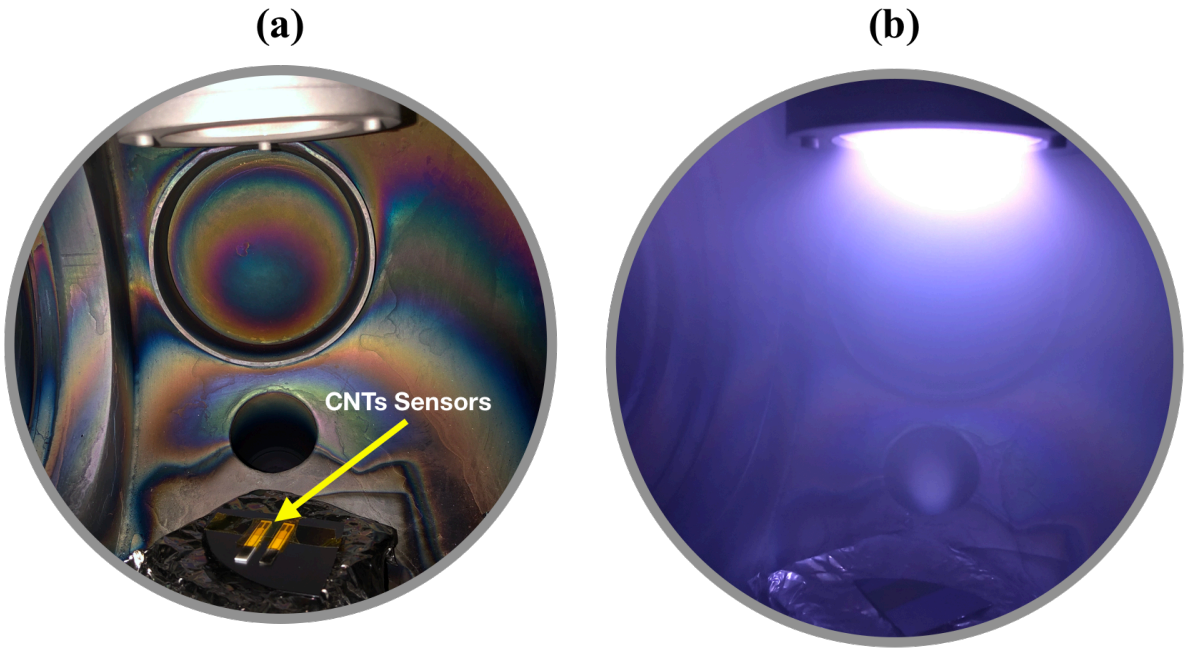

Figure 3.27. (a) Ox-CNTs samples inside the sputtering chamber (yellow arrow). (b) Plasma observed inside the chamber while sputtering palladium into Ox-CNTs.

3.5.2.1 Chemical analysis of Pd-Ox-CNTs

The oxygen functionalized carbon nanotubes (Ox-CNTs) that were sputtered with palladium atoms were analyzed by X-Ray photoelectron spectroscopy to obtain their atomic relative concentration and chemical configuration. Figure 3.28 shows the XPS survey spectrum of Ox-CNTs after the sputtering of palladium. The relative atomic concentration of the sample was: carbon 70.1 at. %, oxygen 26.5 at. %, palladium 2.2 at. % and iron 1.2 at. %. The iron content in the sample may come from the synthesis of carbon nanotubes (catalyst used in the synthesis). The presence of the palladium XPS signal indicates that deposition of palladium was made at the nanotubes surface. Deposition of palladium on CNTs leads to the clustering of Pd atoms on the surface of CNTs as the cohesive energy of Pd is much larger than the adsorption enthalpy [40], the nucleation centers are chemical or structural defects in CNTs, this clustering results in the formation of Pd nanoparticles in the nanotube surface as reported by Felten et al [41].

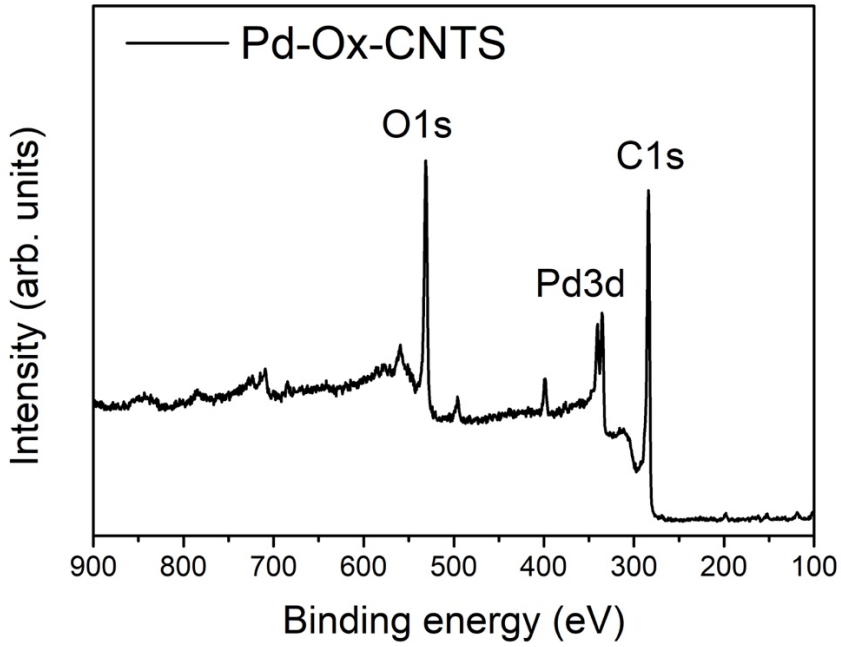

Figure 3.28. Survey XPS spectrum of Ox-CNTs sputtered with palladium. The peaks from C1s, O1s and P3d are observed.

Analysis of the core level spectrum C1s was performed on pristine carbon nanotubes (Figure 3.29a), Ox-CNTs (Figure 3.29b) and Pd-Ox-CNTs (Figure 3.29c) to evaluate the chemical environment of carbon atoms in the surface of each sample. The deconvolution of pristine CNTs C1s shows only the C-sp^2 component centered at 284.4 eV (C1). The C1s spectrum of oxygen functionalized carbon nanotubes is observed in the Figure 3.29b. The widening in the left part of the C1s spectrum due to the presence of carbon bonded to oxygen was already discussed in the *section 3.2.3*. The oxygen components are centered at binding energies of 286.6 eV (C3), 287.5 eV (C4) and 288.8 eV (C5). C3 is assigned to epoxide groups (C–O), C4 to carbonyl groups (C=O) and C5 to carboxyl groups (–COOH). The component at 285.0 eV (C2) is assigned to photoelectrons scattered from carbon with sp^3 hybridization. In the Figure 3.29c the C1s spectrum from the Pd-Ox-CNTs sample shows the same number of components that Ox-CNTs C1s spectrum. The photoelectrons ejected from carbons in a Pd carbide (PdC_x) are reported to have binding energies of 282.0 eV [42], this component is not observed in the Pd-Ox-CNTs spectrum which corroborate that a Pd-C phase is not formed after the sputtering deposition of palladium into CNTs. Pd atoms are mobile and diffuse at the CNT-surface until they find a nucleation center. Considering that Pd strongly interacts with oxygen atoms [43], it can be suggested that Pd nucleation occurs in the proximity of oxygenated defects created during the treatment [41]. In the Table 3.6 is detailed the relative

area from the components in the C1s spectrum recorded on the pristine CNTs, Ox-CNTs and Pd-Ox-CNTs. It can be noticed that the relative area from the C-O and C=O decreases after the Pd sputtering, this may be an indication that these oxygen groups act as preferential sites for the nucleation of Pd-nanoparticles in the CNTs surface.

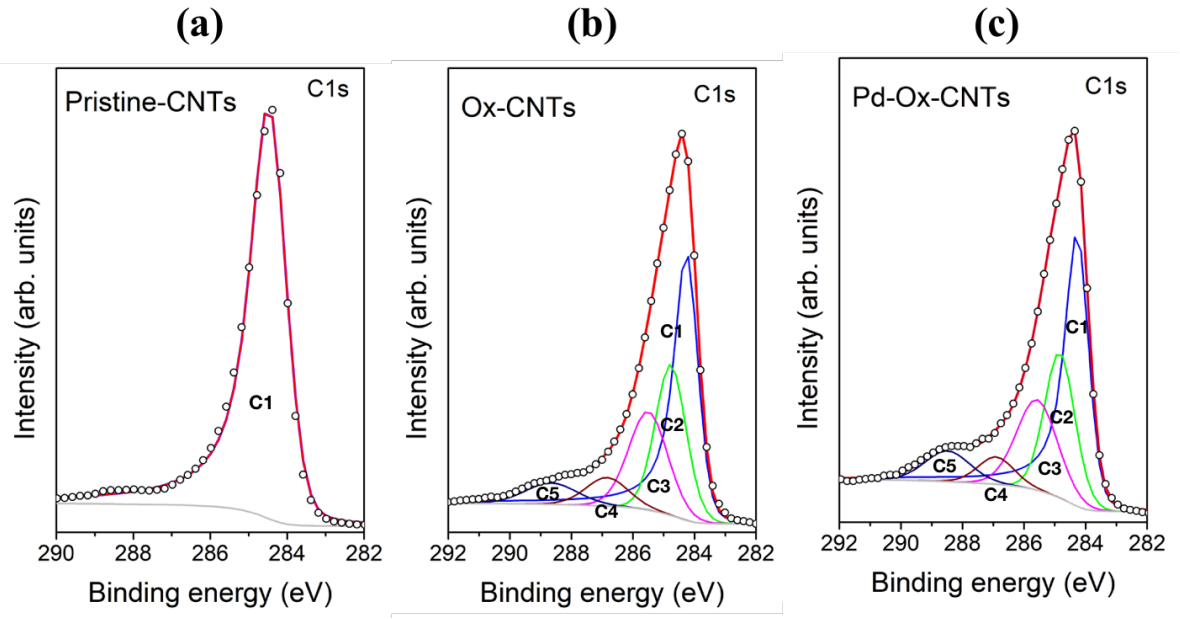

Figure 3.29. C1s XPS analysis spectra of pristine CNTs (a) Ox-CNTs (b) and Pd-Ox-CNTs. Component's assignments: C1 → C-sp^2, C2 → C-sp^3, C3 → C-O, C4 → C=O, C5 → COOH.

Sample	C-sp^2	C-sp^3	C-O	C=O	COOH
Pristine-CNTs	100	0	0	0	0
Ox-CNTs	45.2	23.5	19.5	6.1	5.6
Pd-OxCNTs	46.3	22.5	18.9	5.4	7.6

Table 3.6. Relative area of the components in the C1s spectrum recorded on the pristine CNTs, Ox-CNTs and Pd-Ox-CNTs.

The deconvolution of Pd3d is showed in the Figure 3.30. The spin-orbit splitting of 3d level shows two components in the spectrum (doublet), one belongs to $Pd3d_{5/2}$ and the other to $Pd3d_{3/2}$. Two doublets were needed to reproduce this spectrum. The first doublet (blue) with binding energies of 336.1 and 541.4 eV correspond to metallic Pd (Pd^0) and the second doublet (green) with binding energies of 337.7 and 543. eV is assigned to PdO (Pd^{2+}) [44].

No other components are present, same as the C1s analysis the formation of C-Pd is not observed. The oxidation of palladium corroborate that oxygen-containing functional groups in CNTs may work as active sites for the nucleation of Pd atoms for the formation of nanoparticles as it was reported by Felten et al. in 2009 [41]. These conclusions are supported by the results in Table 3.6 where the relative areas of C-O and C=O groups decrease after the decoration with Pd atoms, the localization of the particles on the defects would reduce the number of photoelectrons emitted from these carbon atoms arriving in the detector.

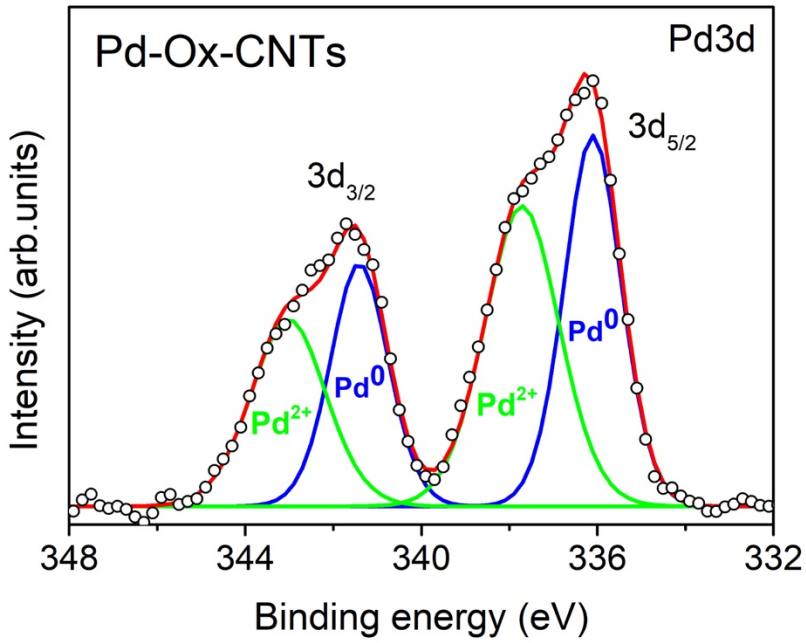

Figure 3.30. Pd3d XPS analysis spectrum of Pd-Ox-CNTs. Blue doublet is assigned to Pd^0 and green doublet to Pd^{2+}.

3.5.3 Nickel sputtering deposition into Pd-Ox-CNTs

After decoration with palladium the samples were decorated with nickel atoms with the purpose of creating bimetallic nanoparticles in the Pd-Ox-CNTs surface, and the stabilization of Pd nanoparticles by nickel atoms. The sample was placed inside the sputtering chamber and it was pumped down to 10^{-5} torr. Then, a flux of argon gas was set into the chamber with a flux of 20 sccm and the pressure in the chamber rise to 25 mTorr. The plasma was obtained using a magnetron power of 100 W. The sputtering was carried out using three different deposition times (5, 10 and 30 seconds) to achieve different Ni amount in the Ni-Pd nanoparticles. After the sputtering, the inlet gas was closed, the pumping was turned off and the vacuum chamber was vented to take out the samples from the chamber.

3.5.3.1 Chemical analysis of Ni-Pd-Ox-CNTs

The Ni-Pd-Ox-CNTs samples were analyzed by X-Ray photoelectron spectroscopy to obtain their atomic relative concentration and chemical configuration. Figure 3.31 shows the survey spectrum of the 30-Ni-Pd-Ox-CNTs, the peaks belonging to C1s, Pd3d, O1s and Ni2p are marked in the spectrum. The relative atomic concentration of each sample is detailed in the Table 3.7. The concentration of nickel in the samples increases as the sputtering time increases as was expected: 0.8 at. % (5 seconds of sputtering), 1.8 at. % (10 seconds) and 5.6 at. % (30 seconds). The low iron content observed in the sample can be associated with the catalyst used for the CNT synthesis.

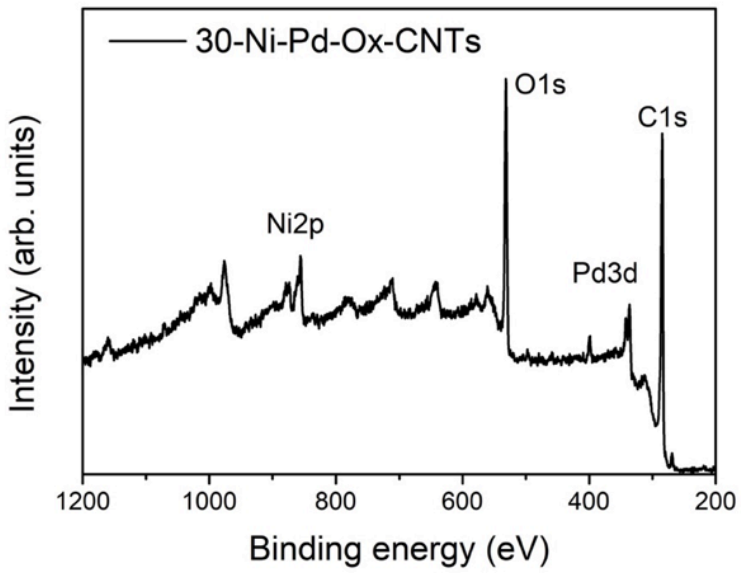

Figure 3.31. XPS survey spectrum of the Pd-Ox-CNTs with nickel sputtered for 30 seconds. The peaks of C1s, O1s, P3d, and Ni2p are observed and tagged in the spectrum.

Relative atomic concentration (at. %)					
	Carbon	Oxygen	Palladium	Nickel	Iron
5Ni-Pd-Ox-CNTs	64.8	29.4	2.7	0.8	2.3
10Ni-Pd-Ox-CNTs	63.3	28.9	2.8	1.8	3.2
30Ni-Pd-Ox-CNTs	63.4	26.8	1.3	5.6	2.9

Table 3.7. Relative atomic concentration of Ni-Pd-Ox-CNTs samples.

The chemical environment of the carbon atoms after nickel decoration was investigated by the XPS analysis of the C1s spectra of the samples to evaluate if Ni-C bonds are being formed. The results from the analysis are showed in the Figure 3.32. For all samples no new components than the ones present in the Ox-CNTs sample were observed in the spectrum which denies the formation of Ni-C bonds. On the other hand, the analysis of Pd3d core level spectrum for the three Ni-Pd-Ox-CNTs samples, showed in the Figure 3.33, compared to Pd-Ox-CNTs, a new doublet component (magenta) is observed in the Ni-Pd samples, located at 338.0 and 343.3 eV of binding energies, this new component can be assigned to Pd^{3+} due to further oxidation of palladium PdO_x or Pd interactions with Ni atoms [44]. However, as the presence of these component is only observed in the Ni-Pd samples and not in the Pd-Ox-CNTs samples we strongly believe that this component belongs principally to PdO-NiO interactions. These results match with the C1s analysis spectrum and indicate that during the Ni sputtering into Pd-Ox-CNTs, the nucleation of Ni atoms take place in the sites were Pd nanoparticles are already formed, creating in this way bimetallic (Ni-Pd) nanoparticles at the surface of CNTs.

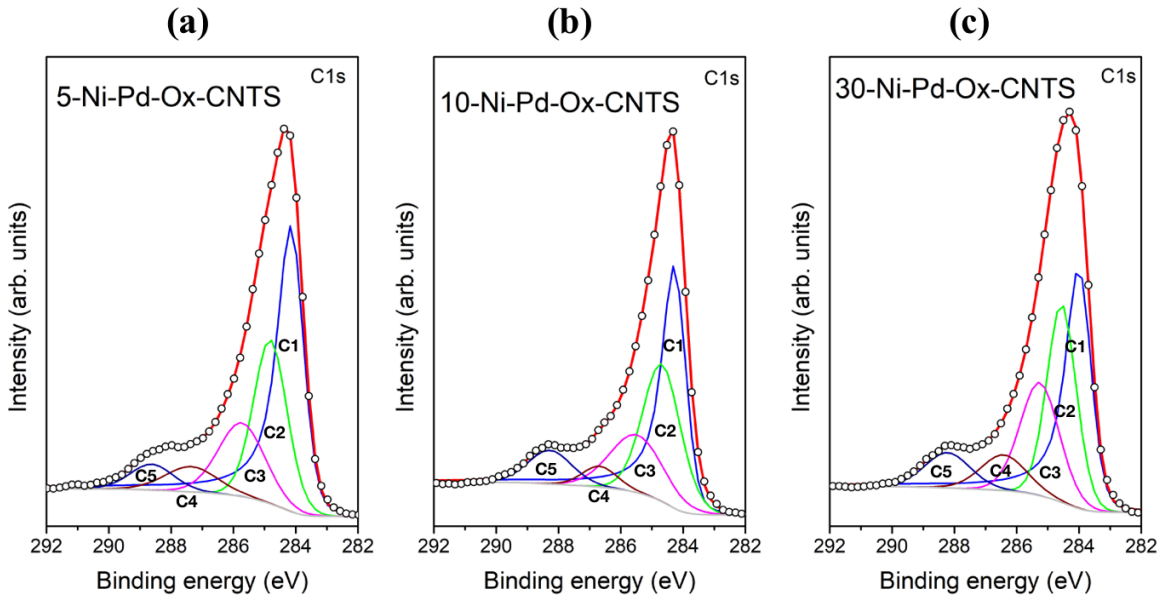

Figure 3.32. C1s XPS analysis spectra of Ni-Pd-CNTs samples. (a) 5-Ni-Pd-Ox-CNTs, (b) 10-Ni-Pd-Ox-CNTs, (c) 30-Ni-Pd-Ox-CNTs. Component's assignments: C1 → C-sp^2, C2 → C-sp^3, C3 → C-O, C4 → C=O, C5 → COOH.

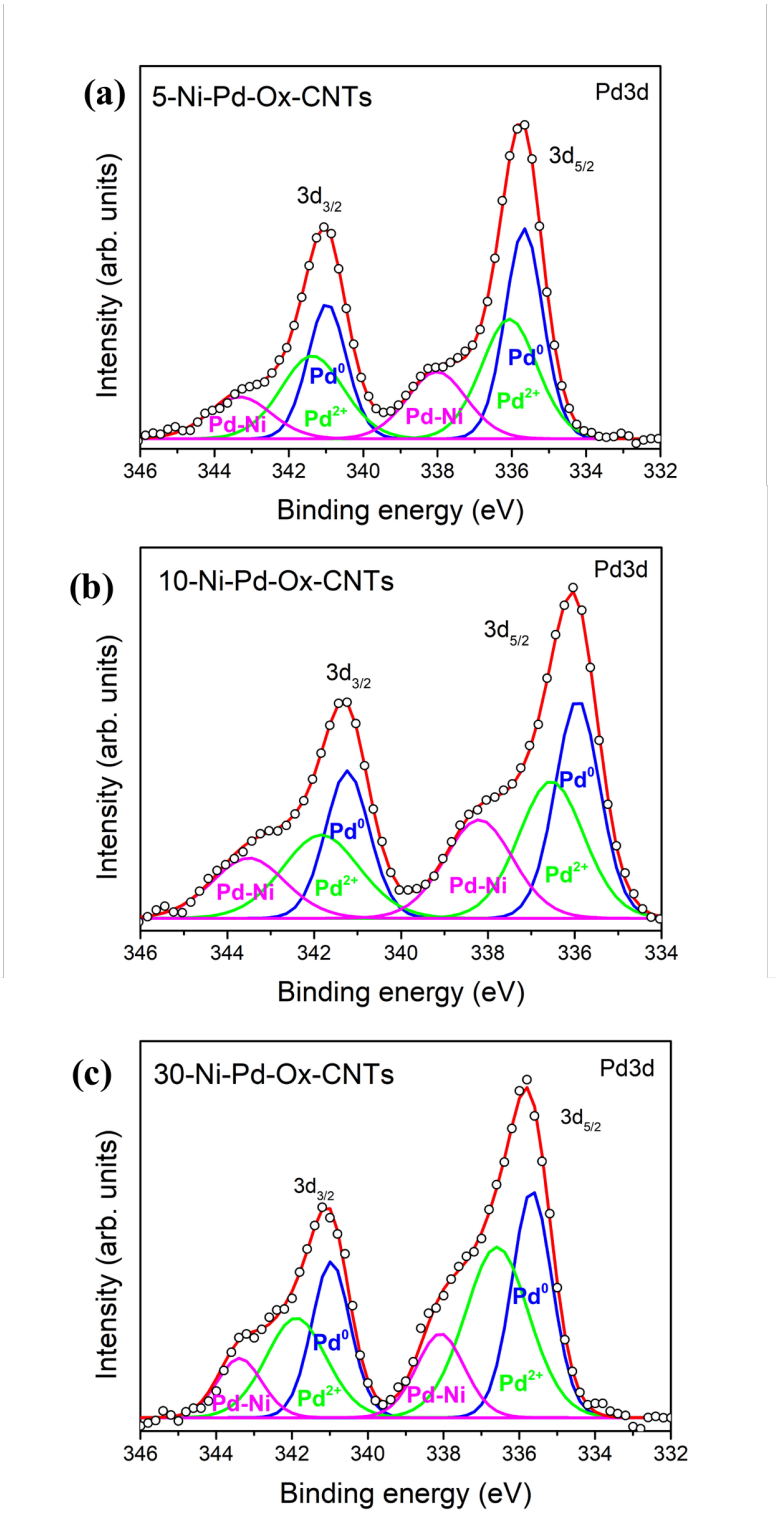

Figure 3.33. Pd3d XPS analysis spectrum of Ni-Pd-OxCNTs. (a) 5Ni-Pd-OxCNTs, (b) 10Ni-Pd-OxCNTs, (c) 30Ni-Pd-OxCNTs. Blue doublet is assigned to Pd^0, green doublet to Pd^{2+}, and magenta doublet to PdO-NiO interactions.

Finally, the Ni2p XPS analysis spectrum was realized for all three Ni-Pd samples and is showed in the Figure 3.34. For simplicity, only the $Ni2p_{3/2}$ part of the spectrum is showed. The same number of components were required to reproduce the Ni2p spectrum of the three samples (5, 10 and 30-Ni). The first component at 853.8 eV is assigned to Ni^0, the component at 855.9 eV corresponds to NiO (Ni^{2+}), further oxidation of nickel is observed in the peak at 858.2 eV (Ni^{3+}), the component at 861.8 eV of binding energy corresponds to shake up satellite peak, observed due to the loss of energy of photoelectrons that interact with the valence band promoting an electron from it to higher levels [44–46]. Even though a small amount of metallic nickel is present in all the samples most of the nickel present is oxidized (Ni^{2+}), the high reactivity of nickel with oxygen it is well known [44].

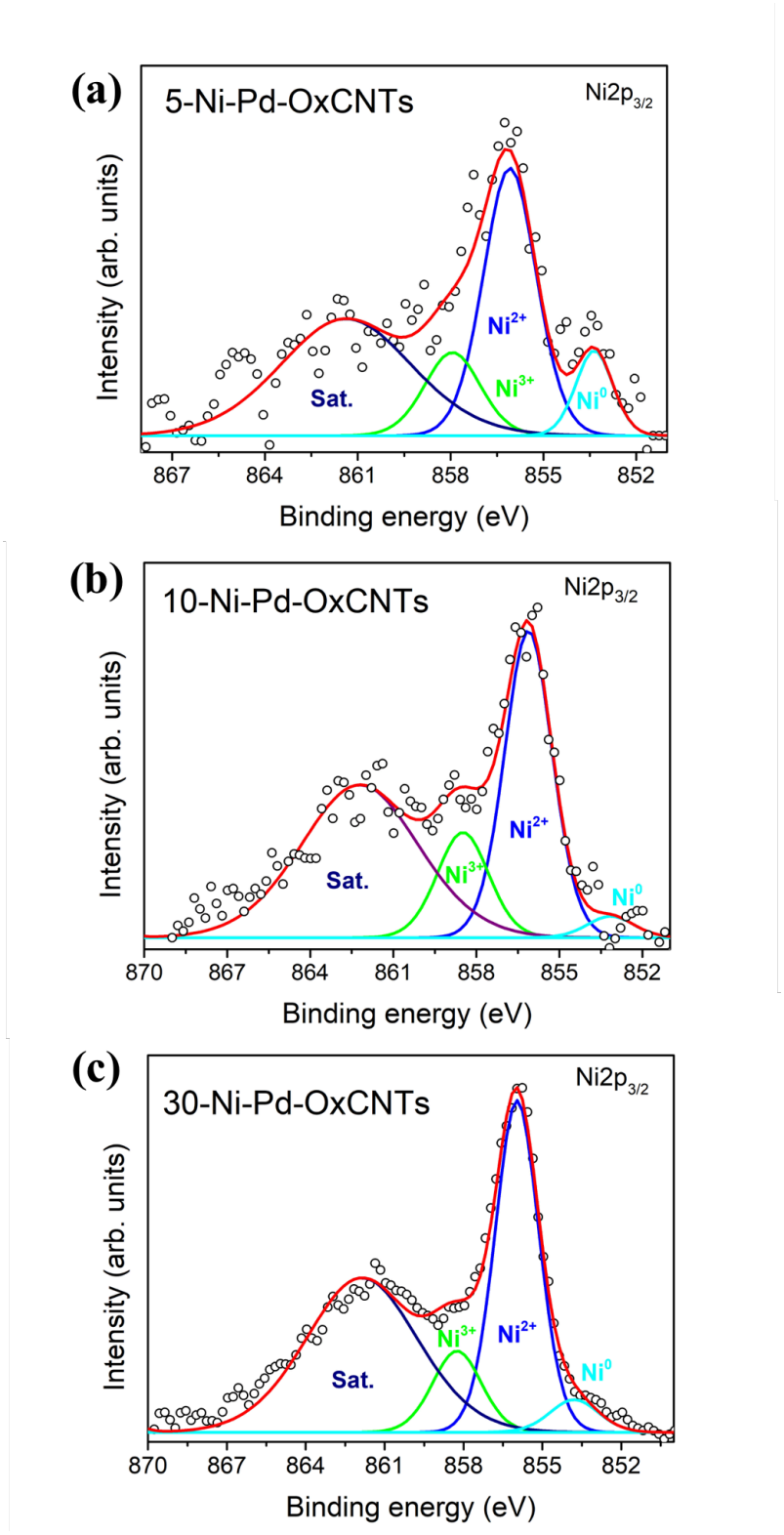

Figure 3.34. Ni2p XPS analysis spectrum of Ni-Pd-Ox-CNTs. (a) 5Ni-Pd-Ox-CNTs, (b) 10Ni-Pd-Ox-CNTs, (c) 30Ni-Pd-Ox-CNTs. Cyan doublet is assigned to Ni^0, blue doublet to Ni^{2+}, green doublet to Ni^{3+}, and purple doublet to the shake-up satellite peak.

3.5.4 Raman spectroscopy of Pd and Ni-Pd Ox-CNTs

The Raman spectra of these samples are compared in the Figure 3.35, the peaks typical of CNTs spectrum are observed, the D-peak band at ~1350 cm^{-1} and the G-peak at ~1580 cm^{-1}. The Raman spectrum for pristine and Ox-CNTs were discussed in the *section 3.2.4*. The objective of this section is to investigate if the sputtering deposition of palladium and nickel onto Ox-CNTs have an effect in the "crystalline structure" of Ox-CNTs. Figure 3.35a shows the Raman spectrum of Ox-CNTs (Blue) and the spectrum after the sputtering with Pd atoms (Pd-Ox-CNTs) (Black). No significant changes between the spectra are observed, the intensity of the D peak related to defects in CNTs does not increase after the deposition of Pd, these results match with the XPS analysis where no C-Pd bonds or increased sp^3 defects are observed in the C1s spectrum after the deposition of Pd. Likewise, the Raman spectrum of Ni-Pd (Figure 3.35b) shows no effect in the "crystalline structure" of Ox-CNTs with the sputtering of nickel atoms.

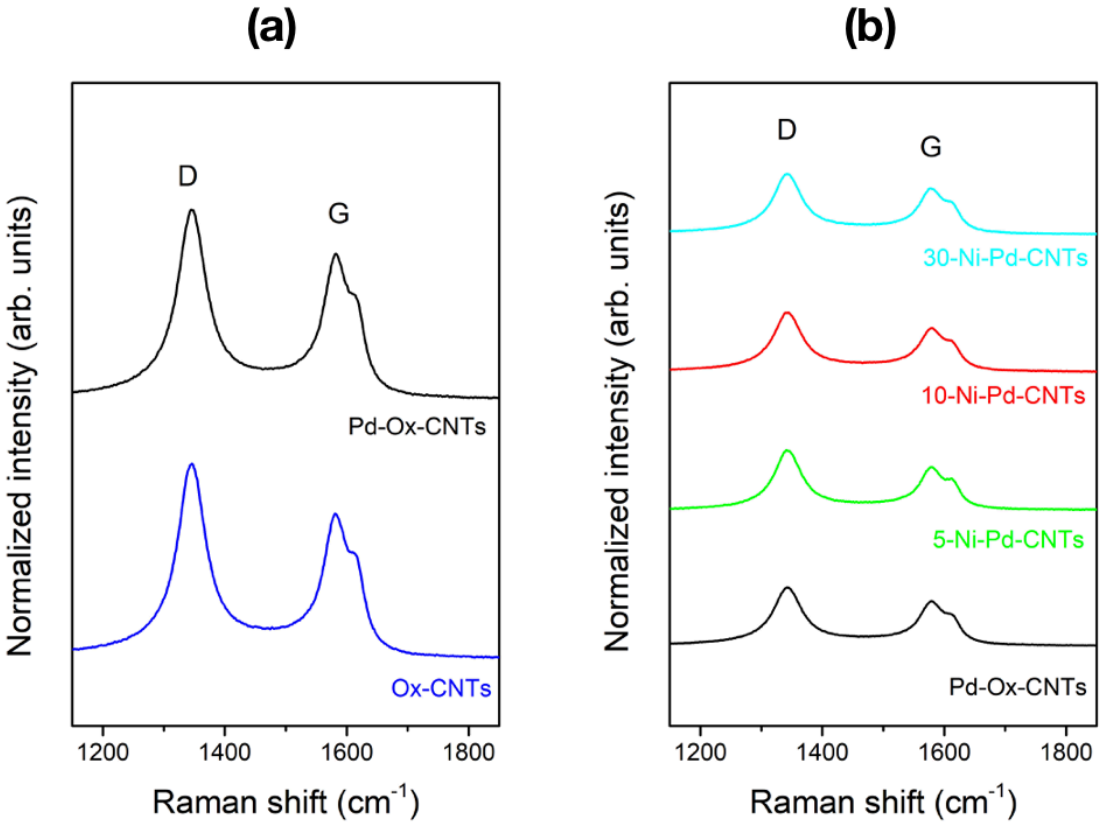

Figure 3.35. Raman spectra of Pd-OxCNTs (a) and Ni-Pd-OxCNTs (b).

3.5.5 Electronic microscopy of pristine-CNTs and Ni-Pd-Ox-CNTs

The morphology of pristine CNTs and Ni-Pd-Ox-CNTs is compared using SEM microscopy and showed in the Figure 3.36. The macroscopic morphology of CNTs does not change after the creation of bimetallic nanoparticles in their surface. Unfortunately, the observation of the bimetallic nanoparticles is not possible using SEM microscopy because of their small size, to observe the nanoparticles, the samples should be analyzed by TEM microscopy, however, the sample preparation for TEM requires the complete destruction of the sample which may not allow the use of Ni-Pd-Ox-CNTs samples as chemical sensors like it is planned for this thesis work.

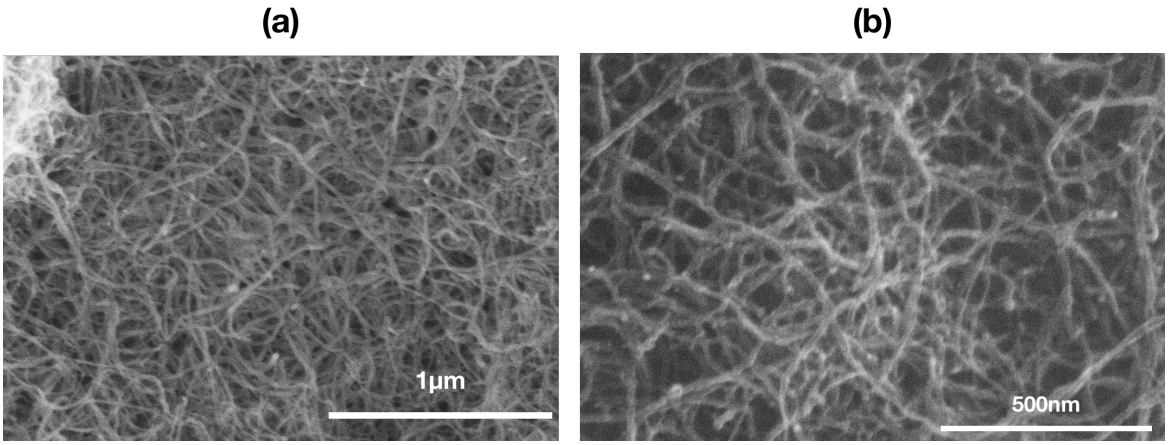

Figure 3.36. SEM images of pristine CNTs (a) and 30-Ni-Pd-Ox-CNTs (b).

3.6 Gas sensing properties of Pd-Ox-CNTs and Ni-Pd-Ox-CNTs

The increasing pollution of the environment has a huge impact on nature and human health and safety. Because of that, most of Worldwide governments have imposed strict environmental and safety regulations to limit the production of toxic emissions, that are for instance generated during metal processing, from automotive, or by chemical and petrochemical industries. To control the presence of toxic emissions in indoor and outdoor air a vast number of systems for gas sensing and air quality monitoring have been developed and employed. Critical air pollutants such as nitrogen oxides (NO_x) and carbon oxides (CO, CO_2), resulting from combustion or automotive emissions, additional harmful vapours in the atmosphere are volatile organic compounds (VOCs) such as benzene, toluene, and ethanol. Problems in respiratory system, skin and eyes damage and pulmonary edema are some of the possible consequences of prolonged exposure to such toxic vapours [47,48]. As mentioned before, sensors used nowadays to detect these harmful gases are based on the infrared spectroscopy, gas chromatography and metal oxides materials presenting a good detection limit, however, they are not compatible with the requirements of real-time analysis,

miniaturization, and cost effectiveness. In this framework, carbon nanomaterials, more specifically CNTs and graphene are promising active sensing layers due to their high chemical stability, high surface area, low-cost and their high conductivity that it is not easily affected by increasing their temperature. Nevertheless, carbon nanotubes, in addition, have important advantages over graphene, their synthesis is easier, the synthesis cost is lower and high-quality CNTs can be synthesized in a large scale. However, as explained before, the introduction of active sites on their pristine structure is needed to boost their reactivity to gases thus improving the sensitivity in the detection of hazardous molecules, for this reason, during this work CNTs were firstly oxygen functionalized and then decorated with bimetallic nanoparticles.

In the following section, Ox-CNTs decorated with bimetallic nanoparticles are evaluated as active materials in gas sensors for the detection of part per million (ppm) of H_2, NO_2, toluene, and ethanol.

3.6.1 Resistive sensors

The working principle of resistive sensing devices comprises the variation of the electrical resistivity on the sensor surface generated by the adsorption of gas molecules. The reversibility of the sensor is the capability to return to its initial state after the interaction with the target gas. The sensing experiments consist in the measurement of the resistance variation as a function of the gas molecules concentration for subsequent cycles (Figure 3.37). The resistance is uninterruptedly measured, allowing a real-time acquisition of its variation from the initial value, R_0. The sensor response is defined according to the following relation:

$$\left|\frac{\Delta R}{R_0}\right|(\%) = \left|\frac{R_0 - R_f}{R_0}\right| \cdot 100 \tag{3.2}$$

where R_f is the resistance value measured when the flow of the gas of interest is stopped. The increment or decrease of the resistance will depend on the type of semiconducting layer (*n*- or *p*- type depending on the electron or hole doping) and on the donor/acceptor behavior of the gas molecules detected. In this work, since holes are the charge carriers in carbon nanotubes, the Ox-CNTs surface behaves as a hole-doped semiconductor (*p*-type semiconductor).

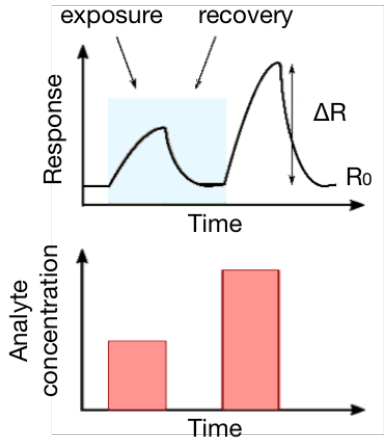

Figure 3.37. Measurement of the resistance variation as a function of the analyte concentration for subsequent cycles.

3.6.2 Device employed to test gas detection

The gas sensing experiments were done at the University Rovira i Virgili of Tarragona, in Spain, by the MINOS–EMaS group, headed by Prof. Eduard Llobet. The experimental procedure begins with the preparation of a solution of CNTs/ethanol, then, the solution is sonicated for 30 min until completely disperse the CNTs into ethanol. Afterwards, the CNTs dispersion is deposited directly on a commercially available transducer by airbrushing. The transducer consists of an alumina sensor substrate with a 10×10 mm screen-printed and Pt-electrodes with a breach of 500 μm between them (Figure 3.38). Through the deposition, the alumina sensors are heated to 100 °C in order of facilitate a rapid evaporation of ethanol. It is important to mention that the oxygen functionalization of CNTs and the deposition of bimetallic nanoparticles was carried out directly into the CNTs deposited in the alumina substrate transducer.

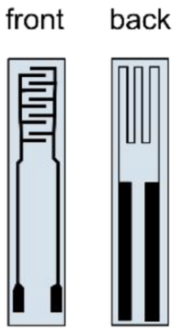

Figure 3.38. Illustration of the commercial alumina sensor in the front side the Pt-electrodes are observed, here, the CNTs are deposited. In the back side of the sensor the heater is located.

The gas sensing device involves a mass flow meters and electro-valves systems that are computer-controlled to obtain the desired concentrations of the gases by mixing them with pure air, then, the gases are distributed to the test chamber (Figure 3.39). The DC resistance of the sensors is measured with an Agilent multimeter during all the interval of the experiments. The chamber consists of a base chamber where the sensors are connected to the arrangement of resistance measure and a chamber lid with the inlet and outlet gas connections, the lid is placed on the top of the base and closed with the help of screws.

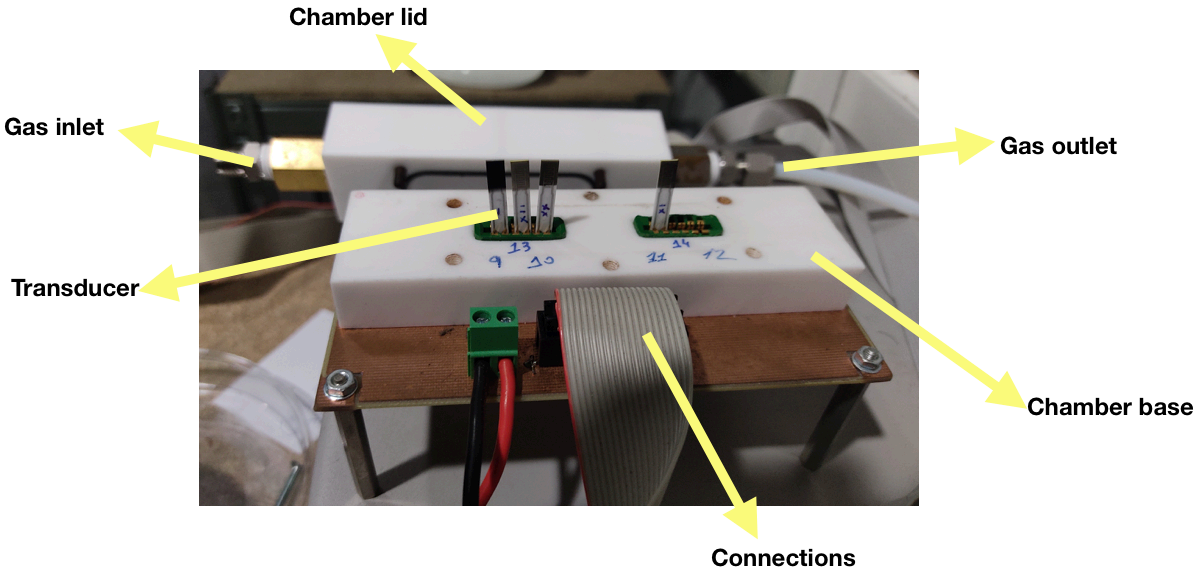

Figure 3.39. Test chamber used for the gas sensing.

The measurements are performed in cycles, in the beginning of one cycle pure dry air is flowed through the chamber until the sample resistance is stabilized to a certain value, this value corresponding to a constant baseline R_0. Afterwards, a mix of pure air with the test gas is delivered into the chamber with the desired concentration of the gas of interest during 5 minutes. At the end of each cycle there is a recovery phase where the flow is switched again to pure air. The measurements can be performed at certain working temperature or at room temperature (RT).

3.6.3 Gas sensing

In this section, the results related to the gas-sensing properties of the Ox-CNTs decorated with Pd and Ni-Pd nanoparticles are detailed and discussed. The sensor response is analyzed as a function of variable concentration of target gases and the sensor working temperature.

The gases analyzed as well as the concentration and working temperature of each experiment are detailed in the Table 3.8.

Target gas	Concentration (ppm)				Working temperature (ºC)	
Toluene	2.5	5	7.5	10	RT	150
Ethanol	5	10	15	20	RT	150
NO_2	250 (ppb)	500 (ppb)	750 (ppb)	1000 (ppb)	RT	150
H_2	250	500	750	1000	150	

Table 3.8. Experimental details for the gas sensing properties test of Pd-OxCNTs and Ni-Pd-OxCNTs samples.

3.6.3.1 Toluene

Toluene (C_7H_8), the common name for methylbenzene, is an important aromatic organic compound widely used in industrial processes (Figure 3.40), it is used mainly as solvent in paints, resins, and adhesives. It is also used to produce benzene. The inhalation of high concentrations of toluene even for low periods of time affects the nervous system, kidney, liver, and heart. Humans can be exposed to toluene if they work in the industry or in the environment after air emissions, furthermore, toluene is also present in the gases produced in the incomplete combustion of gasoline vehicles. Therefore, there is an increasing need for developing efficient sensors to monitor and control the emissions of toluene [49]. The detection of toluene has been performed with several materials such as diamond, copolymer composites [50], and WO_3 [51]. CNTs have been poorly studied for sensing toluene.

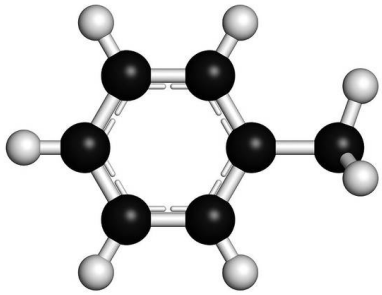

Figure 3.40. Toluene structure scheme. Black spheres: carbon, gray spheres: hydrogen.

Here, Ox-CNTs decorated with Pd and Pd-Ni nanoparticles were evaluated as gas sensors to detect toluene at different ppm concentrations (2.5, 5, 75 and 10 ppm). The variation in the resistance of the active layers was measured. The curves in Figure 3.41 display the cyclic sensors response (R/R_0, left axis) during exposure (5 min) to increasing concentrations of toluene (expressed in ppm on the right axis). The measurements were realized using two working temperatures, room temperature (RT) (Figure 3.41a) and 150 ºC (Figure 3.41b). The resistance increases upon toluene exposure which indicates a charge transfer from toluene to Ox-CNTs surface, CNTs possess p-type characteristics (has more holes than electrons), the electrons donated by toluene molecules decrease the number of positive holes in CNTs by electron-hole recombination, and thus increasing they p-type resistivity. A good recovery of the resistance base line after the end of toluene exposure is observed, this indicates an effective desorption of toluene from the active layer. The response of the sensors is better at room temperature, this represents an advantage for the sensors developed here, because it allows the development of sensors with a low power consumption. At room temperature the sensor with better response is 5-Ni-Pd-Ox-CNTs and at higher temperatures the samples with higher concentration of nickel (10-30Ni) have better responses to toluene. This denotes that bimetallic nanoparticles present a synergetic effect for the Ni-Pd-Ox-CNTs sensors.

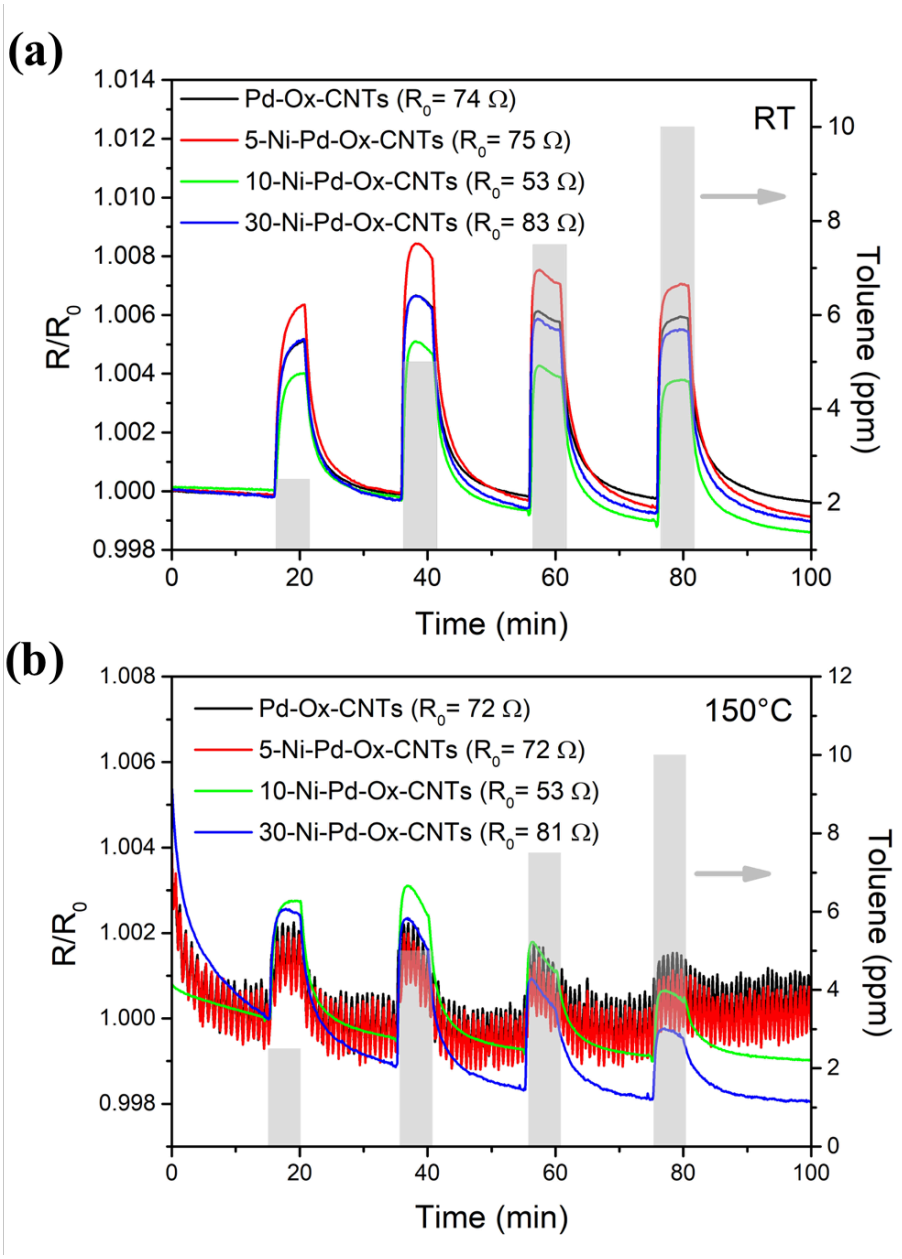

Figure 3.41. Typical responses and recovery curves of Pd-Ox-CNTs and Ni-Pd-Ox-CNTs sensors as a function of variable concentration of toluene. Room temperature (a) and 150 ºC of working temperature (b). The measured resistances are normalized to the relative baseline value R_0 of each sensor (left axis), while the analyte concentration is shown as light grey bar and it is expressed in ppm (right axis).

3.6.3.2 Ethanol

Ethanol (C_2H_6O) also called ethyl alcohol is a volatile and flammable colorless liquid with a

toxic nature (Figure 3.42). Often used in beverages, industrial and scientific sectors. Prolonged heavy alcohol consumption or exposure causes damage in the brain and other organs and increase the risk of cancer [52]. Besides, people that works on ethanol synthesis have high probability of developing respiratory and digestive track cancer [53]. Thus, development of sensors to monitor ethanol gas trace level is of great demand nowadays.

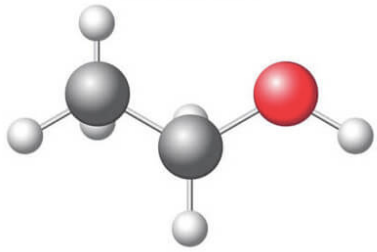

Figure 3.42. Ethanol structure scheme. Black spheres: carbon, gray spheres: hydrogen, red sphere: oxygen.

Here, it is shown that Pd-Ox-CNTs and Ni-Pd-Ox-CNTs are active layer with potential to detect ethanol at ppm concentrations (5, 10, 15 and 20 ppm). The curves in Figure 3.43 display the cyclic sensors response (R/R_0, left axis) during exposure (5 min) to increasing concentrations of ethanol (expressed in ppm on the right axis). The measurements were performed using two working temperatures, room temperature (RT) (Figure 3.43a) and 150 ºC (Figure 3.43b). Same as toluene, ethanol is an electron-donor molecule and thus CNTs Fermi level shifts toward the conduction band, reducing the number of electron holes and increasing the resistance of the active layer. A good recuperation of the resistance base line after the end of ethanol exposure is observed for the nanotubes decorated with bimetallic nanoparticles (Pd-Ni), this indicates an effective desorption of ethanol from the active layer. In this case, the sensors are slightly more sensible to ethanol at higher temperatures. For the case of 150 ºC measurements the Pd-Ox-CNTs and 5-Ni-P-Ox-CNTs sample have no response to ethanol, this may be due the destabilization of Pd nanoparticles at high temperate that are being stabilized with the presence of nickel atoms for the case of nanoparticles with high concentrations of Ni [54,55]. These results evidence the synergetic effect of having bimetallic nanoparticles.

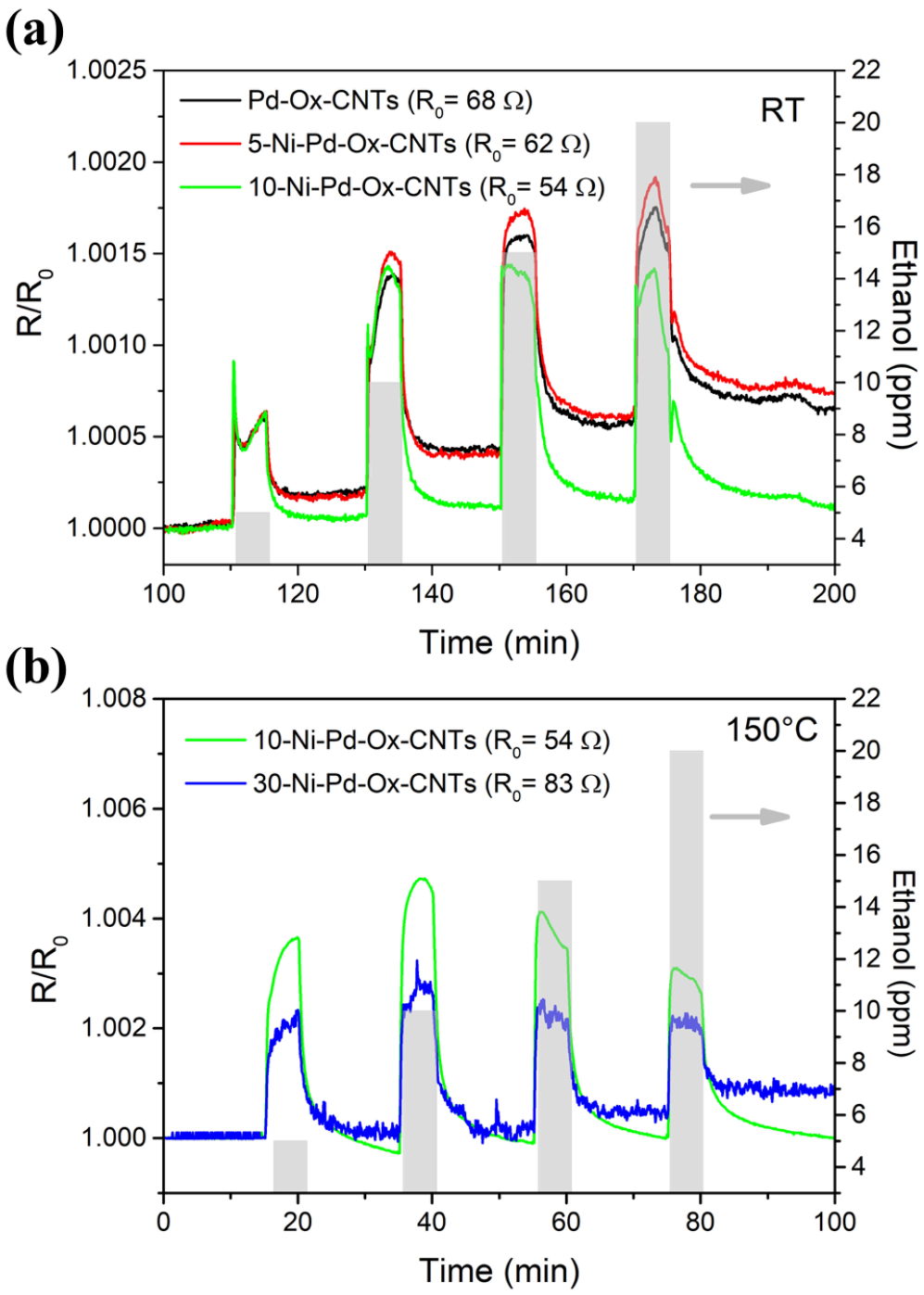

Figure 3.43. Typical responses and recovery curves of Pd-Ox-CNTs and Ni-Pd-Ox-CNTs sensors as a function of variable concentration of ethanol. Room temperature (a) and 150 ºC of working temperature (b). The measured resistances are normalized to the relative baseline value R_0 of each sensor (left axis), while the analyte concentration is shown as light grey bar and it is expressed in ppm (right axis).

3.6.3.3 NO_2

Nitrogen dioxide (NO_2) is one of the most dangerous of the harmful environmental gases (Figure 3.44). Long-term exposure to low NO_2 concentrations (~1 ppm) can affect respiratory function and increase the risk of emphysema and bronchitis [56]. Furthermore, concentrations of 10 ppm NO_2(g) causes immediate distress, including nose and throat irritation, higher concentrations of NO_2(g) (100 ppm) can cause death by asphyxia. The most common sources of NO_2(g) in the environment are internal combustion engines burning fossil fuels such as motor vehicles and butane and kerosene heaters and stoves.

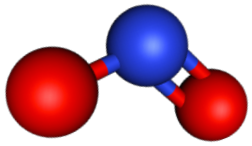

Figure 3.44. NO_2 structure scheme. Red spheres: oxygen, blue sphere: nitrogen.

The high toxicity of NO_2 and the fact that NO_2 can be present outdoors in almost anywhere nowadays, due to traffic from motor vehicles, makes it one of the most studied gases for the development of sensors to monitor and detect NO_2 with high sensitivity and selectivity. In this work, Pd-Ox-CNTs and Ni-Pd-Ox-CNTs were tested as active layer to detect NO_2 at low ppb concentrations (250, 500, 750 and 100 ppb). The curves in Figure 3.45 shows the cyclic sensors response (R/R_0, left axis) during exposure (5 min) to increasing concentrations of NO_2 (expressed in ppb on the right axis). The measurements were performed using two working temperatures, room temperature (RT) (Figure 3.45a) and 150ºC (Figure 3.45b). Contrary to toluene and ethanol, exposure of Pd-Ox-CNTs and Ni-Pd-Ox-CNTs to NO_2 results in the decrease of their resistance, this is due to the oxidizing nature of NO_2, thus a charge transfer from the CNTs to NO_2 molecules occurs. The sensors have an increased response to NO_2 at room temperature rather than increased temperatures. This may be due to the destabilization of the bimetallic nanoparticles in CNTs at increased temperatures as explained before [57]. The Ox-CNTs decorated with nanoparticles with higher concentration of Ni present better responses to NO_2 at RT. These results corroborate that decorated CNTs with bimetallic nanoparticles increases their sensing activity in gas sensors.

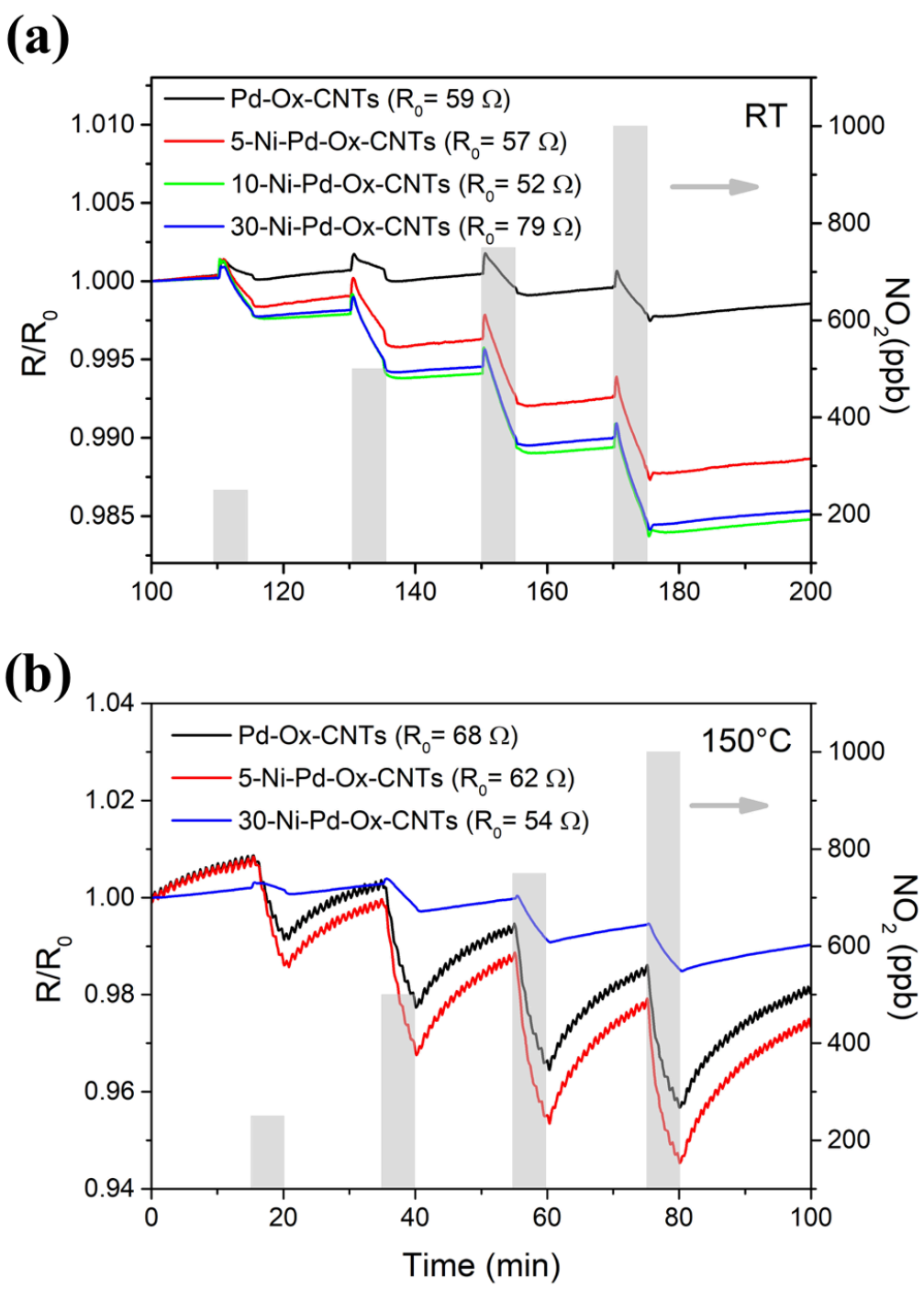

Figure 3.45. Typical responses and recovery curves of Pd-Ox-CNTs and Ni-Pd-Ox-CNTs sensors as a function of variable concentration of NO_2. Room temperature (a) and 150 ºC of working temperature (b). The measured resistances are normalized to the relative baseline value R_0 of each sensor (left axis), while the analyte concentration is shown as light grey bar and it is expressed in ppb (right axis).

3.6.3.4 H_2

H_2 is a colorless and odorless gas used in the industry in petroleum refining, treating metals, production of fertilizer and processing foods (Figure 3.46). The use of hydrogen has been tripled since 1975 and it will continue with a market that will exceed $160 billion by 2026 in the USA [58]. This increment in the use of H_2 demands for the development of rapid and sensitive H_2 sensors to detect leaks because even small amounts exposure to hydrogen can cause burns and respiratory problems, besides, due to it flammable and easily ignited nature H_2 is a potential cause for a severe fire or explosion.

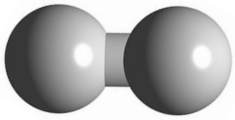

Figure 3.46. H_2 structure scheme. Gray spheres: hydrogen atoms.

The synthetized Pd-Ox-CNTs and Ni-Pd-Ox-CNTs samples were used as active layer in resistive sensors to detect H_2 at ppm concentrations at room temperature (250, 500, 750 and 1000 ppm). The curves in Figure 3.47 shows the cyclic sensors response (R/R_0, left axis) during exposure (5 min) to increasing concentrations of H_2 (expressed in ppm on the right axis). CNTs are widely reported as not sensitive to H_2 gas [59], however, the Ox-CNTs decorated with Pd and Ni-Pd nanoparticles developed here present a notable response to the exposure of H_2 gas at low concentrations, the resistance of the active layer increases after react with H_2, evidencing the charge transfer from H_2 to the p-type semiconductor Ox-CNTs surface. Not significant difference between Pd-Ox-CNTs and Ni-Pd-Ox-CNTs sensors were observed, which suggests that both Pd and Ni-Pd nanoparticles are able to work synergistically with Ox-CNTs to detect H_2.

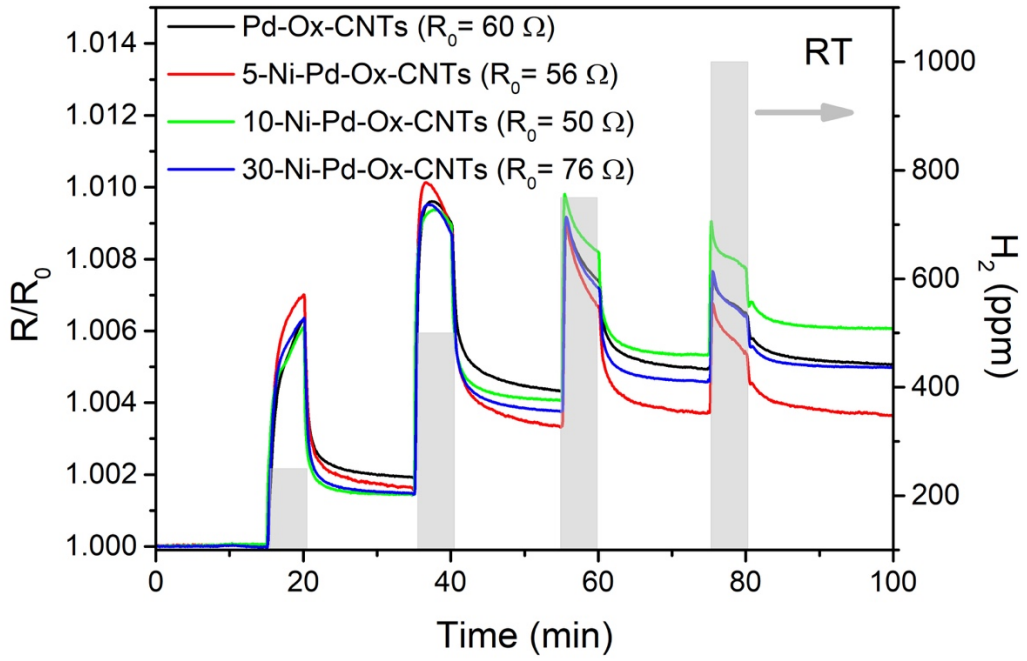

Figure 3.47. Typical responses and recovery curves of Pd-Ox-CNTs and Ni-Pd-Ox-CNTs sensors as a function of variable concentration of H_2. The measurements were realized at room temperature. The measured resistances are normalized to the relative baseline value R_0 of each sensor (left axis), while the analyte concentration is shown as light grey bar and it is expressed in ppb (right axis).

3.6.4 Sensing mechanism

In summary, the sensors developed in this work are able to detect VOCs gases (toluene and ethanol), NO_2 and H_2. Generally, the Ox-CNTs decorated with bimetallic nanoparticles have better responses for all the studied gases except H_2. The sensing mechanism for the Pd-Ox-CNTs and Ni-Pd-OxCNTs arises from interactions among the gas, metallic nanoparticles and Ox-CNTs. These sensors have five potential types of adsorption sites for the gases: external surfaces coated with metal nanoparticles, external surfaces not covered with metal nanoparticles, groove sites, interstitial sites, and internal sites (Figure 3.48). Generally, chemical sensors have two functions, i.e., a receptor function which recognizes a chemical substance (adsorption) and a transducer function which transduces the chemical signal into an output signal (here variation in the resistivity). Even if the adsorption of gas molecules in Pd-Ox-CNTs and Ni-Pd-Ox-CNTs take place at these five places it should be considered that the inert surface of CNTs. In the present built sensors, it can be said that Pd and Ni-Pd nanoparticles identify the gases (receptor function) and Ox-CNTs provide the conducting

path (transducer function), and this cooperative combination allows the gas molecule detection even at room temperature.

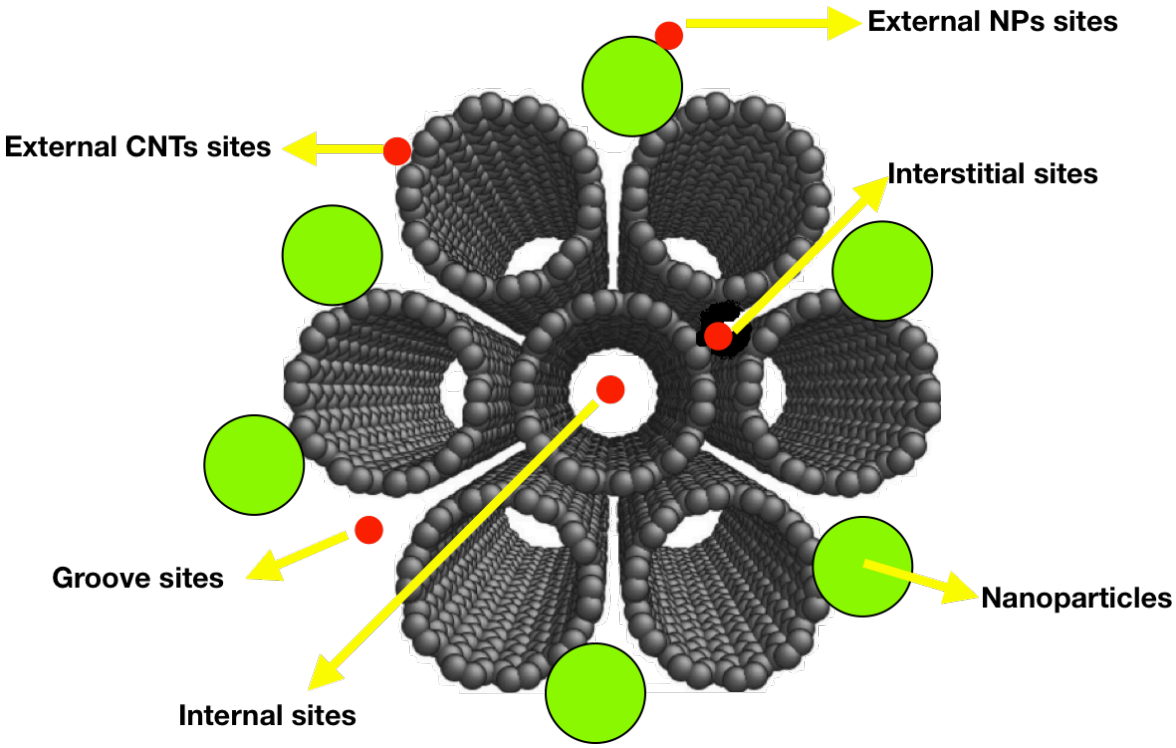

Figure 3.48. Potential types of adsorption sites for the gases in CNTs decorated with metallic nanoparticles.

The sensors developed show response to ethanol, toluene, NO_2, and H_2 which denotes their poor selectivity. The selectivity of Ni-Pd-Ox-CNTs can be improved using modern detections techniques such as pattern recognition sensing, where parameters like response time and recovery time are used to recollect data and through the analysis of these data selective sensors are developed. The selectivity of Ni-Pd-Ox-CNTs can be also reached by proving the sensors at different working temperatures or decorate Ox-CNTs with nanoparticles of different sizes and compare their responses to several gases.

3.7 Conclusions

Multiwall carbon nanotubes were evaluated as an active layer of chemical resistive sensors to detect hazardous gases. The vertically aligned carbon nanotubes were synthetized by chemical vapor deposition. Due to its intrinsically inert surface, CNTs were functionalized

with oxygen-containing functional groups through low kinetic energy oxygen ion irradiation to increase their surface reactivity to the gas target molecules. This work demonstrated that low kinetic energy oxygen ion irradiation is a functionalization technique that permits the effective functionalization of vertically aligned carbon nanotubes with oxygen groups in a rapid, solvent-free, clean and defect control mode. Four different oxygen functional groups were identified by analysis of the C1s XPS spectra: epoxide, hydroxyl, carbonyl, and carboxyl groups. Subsequently, an annealing treatment was used to study the thermal stability of each oxygen group, from this study the epoxide groups were identified like the most unstable and carbonyl like the most stable oxygen group. Studying the thermal stability of oxygen groups in the surface of CNTs was important for this work because some Ox-CNTs gas sensor measurements were performed at relatively high temperatures (150 ºC). Even if there is an evident loss of oxygen, some functional chemical groups remain stable in the CNTs surface after the annealing at 500 ºC. Furthermore, we show that the concentration of each functional group can be adjusted by the thermal treatment of the carbon nanotubes without damaging their overall structure owing to their thermal stability. The combination of low kinetic energy ion-irradiation followed by short time thermal annealing represents an excellent combination for oxygen functionalization of carbon nanotubes, allowing simultaneous control over both overall concentration and concentration of individual functional group types.

Afterwards, the oxygen groups at the CNTs surface were used as active sites for nucleation of metal particles; CNTs were decorated with bimetallic Ni-Pd and Pd nanoparticles using plasma sputtering deposition. XPS core level spectrum analysis of the samples showed that neither C-Pd nor C-Ni bonds are formed during the sputtering deposition.

The variation on the resistance of the Pd-Ox-CNTs and Ni-Pd-Ox-CNTs active layers when they were exposed to different concentrations of NO_2, H_2, toluene and ethanol gases was used as the transducer signal to evaluate the chemical sensing (gas-active layer chemical interaction). The analysis of the results of this part of the research showed that decorate Ox-CNTs with bimetallic Ni-Pd nanoparticles increases the response of Ox-CNTs towards the detection of toluene, ethanol, NO_2, and H_2. The sensors with bimetallic Ni-Pd nanoparticles have higher responses to the probed gases than the sensors decorated with Pd nanoparticles. Furthermore, the fabricated sensors show higher sensitivity for detection of gases at near room temperature measurements, this characteristic shows the potential to use the hybrid system for the engineering of sensors with low power consumption.

Even if it is clear that bimetallic Ni-Pd decorated Ox-CNTs have increased responses to gas molecules than Pd decorated Ox-CNTs, further investigations need to be done to fully understand the role of the relative concentration of nickel in the Ni-Pd nanoparticles for the mechanism of detection of gases.

3.8 References

[1] K.-P. Yoo, K.-H. Kwon, N.-K. Min, M.J. Lee, C.J. Lee, Effects of O2 plasma treatment on NH3 sensing characteristics of multiwall carbon nanotube/polyaniline composite films, Sensors Actuators B Chem. 143 (2009). https://doi.org/10.1016/j.snb.2009.09.029.

[2] R. Malik, C. McConnell, N.T. Alvarez, M. Haase, S. Gbordzoe, V. Shanov, Rapid, in situ plasma functionalization of carbon nanotubes for improved CNT/epoxy composites, RSC Adv. 6 (2016). https://doi.org/10.1039/C6RA23103A.

[3] A. Muhulet, F. Miculescu, S.I. Voicu, F. Schütt, V.K. Thakur, Y.K. Mishra, Fundamentals and scopes of doped carbon nanotubes towards energy and biosensing applications, Mater. Today Energy. 9 (2018). https://doi.org/10.1016/j.mtener.2018.05.002.

[4] A. Barinov, L. Gregoratti, P. Dudin, S. La Rosa, M. Kiskinova, Imaging and Spectroscopy of Multiwalled Carbon Nanotubes during Oxidation: Defects and Oxygen Bonding, Adv. Mater. 21 (2009). https://doi.org/10.1002/adma.200803003.

[5] C. Bittencourt, C. Navio, A. Nicolay, B. Ruelle, T. Godfroid, R. Snyders, J.-F. Colomer, M.J. Lagos, X. Ke, G. Van Tendeloo, I. Suarez-Martinez, C.P. Ewels, Atomic Oxygen Functionalization of Vertically Aligned Carbon Nanotubes, J. Phys. Chem. C. 115 (2011). https://doi.org/10.1021/jp2057699.

[6] V. Datsyuk, M. Kalyva, K. Papagelis, J. Parthenios, D. Tasis, A. Siokou, I. Kallitsis, C. Galiotis, Chemical oxidation of multiwalled carbon nanotubes, Carbon N. Y. 46 (2008). https://doi.org/10.1016/j.carbon.2008.02.012.

[7] P.M. Korusenko, S.N. Nesov, S.N. Povoroznyuk, V. V. Bolotov, E. V. Knyazev, Functionalization of multi-walled carbon nanotubes using ion beams of various intensities, in: 2018. https://doi.org/10.1063/1.5051935.

[8] W. Xia, O.F.-K. Schlüter, C. Liang, M.W.E. van den Berg, M. Guraya, M. Muhler, The synthesis of structured Pd/C hydrogenation catalysts by the chemical vapor deposition of Pd(allyl)Cp onto functionalized carbon nanotubes anchored to vapor grown carbon microfibers, Catal. Today. 102–103 (2005). https://doi.org/10.1016/j.cattod.2005.02.002.

[9] A.V. Krasheninnikov, K. Nordlund, Irradiation effects in carbon nanotubes, Nucl. Instruments Methods Phys. Res. Sect. B Beam Interact. with Mater. Atoms. 216 (2004). https://doi.org/10.1016/j.nimb.2003.11.061.

[10] T. Kamimura, K. Yamamoto, T. Kawai, K. Matsumoto, n-Type Doping for Single-Walled Carbon Nanotubes by Oxygen Ion Implantation with 25 eV Ultralow-Energy Ion Beam, Jpn. J. Appl. Phys. 44 (2005). https://doi.org/10.1143/JJAP.44.8237.

[11] Z. Bai, L. Zhang, L. Liu, Bombarding Graphene with Oxygen Ions: Combining Effects of Incident Angle and Ion Energy To Control Defect Generation, J. Phys. Chem. C. 119 (2015). https://doi.org/10.1021/acs.jpcc.5b09620.

[12] O. Lehtinen, J. Kotakoski, A. V. Krasheninnikov, A. Tolvanen, K. Nordlund, J. Keinonen, Effects of ion bombardment on a two-dimensional target: Atomistic simulations of graphene irradiation, Phys. Rev. B. 81 (2010). https://doi.org/10.1103/PhysRevB.81.153401.

[13] A. V. Krasheninnikov, F. Banhart, Engineering of nanostructured carbon materials with electron or ion beams, Nat. Mater. 6 (2007). https://doi.org/10.1038/nmat1996.

[14] J.-F. Colomer, B. Ruelle, N. Moreau, S. Lucas, R. Snyders, T. Godfroid, C. Navio, C. Bittencourt, Vertically aligned carbon nanotubes: Synthesis and atomic oxygen functionalization, Surf. Coatings Technol. 205 (2011). https://doi.org/10.1016/j.surfcoat.2011.03.040.

[15] T. Lin, V. Bajpai, T. Ji, L. Dai, Chemistry of Carbon Nanotubes, Aust. J. Chem. 56 (2003). https://doi.org/10.1071/CH02254.

[16] S. Doniach, M. Sunjic, Many-electron singularity in X-ray photoemission and X-ray line spectra from metals, J. Phys. C Solid State Phys. 3 (1970). https://doi.org/10.1088/0022-3719/3/2/010.

[17] M. Scardamaglia, M. Amati, B. Llorente, P. Mudimela, J.-F. Colomer, J. Ghijsen, C. Ewels, R. Snyders, L. Gregoratti, C. Bittencourt, Nitrogen ion casting on vertically aligned carbon nanotubes: Tip and sidewall chemical modification, Carbon N. Y. 77 (2014). https://doi.org/10.1016/j.carbon.2014.05.035.

[18] B. Ruelle, A. Felten, J. Ghijsen, W. Drube, R.L. Johnson, D. Liang, R. Erni, G. Van Tendeloo, P. Sophie, P. Dubois, T. Godfroid, M. Hecq, C. Bittencourt, Functionalization of MWCNTs with atomic nitrogen, Micron. 40 (2009). https://doi.org/10.1016/j.micron.2008.01.003.

[19] F. GÜNEŞ, G.H. HAN, H.-J. SHIN, S.Y. LEE, M. JIN, D.L. DUONG, S.J. CHAE, E.S. KIM, F. YAO, A. BENAYAD, J.-Y. CHOI, Y.H. LEE, UV-LIGHT-ASSISTED OXIDATIVE sp^3 HYBRIDIZATION OF GRAPHENE, Nano. 06 (2011). https://doi.org/10.1142/S1793292011002780.

[20] M.S. Dresselhaus, A. Jorio, A.G. Souza Filho, R. Saito, Defect characterization in graphene and carbon nanotubes using Raman spectroscopy, Philos. Trans. R. Soc. A Math. Phys. Eng. Sci. 368 (2010). https://doi.org/10.1098/rsta.2010.0213.

[21] R. Md.Masud, I.D. Sh., M.A. M.R., J. S., T. Amanullah, A review on recent advances of CNTs as gas sensors, Sens. Rev. 37 (2017) 127–136. https://doi.org/10.1108/SR-10-2016-0230.

[22] A. Dey, Semiconductor metal oxide gas sensors: A review, Mater. Sci. Eng. B. 229 (2018) 206–217. https://doi.org/10.1016/j.mseb.2017.12.036.

[23] M. Yudasaka, T. Ichihashi, D. Kasuya, H. Kataura, S. Iijima, Structure changes of single-wall carbon nanotubes and single-wall carbon nanohorns caused by heat treatment, Carbon N. Y. 41 (2003). https://doi.org/10.1016/S0008-6223(03)00076-9.

[24] Y.A. Kim, H. Muramatsu, T. Hayashi, M. Endo, M. Terrones, M.S. Dresselhaus, Thermal stability and structural changes of double-walled carbon nanotubes by heat treatment, Chem. Phys. Lett. 398 (2004). https://doi.org/10.1016/j.cplett.2004.09.024.

[25] A. Mahajan, A. Kingon, Á. Kukovecz, Z. Konya, P.M. Vilarinho, Studies on the thermal decomposition of multiwall carbon nanotubes under different atmospheres, Mater. Lett. 90 (2013) 165–168. https://doi.org/10.1016/j.matlet.2012.08.120.

[26] C. Mattevi, G. Eda, S. Agnoli, S. Miller, K.A. Mkhoyan, O. Celik, D. Mastrogiovanni, G. Granozzi, E. Garfunkel, M. Chhowalla, Evolution of Electrical, Chemical, and Structural Properties of Transparent and Conducting Chemically Derived Graphene Thin Films, Adv. Funct. Mater. 19 (2009). https://doi.org/10.1002/adfm.200900166.

[27] S. Acosta, J. Casanova Chafer, A. Sierra Castillo, E. Llobet, R. Snyders, J.-F. Colomer, M. Quintana, C. Ewels, C. Bittencourt, Low Kinetic Energy Oxygen Ion Irradiation of Vertically Aligned Carbon Nanotubes, Appl. Sci. 9 (2019). https://doi.org/10.3390/app9245342.

[28] C. Struzzi, M. Scardamaglia, A. Hemberg, L. Petaccia, J.-F. Colomer, R. Snyders, C. Bittencourt, Plasma fluorination of vertically aligned carbon nanotubes: functionalization and thermal stability, Beilstein J. Nanotechnol. 6 (2015). https://doi.org/10.3762/bjnano.6.232.

[29] M. Scardamaglia, C. Struzzi, F.J. Aparicio Rebollo, P. De Marco, P.R. Mudimela, J.-F. Colomer, M. Amati, L. Gregoratti, L. Petaccia, R. Snyders, C. Bittencourt, Tuning electronic properties of carbon nanotubes by nitrogen grafting: Chemistry and chemical stability, Carbon N. Y. 83 (2015). https://doi.org/10.1016/j.carbon.2014.11.009.

[30] D.D.L. Chung, Carbon Fiber Composites, Elsevier Inc., 2012. https://doi.org/10.1016/C2009-0-26078-8.

[31] F. Banhart, Irradiation effects in carbon nanostructures, Reports Prog. Phys. 62 (1999). https://doi.org/10.1088/0034-4885/62/8/201.

[32] H. Taghvaei, A. Bakhtyari, M. Reza Rahimpour, Carbon nanotube supported nickel catalysts for anisole and cyclohexanone conversion in the presence of hydrogen and synthesis gas: Effect of plasma, acid, and thermal functionalization, Fuel. 288 (2021). https://doi.org/10.1016/j.fuel.2020.119698.

[33] S. Ali, I.A. Shah, A. Ahmad, J. Nawab, H. Huang, Ar/O2 plasma treatment of carbon nanotube membranes for enhanced removal of zinc from water and wastewater: A dynamic sorption-filtration process, Sci. Total Environ. 655 (2019). https://doi.org/10.1016/j.scitotenv.2018.11.335.

[34] S. Ju, J.M. Lee, Y. Jung, E. Lee, W. Lee, S.-J. Kim, Highly sensitive hydrogen gas sensors using single-walled carbon nanotubes grafted with Pd nanoparticles, Sensors Actuators B Chem. 146 (2010). https://doi.org/10.1016/j.snb.2010.01.055.

[35] A. Abdelhalim, M. Winkler, F. Loghin, C. Zeiser, P. Lugli, A. Abdellah, Highly sensitive and selective carbon nanotube-based gas sensor arrays functionalized with different metallic nanoparticles, Sensors Actuators B Chem. 220 (2015). https://doi.org/10.1016/j.snb.2015.06.138.

[36] D. Depla, S. Mahieu, J.E. Greene, Sputter Deposition Processes, in: Handb. Depos. Technol. Film. Coatings, Elsevier, 2010. https://doi.org/10.1016/B978-0-8155-2031-3.00005-3.

[37] P. Sigmund, Theory of Sputtering. I. Sputtering Yield of Amorphous and Polycrystalline Targets, Phys. Rev. 184 (1969). https://doi.org/10.1103/PhysRev.184.383.

[38] K. Wasa, Sputtering Phenomena, in: Handb. Sputter Depos. Technol. Fundam. Appl. Funct. Thin Film. Nano-Materials MEMS Second Ed., Elsevier Inc., 2012: pp. 41–75. https://doi.org/10.1016/B978-1-4377-3483-6.00002-4.

[39] S. Nguyen-Kuok, The Theoretical Basis of the Low-Temperature Plasma, in: 2017. https://doi.org/10.1007/978-3-319-43721-7_1.

[40] C. Kuhrt, M. Harsdorff, Photoemission and electron microscopy of small supported palladium clusters, Surf. Sci. 245 (1991) 173–179. https://doi.org/10.1016/0039-6028(91)90476-9.

[41] A. Felten, J. Ghijsen, J.-J. Pireaux, W. Drube, R.L. Johnson, D. Liang, M. Hecq, G. Van Tendeloo, C. Bittencourt, Electronic structure of Pd nanoparticles on carbon nanotubes, Micron. 40 (2009). https://doi.org/10.1016/j.micron.2008.01.013.

[42] Y.-F. Han, D. Kumar, C. Sivadinarayana, A. Clearfield, D.W. Goodman, The Formation of PdC_x over Pd-Based Catalysts in Vapor-Phase Vinyl Acetate Synthesis: Does a Pd–Au Alloy Catalyst Resist Carbide Formation?, Catal. Letters. 94 (2004). https://doi.org/10.1023/B:CATL.0000020537.33875.46.

[43] Y.Q. Cai, A.M. Bradshaw, Q. Guo, D.W. Goodman, The size dependence of the electronic structure of Pd clusters supported on Al2O3/Re(0001), Surf. Sci. 399 (1998) L357–L363. https://doi.org/10.1016/S0039-6028(98)00041-7.

[44] A.L. Luna, D. Dragoe, K. Wang, P. Beaunier, E. Kowalska, B. Ohtani, D. Bahena

Uribe, M.A. Valenzuela, H. Remita, C. Colbeau-Justin, Photocatalytic Hydrogen Evolution Using Ni–Pd/TiO $_2$: Correlation of Light Absorption, Charge-Carrier Dynamics, and Quantum Efficiency, J. Phys. Chem. C. 121 (2017). https://doi.org/10.1021/acs.jpcc.7b01167.

[45] D. Xiong, W. Li, L. Liu, Vertically Aligned Porous Nickel(II) Hydroxide Nanosheets Supported on Carbon Paper with Long-Term Oxygen Evolution Performance, Chem. - An Asian J. 12 (2017). https://doi.org/10.1002/asia.201601590.

[46] M. Cheng, H. Fan, Y. Song, Y. Cui, R. Wang, Interconnected hierarchical $NiCo_2O_4$ microspheres as high-performance electrode materials for supercapacitors, Dalt. Trans. 46 (2017). https://doi.org/10.1039/C7DT01289F.

[47] J.D. Ford, P.P. Schnurr, M.J. Friedman, B.L. Green, G. Adams, S. Jex, Posttraumatic stress disorder symptoms, physical health, and health care utilization 50 years after repeated exposure to a toxic gas, J. Trauma. Stress. 17 (2004). https://doi.org/10.1023/B:JOTS.0000029261.23634.87.

[48] B.F. Bessac, S.-E. Jordt, Sensory Detection and Responses to Toxic Gases: Mechanisms, Health Effects, and Countermeasures, Proc. Am. Thorac. Soc. 7 (2010). https://doi.org/10.1513/pats.201001-004SM.

[49] Y.J. Kwon, H.G. Na, S.Y. Kang, S.-W. Choi, S.S. Kim, H.W. Kim, Selective detection of low concentration toluene gas using Pt-decorated carbon nanotubes sensors, Sensors Actuators B Chem. 227 (2016). https://doi.org/10.1016/j.snb.2015.12.024.

[50] M. Matsuguchi, K. Asahara, T. Mizukami, Highly sensitive toluene vapor sensors using carbon black/amino-functional copolymer composites, J. Appl. Polym. Sci. 127 (2013). https://doi.org/10.1002/app.37578.

[51] L. Deng, X. Ding, D. Zeng, S. Zhang, C. Xie, High Sensitivity and Selectivity of C-Doped ${\rm WO}_{3}$ Gas Sensors Toward Toluene and Xylene, IEEE Sens. J. 12 (2012). https://doi.org/10.1109/JSEN.2011.2179980.

[52] D.R. Patil, L.A. Patil, D.P. Amalnerkar, Ethanol gas sensing properties of Al2O3-doped ZnO thick film resistors, Bull. Mater. Sci. 30 (2007). https://doi.org/10.1007/s12034-007-0086-6.

[53] S.-J. Young, Z.-D. Lin, Ethanol Gas Sensors Composed of Carbon Nanotubes with Au Nanoparticles Adsorbed onto a Flexible PI Substrate, ECS J. Solid State Sci. Technol. 6 (2017). https://doi.org/10.1149/2.0211710jss.

[54] Y. Wu, D. Wang, P. Zhao, Z. Niu, Q. Peng, Y. Li, Monodispersed Pd-Ni nanoparticles: Composition control synthesis and catalytic properties in the Miyaura-Suzuki reaction, Inorg. Chem. 50 (2011) 2046–2048. https://doi.org/10.1021/ic102263b.

[55] T. Teranishi, M. Miyake, Novel synthesis of monodispersed Pd/Ni nanoparticles,

Chem. Mater. 11 (1999) 3414–3416. https://doi.org/10.1021/cm990270k.

[56] W. Huang, X. Zhuang, F.S. Melkonyan, B. Wang, L. Zeng, G. Wang, S. Han, M.J. Bedzyk, J. Yu, T.J. Marks, A. Facchetti, UV-Ozone Interfacial Modification in Organic Transistors for High-Sensitivity NO_2 Detection, Adv. Mater. 29 (2017). https://doi.org/10.1002/adma.201701706.

[57] S. Xiao, W. Hu, W. Luo, Y. Wu, X. Li, H. Deng, Size effect on alloying ability and phase stability of immiscible bimetallic nanoparticles, Eur. Phys. J. B. 54 (2006) 479–484. https://doi.org/10.1140/epjb/e2007-00018-6.

[58] Nevadano, https://nevadanano.com/hydrogen-gas-detection/ (accessed March 30, 2021).

[59] J. Li, Y. Lu, Q. Ye, M. Cinke, J. Han, M. Meyyappan, Carbon Nanotube Sensors for Gas and Organic Vapor Detection, Nano Lett. 3 (2003). https://doi.org/10.1021/nl034220x.

Chapter 4

Eu^{3+}-TiO_2 nanothermometer for biological systems

The measurement of the temperature of a system is an important issue in different research subjects. In the previous chapter, the thermal stability of the oxygen functional groups grafted at the CNT surface were investigated through a thermal annealing, in this case the temperature was measured using a thermocouple attached to the sample holder (Figure 3.6). Thermocouples can measure temperature with high precision up to micrometric spatial resolution, for the case of oxygen functionalized carbon nanotubes this spatial resolution is good enough, as knowledge of sample holder temperature, during the thermal annealing, with micrometric spatial resolution is not critical. However, for certain research fields involving nanomaterilas, obtaining knowledge of temperature with submicrometric resolution is of high importance. For example, in electronic devices using nanochips, measuring the temperature within the nanochips with high spatial resolution can prevent the failures induced by increasing temperature due to electromigration. Likewise, in biological systems, measuring temperature with submicrometric resolution allows obtaining temperature differences between organelles in single cells, therefore, increasing knowledge on cells metabolism. The conjugation of nanoscale systems with nanoprobes having properties sensible to temperature variation is a potential solution to achieve temperature measurements with submicrometric resolution because the spatial resolution will be only limited by the size of the nanoprobes (Figure 4.1).

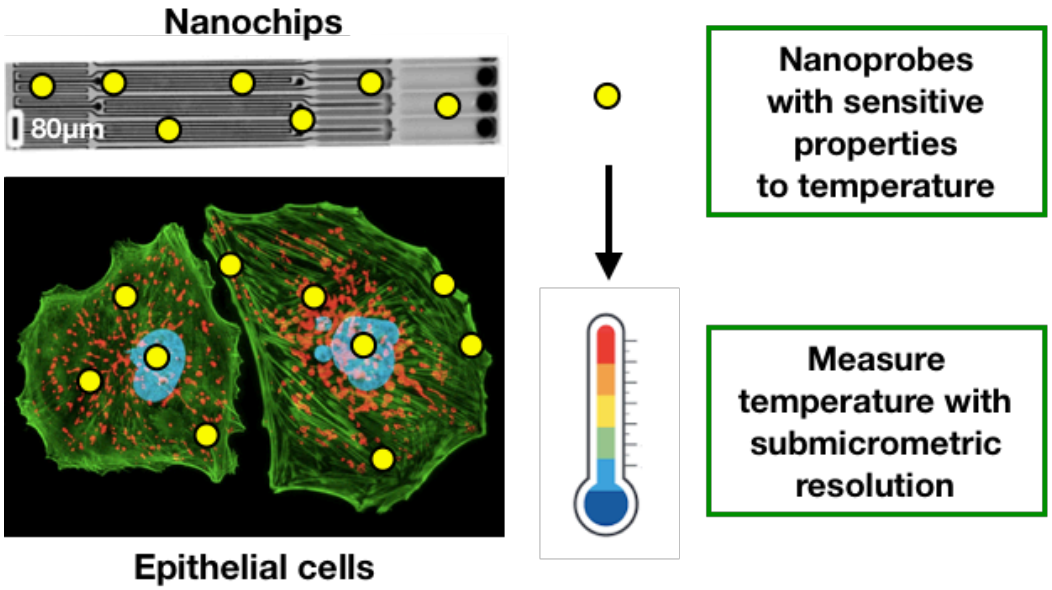

Figure 4.1. Exemplification of systems of interest to obtain temperature with submicrometric spatial resolution. Nanoprobes with properties sensible to temperature variation are used as thermometers and submicrometric measurements can be achieved.

In this chapter, the development of a novel nanothermometer based on europium(III) doped titanium dioxide nanoparticles (Eu^{3+}-TiO_2) able to measure temperature with submicrometric spatial resolution is described. The Eu^{3+}-TiO_2 nanoparticles doped with different concentration of europium were synthetized by the sol-gel technique and it is described in the first part of this chapter. Subsequently, the characterization of the synthetized nanoparticles with different techniques such as SEM, TEM, XRD and XPS is showed. Next, the photoluminescence of the Eu^{3+}-TiO_2 nanoparticles and its dependency with temperature is discussed in detail. It is shown that Eu^{3+}-TiO_2 nanoparticles can be used as nanothermometer using their luminescence intensity dependency with the temperature. The photoluminescence of Eu^{3+}-TiO_2 nanoparticles recorded at different system temperature is investigated and discussed.

At the end of the chapter, it is shown the use of Eu^{3+}-TiO_2 nanoparticles as nanothermometer to evaluate the temperature in a biological system. First, the internalization of Eu^{3+}-TiO_2 nanoparticles in different cells (epithelial and fibroblast mouse cells) is showed, then the development of an appropriated calibration curve of the intensity of luminescence of Eu^{3+}-TiO_2 with temperature variation is discussed. Finally, the ability of Eu^{3+}-TiO_2 nanoparticles to measure differences in temperature within single living cells is discussed.

4.1 Eu^{3+}-TiO_2 based nanothermometers

Luminescence nanothermometry is as a spectroscopic technique based on the temperature dependence of the luminescence emission of some optical materials to measure temperature with submicrometric resolution. As mentioned before, various luminescent materials have been proposed to be used as thermometers, among them, trivalent europium ion (Eu^{3+}) is one of the most studied ions in luminescence nanothermometry, as Eu^{3+} can be used to measure different ranges of temperature depending on the emission line of its spectrum selected (Figure 2.13). Besides, the calibration curve of the Eu^{3+} based nanothermometer can be easily done through a simple emission spectrum measurement. Moreover, the energy transfer between Eu^{3+} neighbor ions that may induce luminescence loss is not observed even at high concentrations of Eu^{3+} ions. Furthermore, the excitations and emission wavelengths of Eu^{3+} occur within the first biological window in the range of 570-720 nm, in which the autofluorescence of biological systems is reduced, therefore the cell autofluorescence does not affect the performance of the Eu^{3+} based nanothermometers. At low dose, Eu^{3+} can be considered as a non-toxic material [1–3], making Eu^{3+} based nanothermometers potential temperature sensors for biological systems.

In turn, titanium dioxide (TiO_2) the matrix used to host Eu^{3+} ions , is a semiconductor metal oxide that exists in three different stable phases: rutile (tetragonal), anatase (tetragonal) and brookite (orthorhombic) [4]. This semiconductor with relatively wide band gap (3.2 eV for anatase, 3.0 eV for rutile, and 1.9 eV for brookite) is widely studied due to its large chemical stability, easy and low-cost way of synthesis methods, high refractive index, additionally to its no-toxic nature, easy-dispersive and high photoactivity [5,6]. These properties make TiO_2 a good candidate for several applications, such as solar cells, gas sensors, water cleaning, as well as host matrix for lanthanide ions to develop nanothermometers [7–12]. Currently, TiO_2 is incorporated in pigments, sunscreens, paints, toothpaste, etc. [4].

The optical properties of TiO_2 depend on the crystallographic phase, density and type of its defects, the presence of dopants, as well as on the synthesis method [13]. The main advantage of TiO_2 as host matrix of Eu^{3+}ions it is the high transparency of TiO_2 in the visible/NIR part of the spectrum. However, it has been shown that doping TiO_2 with lanthanide ions can lead to the change of its optical properties, therefore, the study of the optical properties of TiO_2 and doped- TiO_2 must be carried out if any application involving optical properties are aimed such as luminescence nanothermometry [14–17]. The photoluminescence of TiO_2 and Eu^{3+}-TiO_2 nanoparticles used in this work will be described and discussed in detail in the following sections.

4.2 Synthesis and characterization of Eu^{3+}-TiO_2 nanoparticles: Sol-gel method

The synthesis of TiO_2 nanoparticles doped with europium was carried out using a sol-gel method. Three different Eu^{3+}-TiO_2 nanoparticles were synthetized varying the europium concentration from 1, 3 and 5 wt. %.

TiO_2 nanoparticles can be synthetized by different techniques such as: hydrothermal method, solvothermal method, chemical vapor deposition, sonochemical method, electrodeposition, and the sol-gel method [4]. The sol-gel method was used in this work because is a very well-known method that presents various advantages over the other synthesis techniques. The sol-gel method is low-cost and simple, allows to control the textural and surface properties of the final material as well as the doping concentration. Besides, it can be performed at relative low temperatures [18].

Basically, the sol-gel process consists in the formation of a colloidal suspension (sol) by the hydrolysis and polymerization reactions between the precursors. The precursors materials are normally inorganic metal salts or organimetallic compounds such as metal alkoxides. Afterwards, the complete polymerization and loss of the solvent leads to the formation of the suspension into a solid gel phase (gel) [4]. Finally, after drying and a heat treatment the wet gel is transformed into a dense ceramic.

For the TiO_2 nanoparticles, the sol-gel synthesis begins with the hydrolysis of a titanium precursor usually titanium (IV) isopropoxide via an acid catalyzed reaction (Reaction 1), followed by a condensation (Reaction 2 and 3) were polymeric Ti— O —Ti chains are formed [19]. For the formation of crystalline TiO_2 nanoparticles the polymer matrix formed is often heated by several hours under relatively low temperatures (~100 ºC) to evaporate the solvent and obtain the formed TiO_2 products followed by a heating treatment to higher temperatures (>300 ºC) for the formation of a crystalline structure (Figure 4.2). The presence of rutile and/or anatase phases and the crystal sizes will depend on the parameters of the synthesis method and the temperature of calcination.

$$Ti — OR + H_2O \rightarrow Ti — OH + ROH \quad (1)$$

$$Ti — OH + OR — Ti \rightarrow Ti— O —Ti + ROH \quad (2)$$

$$Ti — OH + OH — Ti \rightarrow Ti— O —Ti + H_2O \quad (3)$$

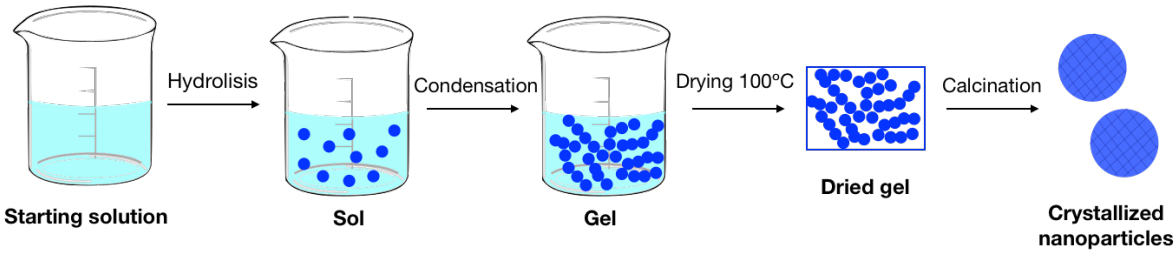

Figure 4.2. Schematic diagram of the sol-gel method for the synthesis of crystalline TiO_2 nanoparticles.

In this work, for the sol-gel synthesis of Eu^{3+}-TiO_2 nanoparticles followed the recipe reported on [20], a solution of 3.4 mL of deionized water, 20 mL of ethanol, 350 µL of 65% HNO_3, and 142.3 mg for the 1 wt. % sample, 435.6 mg for the 3 wt. % or 741.3 mg for the 5 wt. % sample of $Eu(NO_3)_3 \cdot 5H_2O$ was added to a solution of 73 mL of ethanol and 19.3 mL of titanium (IV) isopropoxide under constant stirring. Then, after a gel consistent mixture is formed, the dried gels were heated to 100 ºC for 12 h followed by a calcination at 250, 350 and 450 ºC for 10 h. The nanoparticles calcinated at 450 ºC are the ones used for the next characterizations and experiments because they showed the best crystallinity. Figure 4.3 shows the powder samples obtained after the sol-gel synthesis. The doping causes a slight change of color from bright white to a very pale yellow powder.

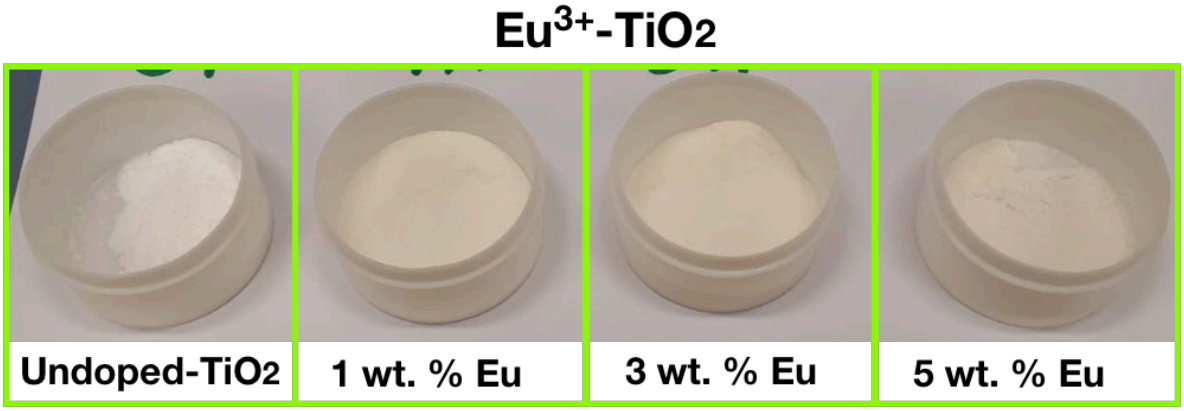

Figure 4.3. Undoped and Eu^{3+}-doped TiO_2 powder samples obtained after the synthesis by the Sol-gel method.

4.2.1 Electron microscopy of Eu^{3+}-TiO_2

The morphology of the synthetized samples was analyzed by scanning electron microscopy

(SEM) and transmission electron microscopy (TEM). Figure 4.4 shows SEM images from undoped-TiO_2 (a), 1 wt.% Eu^{3+}-TiO_2 (b), 3 wt. % Eu^{3+}-TiO_2 (c) and the 5 wt. % Eu^{3+}-TiO_2 (d). Specimens for SEM were prepared by placing a small amount of powder in an agate mortar, few drops of deionized water were added, and mixed with agate pestle. Then one drop of suspension was placed on a polished Al sample holder. Prior to SEM investigation the specimen was coated with 5-nm thick carbon layer. In this specimen preparation no ultrasound was used. The study reveals agglomerated Eu^{3+}-TiO_2 nanoparticles. No significant difference in the morphology of the samples was observed when different amount of europium was added to the samples.

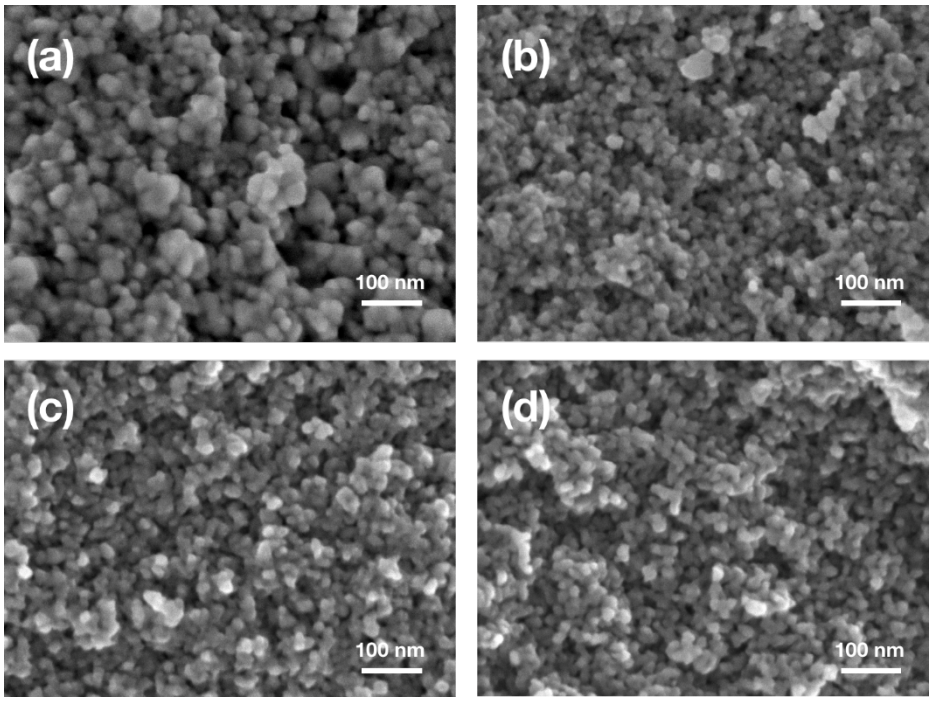

Figure 4.4. SEM images from undoped-TiO_2 (a), 1 wt.% Eu^{3+}-TiO_2 (b), 3 wt. % Eu^{3+}-TiO_2 (c) and 5 wt. % Eu^{3+}-TiO_2 (d).

TEM images from of the 5 wt. % Eu^{3+}-TiO_2 is showed in the Figure 4.5. The sample was sonicated, which significantly reduced agglomeration of Eu^{3+}-TiO_2 nanoparticles. In this case, the smallest aggregates are constituted of two to five crystallites. Nanoparticles have diameters between 15 and 16 nm (Insets Figure 4.5).

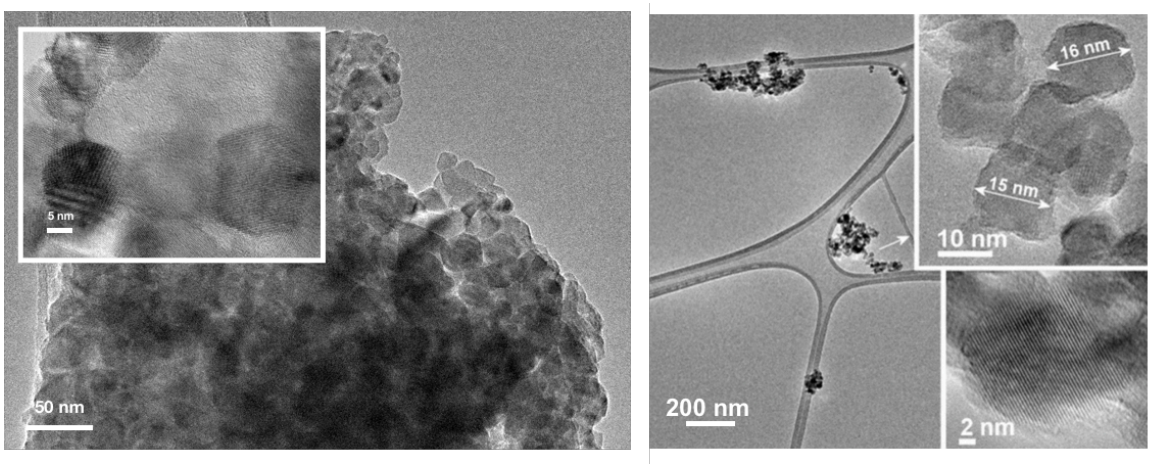

Figure 4.5. Transmission electron microscopy (TEM) of 5 wt. % Eu^{3+}-TiO_2 nanoparticles.

4.2.2 Phase composition of Eu^{3+}-TiO_2

As mentioned before, TiO_2 exist in three different phases, anatase and rutile both with tetragonal crystal system but different lattice parameters and brookite with orthorhombic crystal system (Figure 4.6). The properties of TiO_2 depend critically on its crystal structure, as a bulk material, rutile is the stable phase; however, in solution-phase preparation methods for nanometric TiO_2 the anatase structure is favored [21], this is due to the lower surface energy of anatase over rutile and brookite, as mentioned before, for nanomaterials the surface energy plays an important role in the total energy of the nanoparticles. A combination of rutile and anatase phases may be also present in some nanoparticles depending on the synthesis method and the chemical precursors used. However, anatase nanoparticles with diameters ranging from 6–30 nm are often observed when the synthesis is performed using titanium (IV) isopropoxide and nitric acid, the precursors used during this work [21].

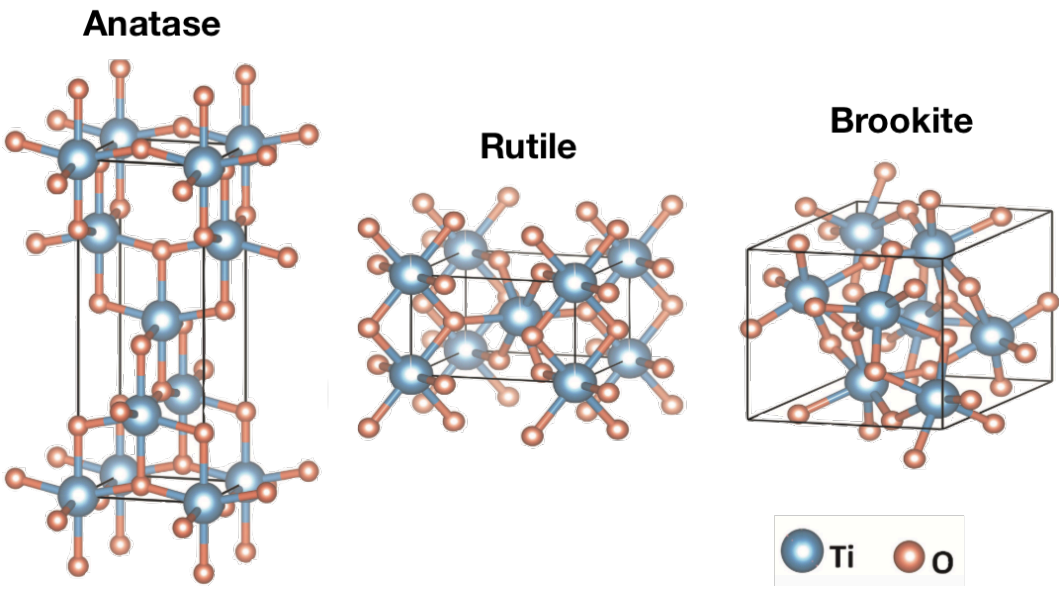

Figure 4.6 Crystal structure of TiO_2. Anatase (tetragonal), rutile (tetragonal) and brookite (orthorhombic). Adapted from Siddiqui et. al [22].

The phase composition of the synthetized nanoparticles was evaluated through X-Ray diffraction analysis (XRD). Figure 4.7 compares the diffractograms of the undoped-TiO_2 and doped Eu^{3+}-TiO_2 (1, 3 and 5 wt. %) samples. The XRD pattern of the undoped TiO_2 exhibits diffraction peaks of anatase and rutile TiO_2 (matching ICCD cards no. 86-1157 and 87-0710, respectively). The XRD patterns of all europium doped TiO_2 samples match to anatase TiO_2 and the rutile phase is no longer observed in the doped samples. These results indicate that the presence of europium ions in the synthesis of TiO_2 inhibits the transformation of anatase into the rutile phase. This phenomenon is explained by the substitution of titanium ions by europium ions within the structural lattice of TiO_2. Europium ions inhibit the formation of the rutile phase through the formation of a Ti–O–Eu bond that locks the Ti–O species at the interface with the TiO_2 domains preventing the nucleation that is necessary for anatase transformation to rutile [23]. The suppression of the rutile phase during the TiO_2 nanoparticle synthesis and the stabilization of anatase phase achieved by lanthanide doping was already observed and reported by other authors [20,23,24].

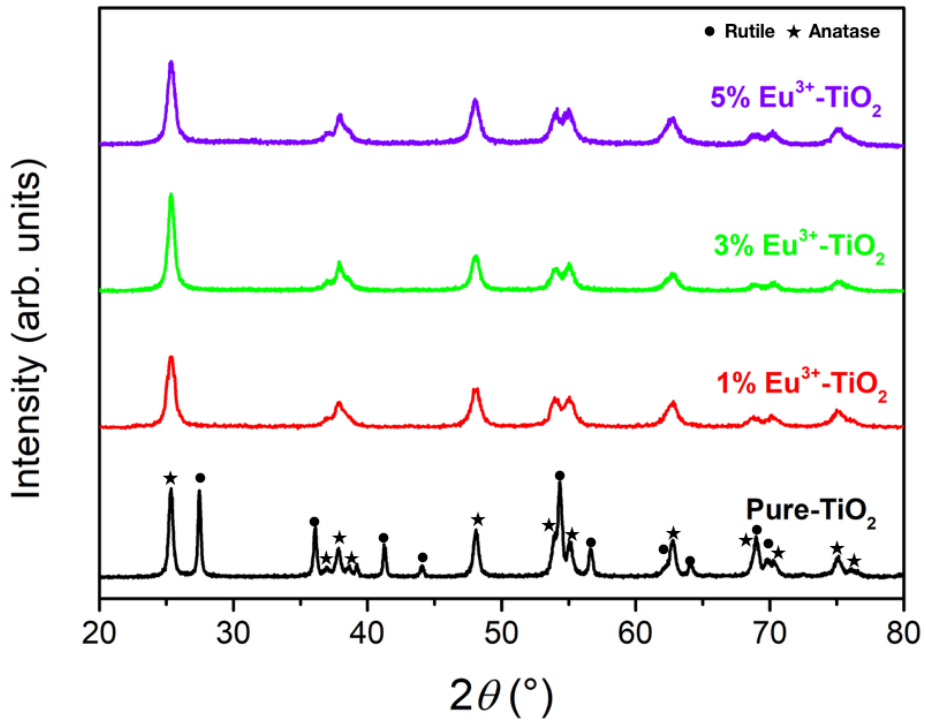

Figure 4.7. Powder XRD patterns of undoped TiO_2 sample and samples doped with 1, 3 and 5 wt. % of Eu^{3+}. Rutile and anatase peaks are marked as • and ★ respectively.

The ionic radius of the Eu^{3+} is 103.6 pm and for the case of Ti^{4+} is 68 pm both in octahedral coordination [20]. Depending on the doping concentration europium ions can be located at different sites in the TiO_2 anatase lattice: they can take the place of Ti^{4+} and be substitutional dopants, they can occupy interstitial sites, and if the concentration of Eu^{3+} is high some segregations of europium ions can form Eu_2O_3 in the nanostructure surface. When the europium ions are accommodated as substitutional or interstitial dopants, there will be an unbalance of charges that will be compensated with the formation of oxygen vacancies mainly, however it is also reported the formation of Ti^{3+} and incorporation of Ti^{4+} in interstitial positions. The defects of under-coordinated Ti^{3+} can be created after the removal of oxygen atoms. The oxygen vacancies can create lone pair of electrons to two neighboring Ti^{4+}, and then, these electrons will reduce Ti^{4+} into Ti^{3+} [23]. The oxygen vacancies and formation of Ti^{3+} and interstitial Ti^{4+} are defects induced in the TiO_2 lattice that can be detected in XRD as widening of the peaks in the diffraction pattern, in the Figure 4.7 can be observed the widening from the anatase peak at 25.3º after doping TiO_2 with europium ions.

4.2.3 Chemical composition of Eu^{3+}-TiO_2

The chemical composition of Eu^{3+}-TiO_2 nanoparticles was investigated through X-Ray photoelectron spectroscopy (XPS). The survey spectrum from the 5 wt. % Eu^{3+}-TiO_2 sample is showed in the Figure 4.8. The samples are composed of titanium, oxygen and europium atoms, some carbon atoms were also observed in the spectrum, this is associated with adventitious carbon contamination from ambient exposure and carbon atoms from the reactant titanium (IV) isopropoxide. The relative concentration of europium incorporated in the samples was 1.7, 3.5 and 5.0 at. %, respectively for the samples prepared using 1 wt. %, 3 wt. % and 5 wt. % of $Eu(NO_3)_3$.

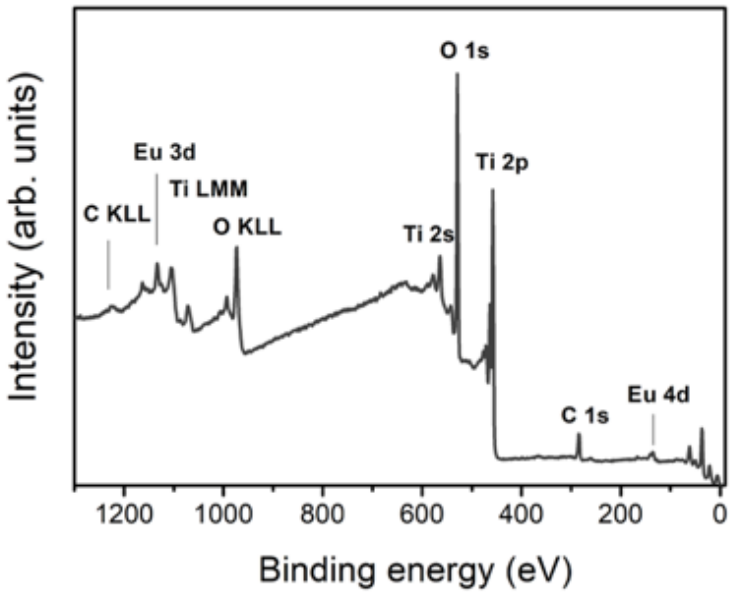

Figure 4.8. X-ray photoelectron survey spectrum (XPS) of 5 wt. % Eu^{3+}-TiO_2.

The oxidation state of europium can be investigated through XPS. The low concentration of europium in the 1 and 3 wt. % samples produce very imprecise the analysis of the 4d core level spectrum of these samples. Figure 4.9 shows the analysis of the Eu4d core level spectrum for the 5 wt.% sample, the spectrum is composed of two doublet components (doublets are generated by the spin-orbit splitting) one for Eu^{2+} and one for Eu^{3+}. In the 5 wt.% sample spectrum, the low binding energy doublet (purple color) at 128.4 and 133.5 eV corresponds to Eu $4d_{5/2}$ and Eu $4d_{3/2}$ respectively, this doublet is assigned to Eu^{2+} [25]. The other doublet (green color) at 135.9 and 141.1 eV corresponds to Eu $4d_{5/2}$ and Eu $4d_{3/2}$ respectively, this doublet is assigned to Eu^{3+} [25], 62% of the europium in the sample has oxidation state Eu^{3+}.

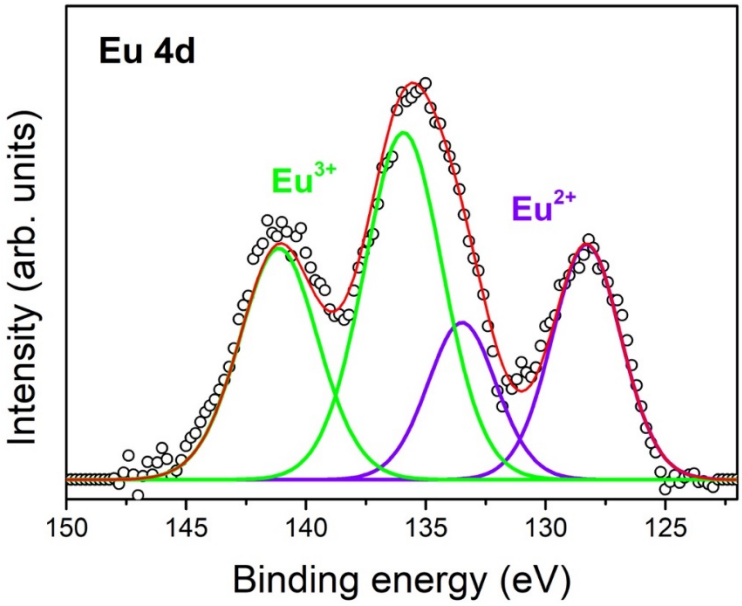

Figure 4.9. Curve-fitting XPS analysis of high resolution Eu4d spectrum from 5 wt. % Eu^{3+}-doped TiO_2. The green doublet is assigned to titanium with oxidation state Eu^{3+} and the purple doublet to Eu^{2+}.

The oxidation state of titanium in the samples is investigated through XPS. The analysis of the Ti2p spectrum of the undoped-TiO_2 sample is showed in the Figure 4.10a, and the same analysis for the 5 wt. % Eu-doped TiO_2 sample is showed in the Figure 4.10b. The spectrum of the undoped sample is composed of one doublet component with binding energies at 459.1 and 464.8 eV assigned to Ti^{4+}. The spectrum of the 5 wt.% Eu-doped sample is composed of two doublets, the first with binding energies of 459.1 and 464.8 eV assigned to Ti^{4+} (blue doublet) and the second with 458.0 and 463.7 eV of binding energies assigned to Ti^{3+} (green doublet). The presence of titanium with oxidation state Ti^{3+} in the Eu-doped sample indicates that doping TiO_2 with Eu^{3+} ions induces the formation of Ti^{3+} defects in TiO_2. As explained before, the oxygen vacancies can create lone pair of electrons to two neighboring Ti^{4+}, and then, these electrons will reduce Ti^{4+} into Ti^{3+}.

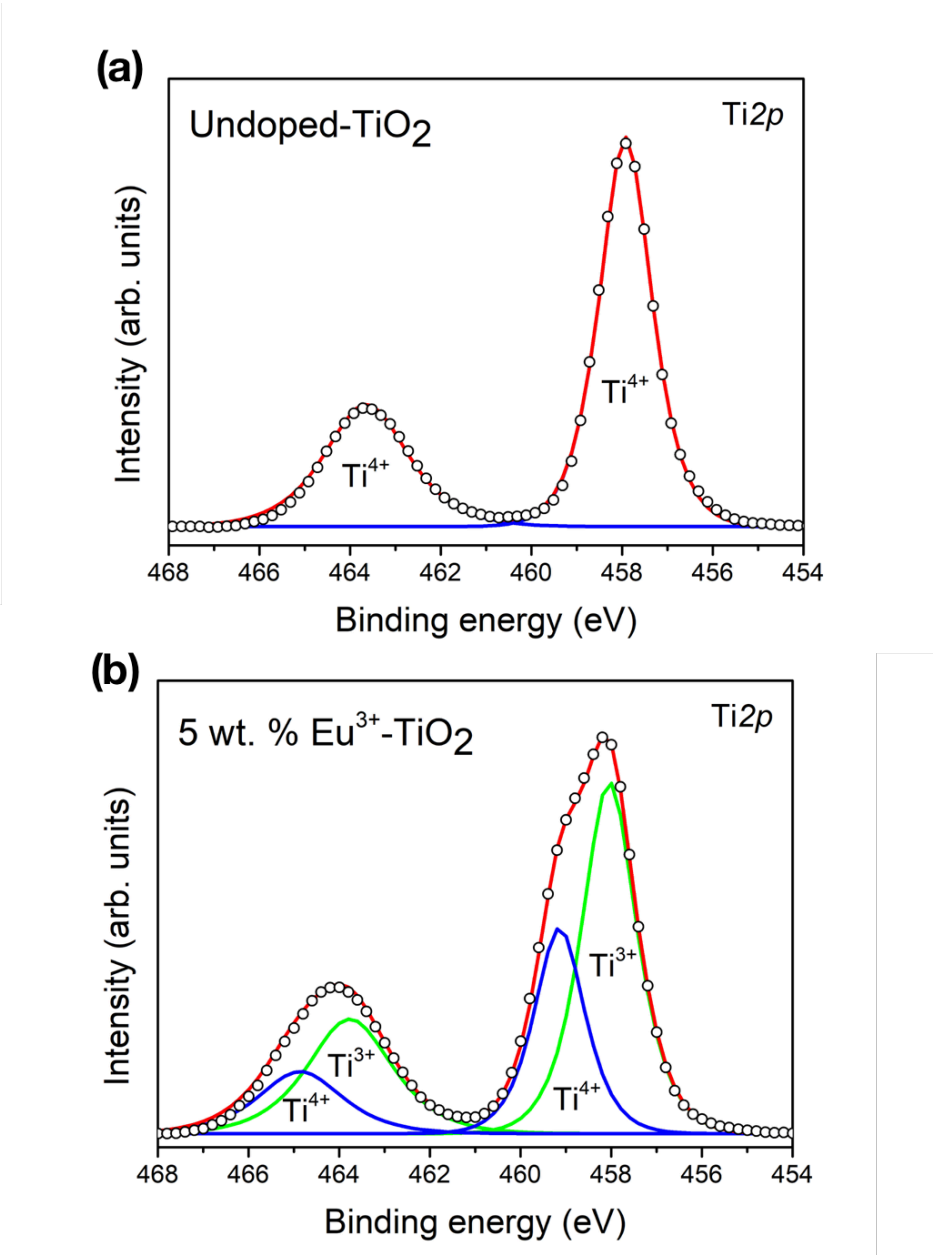

Figure 4.10. Curve-fitting XPS analysis of high resolution Ti2p spectrum from undoped-TiO_2 (a) and 5 wt.% Eu^{3+}-doped TiO_2 (b). The green doublet is assigned to titanium with oxidation state Ti^{3+} and the blue doublet to Ti^{4+}.

4.3 Photoluminescence of TiO_2 anatase

The photoluminescence of semiconductors such as TiO_2 represent the radiative recombination of photogenerated carriers, in another words, photoluminescence in semiconductors quantifies the recombination efficiency of photogenerated charges [26].

The defects in the TiO_2 nanoparticles can be characterized by measuring their room-temperature photoluminescence spectrum. However, it is necessary to understand first the band structure of TiO_2.

The density of states (DOS) and band structure of anatase obtained by Zhang et al. using DFT calculations is showed in the Figure 4.11 [27]. The valence band consist predominantly of O2p states and a few Ti3d states, indicating the strong p–d hybridizations between O 2p and Ti 3d states, which form bonding states in the valence band region. The hybridizations broaden the valence bands and promote the transfer of photogenerated holes. The conduction band is mainly composed by Ti 3d states, mixed with a few O 2p and Ti 3p states. The energy band structure of anatase obtained is showed in the left part of Figure 4.11, the Fermi level is shown by a dashed line and it is set as zero. An indirect band gap of 2.13 eV was observed between the conduction band minimum (CBM) at G point and the valence band maximum (VBM) at B point along the ZM direction. This value is less than the experimental value (3.2 eV) due to well-known shortcoming of the approximation functions used in DFT calculations, the underestimation of the gap width is due to the unknown exact potential of Kohn-Sham density-functional theory, because of derivative discontinuities of the exchange-correlation energy. The center of the gap, however, is predicted exactly by the Kohn- Sham band structure.

Rutile and Brookite phases present a direct band gap, the indirect band gap of anatase results in the excited electrons not being able to recombine directly with holes, resulting in an increase of the photogenerated electron–hole lifetime in anatase relative to that of rutile and brookite.

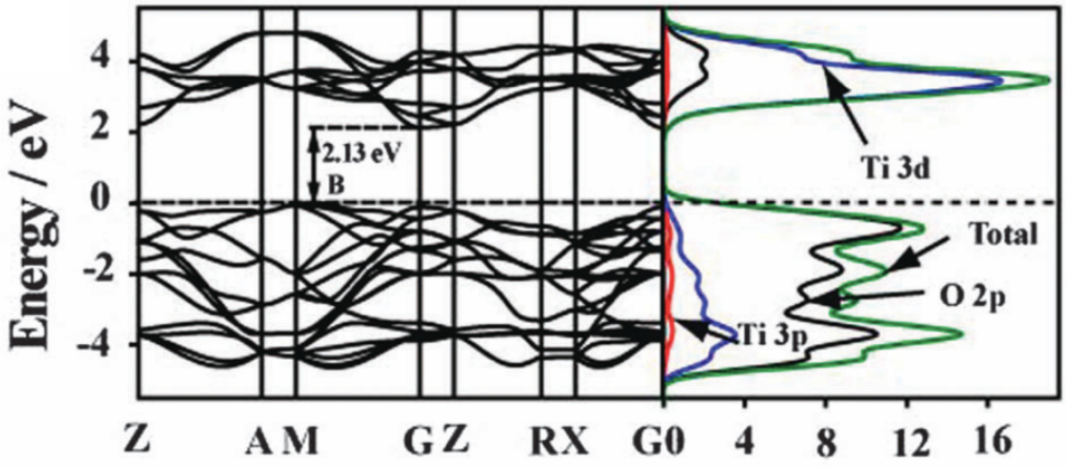

Figure 4.11. Band structure and density of states (DOS) obtained by DFT calculations of anatase TiO_2. Adapted from reference [27].

Crystalline materials may contain many defects; a point defect can be an atom missing from a site in the crystal (a vacancy) or an impurity atom that occupies either a normal lattice site (a substitutional impurity) or a hole in the lattice between atoms (an interstitial impurity). As mentioned before, doping TiO_2 with Eu^{3+} ions generate point defects in the TiO_2 lattice, the formation of defects in TiO_2 leads to the formation of new states between the valence and the conduction bands [28]. For example, in oxygen vacancies, the place of O^{2-} anion in regular lattice is occupied by one or two free electrons in the defective TiO_2, minimizing the energy cost for the vacancy formation. The free electrons in the vacancy states form donor energy levels just below the conduction band. The donor energy levels that originate from oxygen vacancies are reported to be 0.75–1.2 eV below conduction band energy [29]. The new states in the bang gap of TiO_2 work as electron and holes traps, in certain cases, the recombination of electron-holes in these states generates radiative emissions that can be observed in a PL spectrum.

Figure 4.12a shows the photoluminescence spectrum of the undoped sample taken under an excitation of 350 nm. The photoluminescence spectrum of TiO_2 anatase is characterized by a band centered at the range of 490-540 nm, variations can be observed in the band center position because it is strongly dependent different factors including quality of the sample, the defects and crystallinity, as well as on the atmosphere used during the photoluminescence measurement and on the excitation conditions [26]. In our case, the photoluminescence band is composed of two defects contribution bands, the first centered at 560 nm named as red-band and another at 470 nm named as green-band being the red-band the one with larger contribution to the emission intensity. The red band is associated with electron traps of under-coordinated Ti^{3+} defects and the green band is generated from oxygen vacancies defects on anatase TiO_2 [30].

The energy needed for the creation of oxygen vacancies, Ti^{3+} and Ti^{4+} interstitials in TiO_2 was reported by Olson et. al [31]. For oxygen vacancies formation an energy of 24.1 eV is required, -40.5 eV for Ti^{3+} defects and -77.23 eV for Ti^{4+} interstitial. Consequently, under-coordinated Ti^{3+} may form in higher probability than oxygen vacancies during the crystallization of anatase crystal TiO_2, this occurs only in anatase nanoparticles that are annealed at low temperatures because the under-coordinates Ti^{3+} defects have low thermal stability and can be annealed out and transformed to into stable oxygen vacancies on anatase TiO_2 at high annealing temperatures (800–900 ºC) [30]. This may explain the dominancy of the red-band emission associated with electron traps of Ti^{3+} defects in the photoluminescence spectrum of the undoped-TiO_2 anatase sample that were annealed at low temperature (450 ºC).

The photoluminescence mechanism for undoped-TiO_2 anatase is proposed in Figure 4.12b. First, electrons for the valence band are excited to the conduction band. After this, some electrons can be captured by electron traps associated to under-coordinated Ti^{3+} ions, then,

these trapped electrons are recombined with the holes in the valence band under a radiative recombination which generates the red-band at 560 nm. On the other hand, a radiative recombination between free electrons with holes trapped around oxygen vacancies are associated to the green-band centered at 470 nm. The low-intensity peak at 820 nm is associated with defects in the rutile phase [30].

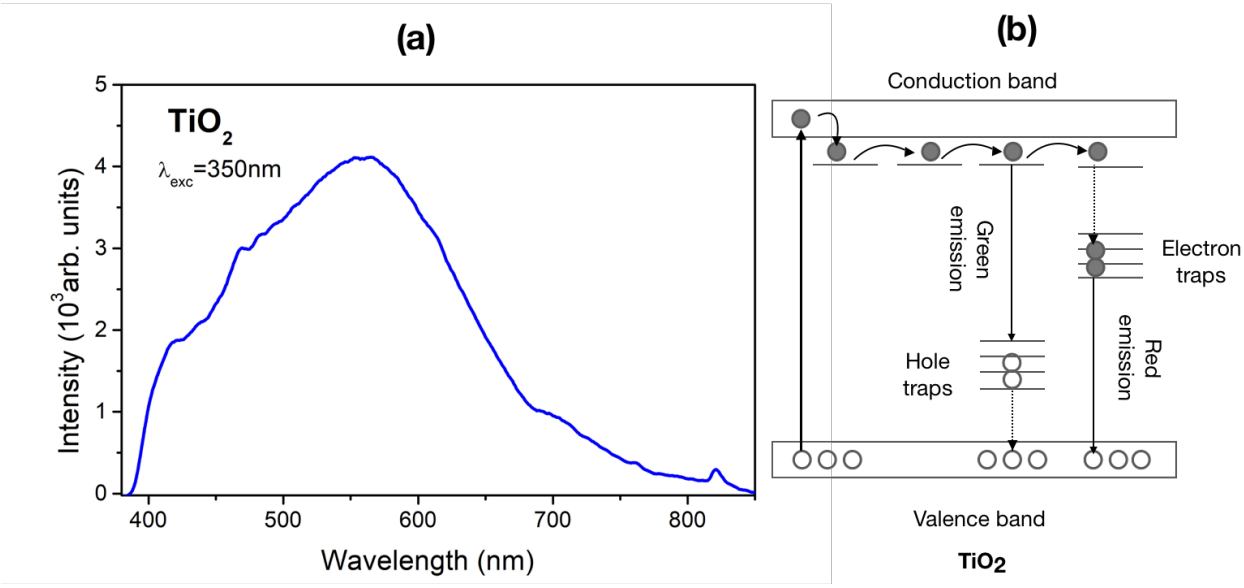

Figure 4.12. (a) Photoluminescence spectrum of undoped TiO_2 sample. The spectrum was acquired under excitation of 350 nm. (b) Mechanism for the photoluminescence of pure-TiO_2 sample. (b) Adapted from reference [30].

In the Figure 4.13 the photoluminescence spectra of undoped-TiO_2 and 5 wt. % Eu^{3+}-TiO_2 are plotted together for comparison. The red line indicates the Eu^{3+}-TiO_2 emission spectrum, the left part of the spectrum shows the wide photoluminescence of TiO_2 followed by the narrower and more intense emission bands of Eu^{3+}. The emission bands of Eu^{3+} will be explained and discussed in the following section. However, if we focus on the TiO_2 emission part we can notice that after doping TiO_2 with europium ions the photoluminescence intensity of the green-band is increased. As mentioned before, the green-band emission is related to oxygen vacancies in the TiO_2 lattice, the increased emission intensity of the green-band in the Eu^{3+}-TiO_2 may indicate that doping TiO_2 with europium ions induces the creation of defects as oxygen vacancies in TiO_2.

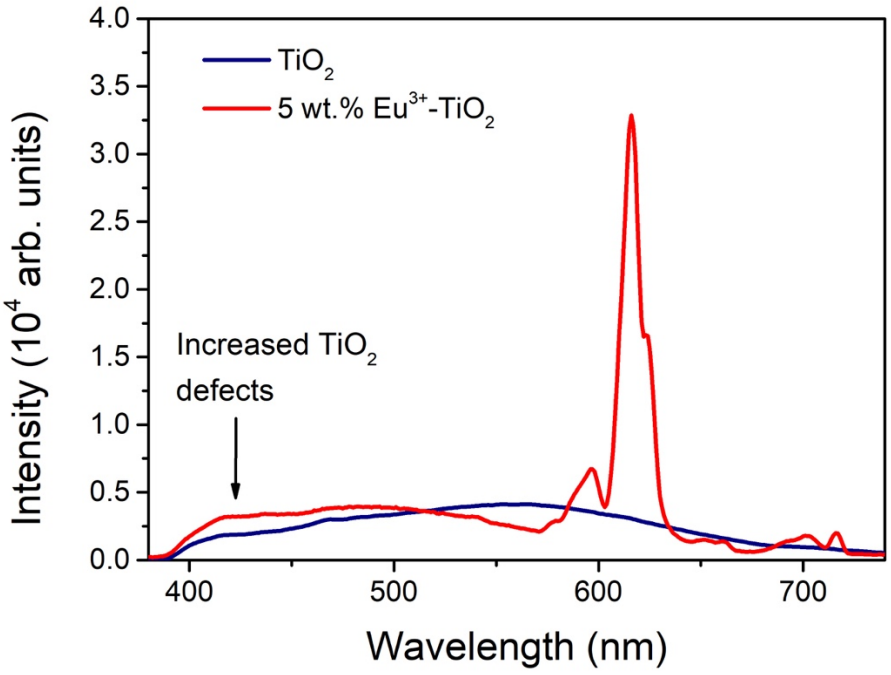

Figure 4.13. Comparison of photoluminescence spectra of undoped-TiO_2 and Eu^{3+}-doped TiO_2. The increased defects in TiO_2 when it is doped with europium ions can be observed by an increase on the emission intensity of the green-band emission of TiO_2 associated to oxygen vacancies.

4.4 Photoluminescence of Eu^{3+}-TiO_2 nanoparticles

Eu^{3+} has 63 electrons (Figure 4.14). Its electronic configuration can be written as $[Xe]4f^7 6s^2$. Electronic transitions in the *4f* shell of Eu atom are investigated in this work to develop a luminescence nanothermometer. The *4f* shell is shielded from the environment by the closed $5s^2$ and $5p^6$ outer shells. The seven electrons in the *4f* shell can be arranged in 3003 different ways into the seven *4f* orbitals due to the degeneracy of states. The degeneracy of the $4f^7$ configuration is generated due to perturbations acting on the Eu^{3+} ion: electron repulsion, spin-orbit coupling, the crystal-field perturbation and the Zeeman effect (Figure 4.15). The electron repulsion is generated by the electrostatic interaction between the electrons in the *4f* shell. The spin-orbit coupling results from the interaction between the spin magnetic moment of the electron and the magnetic field created by the movement of the electron around the nucleus. The crystal-field effect is caused by the interactions between the *4f* electrons and the electrons of the matrix. The Zeeman effect is the splitting of the energy levels by an external magnetic field [32].

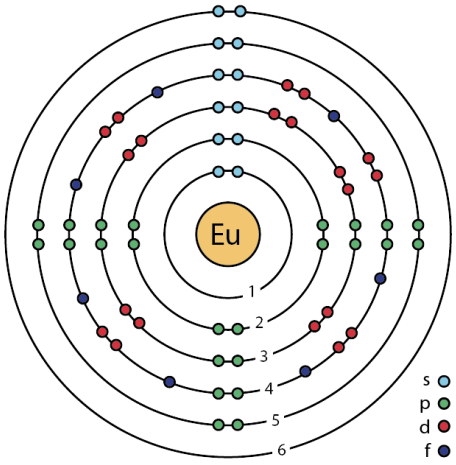

Figure 4.14. Schematic representation of the europium atom.

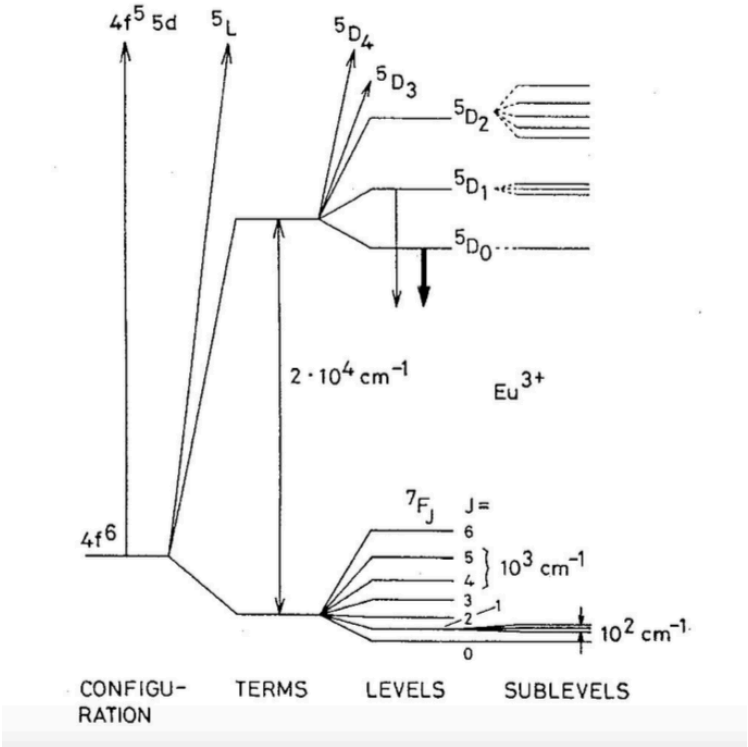

Figure 4.15. Energy diagram of the degeneracy of states in Eu^{3+} ($4f^7$). 2×10^4 cm^{-1} equals 500 nm or 2.48 eV. At room temperature (25 °C), k_BT (k_B, Boltzmann constant), is, 25.7 meV or 200 cm−1.

The photoluminescence emission spectrum of europium appears in the visible range of the electromagnetic spectrum from 500 to 720 nm of wavelength. Europium shows different narrow and defined emission bands related to electronic transitions in the partially filled *4f*

levels. Nevertheless, the exact position and intensity of the bands will depend on the matrix hosting the europium ions as well as the excitation source. Eu^{3+} compounds show an intense photoluminescence, due to the $^5D_0 \rightarrow {}^7F_J$ transitions (J = 0 – 6) from the $^5D_0$ excited state to the J levels of the ground term ^7F.

Intraconfigurational electric dipole transitions (ED) (e.g., *s-s*, *p-p*, *d-d*, or *f-f* transitions) are forbidden by the Laporte selection rule, which says that states with even parity can be connected by ED transitions only with states of odd parity, and odd states only with even ones. For transitions within the $4f$ shell, ED transitions are forbidden, but allowed for magnetic dipole (MD) or electric quadrupole (EQ) radiation. The term forbidden means a transition may occur in principle, but with low probability. Most of the transitions observed in the luminescence spectrum of lanthanides are induced ED transitions (*4f-f* transitions). The observation of ED transitions in lanthanide compounds is explained by a distortion of the electronic motion by crystalline fields in solids, Laport selection rules, valid for free atoms, are no longer valid for lanthanides ions embedded in a medium. The Judd-Olfelt theory describes the intensities of lanthanide and actinide transitions in solids and solutions. The selection rules for ED and MD *f-f* transitions are summarized in Table 4.1 [33].

Induced electric dipole transitions (ED)	**Magnetic dipole transitions (MD)**
$\boldsymbol{\lvert\Delta S\rvert = 0}$	$\Delta S = 0$
$\boldsymbol{\lvert\Delta L\rvert \leq 6}$	$\Delta L = 0$
$\boldsymbol{\lvert\Delta J\rvert \leq 6}$ $\boldsymbol{\lvert\Delta J\rvert = 2, 4, 6\ if\ J = 0\ or\ J' = 0}$	$\Delta J = 0, \pm 1, 0 \leftrightarrow 0\ is\ forbidden$

Table 4.1. Selection rules for intraconfigurational f-f transitions in the Judd-Ofelt Theory.

The $^5D_0 \rightarrow {}^7F_0$ transition is strictly forbidden according to the standard Judd-Ofelt theory. The occurrence of this transition is a well-known example of the breakdown of the selection rules of the Judd-Ofelt theory. The explanation for this transition being observed in Eu emission spectra is explained by *J-mixing* due to the crystal-field perturbation causing mixing of the wavefunctions of terms with different J values. In most Eu^{3+} spectra, the $^5D_0 \rightarrow {}^7F_0$ transition is very weak. The $^5D_0 \rightarrow {}^7F_1$ transition is an allowed magnetic dipole (MD) transition. The $^5D_0 \rightarrow {}^7F_2$ transition is a so-called "hypersensitive transition", which means that its intensity is much more influenced by the local symmetry of the Eu^{3+} ion and the nature of the ligands. The $^5D_0 \rightarrow {}^7F_2$ transition generally dominates the europium emission spectrum. The high intensity of this transition is often attributed to the low symmetry of the Eu^{3+} ions. The $^5D_0 \rightarrow {}^7F_3$ transition is in general very weak because it is forbidden according to the Judd-

Ofelt theory, and this transition can only gain intensity via *J-mixing*. The $^5D_0 \rightarrow {}^7F_4$ is an ED allowed transition, one must be careful with the interpretation of its intensity because appears in a spectral region in which most of spectrometers have a low sensitivity. The $^5D_0 \rightarrow {}^7F_5$ and $^5D_0 \rightarrow {}^7F_6$ transitions will not be discussed in this work. Table 4.2 shows an overview from the transitions observed on Eu^{3+}-compounds.

Transition	Dipole character	Wavelength range (nm)
$^5D_0 \rightarrow {}^7F_0$	ED	570–585
$^5D_0 \rightarrow {}^7F_1$	MD	585–600
$^5D_0 \rightarrow {}^7F_2$	ED	610–630
$^5D_0 \rightarrow {}^7F_3$	ED	640–660
$^5D_0 \rightarrow {}^7F_4$	ED	680–710
$^5D_0 \rightarrow {}^7F_5$	ED	740-770
$^5D_0 \rightarrow {}^7F_6$	ED	810-840

Table 4.2. Transitions observed on Eu^{3+}-compounds.

The sample synthesized with 5 wt. % of Eu exhibit the best signal to noise luminescence, therefore, we report only the results of photoluminescence obtained studying this sample. The luminescence spectrum of the Eu^{3+}-TiO_2 nanoparticles under 395 nm excitation at room temperature is shown in Figure 4.16a. Emission bands centered at 577, 590, 612, 652 and 700 nm can be identified and respectively assigned to the $^5D_0 \rightarrow {}^7F_J$ (J = 0, 1, 2, 3, 4) electronic transitions of the Eu^{3+} ion. The Figure 4.16b shows an energy diagram describing the Eu^{3+} transitions involved in the emission spectrum of 5 wt. % Eu^{3+}-TiO_2. First, there is a resonant excitation of the $^7F_0 \rightarrow {}^5L_6$ transition followed by a non-radiative internal conversion decay from $^5L_6$ to $^5D_{0,1}$ level, finally, subsequent radiative emissions in the visible range from 577 to 700 nm take place by the relaxation to the ^7F_J levels. The transitions to the $^7F_5$ and $^7F_6$ are rarely observed, because they are outside the wavelength range of the detectors of spectrofluorometers.

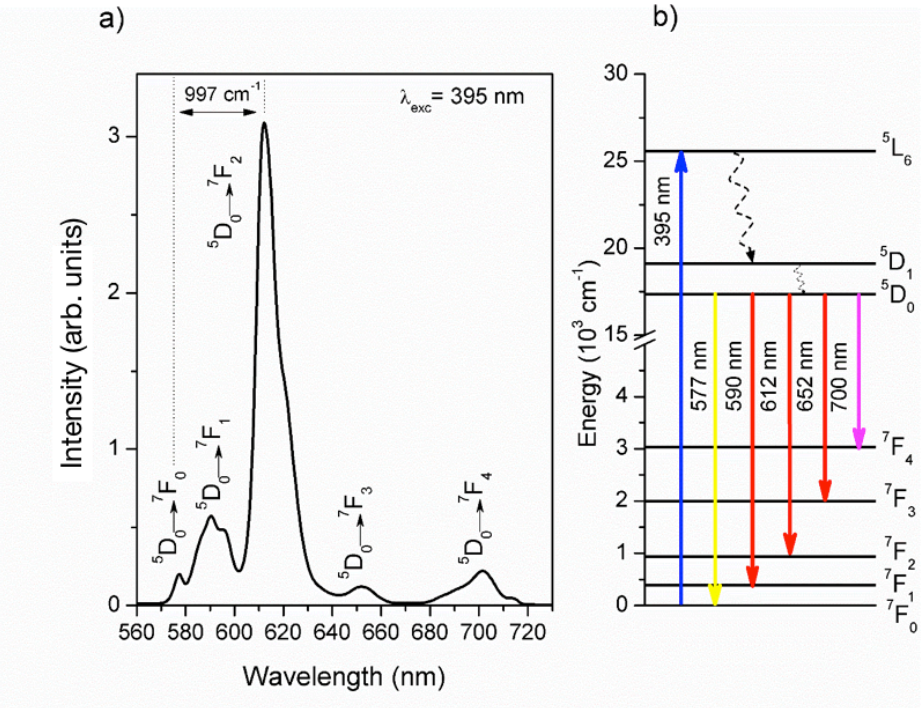

Figure 4.16. (a) Visible photoluminescence spectrum of 5 wt. % Eu^{3+}-TiO_2 under 395 nm excitation. (b) Simplified energy level diagram of Eu^{3+} ion illustrating the excitation, radiative and non-radiative transitions.

4.5 Temperature dependence photoluminescence of Eu^{3+}-TiO_2

Pursuing the objective of this part of the thesis, that is the development of a luminescent nanothermometer based in Eu^{3+}-TiO_2 nanoparticles, the excitation and emission spectra of Eu^{3+}-TiO_2 was investigated recording the spectra at different temperatures, the change in the luminescence intensity of the excitation and emission bands as well as the development of a calibration curve, needed for developing a nanothermometer, are discussed in the following sections.

4.5.1 Excitation spectra of Eu^{3+}-TiO_2

The excitation spectra for the 5 wt. % Eu^{3+}-TiO_2 nanoparticles in the range from 565 to 630 nm were recorded at two different temperatures (288 and 323 K), monitoring the $^5D_0 \rightarrow {}^7F_4$ transition (monitored wavelength λ_{mon} = 700 nm) and it is showed in Figure 4.17a. The spectra clearly show the Eu^{3+} absorption structure with bands centered at 577, 586 and 610 nm due to the $^7F_0 \rightarrow {}^5D_0$, $^7F_1 \rightarrow {}^5D_0$ and $^7F_2 \rightarrow {}^5D_0$ transitions, respectively. It can be observed the variation in the intensity of the excitation spectrum with temperature, when the sample

temperature increases from 288 to 323 K, the intensity at 610 nm increases by a factor ~1.4 while the intensity of the excitation bands at 586 nm and 577 nm decreases by a factor ~0.9 and 0.8, respectively. The excitation and radiative relaxation processes are illustrated in the diagram showed in Figure 4.17b. The different response to temperature changes of the excitation bands can be associated to the thermal coupling of the ^7F_J levels.

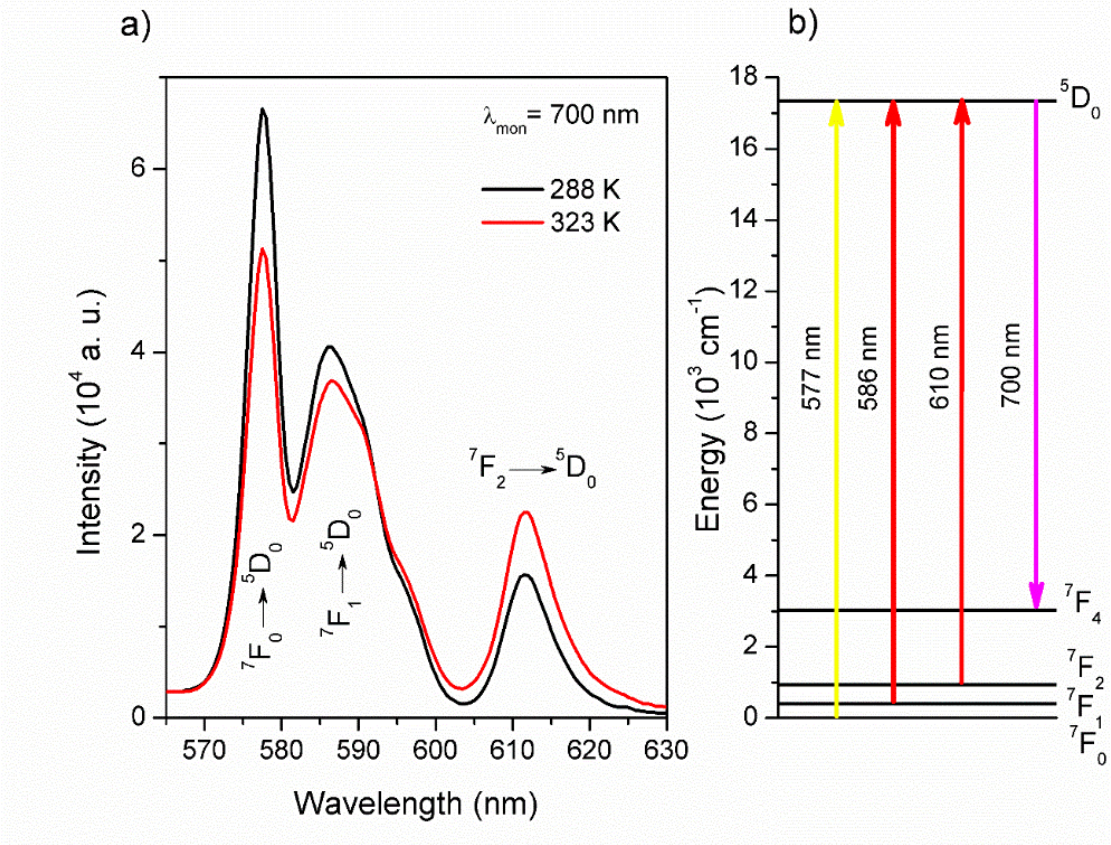

Figure 4.17. (a) Excitation spectra of Eu^{3+} monitoring the emission of the $^5D_0 \rightarrow {}^7F_4$ transition (λ_{mon}= 700 nm). The spectra were acquired at 288 and 323 K. (b) Simplified energy level diagram of Eu^{3+} ion illustrating the excitation and radiative transitions.

4.5.2 Luminescence intensity ratio technique

As mentioned before, the luminescence intensity of the emission bands in europium ions depends critically on the temperature due to the thermally coupled *4f* energy levels, it is through this dependency that a thermometer based on the luminescence of Eu ions can be created. It is important to say that the measure of the photoluminescence intensity of only one transition band does not permit the production of a reliable and reproducible temperature sensor, due to the dependency of the intensity with the sensor concentration and the

characteristics of the detectors. To avoid this problem, the intensity ratio technique uses the luminescence intensity ratio between two different transitions that are thermally coupled to calculate the absolute temperature. Two energy levels are considered thermally coupled when the energy gap between them is less than 2000 cm^{-1} [34]. For example, the energy gap between the $^7F_0$ and $^7F_2$ levels in europium is 997 cm^{-1}. This technique has the following advantages: high spatial resolution, fast response time and wide operating temperature range [35]. The luminescence intensity ratio or radiometric thermal parameter (*R*) is related to the Equation 4.1.

$$R = \frac{Intensity_1}{Intensity_2} = Ae^{-\left(\frac{\Delta E}{K_B T}\right)} \quad (4.1)$$

where, *A* is the calibration factor, *ΔE* is the energy difference between the levels, k_B is the Boltzmann constant and *T* is the absolute temperature.

From the radiometric thermal parameter (*R*) the variation in the emission intensity with small changes in temperature can be obtained using the Equation 4.2. This parameter is known as absolute sensitivity (*Sa*) and it is the most reported figure of merit in optical thermometry defined as the rate of change of *R* related to temperature, *T* [36].

$$S_a = \left|\frac{dR}{dT}\right| \quad (4.2)$$

To obtain comparable sensitivities of different nanothermometers the sensitivity is normally reported as relative sensitivity (S_r) as showed in Equation 4.3.

$$S_r = \frac{1}{R}\left|\frac{dR}{dT}\right| = \frac{\Delta E}{K_B T^2} \quad (4.3)$$

where ΔE (cm^{-1}), *kB* (cm^{-1} per K), and *T* (K).

Equation 4.3 indicates that for pairs of energy levels with larger energy differences increases the relative thermal sensitivity. Nevertheless, it is important to avoid energy levels that are energetically too separate, because in this case thermal population will not occur. The measurement of very low intensity signals can be a problem increasing the costs of the detection system or it can be impracticable.

4.5.3 Temperature dependent emission spectra of Eu^{3+}-TiO_2

In the Eu^{3+} ion because the $^7F_{0,1,2}$ levels are thermally coupled (they have a *ΔE* of ~900 cm^{-1}), the radiometric measurement of the intensity of the transitions from these levels to the $^5D_0$

level allows the construction of an optical nanothermometer that involves only visible optical transitions in the Eu^{3+}-TiO_2 nanoparticles. Therefore, in this part of the work, the luminescence from the $^5D_0 \rightarrow {}^7F_4$ transition with resonant excitation at the $^7F_0 \rightarrow {}^5D_0$ and $^7F_2 \rightarrow {}^5D_0$ transitions are studied.

The temperature influence in the photoluminescence response for the $^7F_0 \rightarrow {}^5D_0$ transition of the Eu^{3+}-TiO_2 nanoparticles is showed in the Figure 4.18a. The 576 nm resonant excitation of the $^7F_0 \rightarrow {}^5D_0$ transition is followed by radiative decay from $^5D_0$ to the $^7F_4$ energy level. The energy levels and selected transitions diagram can be observed in Figure 4.18b. The inset in Figure 4.18a shows the integrated intensity of the $^5D_0 \rightarrow {}^7F_4$ transition as a temperature function, showing a decrease of approximately 13% when temperature increases from 288 to 323 K.

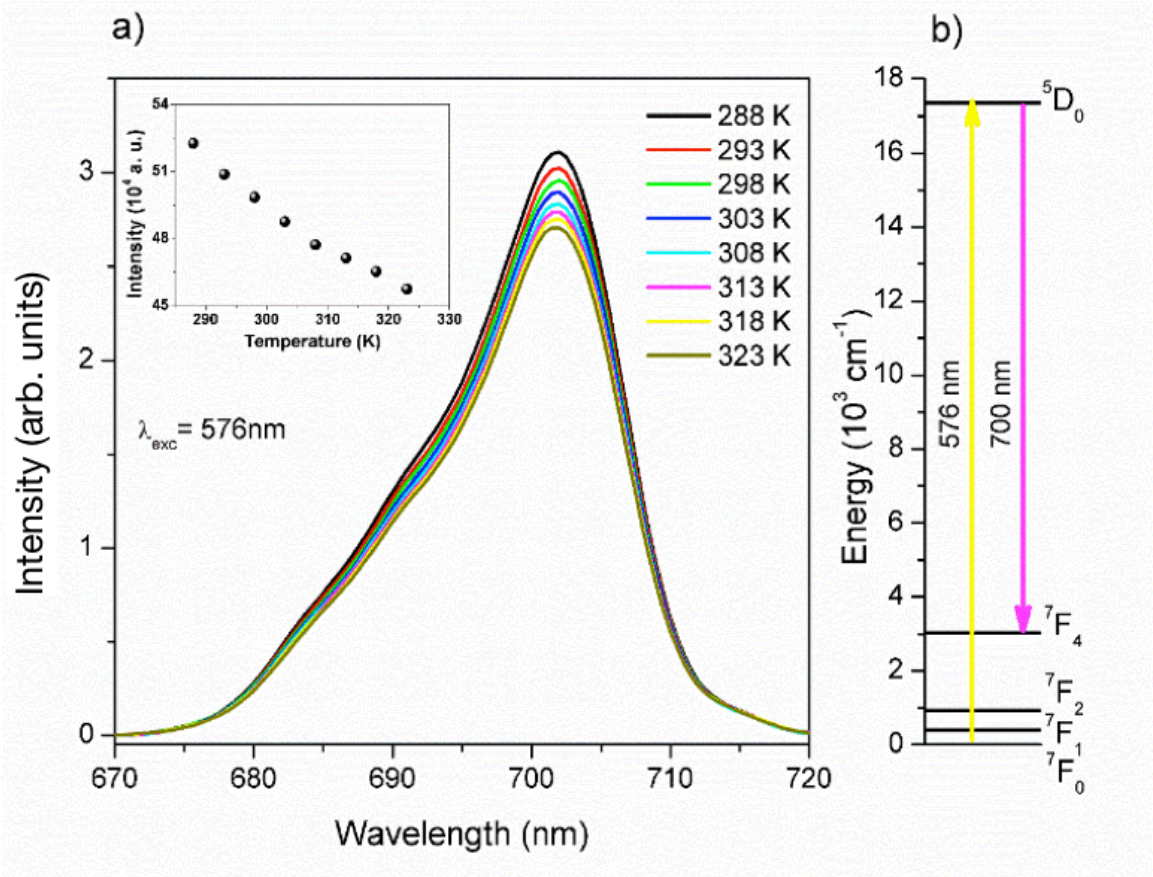

Figure 4.18. (a) Photoluminescence temperature dependence for the emission of the $^5D_0 \rightarrow {}^7F_4$ transition with excitation of $^7F_0 \rightarrow {}^5D_0$ at 576 nm. The inset shows the integrated intensity of the emission band. (b) Simplified energy level diagram of Eu^{3+} ion illustrating the excitation and radiative transitions.

On the other hand, the temperature influence in the photoluminescence response for the $^7F_2 \rightarrow {}^5D_0$ transition of the Eu^{3+}-TiO_2 nanoparticles is shown in the Figure 4.19a, the 610 nm resonant excitation of the $^7F_2 \rightarrow {}^5D_0$ transition is also followed by radiative decay from the level $^5D_0$ to the $^7F_4$ energy level, in the same way as previously, the energy level diagram of the transitions is showed in the Figure 4.19b. The inset in the Figure 4.19a shows the integrated intensity of the $^5D_0 \rightarrow {}^7F_4$ transition as a temperature function, showing an increase at approximately 52% when temperature increases from 288 to 323 K. The opposing change in the emission intensities for increasing temperature can be explained taking in account the thermal depopulation of the $^7F_0$ level, causing the population of the $^7F_2$ level [37].

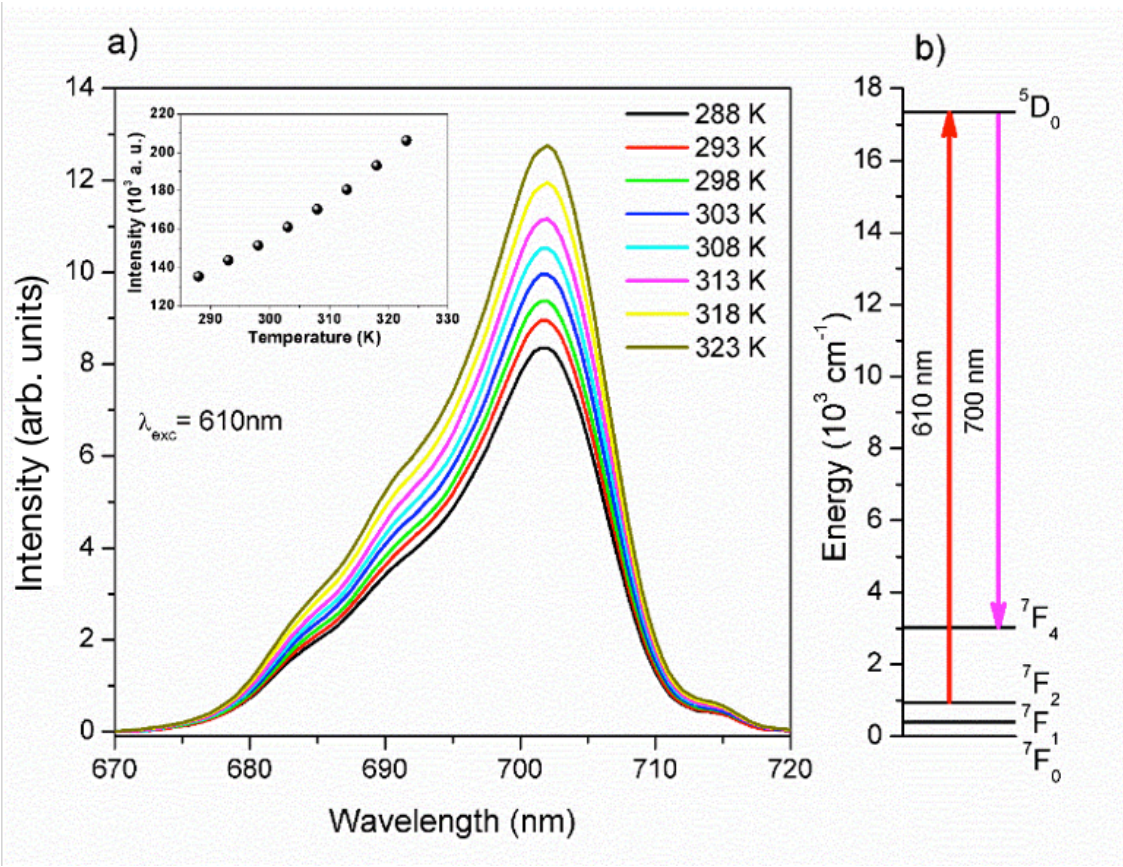

Figure 4.19. (a) Photoluminescence temperature dependence for the emission of the $^5D_0 \rightarrow {}^7F_4$ transition with excitation $^7F_2 \rightarrow {}^5D_0$. The inset shows the integrated intensity of the emission band. (b) Simplified energy level diagram of Eu^{3+} ion illustrating the excitation and radiative transitions.

The radiometric thermal parameter (R) was calculated using the Equation 4.1 evaluating the ratio between the integrated intensities (I) of the transition $^5D_0 \rightarrow {}^7F_4$ when the $^5D_0$ level is excited from the $^7F_2$ level ($Intesity_1$ = Emission Intensity at 700 nm using λ_{exc} = 610 nm), and when the $^5D_0$ level is excited from the $^7F_0$ level ($Intesity_2$ = Emission Intensity at 700 nm

using λ_{exc}= 576 nm). The temperature dependence of *R* obtained from the emission spectra shown in the figures 4.18a and 4.19a is showed in the Figure 4.20. TiO_2 anatase has a high thermal stability being stable up to temperatures of 1200 ºC which allows several luminescence measurements cycles to be performed, with high reproducibility (>99%) in the results, which is also expected for luminescent thermometers based on inorganic hosts doped with lanthanide ions. The error bars in Figure 4.20 were estimated through changes in the areas of the emission bands, resulting in changes in the *R* values by performing consecutive measurements of the Eu^{3+} emission at 700 nm after excitation at 576 nm and 610 nm, respectively. The fitting is showed in the red line. From the fitting of *R* with Equation (4.1), a value of A= 39.0 and ΔE = 997 cm^{-1} were determined. The relative sensitivity (*Sr*) of Eu^{3+}-TiO_2 optical nanothermometer is showed as the blue line in Figure 4.20 with respect of the temperature. S_r decreased from 1.78 to 1.41 $\%K^{-1}$ in the temperature range from 288 to 323 K. Surprisingly, this value is considerably higher than other values reported in literature, for example, Nikolic et al. reported a S_r value of 0.25%K^{-1} at 300 K for Eu^{3+}-doped TiO_2, indicating that the optical nanothermometer here developed has better sensitivity [38]. Besides, in the work reported by Nikolic et al. [38], the radiometric thermal parameter (R) was calculated using the ratio between one emission band in europium and one emission band of TiO_2, using emission bands from different materials that are not thermally coupled leads to the development of not reliable sensors because the luminescence intensity of TiO_2 depends on other factors rather than temperature like lanthanides concentration and number of lattice defects.

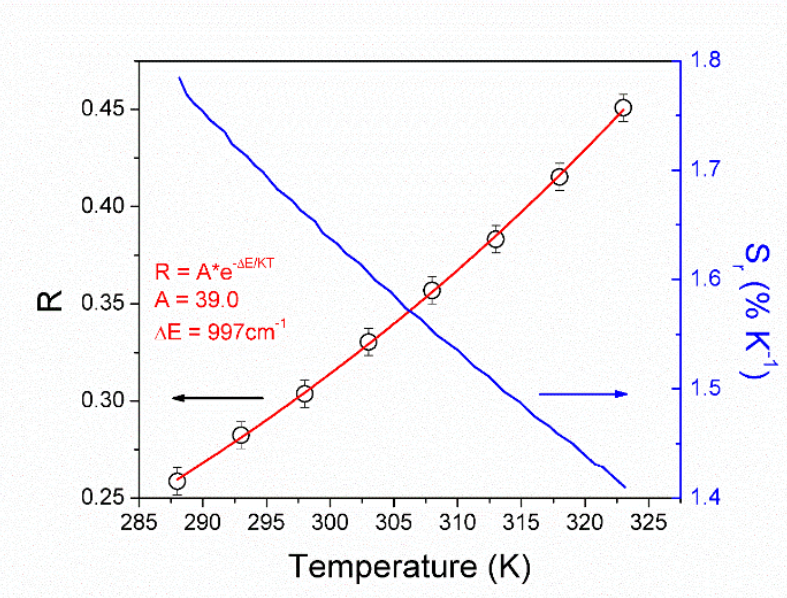

Figure 4.20. Radiometric thermal parameter, *R* (empty circles) as a function of the temperature and the theoretical fitting (red curve) using equation 4.1. Blue line is the calculated relative sensitivity (*Sr)* for different temperatures. The error bars represent the accuracy of luminescence measurements during the cycles.

4.6 Eu^{3+}-TiO_2 as nanothermometer of single cells

In the case of biological systems, temperature plays a very important role as small variations in temperature influence properties and dynamics of biomolecules, affecting the rate of the reactions that occur in living systems. For example, proteins experience a structural change and may lose their native structure if the temperature varies a few degrees around 37 °C, thus possible changes in their function can occur [39]. Multiple cellular processes are also regulated by temperature, such as cell division, membrane lipid compositions and gene expression [40–42]. Due to this strong influence of temperature on biological systems it is important to monitor the temperature while researching on the dynamics and properties of cellular systems is done. In addition to this basic concern, monitoring cellular temperature is also relevant in biomedicine. Cancerous cells were reported to be warmer by few degrees than normal cells due to their higher metabolic activity [43,44]. Following this discovery, temperature sensing in cells may become an important support technique in cancer detection [44]. However, measuring the temperature of living cells requires a subcellular spatial resolution as well as a sub-degree thermal resolution which are impossible to achieve with conventional thermometers, such as thermocouples or infrared thermometers [45,46]. In this perspective, luminescence nanothermometry emerges as a promising technique for measuring temperature of systems with a sub-micrometric size that might be capable of achieving the spatial and temperature resolutions expected. In a work reported by Savchuk et al. The green emission of erbium ions excited in $NaYF_4$:Er^{3+}, Yb^{3+} and NaY_2F_5O:Er^{3+}, Yb^{3+} nanoparticles was used to measure the heat induced by laser illumination in ex vivo experiments using chicken breast, obtaining sensitivities of $0.5\%K^{-1}$ and $1.5\%K^{-1}$ respectively [47]. In the same framework, Zairov et. al reported a temperature sensitivity for intracellular temperature nanosensors of $5.25\%\ K^{-1}$ using $Tb_2(TCA4)_2$ nanoparticles [48].

For systems that do not possess naturally luminescence temperature dependence like living cells it is necessary to conjugate the system of interest with probes whose luminescence is temperature dependent. In the previous section, it was shown that the excitation and detection wavelengths of Eu^{3+}-TiO_2 nanoparticles are within the range of 570–720 nm, this makes Eu^{3+}-TiO_2 nanoparticles good candidates to be used in biological applications because its excitation and emission wavelengths are in the first biological transparent window which rules out the influence of autofluorescence of biological systems that occurs when ultraviolet light is used for excitation. Optical windows are optically transparent regions in a spectrum where there is a maximizing of the transmission in a specified wavelength range, while a minimizing of reflection and absorption is observed. The first biological window extends from 650 nm to 980 nm and corresponds to the spectral range defined between the visible absorption band of hemoglobin and the characteristic water absorption band [49] (Figure 4.21). Besides, it was demonstrated that the emission bands of Eu^{3+}-TiO_2 depend critically on the temperature in the physiological temperature range (288–323 K). Furthermore, europium and europium-based nanoparticles also show low cytotoxicity [1,3,50]. Thus Eu^{3+}-

TiO_2 nanoparticles have promising characteristics to be used as active material in optical nanothermometers working in biological systems.

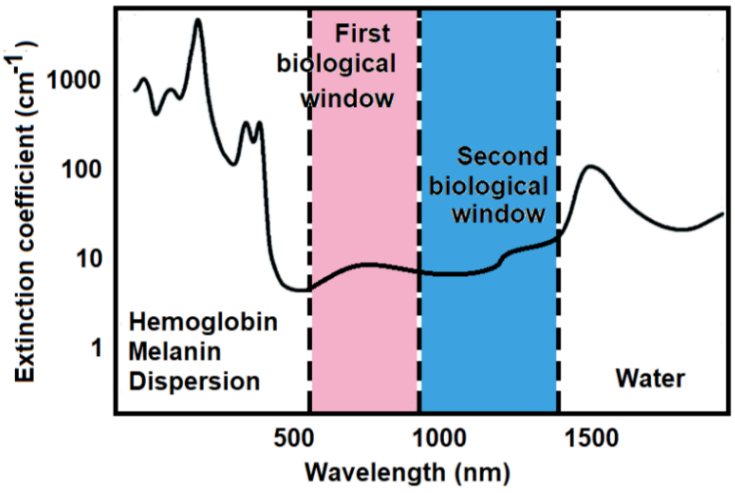

Figure 4.21. Scheme of the extinction spectrum, considering the absorption and dispersion of human tissue. The first and second biological windows are marked in the spectrum. Adapted from reference [49].

In this part of the thesis, 5 wt. % Eu^{3+}-TiO_2 nanoparticles are used as nanothermometers for single cell temperature measurements. This work was performed monitoring the variation of luminescence intensity of the $^5D_0 \rightarrow {}^7F_j$ (j = 0, … 6) emissions (excitation 396 nm) for increasing sample temperature. The luminescence of Eu^{3+}-TiO_2 was acquired in the biological relevant temperature range of 20–40 ºC and local temperature differences in single cells were detected.

4.6.1 Eu^{3+}-TiO_2 nanoparticles incubation in cells

To verify the applicability of 5 wt. % Eu^{3+}-TiO_2 nanoparticles to evaluate the temperature variation in living cells, mouse fibroblasts L929 were used as a test organism and several *in vitro* experiments were done to corroborate the internalization of Eu^{3+}-TiO_2 nanoparticles in L929 cells. Mouse fibroblast L929 were chosen as test organism because they are very well known and often used cell line, with an easy cultivation character. Their adherent phenotype provides an easy long-term process of observation of a single cell-nanothermometers.

The first step was the evaluation of the uptake of the nanoparticles by the selected cells. For the incubation of L929 fibroblast Eu^{3+}-TiO_2 powder was dispersed in a complete cell medium. Cell culture media generally comprise an appropriate source of energy and

compounds which regulate the cell cycle, a typical culture medium is composed of a complement of amino acids, vitamins, inorganic salts, glucose, and serum as a source of growth factors, hormones, and attachment factors. In addition to nutrients, the medium also helps maintain pH and osmolality. After dispersed in the cell medium, Eu^{+3}-TiO_2 were sonicated with a tip sonicator (MISONIX Ultrasound liquid Processor with 419 Microtip TM), with the amplitude set to 70% (power 20–30 W) for t_{run} = 15 min, t_{on} = 5 s, t_{off} = 5 s. Afterwards, dispersed nanoparticles were placed for 20 min under UV light for sterilization. Final concentration of Eu^{+3}-TiO_2 nanoparticles complete cell medium was 100 μg mL^{-1} or 500 μg mL^{-1}. The cell medium was replaced with the nanoparticles medium dispersion and incubated at 37 ºC in a 5% CO_2 atmosphere for two days. After the incubation, cells were stained with Hoechst 33342 stain at nmol concentration for nucleus observation. Membrane fluorophore ((2R,3S,4R,5R,6R)-2-(hydroxymethyl)-5-887-nitrobenzo[c][1,2,5]oxadiazol-4-yl)amino)-6-881-tetradecyl-1H-1,2.3-tiazol-4-yl)methoxy)tetrahydro-2H-pyran-3,4-diol) was added to the cell samples just before imaging. Plasma membrane was labelled with the CellMaskOrange membrane stain (5 μg/mL, Invitrogen), incubated at room temperature for additional 5 min and washed using phosphate buffered saline (PBS).

The internalization of the nanoparticles in mouse fibroblasts was evaluated with combination of different optical microscopy techniques: microscope operating in brightfield mode, fluorescence imaging mode, and fluorescence microspectroscopy mode. First, we obtained a set of images of control cells (no nanoparticles incubated) with the aim to determine cell autofluorescence (Figure 4.22a – brightfield image**,** b – fluorescence). Indeed, the autofluorescence signal of the L929 cells is intense in the range of 400-500nm (Figure 4.22b – fluorescence) rendering detection of the Eu^{3+}-TiO_2 nanoparticles impossible. However, since the Eu^{3+}-TiO_2 nanoparticles have a very sharp emission peak at 615 nm we should be able to distinguish them from the cell autofluorescence signal employing optical microscopy in microspectroscopy mode. We therefore recorded fluorescence emission spectrum in each pixel of the fluorescence image, an example of fluorescence emission spectrum is shown in Figure 4.22d. The emission spectrum was fitted as described previously in Arsov et al. 2011 (Appendix A.6) and its intensity is plotted in Figure 4.22d (Figure 4.22d – autofluorescence component) [51]. Brightfield images of cells after two days of incubation with Eu^{3+}-TiO_2 nanoparticles reveling several dark areas located at same places as cells (Figure 4.22e – brightfield), suggesting that Eu^{3+}-TiO_2 nanoparticles are either located inside the cells or adsorbed at their surface. Although several bright areas appear in the fluorescence image one cannot be sure that they originate from the Eu^{3+}-TiO_2 nanoparticles (Figure 4.22f – fluorescence). However, using fluorescence microspectroscopy, we can decompose the fluorescence emission spectrum in each pixel of the fluorescence image in two components: first corresponding to cell autofluorescence (Figure 4.22g – autofluorescence component) and second component corresponding to emission from the Eu^{3+}-TiO_2 nanoparticles (Figure 4.22h – Eu^{3+}-TiO_2 nanoparticles component). In this way we can clearly locate positions of the nanoparticles and show that luminescence of Eu^{3+}-TiO_2 nanoparticles occurs at the same

position as cells autofluorescence signal, therefore indicating that the nanoparticles are in close proximity to the cells. An emission spectrum showing the characteristic Eu^{3+} emission peak at 615 nm is detected in different cell areas when cells are incubated with nanoparticles (Figure 4.22i). Broad spectral component of the emission spectrum corresponds to cell autofluorescence (Figure 4.22d – autofluorescence emission spectrum) whereas the narrow component of the spectrum shows the europium luminescence band centered at 615 nm (Figure 4.22i – Eu^{3+}-TiO_2 emission spectrum superimposed with autofluorescence spectrum). The band of luminescence is not observed in the spectrum recorded on the sample where cells were not incubated with nanoparticles (Figure 4.22d).

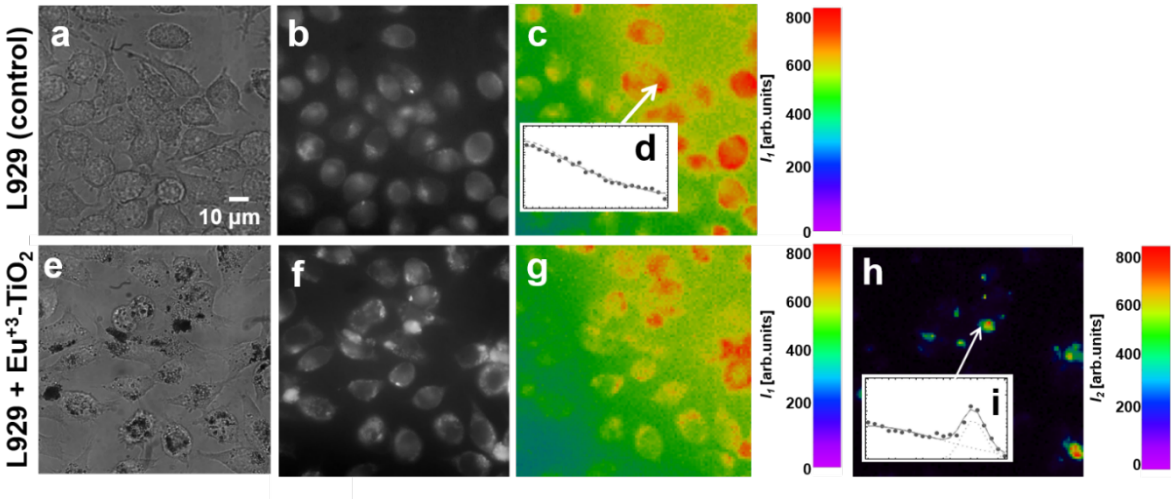

Figure 4.22. (a) Brightfield and (b) widefield autofluorescence images of L929 fibroblasts cells. (c) Fluorescence microspectroscopy image (b). (d) Typical autofluorescence emission spectrum from control cells. (e) Brightfield image of L929 cells incubated with 5 wt.% Eu^{3+}-TiO_2 nanostructures for 2 days. (f) Widefield fluorescence microscopy image of the same area shown in (e). (g) Fluorescence microspectroscopy image – color coded by autofluorescence component from cells, (h) fluorescence microspectroscopy image – luminescence of the europium component. Images (c), (g) and (h) are color coded by fluorescence and luminescence intensity (purple – low; red – high intensity) respectively. (i) Emission spectrum obtained from incubated cells: autofluorescence (left region – linear) and europium luminescence (right region – Gaussian-Loretzian) are present. 430–460 nm excitation, 495 nm dichroic and 523–643 nm emission filter setup was used with 5 nm scan step. All images have the same scale bar.

Figure 4.23 also shows the internalization of Eu^{3+}-TiO_2 nanoparticles. The images were obtained in three different focal points separated by 3 µm each. If we consider the average size of a cell (approximately 10 µm) we can say that in the plane a is the cell surface in focus, in plane b, the interior of the cells, and in plane c the surface of the cells that is in contact with the culture dish. Only when we focus the plane b the fluorescence of the nanoparticles

is in focus, which suggests that Eu^{3+}-TiO_2 nanoparticles are inside the cells.

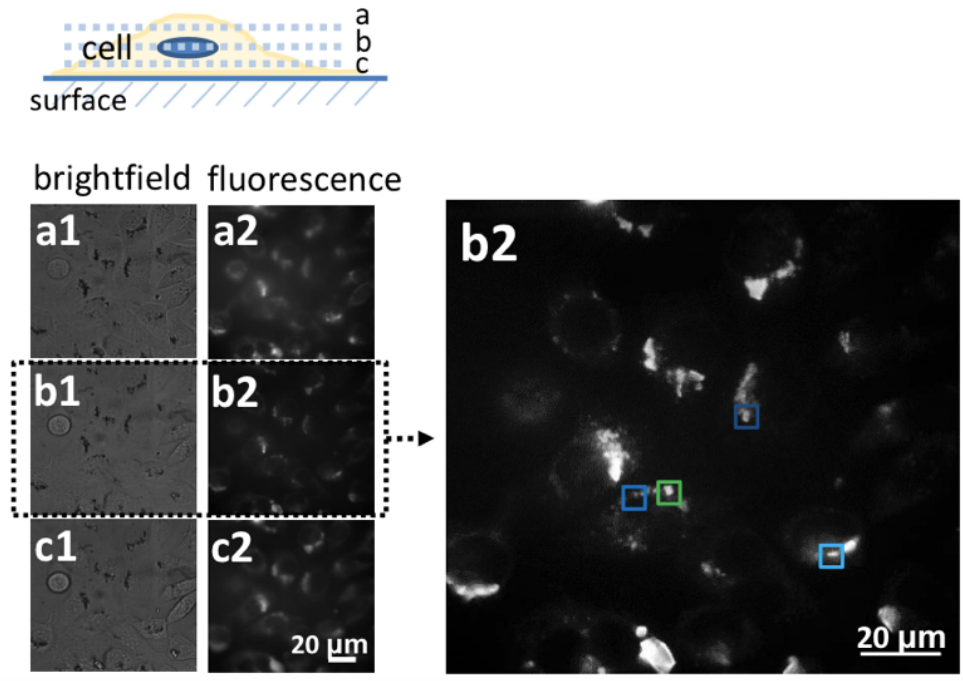

Figure 4.23. Brightfield (a1, b1, c1) and fluorescence (a2, b2, c2) microscopy image of L929 cells incubated with the Eu^{3+} -doped TiO_2 nanoparticles for 2 days. Images of cells were obtained in three different focal plane positions 3 µm apart from each other. Blue and green rectangles are showing aggregates of Eu^{3+}-TiO_2 nanoparticles.

Additional experiments were done to support the idea of successful internalization of Eu^{3+}-TiO_2 nanoparticles in multiple cells. For this, a different type of cell line was used, lung mouse epithelial LA-4. Like L929 fibroblast cells, LA-4 were chosen as test organism because their *in vitro* cultivation is already standardized and present relatively no complications because they have and adherent phenotype. Eu^{3+}-TiO_2 nanoparticles were incubated using the same protocol as for L929 fibroblast cells. To determine whether the nanoparticles are internalized within the cells or adsorbed to their surface confocal fluorescence microscopy with better spatial resolution was used capturing multiple two-dimensional images at different depths in the sample. The red signal belongs to europium and the green signal to the cell plasma membrane dye (Figure 4.24). Figure 4.24a shows a brightfield image from the incubated cells, Figure 4.24b shows the confocal fluorescence microscopy image from Figure 4.24a, the two dotted lines in Figure 4.24b indicate the xz and yz planes that were scanned by the microscope to obtain Figures 4.24c and 4.24d, in these figures the internalization of Eu^{3+}-TiO_2 in LA-4 cells can be easily observed.

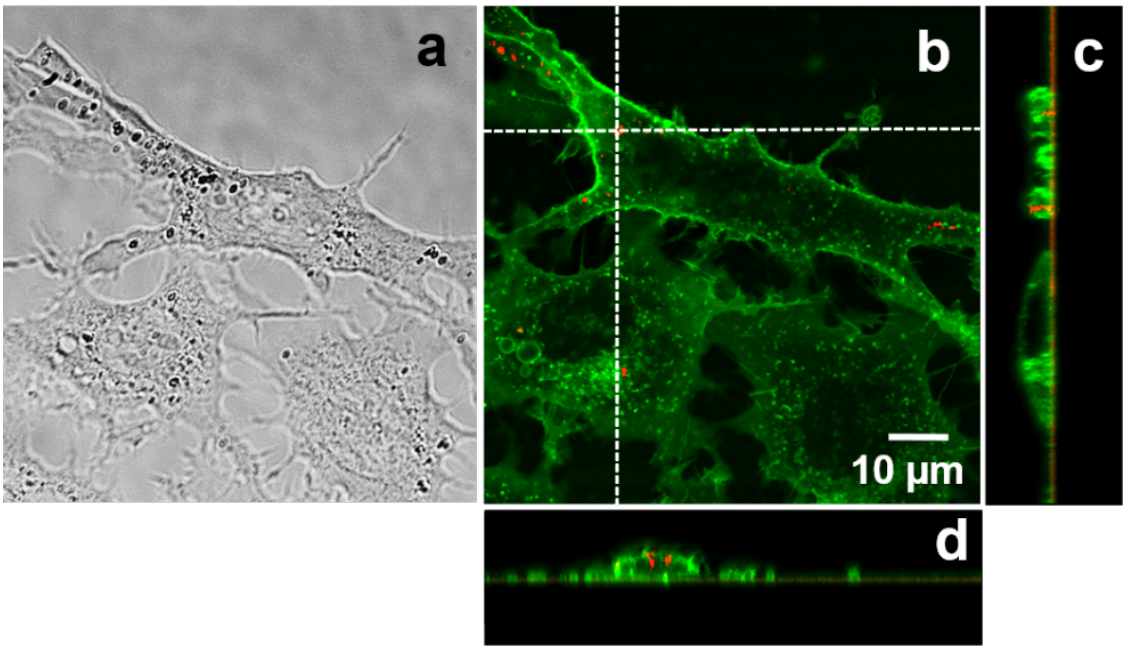

Figure 4.24. Mouse lung epithelial cells LA4 incubated with 5% Eu^{3+}-doped TiO_2 nanoparticles for one day: (a) bright field image and (b) confocal fluorescence microscopy image (green color represents signal of plasma membrane stain CellMaskOrange and red color represents the signal of Europium). Images (c) and (d) were taken in the yz and xz directions. Internalization of Eu^{3+}-doped TiO_2 nanoparticles can be observed. All figures have the same scale bar.

Nanoparticle internalization mechanism depends on the type of cell, the size, and the surface charge of the nanoparticle. The most common nanoparticle uptake mechanisms are clathrin-dependent endocytosis, macropinocytosis, and phagocytosis [52]. Even tough knowing the Eu^{3+}-TiO_2 nanoparticles uptake mechanism could be an interesting input to this investigation it is beyond the scope of this work and will not be further discussed. However, clathrin-mediated endocytosis is the most predominant mechanism involved in non-macrophage cell nanoparticle uptake. Clatrin-mediated endocytosis is the process in which cells internalize nutrients, antigens, grow factors, pathogens and in this case nanoparticles [53]. The mechanism consists of invaginations of the plasma membrane forming vesicles containing the absorbed substances that results in the accumulation of extracellular macromolecules into clathrin coated vesicles, these vesicles are then fused to early endosome vesicles and eventually become degraded by lysosomes. For the nanoparticles to accumulate in other parts of the cells they are required to escape from the endosomes.

The interaction of nanoparticles with cells is known to be strongly influenced by particle size, because of that, most of the investigations follow the change in the size of nanoparticles to study their interaction with cells. However, in a work reported by Gratton et. al [54] the

relevance of nanoparticle shape was demonstrated to be also an important issue in the interaction and internalization of nanoparticles with cells. Here, we investigate the internalization of Eu^{3+}-TiO_2 nanoparticle in LA-4 cells with different morphologies, spherical and nanotubes shapes were tested (Figure 4.25). The same confocal fluorescence microscopy as Figure 4.24 was used, the red signal belongs to europium and the green signal to the cell plasma membrane dye. Figure 4.25a shows the control LA-4 cells which are not incubated with nanoparticles. Figure 4.25b shows the results from the cells incubated with spherical Eu^{3+}-TiO_2 and Figure 4.25c shows the LA-4 cells incubated with Eu^{3+}-TiO_2 nanotubes. Internalization in LA-4 cells of spherical and nanotubes Eu^{3+}-TiO_2 nanoparticles can be observed.

The results showed in the Figures 4. 22, 4.23, 4.24 and 4.25 confirm the internalization of Eu^{3+}-TiO_2 nanoparticles into different types of cells and likewise probe the potential to internalize cells of TiO_2 nanoparticles having different morphologies.

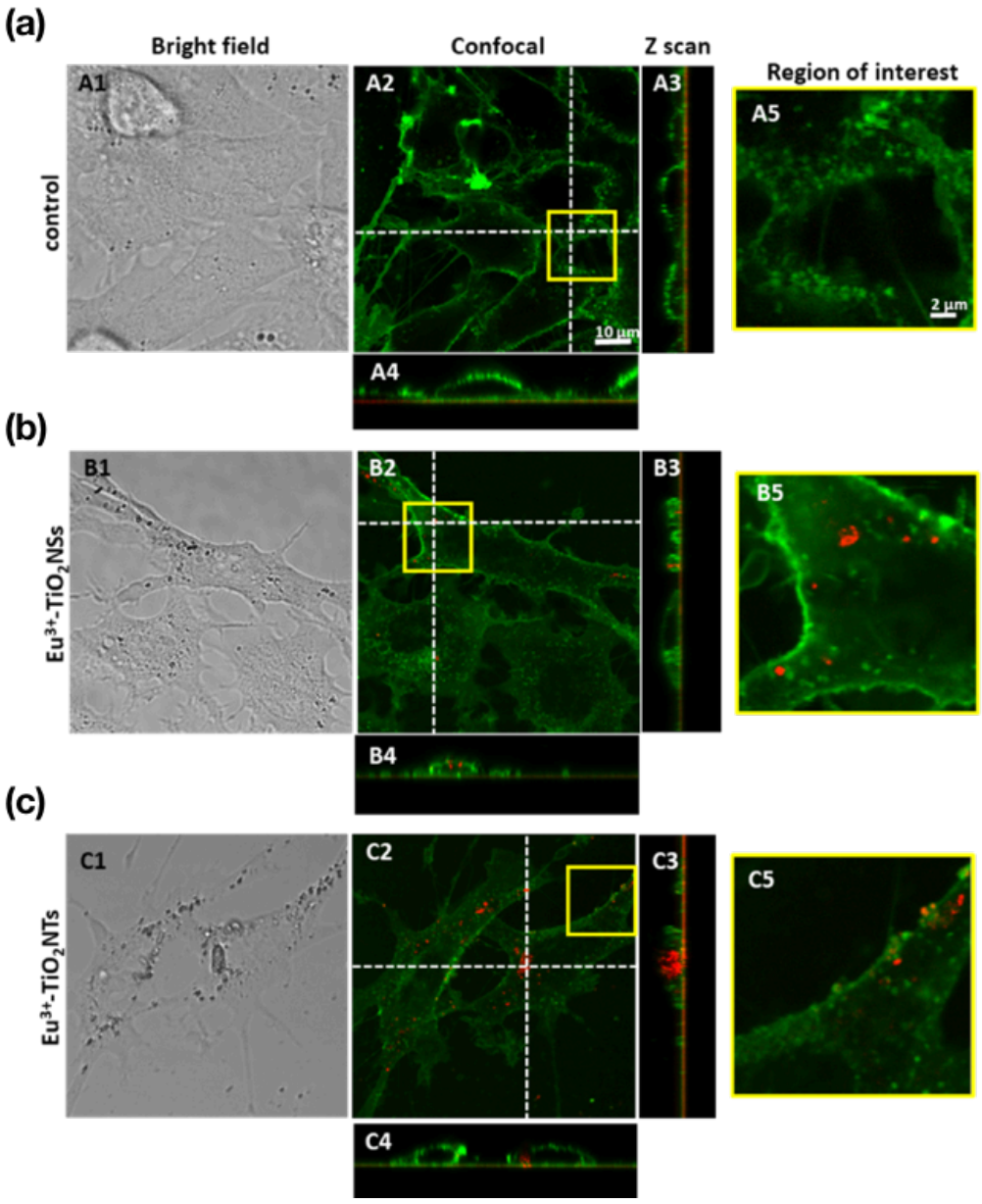

Figure 4.25. Mouse lung epithelial cells LA4 incubated with Eu^{3+}-TiO_2 nanoparticles for one day. Bright field image (1) as well as confocal xy (2), xz (3) and yz (4) images are shown. Green color represents signal of plasma membrane stain CellMaskOrange, red color represents the signal of Eu doped nanoparticles. Internalization of all different types of Eu-nanoparticles can be observed. Two excitation lasers were used (561 nm and 640 nm) with emission detected from 580–625 nm in one channel (green - plasma membrane) and from 655–720 nm in second channel (red – Eu doped nanoparticles). (a) control – cells without nanoparticles; (b) cells incubated with anatase TiO_2 nanospheres (5% Eu^{3+}-TiO_2 nanoparticles); (c) cells incubated with anatase TiO_2 nanotubes (Eu^{3+}-TiO_2 nanotubes).

4.6.2 Variation with temperature of Eu^{3+}-TiO_2 luminescence in cells

To validate the use of Eu^{3+}-TiO_2 nanoparticles as single cell nanothermometer we must be able to measure the change in the Eu^{3+}-TiO_2 luminescence with temperature when they are internalized in cells. First tests to observe the change of Eu^{3+}-TiO_2 luminescence with temperature was performed on L929 cells incubated with 5 wt. % Eu^{3+}-TiO_2 the cells were observed by fluorescence widefield microscopy using a 430-460 nm filter of excitation and a 523–643 nm emission filter. Images were recorded when a spot of the sample was heated using an infrared laser (1064 nm, 200 mW, focal point less than 1 μm) (Figure 4.26). The bright spot inside the area limited by the red rectangle in Figure 4.26 are agglomerated Eu^{3+}-TiO_2 nanoparticles in L929 cells. The images were recorded when the sample was at room temperature or was heated (shown in zoom). The magnified image above in Figure 4.26 corresponds to the heated sample (heating laser turned on for 5 seconds), and the magnified image bellow correspond to the sample at room temperature (heating laser turned off for 10 seconds). It can be observed that when the heating laser is turned on the intensity of luminescence of the Eu^{3+}-TiO_2 nanoparticles decreases, this effect is associated to the increment of non-radiative relaxation processes. Based on the obtained data we can ascertain that the decrease in the luminescence intensity corresponds to the increase in the local temperature.

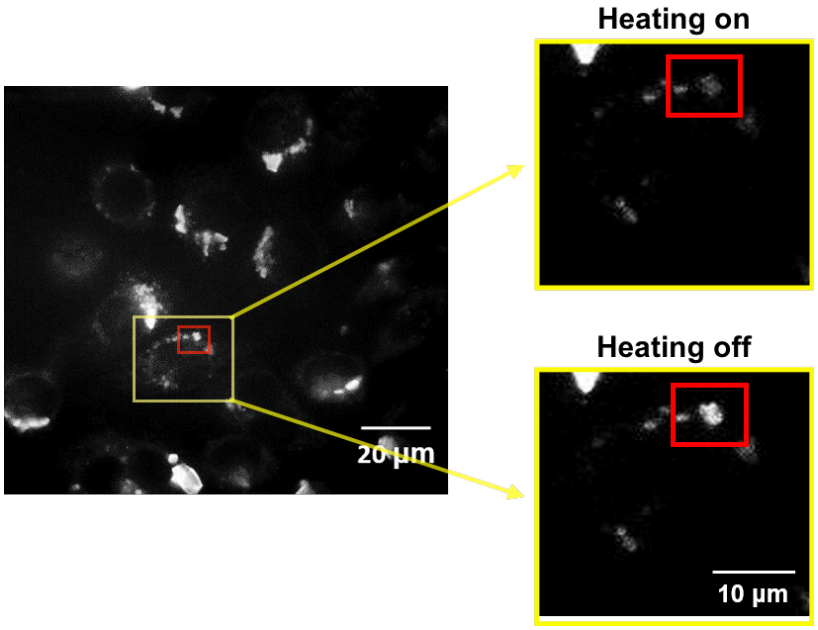

Figure 4.26. Fluorescence widefield microscopy image of a 5%Eu^{3+}-TiO_2 nanoparticles internalized in L929 fibroblasts cells. Red rectangle indicates an area that was heated with infrared heating laser. 430–460 nm excitation, 495 nm dichroic and 523–643 nm filter setup was used. Magnified images have the same scale bar.

4.6.3 Eu^{3+}-TiO_2 nanothermometer calibration curve

In order to use Eu^{3+}-TiO_2 nanoparticles as luminescent nanothermometers, is necessary to calibrate the variation of their luminescence intensity with variation of the temperature.

Unfortunately, the calibration curve obtained in Figure 4.20 for bare nanoparticles cannot be applied for nanoparticles internalized in cells, for various reasons, in the Figure 4.20 the nanoparticles emission spectra were acquired with powder pellets of Eu^{3+}-TiO_2, for the case of Eu^{3+}-TiO_2 nanoparticles internalized in cells the nanoparticles are dispersed in the cell medium, changes in the intensity variation with temperature and position shifts of the Eu^{3+} emission bands can occur. These shifts result from both the interactions of the dipole moment of the luminescent object with the reactive fields induced in the surrounding solvent, and from specific chemical interactions between the luminescent material with the solvent molecules.

Considering that water is the main abundant molecule in cells, accounting for 70% of total cell mass, we used dispersed Eu^{3+}-TiO_2 particles in distilled water simulating cell internalized particles and we obtained the luminescence spectra at different temperatures in the biological relevant range with an excitation of 430–460 nm; the emission transitions $^5D_0$ – ^4F_j (j=0,1,2,3,4) are observed (Figure 4.26a). The calibration curve was obtained using a spectrofluorometer (Figure 4.27a) and a fluorescence microscope, to verify the compatibility of both methods. Figure 4.28 shows fluorescence images recorded at different temperatures; these images are used to determine the emission intensity variation with temperature. The sample was heated using an objective-ring, placed on a water immersion objective, which can heat up the sample precisely enough without severe vertical gradients. For the microscope a 430–460 nm excitation filter and 580–643 nm emission filter were used. The intensity at the peak maximum on 615 nm was used to create the calibration curve. The intensity of luminescence for the case of the fluorescence microscope was obtained integrating the luminescence intensity in each pixel of the image recorded at a chosen temperature.

Both data obtained are plotted in the Figure 4.27b as black circles, since both data were overlapping, they were fitted together with a linear function (black solid line), when temperature increased the luminescence intensity decreased through the whole spectral range, the black solid line is the calibration curve.

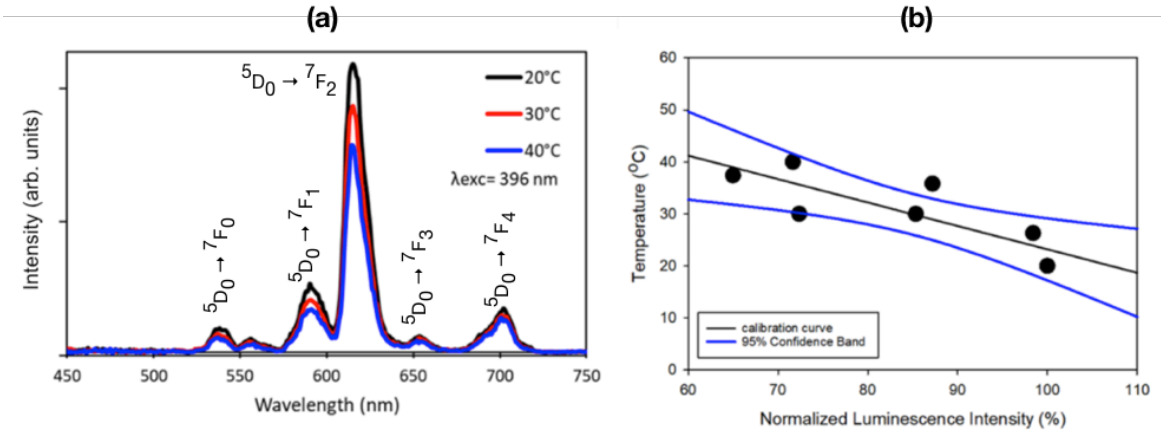

Figure 4.27. (a) Luminescence spectra of 5%Eu^{3+}-TiO_2 nanoparticles taken at different temperatures obtained with spectrofluorometer. (b) Calibration curve of variation of temperature versus normalized luminescence intensity obtained in a water dispersion of Eu^{3+}-TiO_2 nanoparticles. Luminescence intensity of the emitted light was measured using either a fluorescence microscope or a spectrofluorometer (both data represented with black circles), since both data were overlapping, they were fitted together with a linear function (black solid line). The blue lines represent the confidence band.

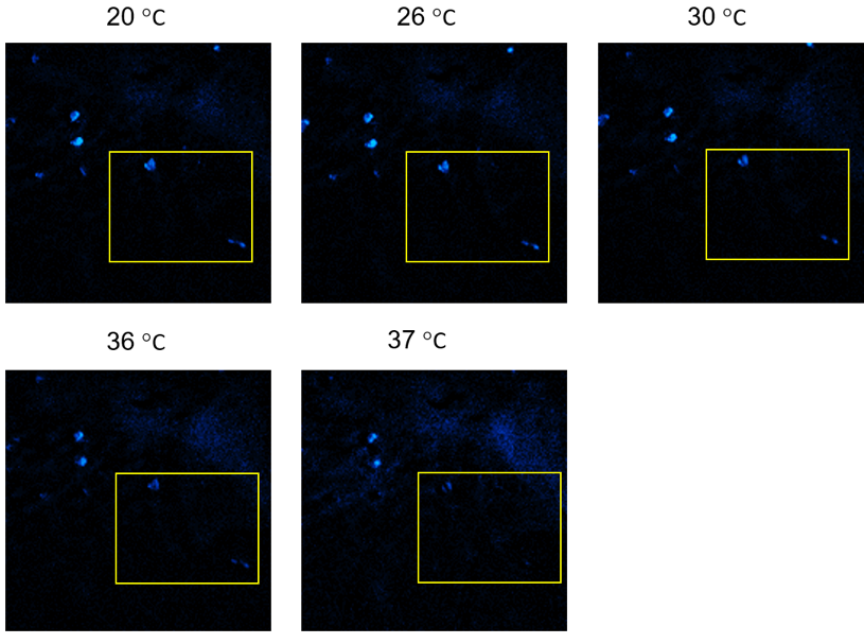

Figure 4.28. Typical widefield fluorescence images recorded on Eu^{3+}-TiO_2 nanoparticles using the fluorescence microscope. The sample was heated via objective ring connected to thermal couple and placed on a water immersion objective. Before recording the fluorescence intensity at five different temperatures, 5 min waiting time was performed to achieve the target temperature. The measure of the widefield fluorescence intensity in each pixel of the whole image was used to obtain temperature calibration curve.

The temperature variation curve is described by Equation 4.4.

$$\Delta T = a \cdot \Delta I \tag{4.4}$$

Where a = (-0.45 ± 0.12) ºC $\%^{-1}$ adjusted to best fit the experimental data (closed circles Figure 4.27b). Using the parameter a one can therefore calculate temperature difference ΔT in ℃ by measuring difference between two normalized luminescence intensities ΔI and multiplying the difference by a. The luminescence intensities are normalized to the luminescence intensity at the initial temperature to obtain a reliable thermometer.

This equation shows the sensitivity of the Eu^{3+} doped TiO_2 nanoparticles as nanothermometers, namely, when luminescence intensity of the nanoparticle decreases by 1 percent ($\Delta I = 1\%$) the nano-thermometer can detect temperature difference of:

$$\Delta T = a \cdot \Delta I = (-0.45 \pm 0.12)℃ \cdot \%^{-1} \cdot (-1\%) = 0.45℃ \pm 0.12℃. \tag{4.5}$$

4.6.4 Single cell temperature probed by Eu^{3+}-TiO_2 luminescence

The use of Eu^{3+}-TiO_2 nanoparticles as temperature sensors of living cells is shown in this section. 5 wt. % Eu^{3+}-TiO_2 nanoparticles were incubated in L929 cells for three days. Then, the incubated cells were marked with fluorophores to be observed in the fluorescence microscope (Figure 4.29). Figure 4.29a shows the brightfield of the incubated cells and Figure 4.29b the fluorescence image. From Figure 4.29b, the blue signal corresponds to the nucleus, the green to the plasma membrane and the luminescence of Eu^{3+}-TiO_2 is observed in red. The green rectangle indicates an area of one cell with nanoparticles that is heated with an infrared laser of 1064 nm with power of 200 mW with a focal point of less than 1μm, whereas blue rectangles indicate nanoparticles also located inside the cells but not heated with the laser.

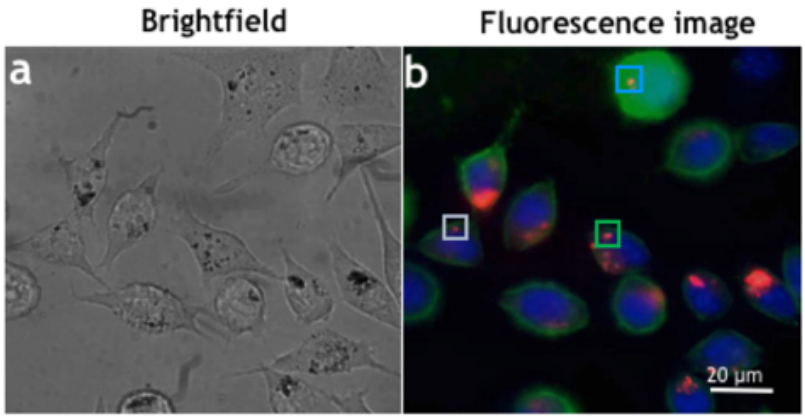

Figure 4.29. (a) Brightfield and (b) overlay of three fluorescence widefield microscopy images of L929 fibroblasts incubated with Eu^{3+}-TiO_2 nanoparticles for 3 days (nanoparticles are presented in red, cell nuclei in blue, and plasma membrane in green). Green rectangle indicates an area heated with an infrared laser, whereas blue rectangles indicate nanoparticles also located inside the cells but not heated with the laser (1064 nm, 200 mW, focal point less than 1 µm).

The center of a laser beam was placed on the Eu^{3+}-TiO_2 nanostructure inside the cell. Multiple cycles of the laser tuned on (heat on) and tuned off (heat off) were performed to change the temperature of the sample (Figure 4.30). Manual switching $turned_{on}$ = 5 s, $turned_{off}$ = 10 s approximately was used for manipulation of the laser, repeatedly. The luminescence intensity response from the regions marked (green and blue rectangles) was monitored with the time and plotted in Figure 4.30. It can be observed that the nanoparticles inside the green area show an evident change in its luminescence intensity, decrease on the intensity was observed when the temperature was increased (laser on/heating on). In contrast, the luminescence intensity in the non-heated regions of cells remains constant with the time. Measured fluorescence intensity data were normalized to initial intensity of 5 wt. % Eu^{+3}-TiO_2 nanoparticles before heating.

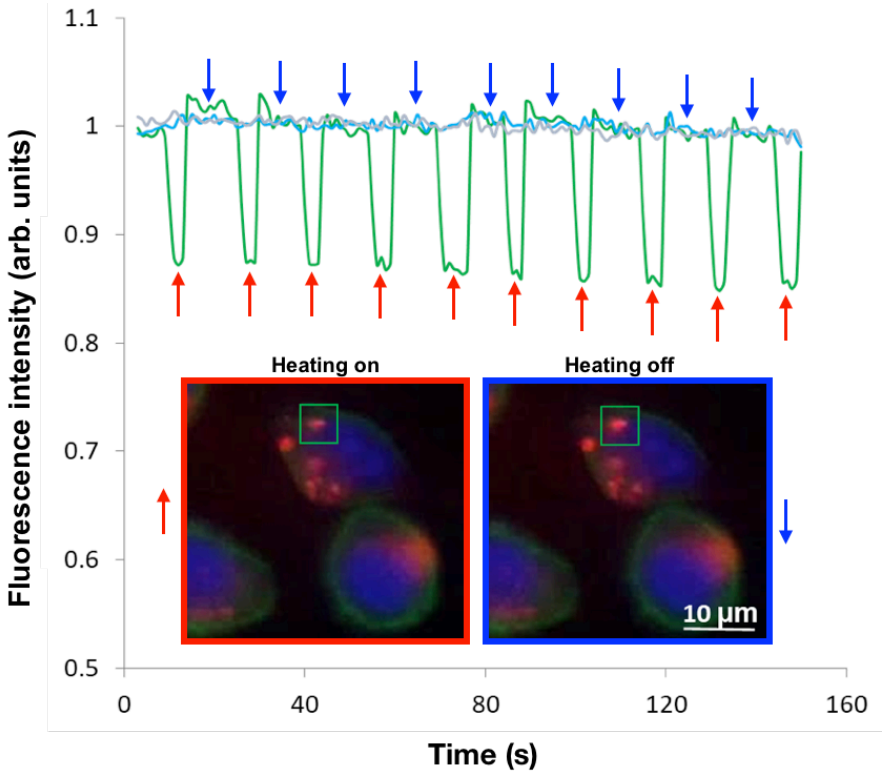

Figure 4.30. Time dependent experiment in incubated L929 fibroblast cells indicating the luminescence intensity response of a heated region (green square) and constant luminescence intensity of non-heated regions (light and dark blue lines). The nanoparticles in the heated area show evident luminescence intensity change. Note that only the nanoparticles inside the green area change the intensity of the emitted light when the area is heated with the infrared laser. The power of the laser (1064 nm) was 200 mW. The filters used in experiments were the following: for the nuclei imaging 352–402 nm excitation, 409 nm dichroic, and 420–520 nm emission filters, for 5%Eu^{3+}-TiO_2 nanoparticles imaging 430–460 nm excitation, 495 nm dichroic and 580–643 nm emission filters were used, and for the membrane imaging 430–460 nm excitation, 495 nm dichroic and 506-594 nm emission filters were used.

Equation 4.4 is used for the transformation of the luminescence intensity variation (ΔI) obtained in the Figure 4.30 to obtain the temperature difference (ΔT) induced in the region of the cell that was heated with the laser (Figure 4.31). Magnified images from an area with heated nanoparticles with evident luminescence intensity variation are shown above the time traces of temperature variation. Maximal temperature cell difference detected was 6 ºC at the laser beam position (Figure 4.31, blue line) [2].

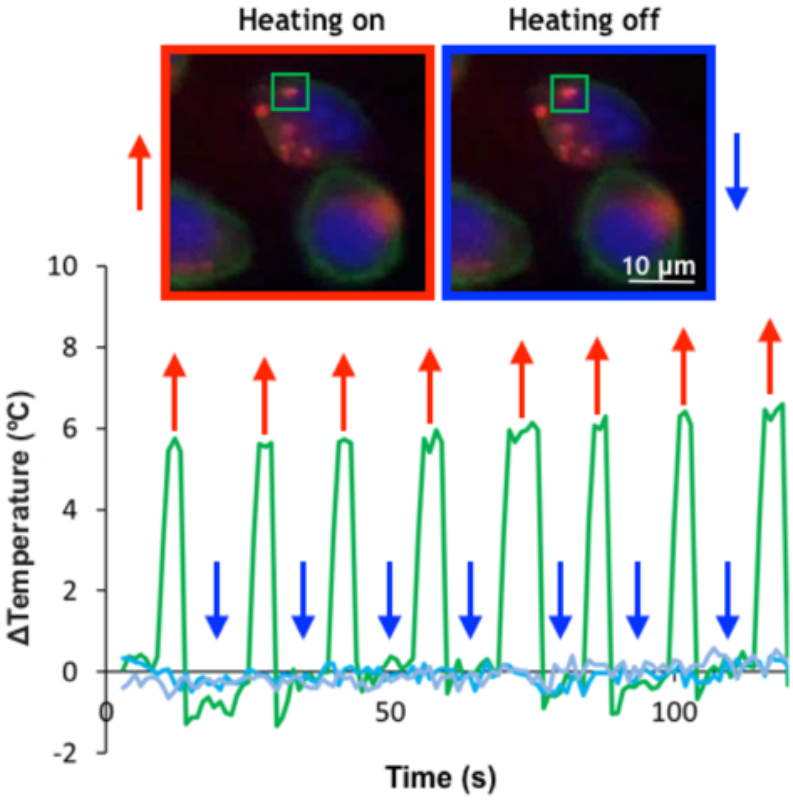

Figure 4.31. Local temperature response of the heated nanoparticles (green) and no response of non-heated nanoparticles (blue). Maximal temperature cell difference detected was 6 ºC at the laser beam position. Magnified images from an area with heated nanoparticles with evident luminescence intensity variation are shown above the time traces of temperature variation. The filters used in experiments were the following: for the nuclei imaging 352–402 nm excitation, 409 nm dichroic, and 420–520 nm emission filters, for 5%Eu^{+3}-TiO_2 nanoparticles imaging 430–460 nm excitation, 495 nm dichroic and 580–643 nm emission filters were used, and for the membrane imaging 430–460 nm excitation, 495 nm dichroic and 506–594 nm emission filters were used.

4.7. Conclusions

The evaluation of temperature with submicrometric spatial resolution is of high importance in different research fields involving nanoscale systems. The conjugation of nanoscale systems with temperature dependent luminescent nanoprobes is a potential solution to achieve temperature measurements with submicrometric resolution because the spatial resolution is only limited by the size of the nanoprobes.

In this work, the temperature-dependent luminescence of Eu^{3+}-TiO_2 nanoparticles was used to develop a temperature nanosensor of biological systems.

Eu^{3+}-TiO_2 nanoparticles were synthesized using the sol-gel method, the nanoparticles obtained have diameters of ~15 nm. The XRD pattern of the undoped TiO_2 exhibits diffraction peaks of anatase and rutile TiO_2, on the other hand, the XRD patterns of all europium doped TiO_2 samples match to anatase TiO_2 and the rutile phase is no longer observed in the doped samples. From these results we conclude that the presence of europium ions in the synthesis of TiO_2 inhibits the transformation of anatase into the rutile phase. Besides, the analysis of the Eu^{3+}-TiO_2 samples by XRD, XPS and photoluminescence spectrum indicates that doping TiO_2 with europium ions generates oxygen vacancies and under coordinated Ti^{3+} defects in the TiO_2 lattice.

Eu^{3+}-TiO_2 nanoparticles synthesized in this work can readily be internalized in different types of cells and their luminescence as well as their luminescence dependence with temperature variation in the physiological temperature range can be measured even after they are internalized.

By measuring the luminescence intensity variation of internalized Eu^{3+}-TiO_2 nanoparticles we obtained information about cells temperature variation with sensitivity of -0.45 ± 0.12 ºC per 1% change in luminosity. This result opens the possibility of the use of Eu^{+3}-TiO_2 nanoparticles in biomedical technologies as nanothermometers for single cell temperature evaluation.

4.8 References

[1] K. Pawar, G. Kaul, Toxicity of Europium Oxide Nanoparticles on the Buffalo (<I>Bubalus bubalis</I>) Spermatozoa DNA Damage, Adv. Sci. Eng. Med. 5 (2013). https://doi.org/10.1166/asem.2013.1230.

[2] C.R. Patra, S.S. Abdel Moneim, E. Wang, S. Dutta, S. Patra, M. Eshed, P. Mukherjee, A. Gedanken, V.H. Shah, D. Mukhopadhyay, In vivo toxicity studies of europium hydroxide nanorods in mice, Toxicol. Appl. Pharmacol. 240 (2009). https://doi.org/10.1016/j.taap.2009.07.009.

[3] V.S. Bollu, S.K. Nethi, R.K. Dasari, S.S.N. Rao, S. Misra, C.R. Patra, Evaluation of *in vivo* cytogenetic toxicity of europium hydroxide nanorods (EHNs) in male and female Swiss albino mice, Nanotoxicology. 10 (2016). https://doi.org/10.3109/17435390.2015.1073398.

[4] X. Chen, S.S. Mao, Titanium Dioxide Nanomaterials: Synthesis, Properties, Modifications, and Applications, Chem. Rev. 107 (2007).

https://doi.org/10.1021/cr0500535.

[5] R. Daghrir, P. Drogui, D. Robert, Modified TiO 2 For Environmental Photocatalytic Applications: A Review, Ind. Eng. Chem. Res. 52 (2013). https://doi.org/10.1021/ie303468t.

[6] M.R.D. Khaki, M.S. Shafeeyan, A.A.A. Raman, W.M.A.W. Daud, Application of doped photocatalysts for organic pollutant degradation - A review, J. Environ. Manage. 198 (2017). https://doi.org/10.1016/j.jenvman.2017.04.099.

[7] M. Grätzel, Perspectives for dye-sensitized nanocrystalline solar cells, Prog. Photovoltaics Res. Appl. 8 (2000). https://doi.org/10.1002/(SICI)1099-159X(200001/02)8:1<171::AID-PIP300>3.0.CO;2-U.

[8] D. Wojcieszak, M. Mazur, M. Kurnatowska, D. Kaczmarek, J. Domaradzki, L. Kepinski, K. Chojnacki, Influence of Nd-Doping on Photocatalytic Properties of TiO 2 Nanoparticles and Thin Film Coatings, Int. J. Photoenergy. 2014 (2014). https://doi.org/10.1155/2014/463034.

[9] M. Mazur, J. Domaradzki, D. Wojcieszak, D. Kaczmarek, P. Mazur, Investigation of physicochemical properties of (Ti-V)Ox (4.3at.% of V) functional thin films and their possible application in the field of transparent electronics, Appl. Surf. Sci. 304 (2014). https://doi.org/10.1016/j.apsusc.2014.01.073.

[10] E.M. Rodríguez, A. Rey, E. Mena, F.J. Beltrán, Application of solar photocatalytic ozonation in water treatment using supported TiO2, Appl. Catal. B Environ. 254 (2019). https://doi.org/10.1016/j.apcatb.2019.04.095.

[11] V.A. Tran, T.T. Truong, T.A.P. Phan, T.N. Nguyen, T. Van Huynh, A. Agresti, S. Pescetelli, T.K. Le, A. Di Carlo, T. Lund, S.-N. Le, P.T. Nguyen, Application of nitrogen-doped TiO 2 nano-tubes in dye-sensitized solar cells, Appl. Surf. Sci. 399 (2017). https://doi.org/10.1016/j.apsusc.2016.12.125.

[12] H. O'Neal Tugaoen, S. Garcia-Segura, K. Hristovski, P. Westerhoff, Compact light-emitting diode optical fiber immobilized TiO2 reactor for photocatalytic water treatment, Sci. Total Environ. 613–614 (2018). https://doi.org/10.1016/j.scitotenv.2017.09.242.

[13] N.D. Abazović, M.I. Čomor, M.D. Dramićanin, D.J. Jovanović, S.P. Ahrenkiel, J.M. Nedeljković, Photoluminescence of Anatase and Rutile TiO 2 Particles †, J. Phys. Chem. B. 110 (2006). https://doi.org/10.1021/jp064454f.

[14] E. Le Boulbar, E. Millon, E. Ntsoenzok, B. Hakim, W. Seiler, C. Boulmer-Leborgne, J. Perrière, UV to NIR photon conversion in Nd-doped rutile and anatase titanium dioxide films for silicon solar cell application, Opt. Mater. (Amst). 34 (2012). https://doi.org/10.1016/j.optmat.2012.02.033.

[15] B. Choudhury, A. Choudhury, Dopant induced changes in structural and optical

properties of Cr3+ doped TiO2 nanoparticles, Mater. Chem. Phys. 132 (2012). https://doi.org/10.1016/j.matchemphys.2011.12.083.

[16] B.K. Kaleji, R. Sarraf-Mamoory, A. Fujishima, Influence of Nb dopant on the structural and optical properties of nanocrystalline TiO2 thin films, Mater. Chem. Phys. 132 (2012). https://doi.org/10.1016/j.matchemphys.2011.11.034.

[17] J. Singh, S. Sharma, S. Sharma, R.C. Singh, Effect of tungsten doping on structural and optical properties of rutile TiO2 and band gap narrowing, Optik (Stuttg). 182 (2019). https://doi.org/10.1016/j.ijleo.2019.01.070.

[18] C. Leostean, M. Stefan, O. Pana, A.I. Cadis, R.C. Suciu, T.D. Silipas, E. Gautron, Properties of Eu doped TiO2 nanoparticles prepared by using organic additives, J. Alloys Compd. 575 (2013). https://doi.org/10.1016/j.jallcom.2013.04.067.

[19] M.E. Simonsen, E.G. Søgaard, Sol–gel reactions of titanium alkoxides and water: influence of pH and alkoxy group on cluster formation and properties of the resulting products, J. Sol-Gel Sci. Technol. 53 (2010). https://doi.org/10.1007/s10971-009-2121-0.

[20] Ž. Antić, R.M. Krsmanović, M.G. Nikolić, M. Marinović-Cincović, M. Mitrić, S. Polizzi, M.D. Dramićanin, Multisite luminescence of rare earth doped TiO2 anatase nanoparticles, Mater. Chem. Phys. 135 (2012). https://doi.org/10.1016/j.matchemphys.2012.06.016.

[21] D. Reyes-Coronado, G. Rodríguez-Gattorno, M.E. Espinosa-Pesqueira, C. Cab, R. de Coss, G. Oskam, Phase-pure TiO_2 nanoparticles: anatase, brookite and rutile, Nanotechnology. 19 (2008). https://doi.org/10.1088/0957-4484/19/14/145605.

[22] H. Siddiqui, Modification of Physical and Chemical Properties of Titanium Dioxide (TiO_2) by Ion Implantation for Dye Sensitized Solar Cells, in: Ion Beam Tech. Appl., IntechOpen, 2020. https://doi.org/10.5772/intechopen.83566.

[23] Y. Zhang, H. Zhang, Y. Xu, Y. Wang, Europium doped nanocrystalline titanium dioxide: preparation, phase transformation and photocatalytic properties, J. Mater. Chem. 13 (2003). https://doi.org/10.1039/b305538h.

[24] E. Setiawati, K. Kawano, Stabilization of anatase phase in the rare earth; Eu and Sm ion doped nanoparticle TiO2, J. Alloys Compd. 451 (2008). https://doi.org/10.1016/j.jallcom.2007.04.059.

[25] D. Kim, Y.-H. Jin, K.-W. Jeon, S. Kim, S.-J. Kim, O.H. Han, D.-K. Seo, J.-C. Park, Blue-silica by Eu^{2+} -activator occupied in interstitial sites, RSC Adv. 5 (2015). https://doi.org/10.1039/C5RA15641F.

[26] D.K. Pallotti, L. Passoni, P. Maddalena, F. Di Fonzo, S. Lettieri, Photoluminescence Mechanisms in Anatase and Rutile TiO_2, J. Phys. Chem. C. 121 (2017).

https://doi.org/10.1021/acs.jpcc.7b00321.

[27] J. Zhang, P. Zhou, J. Liu, J. Yu, New understanding of the difference of photocatalytic activity among anatase, rutile and brookite TiO2, Phys. Chem. Chem. Phys. 16 (2014) 20382–20386. https://doi.org/10.1039/c4cp02201g.

[28] I. Nakamura, N. Negishi, S. Kutsuna, T. Ihara, S. Sugihara, K. Takeuchi, Role of oxygen vacancy in the plasma-treated TiO2 photocatalyst with visible light activity for NO removal, J. Mol. Catal. A Chem. 161 (2000) 205–212. https://doi.org/10.1016/S1381-1169(00)00362-9.

[29] A. Zaleska, Doped-TiO2: A Review, Recent Patents Eng. 2 (2008) 157–164. https://doi.org/10.2174/187221208786306289.

[30] C. Jin, B. Liu, Z. Lei, J. Sun, Structure and photoluminescence of the TiO2 films grown by atomic layer deposition using tetrakis-dimethylamino titanium and ozone, Nanoscale Res. Lett. 10 (2015). https://doi.org/10.1186/s11671-015-0790-x.

[31] C.L. Olson, J. Nelson, M.S. Islam, Defect Chemistry, Surface Structures, and Lithium Insertion in Anatase TiO_2, J. Phys. Chem. B. 110 (2006). https://doi.org/10.1021/jp057261l.

[32] F. Baur, T. Jüstel, (INVITED) Eu3+ activated molybdates – Structure property relations, Opt. Mater. X. 1 (2019). https://doi.org/10.1016/j.omx.2019.100015.

[33] B.M. Walsh, Judd-Ofelt theory: principles and practices, in: Adv. Spectrosc. Lasers Sens., Springer Netherlands, 2006: pp. 403–433. https://doi.org/10.1007/1-4020-4789-4_21.

[34] A.C. Brandão-Silva, M.A. Gomes, S.M.V. Novais, Z.S. Macedo, J.F.M. Avila, J.J. Rodrigues, M.A.R.C. Alencar, Size influence on temperature sensing of erbium-doped yttrium oxide nanocrystals exploiting thermally coupled and uncoupled levels' pairs, J. Alloys Compd. 731 (2018). https://doi.org/10.1016/j.jallcom.2017.09.156.

[35] L.A.O. Nunes, A.S. Souza, L.D. Carlos, O.L. Malta, Neodymium doped fluoroindogallate glasses as highly-sensitive luminescent non-contact thermometers, Opt. Mater. (Amst). 63 (2017). https://doi.org/10.1016/j.optmat.2016.08.038.

[36] C.D.S. Brites, S. Balabhadra, L.D. Carlos, Lanthanide- Based Thermometers: At the Cutting- Edge of Luminescence Thermometry, Adv. Opt. Mater. 7 (2019). https://doi.org/10.1002/adom.201801239.

[37] A.S. Souza, L.A.O. Nunes, I.G.N. Silva, F.A.M. Oliveira, L.L. da Luz, H.F. Brito, M.C.F.C. Felinto, R.A.S. Ferreira, S.A. Júnior, L.D. Carlos, O.L. Malta, Highly-sensitive Eu^{3+} ratiometric thermometers based on excited state absorption with predictable calibration, Nanoscale. 8 (2016). https://doi.org/10.1039/C6NR00158K.

[38] M.G. Nikolić, Ž. Antić, S. Ćulubrk, J.M. Nedeljković, M.D. Dramićanin, Temperature

sensing with Eu3+ doped TiO2 nanoparticles, Sensors Actuators B Chem. 201 (2014). https://doi.org/10.1016/j.snb.2014.04.108.

[39] G.N. Somero, Proteins and Temperature, Annu. Rev. Physiol. 57 (1995). https://doi.org/10.1146/annurev.ph.57.030195.000355.

[40] Brown Robert, Rickless P., A new method for the study of cell division and cell extension with some preliminary observations on the effect of temperature and of nutrients, Proc. R. Soc. London. Ser. B - Biol. Sci. 136 (1949). https://doi.org/10.1098/rspb.1949.0008.

[41] J. Hazel, The role of alterations in membrane lipid composition in enabling physiological adaptation of organisms to their physical environment, Prog. Lipid Res. 29 (1990). https://doi.org/10.1016/0163-7827(90)90002-3.

[42] A.M. Stark, S. Way, The use of thermovision in the detection of early breast cancer, Cancer. 33 (1974). https://doi.org/10.1002/1097-0142(197406)33:6<1664::AID-CNCR2820330629>3.0.CO;2-7.

[43] A.T. Maurelli, P.J. Sansonetti, Identification of a chromosomal gene controlling temperature-regulated expression of Shigella virulence., Proc. Natl. Acad. Sci. 85 (1988). https://doi.org/10.1073/pnas.85.8.2820.

[44] M. Karnebogen, D. Singer, M. Kallerhoff, R.-H. Ringert, Microcalorimetric investigations on isolated tumorous and non-tumorous tissue samples, Thermochim. Acta. 229 (1993). https://doi.org/10.1016/0040-6031(93)80322-2.

[45] G. Kucsko, P.C. Maurer, N.Y. Yao, M. Kubo, H.J. Noh, P.K. Lo, H. Park, M.D. Lukin, Nanometre-scale thermometry in a living cell, Nature. 500 (2013). https://doi.org/10.1038/nature12373.

[46] X. Wang, O.S. Wolfbeis, R.J. Meier, Luminescent probes and sensors for temperature, Chem. Soc. Rev. 42 (2013). https://doi.org/10.1039/c3cs60102a.

[47] O.A. Savchuk, P. Haro-González, J.J. Carvajal, D. Jaque, J. Massons, M. Aguiló, F. Díaz, Er:Yb:NaY2F5O up-converting nanoparticles for sub-tissue fluorescence lifetime thermal sensing, Nanoscale. 6 (2014) 9727–9733. https://doi.org/10.1039/c4nr02305f.

[48] R.R. Zairov, A.P. Dovzhenko, A.S. Sapunova, A.D. Voloshina, K.A. Sarkanich, A.G. Daminova, I.R. Nizameev, D. V. Lapaev, S.N. Sudakova, S.N. Podyachev, K.A. Petrov, A. Vomiero, A.R. Mustafina, Terbium(III)-thiacalix[4]arene nanosensor for highly sensitive intracellular monitoring of temperature changes within the 303–313 K range, Sci. Rep. 10 (2020) 1–13. https://doi.org/10.1038/s41598-020-77512-1.

[49] D. Vásquez Mazzotti, L. Alvarado, R. Puga, H. Loro, Calibration of remote nanothermometers using nanoparticles of NaYF 4 : Er 3+ , Yb 3+ , Nd 3+, in: J. Phys. Conf. Ser., Institute of Physics Publishing, 2018: p. 12023.

https://doi.org/10.1088/1742-6596/1143/1/012023.

[50] C. Bouzigues, T. Gacoin, A. Alexandrou, Biological Applications of Rare-Earth Based Nanoparticles, ACS Nano. 5 (2011). https://doi.org/10.1021/nn202378b.

[51] Z. Arsov, I. Urbančič, M. Garvas, D. Biglino, A. Ljubetič, T. Koklič, J. Štrancar, Fluorescence microspectroscopy as a tool to study mechanism of nanoparticles delivery into living cancer cells, Biomed. Opt. Express. 2 (2011). https://doi.org/10.1364/BOE.2.002083.

[52] K.T. Thurn, E.M.B. Brown, A. Wu, S. Vogt, B. Lai, J. Maser, T. Paunesku, G.E. Woloschak, Nanoparticles for Applications in Cellular Imaging, Nanoscale Res. Lett. 2 (2007). https://doi.org/10.1007/s11671-007-9081-5.

[53] K. Takei, V. Haucke, Clathrin-mediated endocytosis: membrane factors pull the trigger, Trends Cell Biol. 11 (2001). https://doi.org/10.1016/S0962-8924(01)02082-7.

[54] S.E.A. Gratton, P.A. Ropp, P.D. Pohlhaus, J.C. Luft, V.J. Madden, M.E. Napier, J.M. DeSimone, The effect of particle design on cellular internalization pathways, Proc. Natl. Acad. Sci. 105 (2008). https://doi.org/10.1073/pnas.0801763105.

[55] M. Garvas, A. Testen, P. Umek, A. Gloter, T. Koklic, J. Strancar, Protein Corona Prevents TiO2 Phototoxicity, PLoS One. 10 (2015). https://doi.org/10.1371/journal.pone.0129577.

[56] I. Urbančič, M. Garvas, B. Kokot, H. Majaron, P. Umek, H. Cassidy, M. Škarabot, F. Schneider, S. Galiani, Z. Arsov, T. Koklic, D. Matallanas, M. Čeh, I. Muševič, C. Eggeling, J. Štrancar, Nanoparticles Can Wrap Epithelial Cell Membranes and Relocate Them Across the Epithelial Cell Layer, Nano Lett. 18 (2018). https://doi.org/10.1021/acs.nanolett.8b02291.

Chapter 5

Conclusions and perspectives

Nowadays sensors can be considered as devices that extend the range of our senses. We can use different type of sensors to read/translate relevant information at real time from our complex surroundings and information from our body. Sensors can make our life more secure and healthy, advising about the out-side temperature, blood pressure or oxygenation. Due to their large relevance in our daily life, sensors have become an essential part of our life, however, the majority of the presently used sensors are bulky and/or old detection techniques, therefore they have high power consumption. With the aging of the population and the need of real time environmental quality control, there is an urgent need to develop sensors that are small, portable, autonomous and easy to manage and that have low power consumption. In this framework, nanomaterials having different mechanical, optical, and physicochemical properties from their bulk counterparts, can be used for the improvement of the known sensors and the development of novel sensor devices (Figure 5.1). In this work, the properties of nanomaterials (carbon nanotubes, bimetallic nanoparticles and europium(III)-doped titanium oxide) were used to develop two novel sensors, a chemical gas sensor and a temperature sensor.

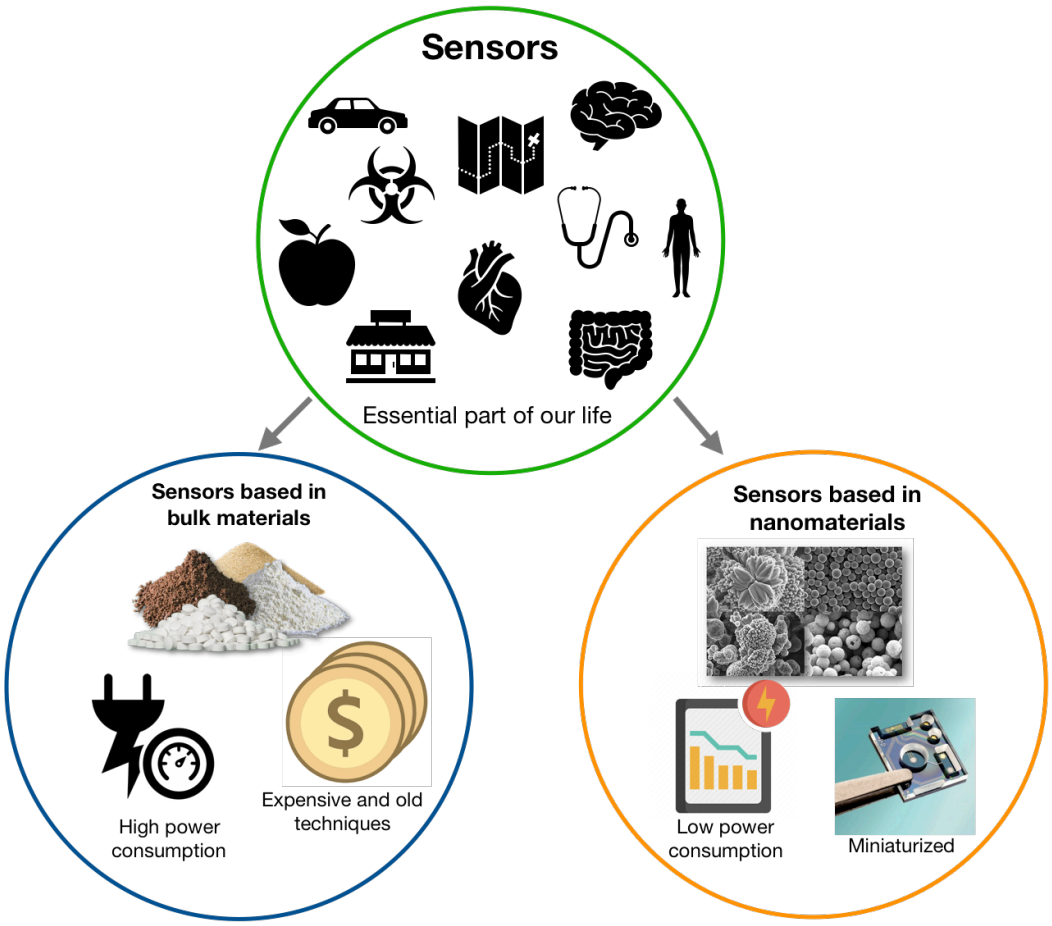

Figure 5.1. Sensors are an essential part of our lives. The majority of the sensors based bulk materials have high power consumptions and/or require expensive and old detection techniques. Taking advantage of nanomaterials properties may lead to the development of novel sensors that will be miniaturized, reliable and with low power consumptions.

Knowledge about synthesis, modification and characterization of nanomaterials was obtained during the development of the work presented in this thesis. Principally, ion irradiation and plasma sputtering deposition were the techniques best studied and employed for the modification of nanostructured materials. Characterization techniques like X-Ray photoelectron spectroscopy, Raman spectroscopy and photoluminescence spectroscopy were the most relevant techniques reviewed during this PhD thesis. This acquired knowledge allows to propose diverse perspectives to continue and improve the development of novel sensors.

For the case of chemical sensors based on carbon nanotubes for the detection of hazardous and toxic gases, decoration of carbon nanotubes with other bimetallic nanoparticles using different metals should be evaluated as catalytic *sensitizers* for the selective detection of

gases. Likewise, different transducer systems such as the fast Fourier transform (FFT) to extract sensor response features, can be investigated to achieve the development of selective, low power consumption, and low cost sensors.

On the other hand, for the case of temperature sensors, during this work the synthetized and characterized Eu^{3+}-TiO_2 nanosensors were demonstrated as effective nanothermometers of single cells. Measuring the luminescence of Eu^{3+}-TiO_2 nanoparticles internalized in cells was possible using fluorescence microspectroscopy. However, cell autofluorescence was observed when the emission spectrum of Eu^{3+}-TiO_2 was evaluated. The Eu^{3+} emission band evaluated was centered at 618 nm, right on the edge of the first biological window, as well as the Eu^{3+} excitation wavelength, resulting in an overlap between cell autofluorescence and europium emission spectrum. In this perspective, in order to completely avoid cell autofluorescence, different mechanisms are proposed to be evaluated, first use the lanthanide neodymium instead of europium to dope TiO_2. Nd^{3+} ions have thermally coupled transitions which excitation and emission wavelengths lay in the first and second biological windows respectively (Figure 5.2). In the same direction, the phenomenon known as upconversion, where sequential absorption of two or more photons leads to the emission of light at shorter wavelength than the excitation wavelength, can be used to excite Nd^{3+} and Eu^{3+} ions in TiO_2 with infrared wavelengths to avoid cell autofluorescence. The upconversion of Nd^{3+} and Eu^{3+} ions has been already studied by other authors [1–4].

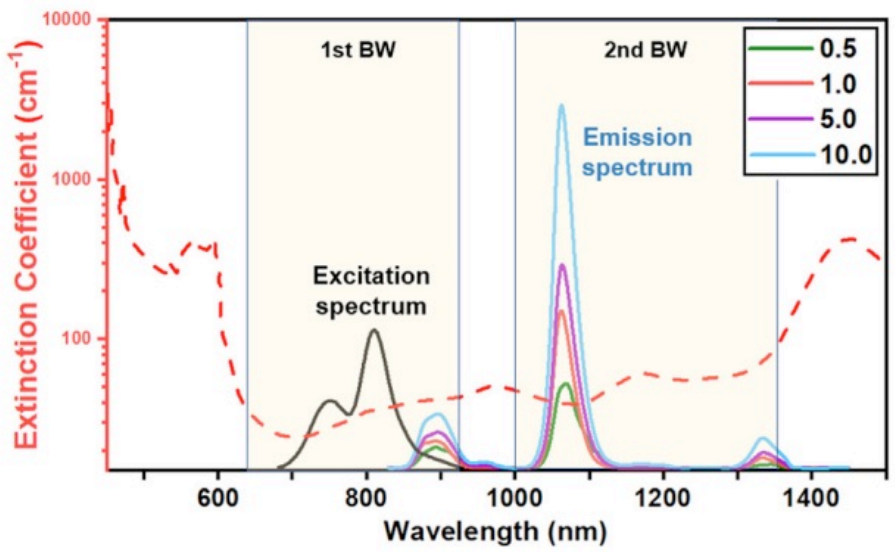

Figure 5.2. Scheme of the extinction spectrum of human tissue (dashed red line) overlapped with the excitation and emission spectrum of Nd^{3+}. The first and second biological windows (BW) are marked in the spectrum.

Even though the cell internalization of Eu^{3+}-TiO_2 nanoparticles into different cell lines was demostrated, the exact localization of Eu^{3+}-TiO_2 inside the cells was not evaluated. In this

perspective, Eu^{3+}-TiO_2 nanoparticles could be functionalized with different biomolecules, which might localize them at specific organelles, and in this way, they could be potentially used as nanothermometers for various cellular organelles, these investigations will lead us to a better understanding of the cell metabolism.

Finally, specific assays of toxicity and maximum tolerated dose should be performed to evaluate the use of Eu^{3+}-TiO_2 nanoparticles in more complex living organisms. Although the Eu^{+3}-TiO_2 nanoparticles showed to be a very reliable nanothermometer, as expected for such a stable material in different harsh chemical environments, further studies are needed as cells present a complex cytosolic environment with different properties, such as viscosity, pH as well as ion concentrations, that might affect luminescence properties of Eu^{+3}-TiO_2 nanoparticles.

References

[1] S. Hao, G. Chen, C. Yang, W. Shao, W. Wei, Y. Liu, P.N. Prasad, Nd3+-Sensitized multicolor upconversion luminescence from a sandwiched core/shell/shell nanostructure, Nanoscale. 9 (2017) 10633–10638. https://doi.org/10.1039/c7nr02594g.

[2] P. Parnicka, W. Lisowski, T. Klimczuk, J. Łuczak, A. Żak, A. Zaleska-Medynska, Visible-light-driven lanthanide-organic-frameworks modified TiO2 photocatalysts utilizing up-conversion effect, Appl. Catal. B Environ. 291 (2021) 120056. https://doi.org/10.1016/j.apcatb.2021.120056.

[3] X. Liu, Y. Li, T. Aidilibike, J. Guo, W. Di, W. Qin, Pure red upconversion emission from CaF2:Yb3+/Eu3+, J. Lumin. 185 (2017) 247–250. https://doi.org/10.1016/j.jlumin.2017.01.023.

[4] X. Huang, Dual-model upconversion luminescence from NaGdF4:Nd/Yb/Tm@NaGdF4:Eu/Tb core-shell nanoparticles, J. Alloys Compd. 628 (2015) 240–244. https://doi.org/10.1016/j.jallcom.2014.12.178.

Appendix

In this section, a short description of the techniques used for the characterization of the sensing materials is presented. In particular, Raman Spectroscopy, X-Ray photoelectron spectroscopy (XPS), and transmission and scanning electron microscopy (TEM and SEM) were used for both sensors Eu^{3+}-TiO_2 and Ni-Pd-Ox-CNTs, these techniques are described first. In addition, photoluminescence spectroscopy, X-Ray diffraction analysis (XRD) and spectral imaging fluorescence microscopy used to characterize the Eu^{3+}-TiO_2 nanoparticles, are described at the end of the Appendix (Figure A.1).

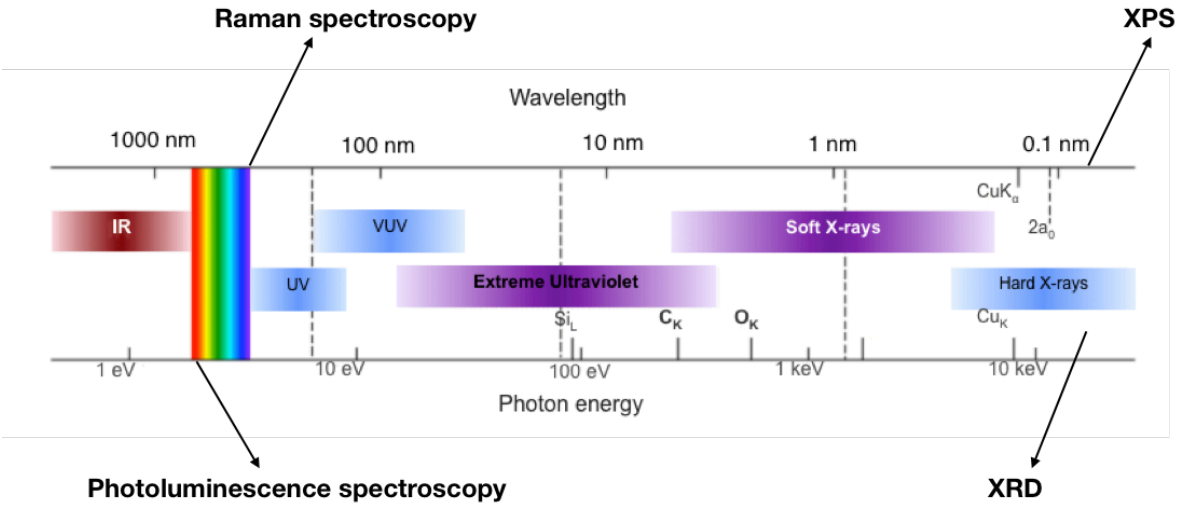

Figure A.1. Electromagnetic radiation spectrum. Raman spectroscopy, photoluminescence spectroscopy, XPS and XRD techniques are positioned in the spectrum according to their excitation sources.

A.1 Raman spectroscopy

Molecules and crystals vibrate with frequencies determined by the mass of their atoms and the force of their bonds. These mechanical frequencies are always in the range of 10^{12}–10^{14} Hz (3–300 µm), in the infrared region of the spectrum, for molecules and crystals.

Raman spectroscopy is sensitive to the atomic arrangement and chemical bonding, this is why it is a structural analysis technique, the Raman spectrum can detect changes in the length, strength and arrangement of bonds. Information about defects and disorder can be obtained

from this technique, however, information about chemical composition is not directly obtained from Raman spectroscopy [1].

Principles

The sample is irradiated with a monochromatic light, usually from a laser in the visible, near infrared or near ultraviolet, a small part of energy from the light beam is storaged by the chemical bonds of the sample, when relaxation occurs, the storaged energy is irradiated and different scattering geometrics can be observed, the vast majority of the energy is irradiated at the same frequency as that of the incident light, known as Raleigh scattering. Nevertheless, a minor part of the storaged energy is transferred to the sample and excites its vibrational modes, resulting in the energy from the light beam being shifted down, this phenomenon is named Stokes scattering. The contrary process can also occur, in the sample there are some vibrational states that are already excited by thermal processes, this exited vibrational states can add their energy to the beam light so the energy from the light beam being shifted up, this is known as anti-Stokes scattering. These three scattering geometries are observed in the Raman spectrum of the samples (Figure A.2). Rayleigh scattering is observed as a strong central line in the spectrum, Stokes scattering lines are observed at lower frequencies that the incident beam with lower intensities than Rayleigh lines, the separation from Stokes and Rayleigh lines gives direct information about the vibrational frequencies of the samples. The anti-Stokes lines appear at higher frequencies that Rayleigh lines and are a mirror image from Stokes lines.

Only Stokes scattering lines are used for Raman spectroscopy due to the low intensity of anti-Stokes scattering lines associated to its strong temperature dependency (anti-Stokes intensities depends on the existence of thermally active vibrational states).

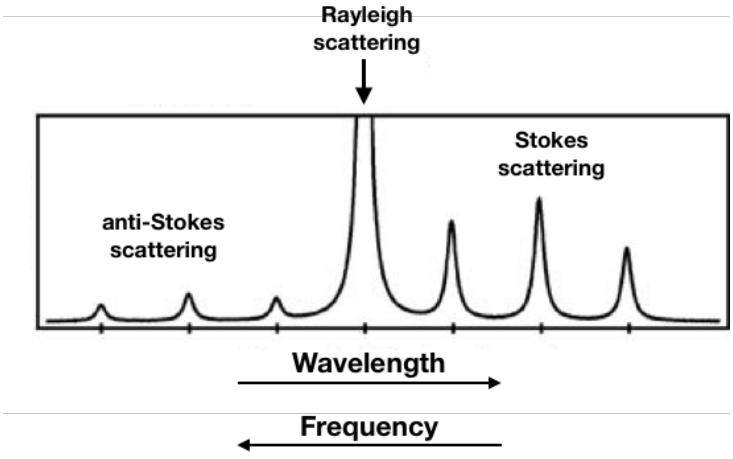

Figure A.2. Schematic representation of Rayleigh, Stokes and anti-Stokes scattering lines in a Raman spectrum.

The majority of the Raman spectrometers report the difference between Stokes lines and Rayleigh lines, to directly observed the vibrational frequencies of the sample, this difference on frequencies is named wavenumber.

Raman spectrometer

Two types of Raman spectrometers are the most commercialized devices: dispersive spectrometers and Fourier-transform Raman spectrometers. However, both types have a general instrumentation (Figure A.3). A light source brought into the sample, a dispersion system and a detection system.

The usual light source for Raman spectrometers are lasers. In general, lasers with wavelengths in the UV area (< 200 nm) until the near infrared (1064 nm) are used, the wavelength selected would depend of the type of sample that will be analyzed [2]. A polarization rotator is usually used to control the polarization orientation with respect to the sample.

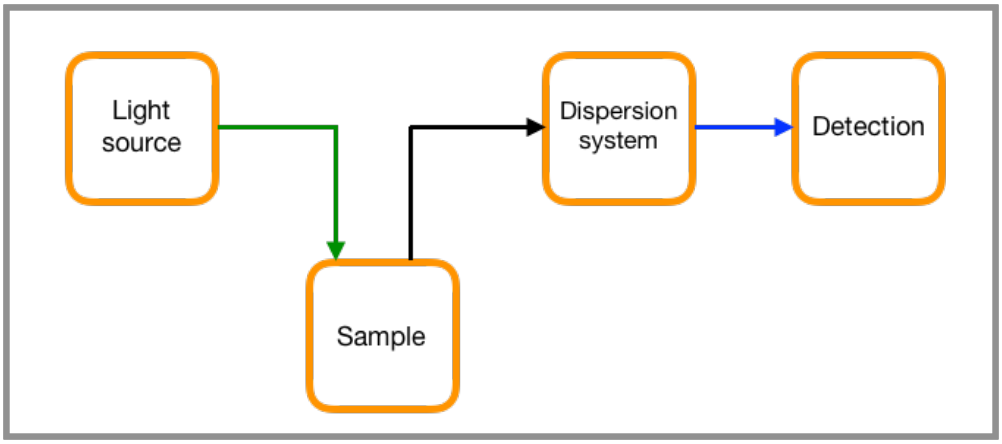

Figure A.3. Diagram of a typical Raman spectrometer.

Different types of detectors are used depending on the spectrometer, for the case of dispersive instruments single or multi-channel detectors are utilized, and for Fourier-transform devices semiconductor like silicon and germanium are used. Photomultiplier tubes are used in single channel detections, this method have the disadvantage of being high time-consuming because only one wavelength can be measured at the time and the analysis of the complete spectrum needs to be done sequentially, conversely, with the multichannel detector different wavelengths are detected at the same time. The most common used multichannel detectors are charge-coupled device (CCD) detectors these detectors consist of a 2-dimensional array of light sensitive elements; those elements are known as pixels. Each pixel interacts with a certain wavelength of light, and the entire spectrum is captured at one time [1,2]. FT-Raman

devices are equipped with semiconductor detectors with small band gap that allows low energy photons to create electronic currents in the semiconductor.

Referring to the dispersion systems, all Raman spectrometers need to be able of disperse light in function of wavelength. The dispersive Raman spectrometers use the diffraction of light, diffraction gratings are usually used, while as it name indicates FT-Raman spectrometers use Fourier transformations to obtain the spectrum. The Michelson interferometer is used in FT-Raman spectrometers, this consist of a beam-splitter and two mirrors, one mirror is fixed and the other can be moved in performance. In the beam splitter, half of the light hit the fixed mirror and the other half hits the mobile mirror, both beams are sent back to the splitter and then sent to the detector. These two beams generate constructive or destructive interference, so the detector register or not a signal depending if the mirror is moved. So the detector detects signal as a function of time. During Raman spectrum recording, light of different wavelengths arrives to the interferometer, each wavelength generates its own pattern and a interferogram is obtained. To obtain a normal Raman spectrum, an inverse Fourier-transformation is performed on the interferogram [3].

Samples requisites for Raman spectroscopy

Raman spectroscopy can be recorded in a vast number or samples with different form, particle size and compositions. The Raman spectrum from liquids, powders and polycrystalline solids, single crystals, and thick and thin films can be acquired. Liquid samples required to be supported in a special cell with optical windows at right angles. The size of solid samples is not usually a problem for Raman spectroscopy, (particles with sizes higher than 100nm can be measured). The Raman spectrum from powders can be realized by creating pellets of the sample, these pellets together with polycrystalline bulk specimens like ceramics and rocks are measured through the reflection of the laser from the sample surface. For the case of films, the minimal thickness at which Raman spectroscopy can be performed varies according to the transparency of sample but generally is in the range of few μm [1].

Fingerprinting

The Raman spectrum is composed of a pattern of relatively sharp lines for molecules and crystals. The wavenumber range goes from 50 cm^{-1} to 3500 cm^{-1}; however, the majority of molecular vibrations are within the range of 50 cm^{-1}–1800 cm^{-1}. The Raman spectrum can be considered as a fingerprint for each material. Identification of substances can be realized by the analysis of the Raman spectrum and a comparison of this with catalogs of known materials [4].

Defects and Structural disorder

Lattice defects, like vacancies in crystals and other structural defects in solids are observed

in Raman spectra like a broadening of the Raman lines. For the specific case of noncrystalline solids the Raman spectra shows broad bands centered at the frequencies corresponding to the vibrational modes of the corresponding crystal. The formation of glasses can be followed by Raman spectroscopy due to the easy distinction between the sharp lines of crystals and the weaker and broader glass Raman bands.

Microfocus Raman Spectroscopic Analysis

The conjugation of a Raman spectrometer and an optical microscope allowed to obtain spectra with spatial resolution of few μm (limited by the spatial resolution of the microscope). This conjugation works thanks to a beam splitter which allows the laser to pass into the microscope objective and arrive to the sample that is placed in a normal microscope stage. In the same way, the scattered light passes through the splitter and reaches an entrance slit to the dispersion system [1]. This type of Raman spectroscopy permits to do a mapping in the sample surface, studying in this way individual grains, grain boundaries, growth zones, and phase separated region on one sample [5,6]. Liquid-solid interfaces can also be analyzed using microfocus Raman employing water immersion lens [7], furthermore, films composition can likewise be investigated with microfocus spectra [8].

Raman spectroscopy analysis was performed using a Microfocus-Raman spectrometer system from Senterra Bruker Optik GmbH, Ettlingen, Germany. The resolution of the Raman spectra acquired is 3 cm^{-1}. The excitation source used for all the spectra showed in this work is a laser with a wavelength of 532 nm and 20 mW of power. The spectra were recorded with 5 seconds of acquisition time.

A.2 X-Ray Photoelectron Spectroscopy

Basic principles: photoemission

The process when a photon is absorbed by a material and an electron is emitted is named photoemission. Albert Einstein was awarded with the Nobel Prize in 1921 for his contribution to interpret photoemission. He postulated the photoelectric effect as the absorption of the necessary energy in form of light for electrons to escape from a metal, and he proposed that light was composed of discrete quanta of energy, and that this energy was proportional to the frequency of the light (hv). Equation A.1 describes the photoelectric effect; this equation is the basis of photoelectron spectroscopy:

$$E_K = hv - \phi - B_E \tag{A.1}$$

Knowing the energy of the photons, (hv) and when kinetic energy of the photoemitted electron (E_K) is measured, the binding energy (B_E) of the electrons can be calculated (Figure A.4).

The binding energy is generally referred to the Fermi level in solids (E_f) and in free atoms or molecules to the vacuum level (E_{vac}). ϕ is the energy difference between the vacuum level and the Fermi level and is named as photoelectric threshold energy. In real data accumulation for the case of solids, the Fermi energy is taken as the natural "zero" in the photoemission spectrum.

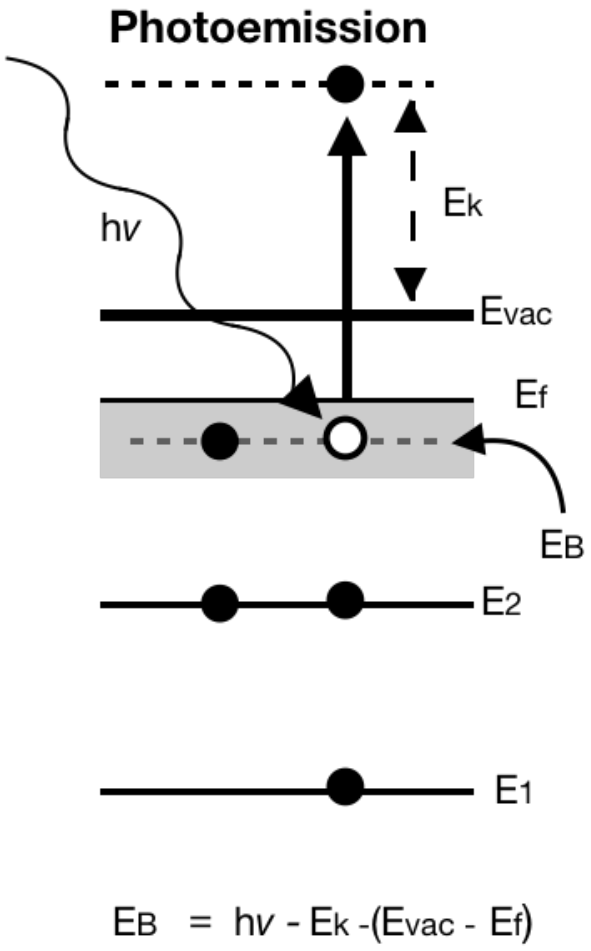

Figure A.4. Schematic representation of photoemission process.

For the interpretation of photoemission experiments two models have been proposed. The one step model describes the photoemission process as the excitation of an occupied electronic state inside a solid by the absorption of an incident photon into an empty state outside the solid. The ejected electron must have a velocity pointing away from the solid in order to be analyzed and detected [9]. Although this model seems to be very simple, present various problems in the computational calculations needed to generate a quantitative evaluation. On the other hand, the three-step model, a phenomenological approach, has proved to be very useful. This model supposes an excitation of an electron from an occupied valence state to an empty conduction state (step 1) this is followed by the propagation of the photoelectron to the surface (step 2) and transmission across the surface (step 3).

Sampling depth

For the case of photoemission, the sampling depth becomes the escape depth of the emitted electrons, which depends on their energy. The mean free path of the electrons is determined by electron-electron and electron-phonon collisions. The scape depth plotted against the energy falls on a universal curve for most solids (Figure A.5), these scape depth is in the range of 5-60 Å. Such small scape depth is the reason that photoemission spectroscopy is considered as a surface technique rather than a bulk technique.

Photoelectron spectroscopies require to be performed in Ultra High Vacuum systems (UHV) due to the small scape depth of the emitted photoelectrons, in order to obtain useful information from the surface of the sample, and in this way learn about the bulk properties of the material, the surface of the sample must be atomically clean to prevent interference from adsorbed contaminants, this is only achieved if the measurements are carried out inside UHV systems. Ultra-high vacuum is achieved with turbomolecular pumps, ion pumps, sublimation pumps and diffusion pumps depending of the type of device.

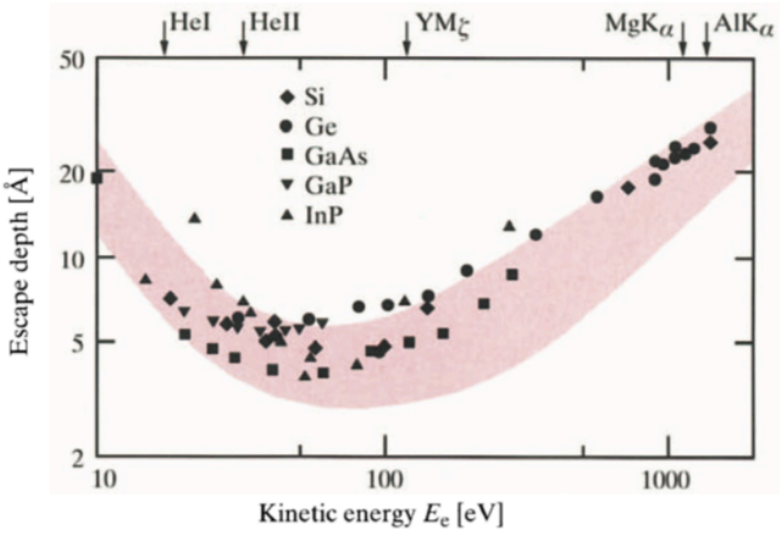

Figure A.5. Universal curve of electron escape depth as function of kinetic energy in various solids. Adapted from reference [9].

Essential parts of an X-Ray photoelectron spectrometer

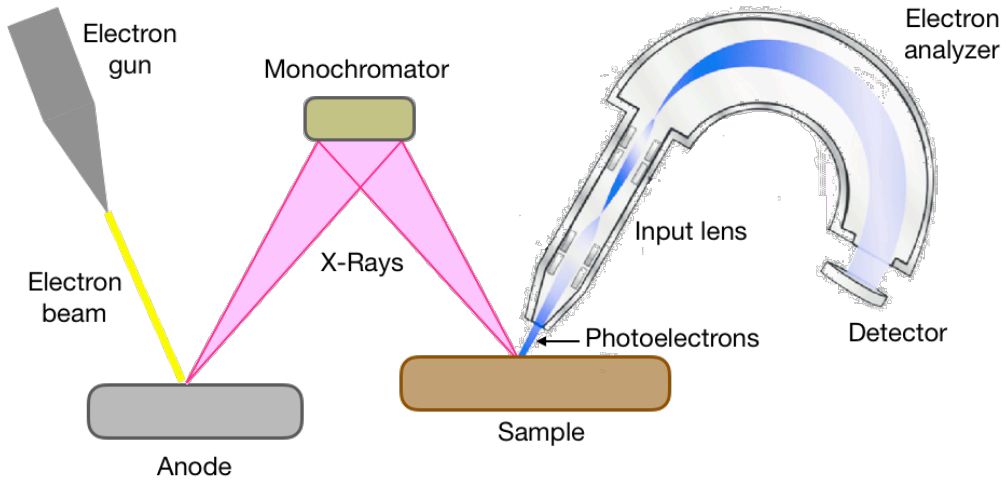

Figure A.6. Diagram of a typical X-Ray photoelectron spectrometer device.

X-Ray source

X-ray tubes are used as light source. An X-Ray tube converts electrical input into X-Rays, inside the tube there is a cathode that produces an electron beam that is collected in the anode, a high voltage power source is connected across the system to accelerate the electrons. The X-Ray specific energy depends of the anode material and the accelerating voltage. The most common emission line used for the anode is the *K*α of aluminum at 1486.6eV, for this kind of source a monochromator is used to reduce the width of line emission from ~ 1eV to ~ 0.1 eV, allowing to obtain better resolutions, however some loss of intensity and deterioration of the signal is generated. Aluminum *K*α photons produce electrons with energies around 1.4 keV and escape depths of about 40 Å. This photon energy allows to investigate core levels and valence of atoms.

Electron analyzers

Hemispherical analyzers are the most common analyzers for photoelectron spectroscopies (Figure A.7). This type of analyzer is based in electrostatic forces. It is composed of two hemispherical metallic walls, with an electrostatic potential (V_a) applied between the walls. Usually, electron lenses are used to slow the electrons before entering to the analyzer to increase resolution and also to define an area of analysis in the sample. Once the electrons are inside the analyzer only the ones with a given energy E_e determined by V_a are focused to the exit slit of the analyzer and fall on the detector. All other electrons with different energy collapse into the metallic walls. The photoelectron spectrum is obtained measuring the current in the detector.

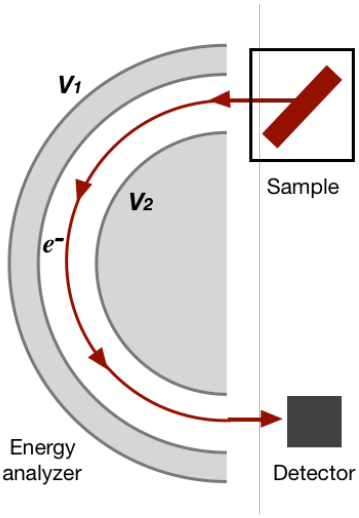

Figure A.7. Diagram of hemispherical photoelectron analyzer.

Detector

A channeltron, that is an electron multiplier, is used as a detector, it is composed of a glass funnel followed by a tube that has in its interior a secondary emitter. This emitter produces a number of electrons for each electron detected. There are two types of channeltrons, single and multiple channel detectors. Using single channel detectors only one electron energy is recorded at a given time. On the other hand, multichannel systems allow the simultaneous detection of the whole photoelectron spectrum, in this way, the signal-to-noise ratio is highly augmented. Additionally, the use of multichannel detectors decreases considerably the measurement time.

A general diagram for X-Ray photoelectron spectrometer used in this work is showed in the Figure A.6. The spectrometer used for all the XPS spectra recorded is a VERSAPROBE PHI 5000 from Physical Electronics, Chanhassen, MN U.S. Equipped with a monochromatic Al Kα X-ray source. Core level spectra of the samples were recorded with an energy resolution of 0.6 eV.

Core levels and valence band

The electron energy levels of atoms can be classified in core levels, which are tightly bound to the nucleus, and valence levels, which are further from the nucleus and as consequence only weakly bounded to it. As an example, for the carbon atom, the C1s level is a core level and the C2s and 2p levels are valence levels. XPS can be used in the valence band as well as in the core-level regime. However, the structure of the valence band is best investigated with lower photon energies because of the superior energy and momentum resolution then

available.

Photoelectrons originating from the core levels identify the elements present in the samples from their binding energies. The relative concentrations of the different elements present in a sample can be determined from relative peak intensities. With X-Ray photoelectron spectroscopy is possible to identify all elements except hydrogen and helium.

After photoelectron emission, the other electrons in the atom respond to the hole created by the ejected electron, one effect of this response is the spin-orbit splitting from a coupling of the spin of the unpaired electron left behind in the orbital with the angular momentum of that orbital, from this splitting two possible different energy final states are generated (Figure A.8). The splitting occurs for all levels with exception of s levels which have no angular momentum. The splitting is observed in XPS spectra as double peaks from one energy level. For example, the *p*-like core level split into the components $j = \frac{3}{2}$ and $j = \frac{1}{2}$ (the splitting value depends of each atom for example for Ti 2p in TiO_2 is 6.17 eV). Similarly, *d*-like core levels split into $j = \frac{5}{2}$ and $j = \frac{3}{2}$, for example in Eu *3d* the splitting is 5.2 eV.

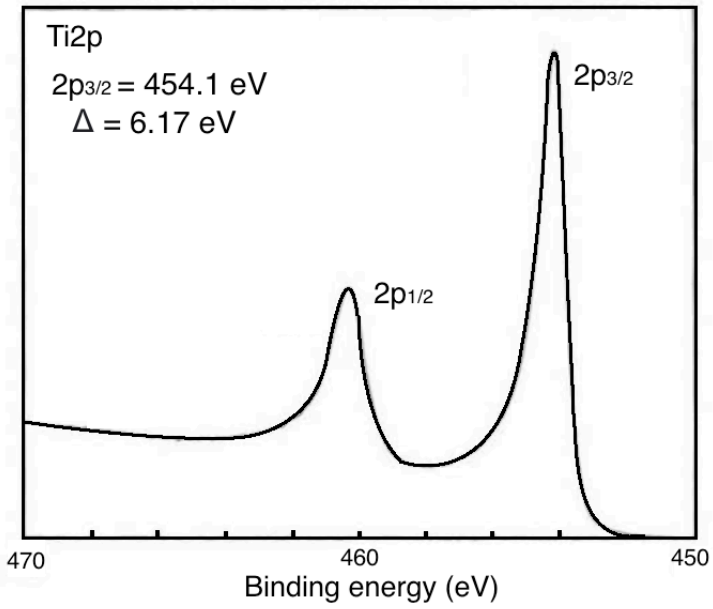

Figure A.8. Ti2p core level XPS spectrum showing the spin-orbit splitting into $Ti2p_{3/2}$ and $Ti2p_{1/2}$ in TiO_2.

Binding energy and chemical shift

The binding energy at which photoelectrons appear in the XPS spectrum are different and

very well known for each atom. This information is used to identify the chemical composition of the samples. However, exist a small change in the binding energy of a particular core level between different chemical forms of the same atom, this change is called the "chemical shift" and provide additional information of the chemical configuration of the sample surface. The typical range from the chemical shift goes from 1 to several eV, however, in some cases the shift can be even smaller [10]. The explanation for this chemical shift remains on the Coulomb forces interactions that electrons in core levels feel, even though it is well known that valence electrons are the mostly involved in forming bonds and core electrons states remain almost unchanged, the chemical environment induces small changes in the Coulomb interactions of core electrons. Generally, the binding energy increases with increasing charge on the atom.

Auger electron emission

After the emission of the photoelectron, the hole in the energy level left behind can be filled up by another electron from a more energetic level, the energy released from this transition can induce the ejection of a second electron, this is called Auger electron emission. Even if a special technique is used to study the Auger electrons (Auger electron spectroscopy), during a normal XPS measurements the Auger electron contribution peaks are superimposed in the spectrum, the analysis of Auger peaks provides additional information about the elements present in the samples. For example, chemical shifts of Auger peaks are larger than normal photoelectrons, this permits to identify chemical states of atoms that are not possible to identify with photoelectrons. This is the case for the distinction of Zn^{2+} and Zn^{0} states [10].

A.3 Electron microscopies

Microscopy involves the study of objects that are too small to be examined by the unaided eye. A microscope is an optical system that transforms an object into an image.

In the 20th century, physicists discovered that material particles such as electrons possess a wavelike character. The electron wavelength is given by the following equation:

$$\lambda = \frac{h}{p} = \frac{h}{mv} \tag{A.2}$$

where h = is the Planck constant; p, m, and v represent the momentum, mass, and speed of the electron, respectively.

For the case of electrons being emitted into vacuum from a heated filament and accelerated through a potential difference of 50 V, $v \approx 4.2\times10^{6}$ m/s and $\lambda \approx 0.17$ nm. Since this wavelength is close to atomic dimensions, these emitted electrons are strongly diffracted from the regular array of atoms present at the surface of a crystal. Raising the accelerating potential, the electron wavelength decrease to about 5 pm and such higher-energy electrons

can penetrate distances of several microns (μm) into a solid. If this solid is crystalline, the electrons are diffracted by planes of atoms inside the material. When these diffracted electrons are focused, an image with a spatial resolution superior to that of the light-optical microscope can be created.

A.3.1 Transmission electron microscopy

Transmission electron microscopy (TEM) is is a technique in which a beam of electrons is transmitted through an ultra-thin specimen (typically lower than 100 nm thick), TEM is capable of recording magnified images of a thin specimen, typically with a magnification in the range 10^3–10^6. This technique allows to reach high resolution image at a small size scale (typically 1–2 nm) and is thus necessary to get space-resolved information about the distribution of the crystalline composition. In addition, the instrument can be used to produce electron-diffraction patterns, useful for analyzing the properties of crystalline specimens. The instrument used in TEM can be divided in the following three sections [11] (Figure A.9):

Illumination system. Consist of the electron gun which produces the beam of electrons together with two or more condenser lenses that focus the electrons onto the specimen.

Specimen stage. Allows specimens to be held stationary, or else intentionally moved, and to be inserted or withdrawn from the TEM. Its mechanical stability is an important factor in determining the spatial resolution of the TEM image.

Imaging system. Consisting of the objective lens and intermediate and projector lenses, which focus the electrons passing through the specimen to form a real, highly magnified image. The image-recording system converts the electron image into some form perceptible to the human eye. The image-recording system usually consists of a fluorescent screen for viewing and focusing the image and a digital camera for permanent records. In addition, a vacuum system, consisting of pumps and their associated gauges and valves, and power supplies are required. How the imaging lenses are operated determines the magnification of the TEM image, while their design specifications largely determine the spatial resolution that can be obtained from the microscope [12].

The TEM images reported in this thesis were taken using a transmission electron microscope JEM-1011 Jeol Ltd. Tokyo, Japan. For some other samples a TECNAI T20 microscope working under 200 kV was used.

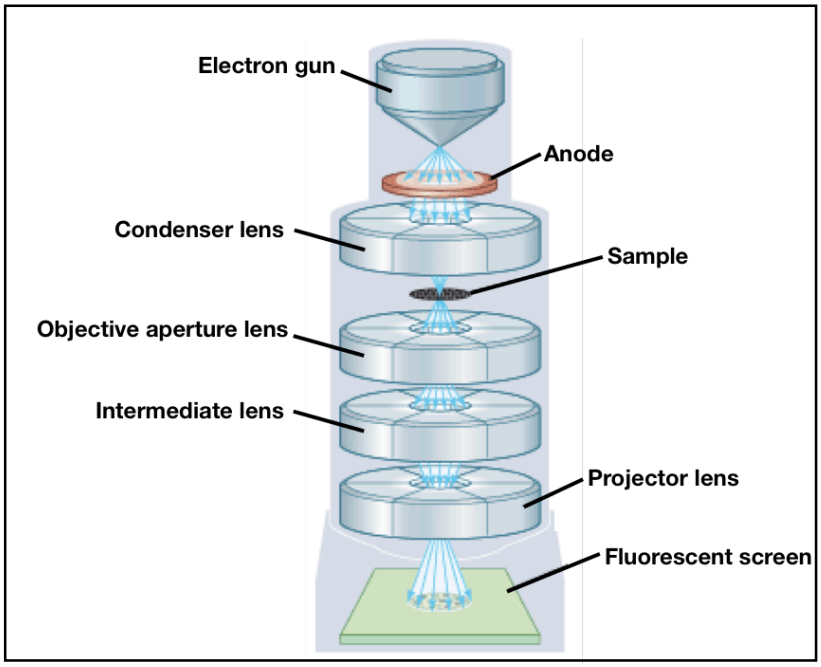

Figure A.9. Schematic representation of a transmission electron microscope.

A.3.2 Scanning electron microscopy

Scanning electron microscope (SEM**)**, is another type of electron microscope designed for directly studying the surfaces of solid objects, that utilizes a beam of focused electrons of relatively low energy as an electron probe that is scanned in a regular manner over the sample. The electron source and electromagnetic lenses that generate and focus the beam are like those described for the transmission electron microscope (TEM). The action of the electron beam stimulates emission of high-energy backscattered electrons and low-energy secondary electrons from the surface of the specimen.

The electron source used in the SEM can be a tungsten filament, a LaB_6 crystal or a tungsten field-emission tip, from the electron source is generated the electron beam which is then focused on the sample through precise electromagnetic lenses operating under vacuum condition. Because the maximum accelerating voltage (typically 30 kV) is lower than for a TEM, the electron gun is smaller, requiring less insulation. Axially symmetric magnetic lenses are used but they are also smaller than the lenses employed in the TEM (Figure A.10) [12].

Whereas the conventional TEM uses a stationary incident beam, the electron probe of an SEM is scanned horizontally across the specimen in two perpendicular (x and y) directions. The electron beam scanned over the surface interact with it and penetrate a few μm. Consequently, electrons (secondary, backscattered and Auger) and X-rays are emitted. In Figure A.11, the energy distribution of the emitted electrons is illustrated for irradiation with a primary electron beam. A consistent part of the emitted electrons undergoes several elastic scatterings that cause the change in direction until the electrons leave the sample again

(backscattering process). The so-called "secondary electrons" represent the part of emitted electrons that suffers inelastic scattering between energetic electrons from the beam and the conduction band electrons. The secondary electrons are characterized by low energy (E< 50 eV) and consequently their mean free path in the sample's volume is reduced so that the probability the electron leaves the sample is exponentially decaying with depth. SEM images are produced by collecting the emitted secondary electrons through a positive biased detector. However, there exists also backscattered electron detectors that allow the acquisition of SEM images with better chemical contrast and elemental composition information, respectively (Figure A.11).

The SEM images reported in this thesis were taken using a JEOL-JSM-7500F-Field Emission Scanning Electron Microscope operated at 2 kV.

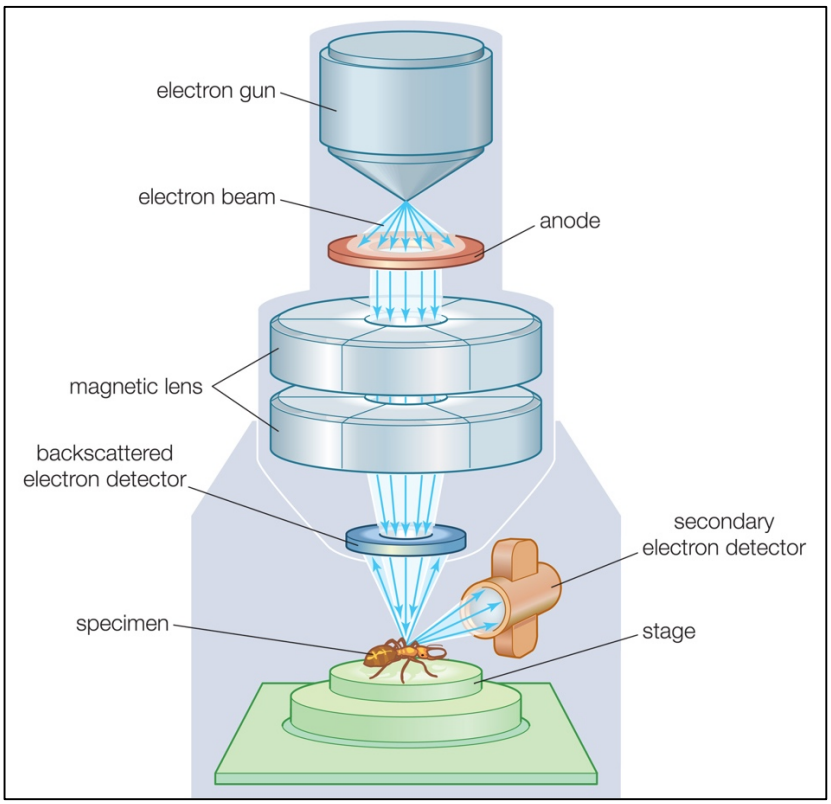

Figure A.10. Schematic representation of a scanning electron microscope.

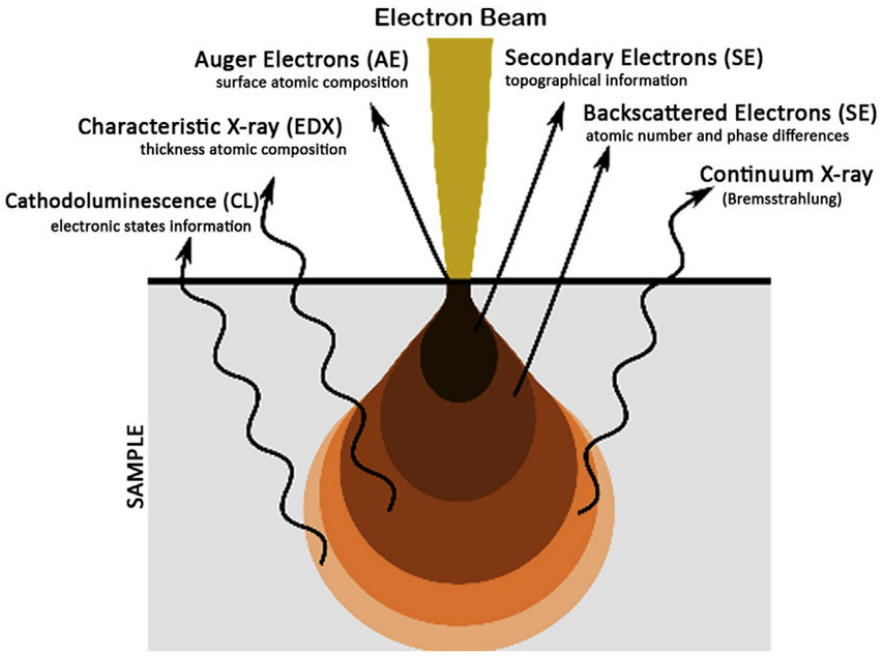

Figure A.11. Signals emitted from different parts of the interaction volume.

A.4 X-Ray diffraction analysis

X-ray diffraction (XRD) is a powerful nondestructive technique for characterizing crystalline materials. All crystalline materials adopt a regular distribution of atoms or ions in space. The simplest portion of the structure that reproduces the entire crystal when repeated by translation is defined as a unit cell. XRD provides information on structures, phases, preferred crystal orientations (texture), and other structural parameters, such as average grain size, crystallinity, strain, and crystal defects. XRD peaks are produced by constructive interference of a monochromatic beam of X-rays scattered at specific angles from each set of lattice planes in a sample, following the Bragg's rule [17] (Equation A.3).

$$n\lambda = 2d \sin\theta \tag{A.3}$$

where d is the interplanar spacing of the detected crystal phase, θ is the incident angle resolving the interference condition and λ is the X-rays wavelength.

Diffraction is therefore essentially a scattering phenomenon. Atoms scatter incident radiation in all directions, and in some directions the scattered rays will be completely in phase and therefore present constructive interference to form diffracted rays (Figure A.12). Since atoms are periodically arranged in a lattice, destructive interference occurs in most directions but constructive interference occurs in a few directions and diffracted rays are formed.

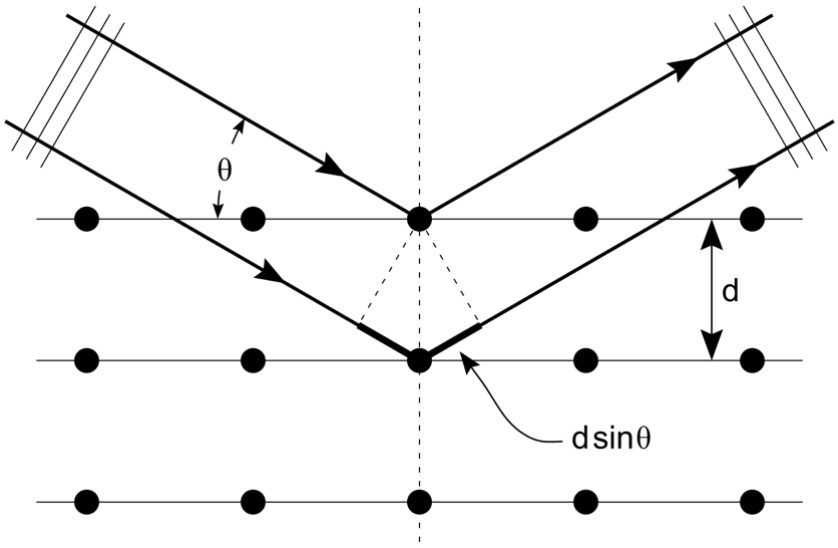

Figure A.12. Schematic representation of Bragg diffraction.

The peak intensities are determined by the atomic positions within the lattice planes. Consequently, the XRD pattern is the fingerprint of periodic atomic arrangements in a given material. An online search of a standard database for X-ray powder diffraction patterns enables quick phase identification for a large variety of crystalline samples.

The unit of measurement of the X-Ray wavelength is in angstroms (Å), and the x-rays used in diffraction have wavelengths in the range 0.5-2.5 Å.

Diffractometers consist of an X-Ray source, generally X-Ray tubes are used, and a detector to collect the diffracted X-Rays. Scintillation and semiconductors detectors are commonly used and they are based in the ability of X-Rays to ionize atoms.

X-ray powder diffraction carried out in this thesis were performed using a D4 Endeavor, Bruker AXS diffractometer with Cu-Kα radiation (λ = 1.5406 Å) and a Sol-X energy-dispersive detector was used to determine phase composition. Diffractograms were measured in the 2θ angular range between 20º and 80º with the step size of 0.02 s^{-1} (collection time of 3 s).

A.5 Photoluminescence spectroscopy

Photoluminescence is a technique used in many fields, such as, biomedicine, biology, nanotechnology among many others [13].

Luminescence is the emission of light from electronic excited states for any substance, the process of luminescence begins when light is directed onto a substance, the substance absorbed a photon and photoexcitation occurs, the substance cannot remain in the excited

state for long and, therefore, it releases the absorbed energy in the form of a photon and relaxes to its basal state.

Luminescence can be classified in fluorescence and phosphorescence depending on the nature of the excited state. For the case of fluorescence, the electron in the excited orbital is paired (by opposite spin) to the second electron in the ground-state orbital. Consequently, return to the ground state is spin allowed and occurs rapidly by emission of a photon (typical fluorescence lifetime is near 10 ns). Phosphorescence is emission of light from triplet excited states, in which the electron in the excited orbital has the same spin orientation as the ground-state electron. Transitions to the ground state are forbidden and the emission rates are slow (phosphorescence lifetimes are typically milliseconds to seconds) [13].

Jablonski diagram

The process of absorption and emission of light are typically exemplified using the Jablonski diagram (Figure A.13). The single states are tagged as S_0, S_1 and S_2. Electronic transitions between states are represented with vertical arrows, these transitions are instantaneous. Absorption of light is represented with the blue arrow, after absorption several process can happen, the substance is excited to a vibrational level S_2, in most of the cases, occurs a rapid non-radiative relaxation to the vibrational level S_1 called internal conversion (IC), this process is marked in the diagram as a black index arrow. The emission of light (fluorescence) occurs from S_1, a thermally equilibrated excited state. From the S_1 state an intersystem crossing can also occur, this is a spin conversion to the first triplet state T_2, then after internal conversion to T_1 emission of light occurs, this type of emission is known as phosphorescence and is shifted to longer wavelengths than fluorescence [13].

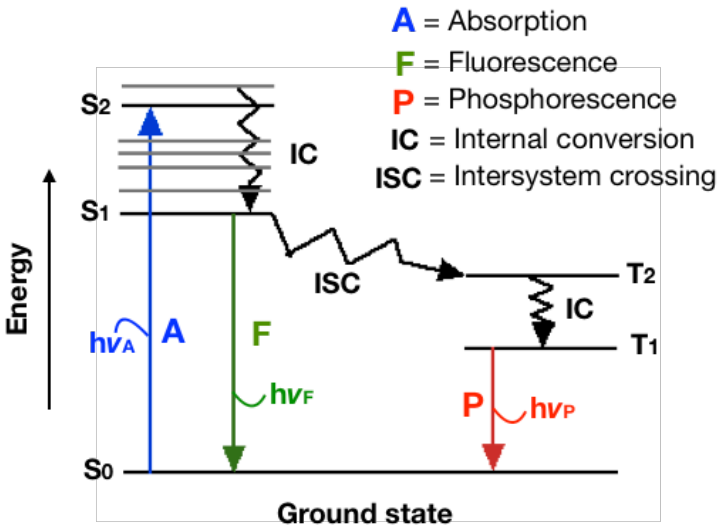

Figure A.13. Modified Jablonski diagram.

Characteristics of luminescence emission

The energy of the light emitted during luminescence is generally less than the light absorbed, this phenomenon is called the Stokes shift [14] (Figure A.14). The explanation for this shift is the rapid decay from the excited level S_2 to the lowest vibrational level S_1 after the absorption. Besides this, the most of luminescent molecules decay to higher vibrational states than S_0 due to thermalization process. Other phenomena that trigger the loss of excitation energy are solvent effects, excited-state reactions, complex formation and energy transfer. Another characteristic of luminescence is that the same emission spectrum is observed independently of the excitation wavelength. This is observed due to the dissipation of energy to the lowest vibrational level S_1 when the luminescent object is excited with more energetic photons.

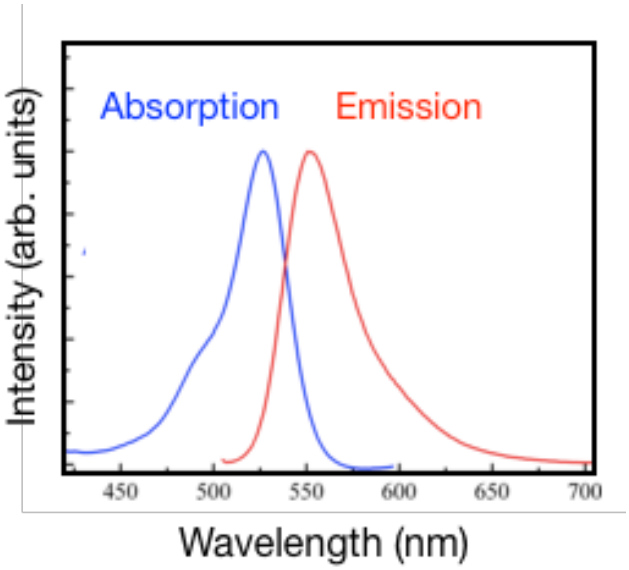

Figure A.14. Absorption and emission spectra from a substance denoting the Stokes shift.

The luminescent yield and lifetime are the most important characteristics of a luminescent object. The quantum yield is defined as the number of emitted photons relative to the number of absorbed photons. Substances with the brightest emission have the larger quantum yield. In the other hand, lifetime luminescence is an average value of the time the substance spends in the excited state before emitting a photon and returning to the ground state, the lifetime of different objects varies from picoseconds to hundreds of nanoseconds [15].

The intensity of luminescence can be affected by several factors; this decrease of intensity is known as quenching. When the quenching occurs due to the contact with some other molecule is called collisional quenching and the molecule that induce it is the quencher. The mechanisms of quenching depend on the molecules involved. For example, the quenching of indole by acrylamide is due to electron transfer. Large number of molecules can trigger the

quenching of luminescent substance like halogens, amides and electron deficient molecules. Quenching can be also incited by other process like diminution of the incident light and by absorption of other species.

Non-radiative relaxation process

Exist the possibility of the molecule to relax without emitting light, these phenomena are named as non-radiative relaxation processes. Four types of non-radiative process are known. Vibrational relaxation, refers to the loss of energy of a molecule in an excited vibrational state by moving to a lower vibrational energy level in the same electronic state. Internal conversion, in which the molecule in the ground vibrational level of an excited state moves directly into a higher vibrational level of a lower energy electronic state. Combining vibrational relaxations and internal conversion the molecule can get to the ground state with no emission of light. External conversion may also happen, here the energy is transferred to other components surrounding the molecule, like the solvent. Lastly, intersystem crossing, where a molecule in the ground vibrational level of an excited state passes into a higher vibrational level of a lower energy electronic state with a different spin state.

Resonance energy transfer

Resonance energy transfer occurs when the emission spectrum from a substance (donor) overlaps with the absorption spectrum from another substance (acceptor). So the energy from the donor in the excited state can be absorbed by the acceptor. The acceptor can be or not a luminescent object. It is important to notice that there is no photon intermediate in resonance energy transfer. The amount of energy transferred depends on the distance between the substances and how much their spectra overlap.

Steady-state vs time-resolved measurements

Luminescence can be measured with two types of techniques, using steady-state or time-resolved measurements. The most used is steady-state measurements, here, the sample is constantly illuminated and the emission intensity is likewise continuously recorded. Contrary, in time-resolved measurements the sample is exposed only to a pulse of light, this technique allows to measure intensity decays on the time scale of nanoseconds using high speed detectors. From this information it can be deducted that steady-state measurements are an average of time-resolved measurements. However, time-resolved measurements require more expensive and complex equipment than steady-state measurements.

Instrumentation for luminescence spectroscopy: spectrofluorometer

The devices used to measure luminescence are spectrofluorometers. Excitation and emission spectra can be usually recorded with all spectrofluorometers. The excitation spectrum is the dependence of emission intensity upon scanning the excitation wavelength measured at a single emission wavelength. On the other hand, emission spectrum show the wavelength distribution of an emission measured at a single excitation wavelength.

A general schematic representation of a spectrofluorometer is showed in Figure A.15. As the light source an arc xenon lamp is commonly used due to their higher intensity at all wavelengths above 250 nm, however other types of light can be used such as pulsed xenon lamps, mercury lamps, Xe-Hg lamps, LED light sources and laser diodes [16]. The spectrofluorometer is equipped with two monochromators, one for the excitation light and the other for the emission light. A monochromator is composed of diffraction gratings that disperse polychromatic light into the various colors or wavelengths. After passing through the emission monochromator, the emission light is detected by a photomultiplier tube and quantified with the suitable electronic devices. A beam splitter is used to split the excitation light; a part of the light is reflected to a reference cell that contains a reference luminescent object, this reference cell allows to correct changes in the intensity of the light source.

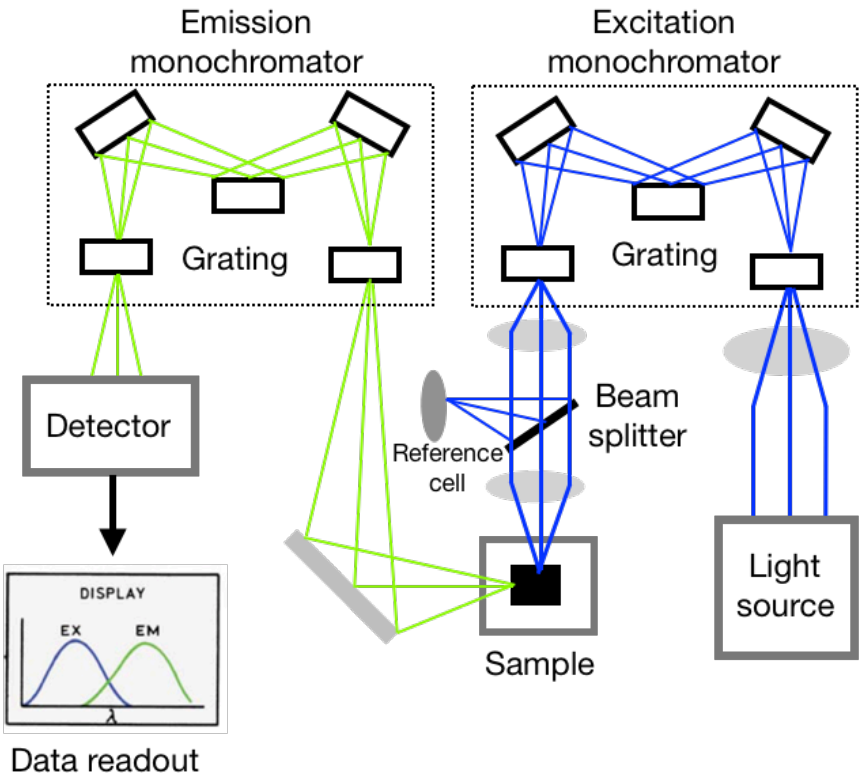

Figure A.15. Schematic representation of a spectrofluorometer.

A SPEX Fluorolog spectrofluorometer (0.22 m, Spex/1680) equipped with a Xenon Arc Lamp as the excitation source (Figure A.16b and c) and a photomultiplier detector (Hamamatsu/ R928) (Figure A.16a), was used to record the excitation and luminescence spectra reported in this thesis. A photodiode reference detector was used to record the reference spectrum, used to correct the excitation spectrum of the samples. The same excitation power was used to record the emission spectra which were corrected using the spectral response of the spectrofluorometer. When the luminescence spectra were recorded at different temperatures, the temperature was varied using a Peltier cooling/heating homemade system equipped with a temperature controller (AUTONICS - TZN4S), with resolution of 0.10 K. The temperature was varied in range (280–325 K).

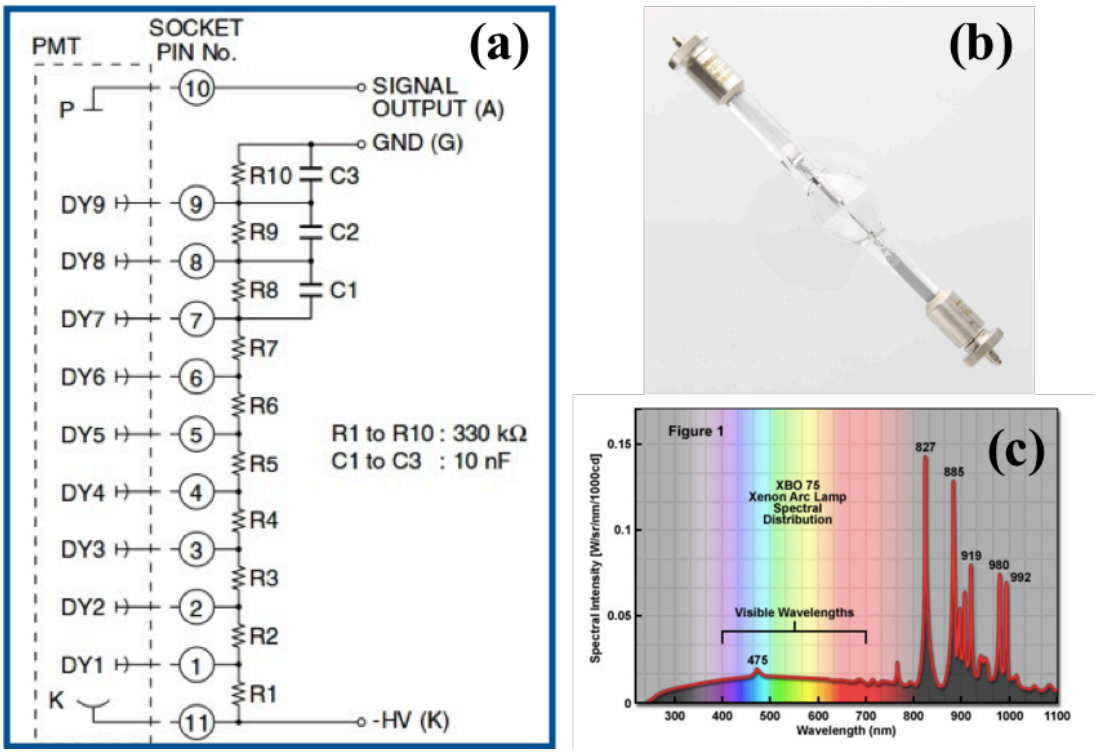

Figure A.16. (a) Schematic representation of the R928 photomultiplier detector, (b) Xenon Arc Lamp, (c) Emission spectrum of the Xenon Arc Lamp.

A.6 Spectral imaging fluorescence microscopy

Fluorescence imaging is a very important tool for the study of cell biology. Different fluorescent substances can be observed in a normal fluorescence microscope by using optical filters. Even though, this kind of microscopes can acquire fluorescence images at multiple

wavelengths, fluorescence emissions which spectra overlaps can produce interferences between emission signals.

Spectral imaging fluorescence microscopy also named fluorescence microspectroscopy is a technique capable of resolving the spectra of fluorescence images. This kind of microscopy combines fluorescence microscopy and spectroscopy to determine both the intensity and spectral properties of a sample for each pixel in an image [18]. Obtaining the emission spectra of a sample makes possible to overcome the emission overlap between fluorophores.

Fluorescence microspectroscopy can be useful to distinguish between measuring artifacts like autofluorescence, refractive index fluctuations, unsuspected fluorophore interactions, environmental inhomogeneities, and obtaining the desired signal from the probes of interest. Specifically, in biology live-cell imaging, immunofluorescence, clinical pathology, *in vivo* imaging, and drug discovery can be improved using fluorescence microspectroscopy. The information obtained can be used to determine the location of a specific probe with high spatial precision, besides, information about interactions between two or more probes can be obtained.

The acquisition of the image spectrum is done through the dispersion of the emitted light into its component wavelengths, then the intensity of emission at each wavelength or a narrow band of wavelengths is measured. The spectral resolution depends on the closest wavelengths that can be distinguished from one another.

Lambda Stacks

Spectral image lambda stack consists of a collection of images from the same specimen field acquired at different wavelength bands ranging from 2 to 20 nm of width. Traditional imaging in optical microscopy involves acquiring a single image for all the wavelengths response band of the detector. Then, an intensity value for every pixel in the image is showed. Contrary to this, the lambda stack provides a spectral value at each pixel to create a collection of images in which each image is acquired at different wavelength (or narrow band of wavelengths), or as collection of different wavelength values for each pixel location. Thus, plotting the pixel intensity on function of wavelength the emission spectrum of the probe spatially located it the pixel can be determined (Figure A.17). Generally, the lambda stacks are generated through a wavelength-scan where a set of narrow bandpass interference filters are used to generate the stack of imaged with each filter.

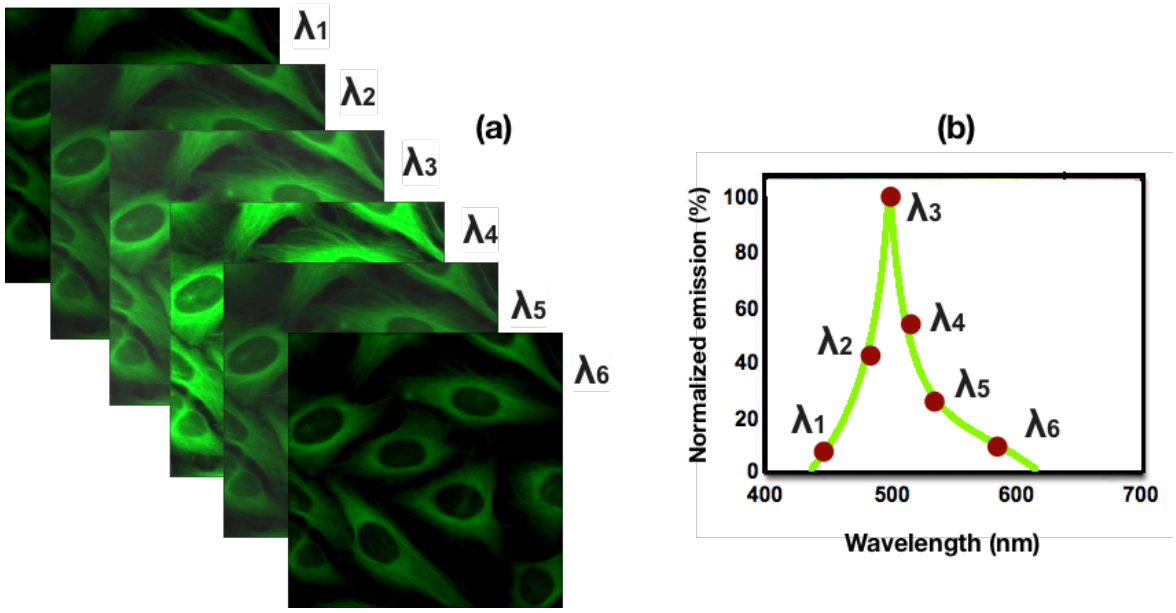

Figure A.17. Schematic representation of spectral imaging obtained from lambda stack. (a) lambda stack of images each of it collected at a certain wavelength ($\lambda_{1\text{-}6}$). (b) emission spectrum obtained from lambda stack.

Spectral imaging techniques

The main instrument needed to acquire fluorescence spectral images is a dispersive device that segregates the emission light into its component wavelengths. The most used instruments are laser scanning confocal microscopes equipped with spectral detectors that rely on prisms or diffraction gratings to disperse the emitted light, after being dispersed, the emission light is directed to a photomultiplier. Other instruments use interference filters, acousto-optical tunable filters (AOTFs), liquid crystal tunable filters (LCFTs) or prims coupled to gratings to disperse light. AOTF and LCTF filters have the advantage of have no moving parts and be faster in switching times.

LCTF transmit a specific narrow band of wavelengths when a voltage is applied to the liquid crystal. This type of filter device has the disadvantage that when non-polarized light is used (such as fluorescence emission) they exhibit a very low light throughput, however, the efficiency of LCTF can be increased by adding a polarizing beamsplitter before the LCTF. On the other hand, AOTF uses a crystalline compound such as tellurium dioxide which lattice can be deformed with acoustic waves, depending on the acoustic frequency, the crystal is deformed and produces a diffraction grating having a specific period that transmit a different wavelength. Similar to LCTF, AOTF presents a low light throughput when is putted right after the sample. Besides some image blur and wavelength shifts can be expected using AOTF.

Besides distinguish between the emission of one or another luminescent probe, imaging spectroscopy allows to modulate the resolution by changing the acquisition parameters. However, some drawbacks of this technique is that the complete spectrum of a probe must be recorded in all cases, besides if microspectroscopy is aimed a custom-built instrument is required in a normal confocal microscope because no specific microscope devices are commercially available nowadays.

The fluorescence microspectroscopy system (FMS) used in this thesis is built on an inverted microscope Nikon Eclipse TE 2000-E platform [19], Brightfield and Fluorescence field can be used with this microscope (Figure A.18). As an excitation source a high power 300 W xenon Lambda LS arc-lamp (Sutter, Novato, CA, USA) is used. All electronic microscope functions as well as camera control, shutters, stage, and focus, are controlled using a home-built software. For the confocal images acquired in this work a different microscope was used, a Nikon U-STEM microscope.

The fluorescence emission light that leaves the CARV unit can be directed to the camera in two ways. In the microspectroscopy mode the light goes through the liquid crystal tunable filter (LTCF) (Figure A.18a). In the other alternative, the light goes directly to the camera by inserting the movable mirrors for conventional microscopy operation (Figure A.18b). The lenses in the latter option are used to correct for the focus shift produced by passing light through the LCTF.

The microspectroscopic images are taken successively at different wavelengths, i.e. as a wavelength stack or λ-stack. The LCTF is Varispec VIS-10-20 from CRi (Woburn, MA, USA), tunable in the range from 400 to 720 nm, with the bandwidth of around 10 nm. The uncertainty in setting the wavelength value of LCTF is about 1 nm. The last component in the system is a highly sensitive QImaging Rolera MGi back- illuminated EMCCD (Electron Multiplying Charge-Coupled Device) (Surrey, BC, Canada) camera with a very high quantum efficiency (>90% between 500 and 700 nm), which is needed mainly because of the light intensity losses due to spinning disk and LCTF.

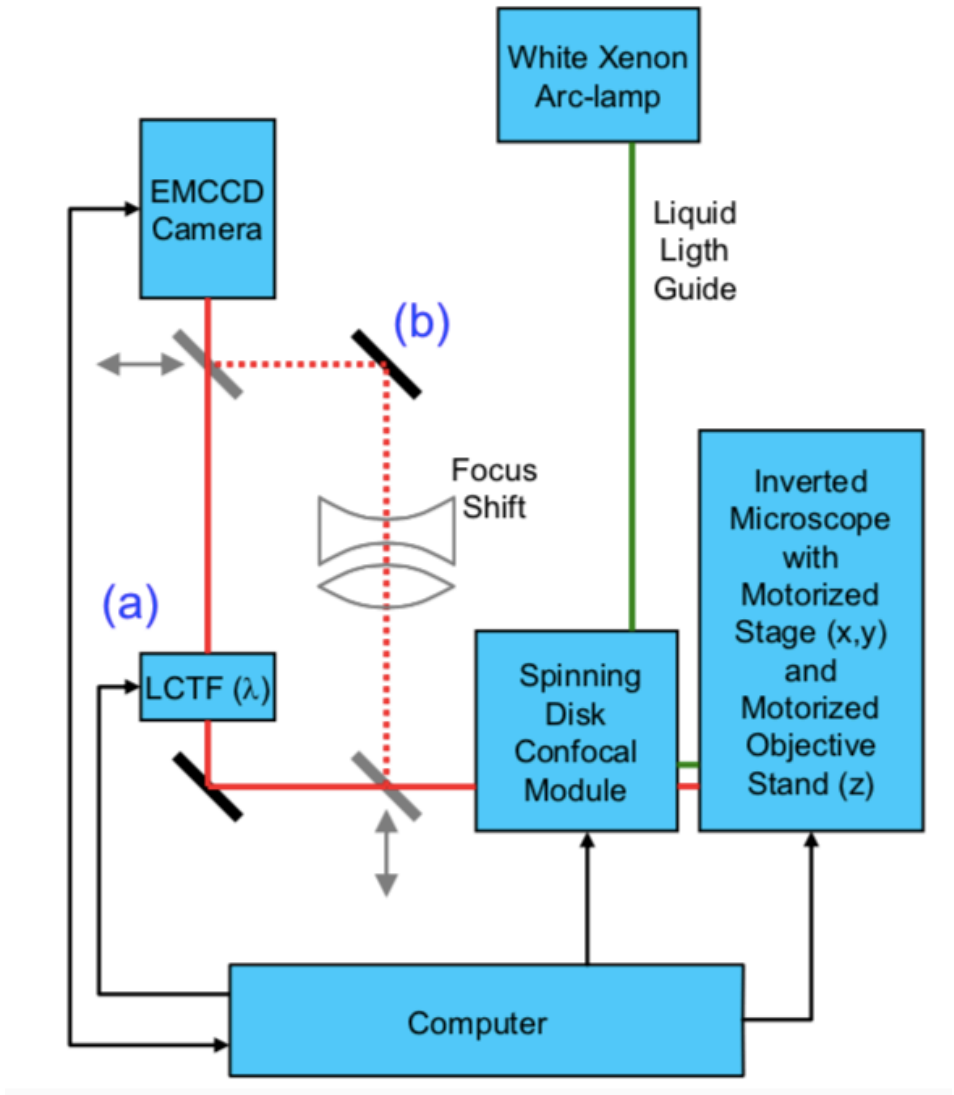

Figure A.18. Schematic presentation of the configuration of the confocal fluorescence microspectroscopy system. The confocal unit represented in this schema was not used during the confocal experiments due to its to low signal.

References

[1] W.B. Withe, INTRODUCTION TO VIBRATIONAL SPECTROSCOPIES AND NMR, in: R. Bundle, C.A. Evans Jr., S. Wilson (Eds.), Encycl. Mater. Charact., Elsevier, 1992. https://doi.org/10.1016/B978-0-08-052360-6.50040-0.

[2] Raman Instrumentation, in: Pract. Raman Spectrosc. - An Introd., John Wiley & Sons, Ltd, Chichester, UK, 2013. https://doi.org/10.1002/9781119961284.ch4.

[3] D.B. Chase, Fourier transform Raman spectroscopy, J. Am. Chem. Soc. 108 (1986).

https://doi.org/10.1021/ja00284a007.

[4] M. Bouchard, D.C. Smith, Catalogue of 45 reference Raman spectra of minerals concerning research in art history or archaeology, especially on corroded metals and coloured glass, Spectrochim. Acta Part A Mol. Biomol. Spectrosc. 59 (2003). https://doi.org/10.1016/S1386-1425(03)00069-6.

[5] T.H. Ly, M.-H. Chiu, M.-Y. Li, J. Zhao, D.J. Perello, M.O. Cichocka, H.M. Oh, S.H. Chae, H.Y. Jeong, F. Yao, L.-J. Li, Y.H. Lee, Observing Grain Boundaries in CVD-Grown Monolayer Transition Metal Dichalcogenides, ACS Nano. 8 (2014). https://doi.org/10.1021/nn504470q.

[6] K.-D. Park, M.B. Raschke, J.M. Atkin, Y.H. Lee, M.S. Jeong, Probing Bilayer Grain Boundaries in Large-Area Graphene with Tip-Enhanced Raman Spectroscopy, Adv. Mater. 29 (2017). https://doi.org/10.1002/adma.201603601.

[7] Y. Jian, W. Hu, Z. Zhao, P. Cheng, H. Haick, M. Yao, W. Wu, Gas Sensors Based on Chemi-Resistive Hybrid Functional Nanomaterials, Nano-Micro Lett. 12 (2020) 71. https://doi.org/10.1007/s40820-020-0407-5.

[8] L.H. Robins, D.L. Kaiser, L.D. Rotter, P.K. Schenck, G.T. Stauf, D. Rytz, Investigation of the structure of barium titanate thin films by Raman spectroscopy, J. Appl. Phys. 76 (1994). https://doi.org/10.1063/1.357978.

[9] P.Y. Yu, M. Cardona, Photoelectron Spectroscopy, in: Fundam. Semicond., Springer Berlin Heidelberg, Berlin, Heidelberg, 1999. https://doi.org/10.1007/978-3-662-03848-2_8.

[10] C.R. Brundle, C.A.. Evans, J.S. Wihon, INTRODUCTION TO ELECTRON EMISSION SPECTROSCOPIES, in: Encycl. Mater. Charact., Elsevier, 1992. https://doi.org/10.1016/B978-0-08-052360-6.50027-8.

[11] S.J. Pennycook, Transmission Electron Microscopy, in: Encycl. Condens. Matter Phys., Elsevier, 2005. https://doi.org/10.1016/B0-12-369401-9/00582-9.

[12] R.F. Egerton, Physical Principles of Electron Microscopy, 2016.

[13] J.R. Lakowicz, ed., Introduction to Fluorescence, in: Princ. Fluoresc. Spectrosc., Springer US, Boston, MA, 2006. https://doi.org/10.1007/978-0-387-46312-4_1.

[14] G. Stokes, On the change of refrangibility of light, Philos. Trans. R. Soc. London. 142 (1852). https://doi.org/10.1098/rstl.1852.0022.

[15] B.P. Kafle, Molecular luminescence spectroscopy, in: Chem. Anal. Mater. Charact. by Spectrophotometry, Elsevier, 2020. https://doi.org/10.1016/B978-0-12-814866-2.00009-9.

[16] J.R. Lakowicz, ed., Instrumentation for Fluorescence Spectroscopy, in: Princ.

Fluoresc. Spectrosc., Springer US, Boston, MA, 2006. https://doi.org/10.1007/978-0-387-46312-4_2.

[17] R. Kohli, Methods for Assessing Surface Cleanliness, in: Dev. Surf. Contam. Cleaning, Vol. 12, Elsevier, 2019: pp. 23–105. https://doi.org/10.1016/b978-0-12-816081-7.00003-6.

[18] T. Haraguchi, T. Shimi, T. Koujin, N. Hashiguchi, Y. Hiraoka, Spectral imaging fluorescence microscopy, Genes to Cells. 7 (2002) 881–887. https://doi.org/10.1046/j.1365-2443.2002.00575.x.

[19] Z. Arsov, I. Urbančič, M. Garvas, D. Biglino, A. Ljubetič, T. Koklič, J. Štrancar, Fluorescence microspectroscopy as a tool to study mechanism of nanoparticles delivery into living cancer cells, Biomed. Opt. Express. 2 (2011). https://doi.org/10.1364/BOE.2.002083.

Scientific contributions

The papers published in peer-reviewed journals and book chapters, including those strictly related to the research subject discussed in this PhD Thesis, are listed below. Additional scientific contributions include oral presentations and poster contributions in national and international conferences.

Scientific articles

- **Acosta, S**., Casanova Chafer, J., Sierra Castillo, A., Llobet, E., Snyders, R., Colomer, J. F., Ewels, C., Bittencourt, C. (2019). Low Kinetic Energy Oxygen Ion Irradiation of Vertically Aligned Carbon Nanotubes. *Applied Sciences*, *9*(24), 5342.

- **Acosta, S.**, Moreno-Aguilar, C., Hernández-Sánchez, D., Morales-Cruzado, B., Sarmiento-Gomez, E., Bittencourt, C., Sánchez-Vargas, L. O., Quintana, M. (2020). A few-layer graphene/chlorin e6 hybrid nanomaterial and its application in photodynamic therapy against Candida albicans. *Beilstein Journal of Nanotechnology*, *11*(1), 1054-1061.

- **Acosta, S.**, Sierra-Castillo, A., Colomer, J. F., Ewels, C., Snyders, R., Bittencourt, C. Thermal stability of oxygen functionalizations in v-CNTs introduced by low kinetic energy ion irradiation. (Under consideration in *Vacuum* journal).

- Sierra-Castillo, A., Haye, E., **Acosta, S.**, Bittencourt, C., Colomer, J. F. (2020). Synthesis and Characterization of Highly Crystalline Vertically Aligned WSe2 Nanosheets. *Applied Sciences*, *10*(3), 874.

- Borrero-González, L. J., **Acosta, S**., Bittencourt, C., Garvas, M., Umek, P., Nunes, L. A. O. (2020). Eu3+− doped titanium oxide nanoparticles for optical thermometry in the first biological window. *Optical Materials*, *101*, 109770.

- Primo, J. D. O., Bittencourt, C., **Morales, S. A.**, Sierra-Castillo, A., Colomer, J. F., Jaerger, S., Teixeira, V.C., Anaissi, F. J. (2020). Synthesis of Zinc Oxide nanoparticles by Ecofriendly Routes: Adsorbent for Copper Removal from Wastewater. *Frontiers in Chemistry*, *8*, 1100.

- Garvas, M., **Acosta, S.**, Urbančič, I., Koklič, T., Štrancar, J., Nunes, L. A. O., Guttmann, P., Umek, P., Bittencourt, C. Single cell temperature probed by Eu^{+3} doped TiO_2 nanoparticles luminescence. (2020). Nano Select.

- G. El Fidha, N. Bitri, F. Chaabouni, **Selene Acosta**, Carla Bittencourt, Juan Casanova-Chafer, Eduard Llobet. Physical and photocatalytic properties of sprayed Dy doped ZnO thin films under sunlight irradiation. *RSC Advances*, *11*(40), 24917-24925.

- Casanova, J. **Acosta, S**. Bittencourt, C. Llobet, E. (2020). Graphene-based Gas Sensors, Working Principles and Sensing Parameters. In: *Graphene* (pp. 459-486). Woodhead Publishing.

- **Acosta, S.,** Borrero-González, L. J., Umek, P., Nunes, L. A., Guttmann, P., & Bittencourt, C. (2021). Nd3+-Doped TiO2 Nanoparticles as Nanothermometer: High Sensitivity in Temperature Evaluation inside Biological Windows. *Sensors*, *21*(16), 5306.

- González, E., Casanova-Chafer, J., Alagh, A., Romero, A., Vilanova, X., **Acosta, S.,** ... & Llobet, E. (2021). On the Use of Pulsed UV or Visible Light Activated Gas Sensing of Reducing and Oxidising Species with WO3 and WS2 Nanomaterials. *Sensors*, *21*(11), 3736.

- Juan-Casanova Chafer, **Selene Acosta**, Carla Bittencourt and Eduard Llobet. Perovskite@Graphene nanohybrids for gas detection: a proof-of-concept. (In preparation).

- **Selene Acosta**, Polona Umek, Peter Guttmann and Carla Bittencourt. Characterization of Eu^{3+}-doped TiO_2 nanoparticles. (In preparation).

- **Selene Acosta,** Ayton Sierra, J. F. Colomer, Juan Casanova Chafer, Eduard Llobet, Polona Umek, Axel Hemberg, Carla Bittencourt. Decoration of CNTs with Pd-Ni nanoparticles. (In preparation).

- Sierra-Castilo, A., Haye, E., **Acosta, S.**, Bittencourt, C., Colomer, J.F. (2021) Atmospheric pressure chemical vapor deposition growth of vertically aligned SnS_2 and $SnSe_2$ nanosheets. (In preparation)

Oral presentations

- Temperature dependent photoluminescence of Nd^{+3} doped TiO_2: a suitable nanothermometer candidate. Virtual conference: XIII International Conference on Surfaces, Materials and Vacuum 2020. October 18-22, 2020.

- Application of a hybrid of graphene and chlorine e6 in photodynamic therapy against C. albicans. IV Meeting in Engineering and Materials Science. Industry, Technology and Scientific Innovation: Applied Materials. San Luis Potosí, México. September 19-21, 2018.

Poster presentations

- Mardi des Chercheurs (MdC), à l'Amphithéâtre Richard Stiévenart de l'UMONS, 5 mars 2019, Poster: TiO_2: Eu^{3+} nanoparticles as nanothermometers for single cell temperature measurements: synthesis, analysis and first tests.

- Training School on Nanomaterials and advanced characterization techniques at nanometer and atomic scale. Bucharest, Rumania. June 4-7, 2019. Poster presentation: Functionalization of vertically aligned carbon nanotubes with oxygen groups trough low energy ion implantation.

- Functionalizing vertically aligned carbon nanotubes with oxygen groups trough low energy ion implantation. Conference: Advances and applications in carbon related nanomaterials: From pure to doped structures including heteroatom layers, Benasque, Spain. December 9-13, 2019.

- Low Kinetic Energy Oxygen Ion Irradiation of Vertically Aligned Carbon Nanotubes. AVS 2020 International Twitter Poster Competition. July 8, 2020.

- Synthesis and characterization of neodymium doped TiO2 nanoparticles and their application as nanothermometers. Virtual BESSY@HZB User Meeting. December 10, 2020.